

12-2013

Characterization of the Elastic, Piezoelectric, and Dielectric Properties of Langatate At High Temperatures Up To 900 °C

Peter Mark Davulis

Follow this and additional works at: <http://digitalcommons.library.umaine.edu/etd>

 Part of the [Electrical and Computer Engineering Commons](#)

Recommended Citation

Davulis, Peter Mark, "Characterization of the Elastic, Piezoelectric, and Dielectric Properties of Langatate At High Temperatures Up To 900 °C" (2013). *Electronic Theses and Dissertations*. 2064.
<http://digitalcommons.library.umaine.edu/etd/2064>

This Open-Access Dissertation is brought to you for free and open access by DigitalCommons@UMaine. It has been accepted for inclusion in Electronic Theses and Dissertations by an authorized administrator of DigitalCommons@UMaine.

**CHARACTERIZATION OF THE ELASTIC, PIEZOELECTRIC, AND
DIELECTRIC PROPERTIES OF LANGATATE AT HIGH
TEMPERATURES UP TO 900 °C**

By

Peter Mark Davulis

B.A. University of Maine, 2006

B.S. University of Maine, 2010

A DISSERTATION

Submitted in Partial Fulfillment of the
Requirements for the Degree of
Doctor of Philosophy
(in Electrical and Computer Engineering)

The Graduate School

The University of Maine

December 2013

Advisory Committee:

Mauricio Pereira da Cunha, Professor of Electrical and Computer Engineering,
Advisor

Nuri Emanetoglu, Assistant Professor of Electrical and Computer Engineering

Donald Hummels, Professor of Electrical and Computer Engineering

Robert Lad, Professor of Physics

John Vetelino, Professor of Electrical and Computer Engineering

DISSERTATION ACCEPTANCE STATEMENT

On behalf of the Graduate Committee for Peter Mark Davulis, I affirm that this manuscript is the final and accepted dissertation. Signatures of all committee members are on file with the Graduate School at the University of Maine, 42 Stodder Hall, Orono, Maine.

Dr. Mauricio Pereira da Cunha, Professor of Electrical and Computer Engineering

May 7, 2013

© 2013 Peter Mark Davulis
All Rights Reserved

LIBRARY RIGHTS STATEMENT

In presenting this dissertation in partial fulfillment of the requirements for an advanced degree at The University of Maine, I agree that the Library shall make it freely available for inspection. I further agree that permission for “fair use” copying of this dissertation for scholarly purposes may be granted by the Librarian. It is understood that any copying or publication of this dissertation for financial gain shall not be allowed without my written permission.

Peter Mark Davulis

May 7, 2013

CHARACTERIZATION OF THE ELASTIC, PIEZOELECTRIC, AND DIELECTRIC PROPERTIES OF LANGATATE AT HIGH TEMPERATURES UP TO 900 °C

By Peter Mark Davulis

Dissertation Advisor: Dr. Mauricio Pereira da Cunha

An Abstract of the Dissertation Presented
in Partial Fulfillment of the Requirements for the
Degree of Doctor of Philosophy
(in Electrical and Computer Engineering)
December 2013

The acoustic wave constants of the piezoelectric crystal langatate (LGT, $\text{La}_3\text{Ga}_{5.5}\text{Ta}_{0.5}\text{O}_{14}$) are characterized up to 900 °C for the first time in this work, targeting the development of high-temperature acoustic wave (AW) devices. There is a pressing need for sensors and frequency control systems that operate at high temperature, above 200 °C, and in harsh environments, with applications found in the industrial process control, automotive, aerospace, and power generation industries and in gas and petroleum exploration. Surface acoustic wave (SAW) and bulk acoustic wave (BAW) devices, using piezoelectric crystals such as LGT, have the capability to provide the desired high-temperature sensors for temperature, pressure, strain, and gas species measurement. Langatate, a member of the langasite crystal family, retains crystal structure up to the melting point at 1470 °C and has higher piezoelectric coupling than quartz and langasite; however, a full set of LGT AW constants required for SAW and BAW device design had not previously been characterized above 150 °C.

In this work, the LGT elastic, piezoelectric, and dielectric constants have been extracted up to 900 °C, providing a complete set of AW constants. The LGT elastic and piezoelectric constants were measured using resonant ultrasound spectroscopy (RUS) and determined by fitting predicted resonance modes with measured spectra of LGT samples heated in a custom-fabricated high-temperature furnace. The LGT dielectric permittivity and conductivity constants were extracted from parallel-plate capacitor measurements. Langatate SAW devices were fabricated and the measured properties up to 900 °C were found to be in very good agreement with the predictions, thus validating the extracted LGT high-temperature constants.

The newly determined LGT constants were used to locate SAW orientations for high-temperature operation by calculating the SAW velocity and temperature coefficient of delay (TCD) up to 900 °C along multiple regions in space. Multiple SAW orientations were identified with potentially desirable properties such as turnover temperatures, TCD=0, at elevated temperatures up to 500 °C, and either low or high sensitivity to temperature. Differential high-temperature sensors utilizing a suite of SAW sensors on the same wafer were proposed and experimentally demonstrated. Additionally, BAW orientations were identified with turnover temperatures ranging from 100 °C to 550 °C.

DEDICATION

To my parents, John and Theresa Davulis.

ACKNOWLEDGEMENTS

I thank my advisor Dr. Mauricio Pereira da Cunha for his guidance on scientific research, engineering, communication, and many other aspects. I am grateful for his mentorship and support over these past years. I thank Dr. Robert Lad, Dr. John Vetelino, Dr. Nuri Emanetoglu, and Dr. Donald Hummels for serving on my advisory committee and for their comments, difficult questions, and insights on my work.

I am grateful to Dr. Alberto Canabal, Dr. Scott Moulzolf, Thomas Moonlight, Dr. George Bernhardt, Dr. David Frankel, Michael Call, Roby Behanan, Eric Martin, and George Harris at the Laboratory for Surface Science & Technology for device fabrication, measurement assistance, technical advice, and a friendly atmosphere for learning. I wish to thank Eric Beenfeldt for his advice and helping with the cutting and polishing of the langatate samples. Amit Shyam and Edgar Lara-Curzio at the High Temperature Materials Laboratory at the Oak Ridge National Laboratories were very helpful in teaching me about resonance ultrasound spectroscopy.

Blake Sturtevant provided much help with the aligning, cutting, and polishing of the SAW devices and on many other aspects of academic research. I thank Bennett Meulendyk, Thomas Pollard, Evan Dudzik, Thomas Kenny, Dana Gallimore, and the other University of Maine students who have helped me in my research and coursework. I would also like to thank Patricia Paul, Susan Ashley, Janice Gomm, Steven Hokschi, Susan Niles, Laura Hall, and Cindy Plourde.

My family and friends have provided great support and encouragement, without which I would not have been able to get to this point. I am especially grateful for my parents, John (1945-2012) and Theresa, for their support, encouragement, and love.

Financial support for this work was provided in part by DEPSCoR grant # FA9950-07-1-0519 (capacitance measurement and data extraction), National Science Foundation Grant # ECS 0134335 (laboratory equipment purchasing), Petroleum

Research Fund Grant ACS PRF # 42747-AC10 (RUS equipment purchase and set-up, numerical programing, and measurement), and Air Force Office AFO Grants # FA8650-05-D-5807, # FA9550-07-1-0519, and # F33615-03-D-5204 (RUS measurement and data extraction, SAW device fabrication and testing, SAW orientation identification), and DOE/NETL # DE-FE0007379TDD (BAW orientation analysis). The research work at the High Temperature Materials Laboratory was sponsored by the Assistant Secretary for Energy Efficiency and Renewable Energy, Office of Vehicle Technologies, as part of the High Temperature Materials Laboratory User Program, Oak Ridge National Laboratory, managed by UT-Battelle, LLC, for the U.S. Department of Energy under contract number DE-AC05-00OR22725. I would like to thank the IEEE Ultrasonics, Ferroelectrics, and Frequency Control Society Administrative Committee, the University of Maine Graduate Student Government, and the Nancy Morse Dysart '60 Travel Award for travel funds enabling me to present the work at international conferences. I have received support from the University of Maine Summer Graduate Research Fellowship and the University of Maine Provost Fellowship. I would also like to thank the NSF Research Experience for Undergraduates program for helping me get started in academic research prior to graduate school.

TABLE OF CONTENTS

DEDICATION.....	iv
ACKNOWLEDGEMENTS.....	v
LIST OF TABLES.....	xii
LIST OF FIGURES.....	xiv
LIST OF ABBREVIATIONS.....	xviii

Chapter

1. MOTIVATION AND BACKGROUND	1
1.1. Motivation Overview.....	1
1.2. The Need for High-Temperature Sensors and Frequency Control.....	3
1.3. Alternative High-Temperature Sensor and Device Technologies.....	6
1.4. High-Temperature Frequency-Control and Filtering Applications.....	10
1.5. Acoustic Wave Materials for High-Temperature Applications.....	11
1.5.1. Piezoelectric Crystals with Limited High-Temperature Applicability	12
1.5.2. Piezoelectric Crystals for High-Temperature Operation	17
1.5.3. Langatate: State-of-the-Art	21
1.5.3.1. Development and Growth of Langatate.....	21
1.5.3.2. Langatate Characterization Below 250 °C	24
1.5.3.3. Langatate Characterization at Elevated Temperatures Above 250 °C	26

1.5.4.	Thin-Film Piezoelectric Materials	29
1.5.5.	Thin-Film Electrodes for High-Temperature Operation.....	30
1.6.	Crystal Acoustic Wave Properties Characterization Techniques for High Temperature	31
1.6.1.	Fundamental Crystal Properties for Acoustic Wave Technology.....	31
1.6.2.	Extraction Techniques for High-Temperatures Elastic and Piezoelectric Constants	33
1.6.3.	Extraction Techniques for High-Temperature Permittivity and Conductivity.....	40
1.7.	Objective and Dissertation Organization	43
2.	DIELECTRIC PERMITTIVITY AND CONDUCTIVITY	46
2.1.	Dielectric Permittivity and Conductivity Extraction Method.....	46
2.1.1.	Complex Permittivity and Losses	46
2.1.2.	Dielectric Extraction with Parallel-Plate Capacitors	49
2.1.3.	Compensating for Electric Field Fringing.....	52
2.1.4.	Temperature Dependence and Curve Fitting Process.....	54
2.2.	LGT Dielectric Permittivity Extraction Process.....	57
2.2.1.	LGT Capacitor Fabrication	57
2.2.2.	Capacitance Measurement Setup.....	58
2.2.3.	Dielectric Extraction Calculations	61

2.3.	LGT Dielectric Permittivity Results	63
2.4.	Conclusions	75
3.	RESONANT ULTRASOUND SPECTROSCOPY	78
3.1.	Background	78
3.2.	Resonant Spectra Calculation	85
3.2.1.	Mathematical Formulation	85
3.2.2.	Numerical Implementation	91
3.3.	RUS Experimental Process	94
3.3.1.	RUS Sample Preparation	94
3.3.2.	RUS Measurement System	96
3.3.3.	RUS Fitting and Constants Extraction Process	100
3.4.	RUS Results	105
3.4.1.	Validation of RUS Technique	105
3.4.2.	LGT High-Temperature Resonant Spectra	106
3.4.3.	LGT Extracted Stiffened Elastic Constants	108
3.4.4.	LGT Extracted Elastic and Piezoelectric Constants	111
3.5.	Conclusions	121
4.	VERIFICATION OF HIGH-TEMPERATURE LGT CONSTANTS	122
4.1.	Verification Methodology	122
4.2.	Calculation of SAW Propagation Properties	124

4.3.	High-Temperature SAW Fabrication and Characterization	127
4.3.1.	SAW Device Fabrication.....	127
4.3.2.	High-Temperature SAW Characterization	131
4.4.	Comparison of Predicted and Measured SAW Properties Results	135
4.5.	Conclusions	144
5.	HIGH-TEMPERATURE SAW ORIENTATIONS ON LANGATATE.....	146
5.1.	Introduction	146
5.2.	High-Temperature SAW Properties Calculation	148
5.3.	High-Temperature LGT SAW Properties and Orientations	149
5.3.1.	LGT SAW Electromechanical Coupling	149
5.3.2.	LGT SAW TCD at High Temperature.....	153
5.3.3.	LGT SAW Frequency Change at High Temperature	153
5.3.4.	LGT SAW Planes for High-Temperature Sensor Suites	162
5.3.5.	Demonstration of LGT Differential SAW Sensors on a Single Wafer	164
5.4.	Conclusions	165
6.	HIGH-TEMPERATURE BAW ORIENTATIONS ON LANGATATE	167
6.1.	Introduction	167
6.2.	Bulk Acoustic Wave Calculation Method.....	168

6.3. High-Temperature LGT BAW Properties and Orientations	169
6.3.1. LGT BAW Orientations with Zero TCF at High Temperature	170
6.3.2. LGT BAW Orientations with Transverse-Shear Modes	175
6.4. Conclusions	179
7. CONCLUSIONS AND SUGGESTED FUTURE WORK	180
7.1. Summary of Work and Conclusions.....	180
7.2. Statement of Contribution.....	183
7.3. Suggested Future Work.....	184
REFERENCES.....	189
APPENDIX A – ACOUSTIC CONSTANTS OF CRYSTAL CLASS 32	226
APPENDIX B – DIELECTRIC CONSTANTS FITTING AND EXTRAC- TION DETAILS	228
APPENDIX C – ADDITIONAL RUS CALCULATION, FABRICATION, AND MEASUREMENT DETAILS	233
BIOGRAPHY OF THE AUTHOR	253

LIST OF TABLES

Table 2.1. High-temperature LGT real dielectric permittivities and temperature coefficients from 25 °C to 900 °C	69
Table 2.2. Room-temperature LGT relative dielectric permittivities from the literature.....	71
Table 2.3. High-temperature LGT imaginary dielectric permittivity	73
Table 2.4. High-temperature LGT conductivity parameters.....	75
Table 3.1. Unit scaling used for RUS calculations.....	95
Table 3.2. LGT RUS sample dimensions	97
Table 3.3. Preliminary LGT elastic, piezoelectric, and stiffened elastic constants extracted by RUS	110
Table 3.4. LGT elastic and piezoelectric constants and temperature coefficients from 25 °C to 900 °C	115
Table 3.5. LGT elastic and piezoelectric constants from the literature at room temperature	120
Table 4.1. Disagreement between predicted and measured LGT SAW properties for plane (90°, 23°, Ψ) from 25 °C to 900 °C	143
Table 4.2. Disagreement between predicted and measured LGT SAW turnover temperatures for plane (90°, 23°, Ψ).....	145
Table 5.1. LGT SAW orientations with low or zero TCD at 400 °C.....	160
Table 5.2. LGT SAW orientations with low or zero TCD at 500 °C.....	161
Table 5.3. LGT SAW orientations with largest TCD at 500 °C	161

Table 6.1. LGT BAW mode TCF ranges at selected temperatures.....	171
Table C.1. Voigt index notation	241
Table C.2. Mode grouping of the Legendre polynomial basis functions.....	244

LIST OF FIGURES

Figure 2.1. Fabricated LGT capacitors	54
Figure 2.2. UMaine capacitance measurement setup	60
Figure 2.3. High-temperature capacitance measurement fixture with high- temperature cables	61
Figure 2.4. Example LGT measured capacitor admittances.....	64
Figure 2.5. LGT measured permittivity and best-fit surface	65
Figure 2.6. Extracted LGT real permittivity ϵ_{R11}	67
Figure 2.7. Extracted LGT real permittivity ϵ_{R33}	68
Figure 2.8. Extracted LGT imaginary permittivities.....	72
Figure 2.9. High-temperature LGT conductivity	74
Figure 2.10. LGT loss tangent, $\tan \delta$	76
Figure 3.1. RUS measurement system types.....	82
Figure 3.2. RUS system with high-temperature buffer rods	84
Figure 3.3. RUS high-temperature furnace assembly at UMaine	99
Figure 3.4. Example LGT RUS spectrum at 25 °C of LGT10 sample	108
Figure 3.5. Extracted high-temperature LGT stiffened elastic constants.....	112
Figure 3.6. Extracted high-temperature LGT elastic constants.....	116
Figure 3.7. Extracted high-temperature LGT piezoelectric constants	118
Figure 4.1. LGT SAW coupling, K^2 , along plane (90°, 23°, Ψ) at high temperature.....	124

Figure 4.2. Cutting of LGT boule for SAW devices	129
Figure 4.3. Polishing LGT wafers with an alumina slurry	130
Figure 4.4. Fabricated LGT SAW delay lines	132
Figure 4.5. High-temperature LGT SAW device fixture	132
Figure 4.6. Example LGT SAW S_{21} response for $(90^\circ, 23^\circ, 119^\circ)$ at 25°C	134
Figure 4.7. Comparison of measured and predicted v_p and TCD for LGT SAW orientation $(90^\circ, 23^\circ, 0^\circ)$	136
Figure 4.8. Comparison of Measured and Predicted v_p and TCD for LGT SAW Orientation $(90^\circ, 23^\circ, 13^\circ)$	137
Figure 4.9. Comparison of measured and predicted v_p and TCD for LGT SAW orientation $(90^\circ, 23^\circ, 48^\circ)$	138
Figure 4.10. Comparison of measured and predicted v_p and TCD for LGT SAW orientation $(90^\circ, 23^\circ, 77^\circ)$	139
Figure 4.11. Comparison of measured and predicted v_p and TCD for LGT SAW orientation $(90^\circ, 23^\circ, 119^\circ)$	140
Figure 4.12. Comparison of measured and predicted v_p and TCD for LGT SAW orientation $(90^\circ, 23^\circ, 123^\circ)$	141
Figure 4.13. Measured TCD for LGT SAW orientations $(90^\circ, 23^\circ, \Psi)$	142
Figure 5.1. Contour plots of predicted LGT SAW K^2 for Region A, Euler angles $(0^\circ, \Theta, \Psi)$	150
Figure 5.2. Contour Plots of predicted LGT SAW K^2 for Region B, Euler angles $(90^\circ, \Theta, \Psi)$	151

Figure 5.3. Contour Plots of predicted LGT SAW K^2 for Region C, Euler angles (Φ , 90° , Ψ).....	152
Figure 5.4. Contour plots of predicted LGT SAW TCD for Region A, Euler angles (0° , Θ , Ψ)	154
Figure 5.5. Contour plots of predicted LGT SAW TCD for Region B, Euler angles (90° , Θ , Ψ)	156
Figure 5.6. Contour plots of predicted LGT SAW TCD for Region C, Euler angles (Φ , 90° , Ψ).....	158
Figure 5.7. Contour plots of predicted LGT SAW frequency change from 400°C to 800°C	163
Figure 5.8. Measured differential frequency for LGT delay line sensor pair (90° , 23° , 0°) and (90° , 23° , 48°) up to 900°C	166
Figure 6.1. Definition of electric field, Ψ_E , angle for lateral-field excitation	170
Figure 6.2. Contour plots of predicted LGT BAW velocity at 100°C	171
Figure 6.3. Contour plots of predicted LGT BAW $QS2$ -mode coupling	172
Figure 6.4. Predicted LGT BAW $QS2$ -mode high-temperature TCF	173
Figure 6.5. Predicted LGT BAW $QS2$ -mode turnover temperatures between 100°C and 550°C	174
Figure 6.6. Predicted LGT BAW $QS1$ -mode TCF and coupling at 150°C	176
Figure 6.7. LGT BAW longitudinal components of the eigenvector for $QS1$ and $QS2$ Modes.....	177
Figure 6.8. LGT BAW $S2$ TSM coupling for (0° , Θ , 90°) at 25°C	179

Figure C.1. LGT samples polished for RUS	246
Figure C.2. Example LGT RUS spectra from 25 to 1100°C for selected modes of sample LGT10.....	251

LIST OF ABBREVIATIONS

C	Capacitance
C_{meas}	Measured Capacitance
D_i	Electric displacement tensor
E_a	Activation energy
E_i	Electric field tensor
J	Current density
L	Lagrangian function
S_l, S_m, S_c	Scale factors for the length, mass, and current
S_{ij}, S_p	Strain tensor
T	Temperature
$TC_x^{(n)}$	n^{th} temperature coefficient for parameter x
T_0	Reference temperature
Y	Admittance
Δ	Differential temperature with respect to T_0
Δ_a, Δ_b	Differential temperature over temperature region a or b
Ψ	Basis function for RUS calculations
α'	Fringing parameter of real permittivity
α''	Fringing parameter of imaginary permittivity

α_σ	Fringing parameter of conductivity
ϵ_0	Dielectric permittivity of free space
ϵ''_{ij}	Imaginary dielectric permittivity constant tensor
ϵ'_{ij}	Real dielectric permittivity constant tensor
ϵ_{meas}	Measured permittivity
ω	Angular frequency
$\overline{P}_\alpha(x)$	Normalized Legendre polynomial with degree α
ρ	Mass density
σ_{ij}	Conductivity tensor
$\mathcal{T}_{ij}, \mathcal{T}_p$	Stress tensor
D (superscript)	At constant electric displacement
E (superscript)	At constant electric field
S (superscript)	At constant strain
$_R$ (subscript)	Permittivity relative to ϵ_0
$a^{(p)}, \mathbf{a}, b^{(r)}, \mathbf{b}$	Basis function coefficient vectors
c_{ijkl}, c_{pq}	Elastic stiffness constant tensor
e_{ijk}, e_{ip}	Piezoelectric constant tensor
f	Frequency
h	Wafer thickness
j	Imaginary number

r	Parallel-plate electrode radius
s_{pq}	Elastic compliance constant tensor
v_i	Particle velocity tensor
(α, β, γ)	Integer powers or degrees of RUS basis functions
τ (superscript)	At constant stress
$\tan \delta$	Loss tangent
AW	Acoustic wave
BAW	Bulk acoustic wave
HTML	High Temperature Materials Laboratory at the Oak Ridge National Laboratories
LFE	Lateral-field excitation
LGN	Langanite crystal
LGS	Langasite crystal
LGT	Langatate crystal
LGX	Langasite-family of crystals (LGS, LGT, and LGN)
OLS	Ordinary Least Squares
PZT	Lead zirconate titanate
QCM	Quartz crystal monitor or microbalance
RUS	Resonance ultrasound spectroscopy
SAW	Surface acoustic wave

SEC	Stiffened elastic constants
TCD	Temperature coefficient of delay
TCE	Temperature coefficient of expansion
TCF	Temperature coefficient of frequency
TCV	Temperature coefficient of velocity
TFE	Thickness-field excitation
TLS	Total Lease Squares
UEC	Unstiffened elastic constants
UMaine	University of Maine

Chapter 1

MOTIVATION AND BACKGROUND

1.1 Motivation Overview

There has been increasing demand for sensors and electronic systems that operate at high temperatures ($>200^{\circ}\text{C}$) and in harsh environments that is fueling research in high-temperature materials [1–8]. The growing demand for high-temperature devices has been spurred by recent factors such as the rising cost and scarcity of oil, the increasing push for high efficiency and low emission power generation, manufacturing, and transportation, and the need to monitor and reduce the cost of gas turbine maintenance [5, 8–10]. High-temperature applications are found in the automotive, aerospace, power generation, nuclear, gas and petroleum exploration, nondestructive testing (NDT), metal and ceramic part manufacturing, and industrial process control industries [7, 8, 11–15]. These applications often involve harsh environments that experience temperatures above 500°C and up to 1600°C for some applications, high pressure, corrosion, and vibration [9, 10, 16]. The desired harsh-environment sensors include pressure, temperature, vibration, and strain measurement, as well as gas species identification and quantification. Selectivity, sensitivity, durability, reliability, small size, and wireless interrogation are some of the desired characteristics of high-temperature sensors [1, 5]. Additionally, there is a need for frequency control and filtering for communication and electronic systems that operate at high temperature [7].

Current sensor technologies are unable to simultaneously address the needs of wireless and high-temperature operation, as discussed next. Sensors based on semiconductor devices and microelectromechanical systems (MEMS) can communicate wirelessly can be used up to around 600°C but require a power source such as batteries [16–19]. Energy harvesting from RF or vibrational energy has been used to create

batteryless wireless sensors [20] but requires rectifying diodes and have reduced performance above 600 °C [17–19]. Thermocouples, piezoresistive strain-gauges, and fiber optics can be used above 1000 °C but require wires that often are expensive to install in harsh-environments, prone to failure, and need regular maintenance [5]. Non-contact ultrasonic transceivers can probe acoustic properties of high-temperature gas or liquid media to sense temperature and pressure averaged over the acoustic medium so are not accurate for environments with gradient fields [21, 22]. Optical pyrometry techniques are used to measure the temperature of an objects hotter than 500 °C using the emitted thermal radiation, but the process requires line-of-sight, has limited accuracy that depends on the object surface and the surrounding environment, and the utilized optic fiber probes are prone to thermal shock, chemical attack, and corrosion [23].

Acoustic wave (AW) devices, such as bulk acoustic wave (BAW), surface acoustic wave (SAW), solidly mounted resonators (SMR), and film bulk acoustic resonator (FBAR) devices, are currently used as sensitive, accurate, small, and wireless sensors and as small, reliable, high-performance filters and frequency-control devices [24–30]. Acoustic wave devices fabricated with common piezoelectric substrates, such as quartz, lithium niobate, lithium tantalate, and lead zirconate titanate (PZT), cannot operate in high-temperature environments above 500 °C due to phase transitions, material degradation, or significant acoustic wave propagation losses. However, new piezoelectric crystals, such as gallium orthophosphate (GaPO_4) and the langasite family of crystals, that operate at high temperatures are being investigated and utilized for harsh environment applications [2, 6, 7, 31, 32]. Specifically, the langasite family of crystals (langasite, LGS, $\text{La}_3\text{Ga}_5\text{SiO}_{14}$; langanite, LGN, $\text{La}_3\text{Ga}_{5.5}\text{Nb}_{0.5}\text{O}_{14}$; langatate, LGT, $\text{La}_3\text{Ga}_{5.5}\text{Ta}_{0.5}\text{O}_{14}$), collectively called LGX, retain piezoelectricity up to their melting points around 1470 °C, have higher piezoelectric coupling than quartz, and have proven AW temperature-compensated orientations around room temperature [31, 33–38]. Among the LGX crystals, LGT has higher piezoelectric

coupling, lower acoustic losses, and less variation in acoustic properties across a wafer than LGS and is easier to grow with less twinning defects than LGN [39–43].

The design and simulation of AW devices at elevated temperatures require the acoustic wave properties of the piezoelectric substrate to be characterized in the target temperature range. Specifically the density, thermal expansion, dielectric permittivity, elastic stiffness, and piezoelectric constants are needed. A full set of the LGT dielectric permittivity, elastic stiffness, and piezoelectric constants have not previously been measured above 150 °C, preventing the exploitation of LGT properties at high temperatures. The high-temperature set of AW constants allows the prediction of LGT AW behavior and the selection of crystal orientations for harsh environment applications.

1.2 The Need for High-Temperature Sensors and Frequency Control

The increasing demand for and rising expense to extract fossil fuels creates a need for technological advances, such as extended reach and deep sea drilling, which require improved sensors that operate in these harsh environments [44, 45]. Starting with the energy crisis in the 1970’s oil industries expressed their need for high-temperature sensors and electronics for deep drilling and geothermal exploration [1]. Recent reductions in the cost of wireless communication and increases in the expense of wire installations has improved the payoff of wireless sensors [5, 46]. Robust, low-maintenance wireless sensors that can operate in down-hole harsh environments with extreme temperatures between 300 °C and 600 °C, humidity, dust, and corrosion will reduce the installation and operation costs compared to wired sensors, and improve monitoring of remote areas for increased safety and reduced shutdowns [16, 45, 46]. In 1997 the President’s Committee of Advisors on Science and Technology Panel of Energy Research and Development reported that the adoption of wireless sensors for energy generation could improve efficiency by 10 % and reduce emissions by 25 % [47].

Wireless sensors have been increasingly adopted due to proven reliability and usefulness [8].

New high-temperature fuel cells are being developed for energy generation and would have improved performance and longevity with the use of temperature and pressure sensors. The National Energy Technology Laboratory (NETL) at the Department of Energy (DOE) is focusing its research efforts on two types of high-temperature fuel cells: molten-carbonate fuel cells (MCFC), which operate at 650 °C; and solid-oxide fuel cells (SOFC), which operate between 600 °C and 1000 °C [10, 48]. High-temperature fuel cells can use a wider variety of fuel and are more applicable to integration with fuel reforming, which takes place between 600 °C and 900 °C, and in hybrid power systems, which use gas turbine engines in conjunction with fuel cells for higher efficiency [10, 49]. Temperature and gas sensors are useful in high temperature fuel cells for optimal control, detection of gas leaks, and quantification of emissions [48, 50]. Rapid pressure measurements are also needed because fuel cells contain brittle ceramic components that are prone to damage if due to rapid pressure changes, especially in hybrid systems where the exhaust of a turbine engine use to feed fuel into the fuel cell [10].

There is a growing need for harsh-environment and high-temperature sensors in modern jet turbine engines in the aerospace and energy generation industries [9, 51, 52]. Small, reliable, and wireless sensors to measure blade temperature, air temperature, static pressure, dynamic pressure, static strain, dynamic strain, vibration, and to identify and quantify exhaust gas species are in high demand for gas turbine engines [9, 51, 52]. The in-situ wireless sensors are needed to validate engine model simulations for improved design, provide real-time diagnostics for improved efficiency and performance, and enable health monitoring for condition based maintenance [9]. Modern and next-generation turbine engines are targeting operation at higher temperatures and larger compression ratios with more exacting operation,

design, and material standards that need accurate sensors for the measurement of blade and gas temperatures to prevent damaging the engine parts with excessive temperature [23].

The accurate measurement of critical engine parameters is necessary to reduce development time and cost of engine design, optimization, verification of engine simulations, and validation of the finished product. Engine validation is required to prove flight worthiness and can require up to 3000 pieces of instrumentation but current technologies using wired sensors are expensive, time-consuming to install, and have short sensor lifetimes which limit the testing procedure [9, 51, 53]; the entire engine certification process can take 6 to 9 months and cost several million dollars [51]. Wireless sensors operating in such harsh environments would reduce the time, cost, and complexity of installation.

The use of gas turbines for power generation has grown recently due to their efficiency and low emissions. Strict emission restrictions of NO_x require operation with lean combustion, low fuel-to-air ratio, and this requires sensors to monitor combustion dynamics [10, 52–55].

The corrosive, extremely hot, high pressure, and high vibration environment inside a turbine engine requires robust sensors to survive harsh conditions. Internal temperatures range from -40°C to 100°C in the front fan, 150°C to 425°C in the compressor, up to 1650°C in the high pressure turbine, and around 550°C at the exhaust [9, 51]. Next generation engines will have even higher temperatures for increased efficiency; however, there is a delicate balance between higher performance and degradation of engine parts, thus the engine temperatures need to be accurately measured and controlled [23]. The revolving parts in a typically gas turbine engine experience centripetal acceleration up to $100\,000\,g$ and rotations in the range of $20\,000\text{ rpm}$ to $60\,000\text{ rpm}$ [9, 51]. Case vibrations are on the order of $100\,g$ at frequencies below 20 kHz and the acoustic output of the engine is 120 dB Hz^{-1} up

to 10 kHz [9]. Sensors in a turbine engine need to survive absolute pressures up to 4.8 MPa (700 psi, 48 atm) [9].

Industrial process control of high-temperature processes, such as annealing, curing, refining, and baking of epoxies, metals, and ceramics, require accurate temperature measurement [56]. Currently, sensors measure only the temperature of the environment surrounding the part or material of interest, causing uncertainty and inaccuracy due to temperature gradients and thermal time constants. Wireless temperature and pressure sensors on the surface of or embedded in the parts during manufacture will give more accurate measurements of the instantaneous temperature and are needed to improve the process control for the reduction of energy expenditures [16, 57].

The use of high-temperature sensors, actuators, and electronics in the automotive industry is continually increasing due to their benefits on the efficiency and reliability of combustion engines [54, 58]. The sensors are used to measure the temperature, pressure, and other engine conditions and must be able to operate in a 150 °C environment with multiple thermal cycles. Engine temperatures are also being pushed higher for improved fuel efficiency and lower emissions so sensors requirements are becoming more stringent [1, 58].

Quartz crystal microbalances (QCM) are currently used to monitor the rate of thin-film deposition but are limited to an upper temperature limit of 573 °C by the $\alpha - \beta$ transition of quartz [32, 59, 60]; the temperature limitations of quartz will be discussed on page 12 in Section 1.5.1. Piezoelectric crystals that can survive higher temperatures would allow for in-situ rate monitoring of films deposited at high temperatures [61, 62].

1.3 Alternative High-Temperature Sensor and Device Technologies

Despite the demand for high-temperature sensors, current technologies are unable to simultaneously satisfy the requirements of durability, reliability, accuracy, and

wireless operation at temperatures above around 500 °C. A few common sensing technologies that have partial applicability for harsh environments will be outlined with their limitations.

Active semiconductor devices are widely used at room temperature for wireless communication and for sensing a wide variety of measurands but silicon technology is typically limited to around 350 °C because of increasing leakage current [16, 57]. Silicon-on-insulator (SOI) transistors are less affected by leakage current and have been operated up to 450 °C [57]. Wide bandgap semiconductors are more applicable to high-temperature use, specifically silicon carbide (SiC), diamond, and the group III-V nitrides: aluminum nitride (AlN), gallium nitride (GaN), and boron nitride (BN) [16, 57]. The III-V nitrides and SiC are the most suited for high temperature and have been utilized in devices operated up to 600 °C [16, 17, 57, 63]. While SiC single-crystal wafers are commercially available and have lower defect rates than the nitrides, SiC devices are still affected by crystal defects that need to be reduced for high-temperature electronics [16]. The packaging, soldering, and bonding of electronics presents a major challenge due to low durability and reliability when exposed to elevated temperatures and thermal cycling [16, 17, 57, 64].

Discrete passive electrical components, such as inductors, capacitors, and resistors, are increasingly available at elevated temperatures up to 500 °C but suppliers typically focus on operation below 200 °C [64, 65]. The passive components can have significant variation due to temperature and have long-term drifting, making it complicated to design reliable circuits [65].

Semiconductor devices require external power typically in the form of a direct wire connection or a battery. High-melting point (>100 °C) molten ionic salts can be used in high-temperature batteries for operation above 500 °C but low current densities limit the useful operation [66]. Energy harvesting from RF or vibrational energy has been used to create batteryless wireless sensors [20] but require rectifying

diodes, which even for high-temperature semiconductors like SiC are limited to about 600 °C [17–19].

Piezoresistive pressure sensors fabricated on SOI can be used at elevated temperatures around 200 °C and can survive temperatures above 1000 °C when exposed for under a second [67]. Resistive strain gages are simple and can operate up to 1000 °C but are not as sensitive as piezoelectric strain sensors and require direct wiring [1]. Electrochemical, semiconducting, and potentiometric ceramic sensors for NO_x, CO, CO₂, and O₂ gases have been fabricated that operate in the range from 400 °C to 800 °C but require wiring and electronics to read out [68].

Passive inductor-capacitor (LC) resonators can be fabricated using high-temperature electrodes on insulators, such as Al₂O₃ or high-temperature co-fired ceramics, and used for sensing temperature but have short range, a few cm, and low quality factors, typically below 100 [51]. LC resonators have also been covered with metal-oxide films and used for chemical sensing up to 675 °C [69].

The most common methods of measuring temperature involve thermocouples, thermistors, or resistance temperature detectors (RTDs), also called resistive thermal devices. Thermistors are limited to operation below 300 °C, RTDs to about 1000 °C, and thermocouples can survive at temperatures as high as 1800 °C, depending on the metals used, but are less accurate than RTDs and thermistors [70–74]. However, TCs, RTDs, and thermistors all require wired connections so are expensive to install, especially on rotating parts, and have reliability issues because of the wiring [5, 9].

Fiber optic Fabry-Perot interferometer can be used as sensors by measure the optic properties of a region of fiber optic cable inserted into a harsh environment using transmission or reflection of light through the cable. The Fabry-Perot sensors can measure strain, vibration, pressure and temperature up to 1000 °C [1, 75–78].

However, the fibers are prone to thermal shock, have unproven durability and reliability, and the fiber installation is complicated by the limited bend radius and optic interconnections [1, 23, 79].

Optical pyrometry is a measurement technique that can measure temperatures of remote parts, such as the blades in a jet turbine engine, by reading the thermal radiation emitted by the target. There is no theoretical upper temperature limit for optical pyrometry but it is only applicable above 500 °C because the amount of energy emitted increases with temperature [23]. A sight tube receives the thermal radiation and transports it through a fiber optic fiber to a detector unit and must be aligned to achieve a line-of-sight with the target being investigated and the sample must be larger than the detection spot size. The sight tube must survive the temperatures, thermal shock, and chemical attack of the harsh environment and the lens can be contaminated, preventing reliable readings and corrupting the calibration [23]. The accuracy is limited by the sensitivity of the components to temperature [1]. Installation into a turbine engine requires the pyrometer to be designed and calibrated for the engine, taking into account the blade material, surface preparation, and angle with respect to the pyrometer sight tube [1, 23].

Ultrasonic transceivers can be used to measure temperature or density of solid, liquid, or gas media by transmitting an ultrasonic wave into the media either directly, remotely, or through-wall and using the time delay and attenuation of the returning wave to measure the velocity of sound and attenuation in the media, which can be correlated to the measurand. This method can only measure the average temperature, pressure, or acoustic impedance of a homogeneous well-characterized media in a known cavity, thus is not accurate for environments with thermal gradients or transients without a priori knowledge of the system [21, 22, 71, 80–83].

Time-of-flight reflection measurements on acoustic buffer rods can be used to access harsh environments for the sensing of temperature, pressure, or strain and are

suited to many industrial applications but require the buffer rod to enter the target environment, therefore they cannot meet the need for wireless sensing [80, 84–86].

Acoustic microscopy can be applied to remotely measure the acoustic velocities of heated samples; a pulsed laser is used to excite the acoustic wave and an interferometer to measure the AW velocity of the wave [87]. Laser ultrasonics have been applied to extract the elastic moduli of metals at temperatures up to at least 1000 °C [88–91], the elastic constants of cubic crystals up to 1200 °C [92], and the Young’s modulus of ceramics up to 1600 °C [81]. However, the technique was demonstrated on stationary samples in a controlled environment and would not be suitable for sensing in most harsh environments because of the requirements for precise laser alignment and the durability issues of fiber optics, described above.

1.4 High-Temperature Frequency-Control and Filtering Applications

In addition to sensors, high-temperature frequency-control and filtering devices will increase functionality and performance for many high-temperature active circuits [7]. Wireless sensor networks that operate in harsh environments are needed in industrial processing and the extraction of oil and gas to better monitor and integrate information from a variety of sensors for improved process control, safety, and system reliability [5, 44–46]. The wireless systems require filters and timing circuitry that are stable at elevated temperatures.

Active circuits operating around room temperature typically use piezoelectric crystal oscillators for timing because of the stability and precision and also use piezoelectric filtering for wireless communication. As active circuits and communications systems become implemented in harsh environments with temperatures between 150 °C and 500 °C they will require new crystal oscillators for precision timing and filtering applications [16, 57]. Crystal oscillators that can operate at high temperature

will be used for timing and clock circuitry in high-temperature circuits for communication, synchronization, digital clocking, and precision timing. High-temperature analog filters could improve communications at elevated temperature and allow for increased transmission rates.

The design of crystal oscillators and filters in the temperature range between 150 °C and 500 °C requires a piezoelectric substrate with high coupling, low loss, stable behavior, and temperature-compensated orientations in the range of temperature operation.

1.5 Acoustic Wave Materials for High-Temperature Applications

Acoustic wave (AW) technologies, such as bulk acoustic wave (BAW), surface acoustic wave (SAW), resonant beam, solidly mounted resonator (SMR) and film bulk acoustic resonator (FBAR) devices, can be utilized as very sensitive, accurate, reliable, small, and batteryless sensors that can be wirelessly interrogated [12, 28, 30, 93–97]. Acoustic wave devices are widely used around room temperature for wireless sensing and radio frequency identification operations, such as tagging trains and automobiles [27], measuring automobile tire pressure and friction [28, 98], measuring temperature, strain, vibration, torque, acceleration, and water content [28, 93, 99]. High-temperature wireless SAW devices have been proven applicable up to 700 °C [100–102] and recently up to 850 °C [96, 97].

Acoustic wave devices are enabled at high temperature by piezoelectric crystals, such as GaPO_4 and the langasite family of crystals, and by metal electrode materials that operate in the harsh environments. The temperature limitations and the relative benefits and disadvantages of candidate and piezoelectric substrates for high-temperature AW devices are discussed in the following sections.

1.5.1 Piezoelectric Crystals with Limited High-Temperature Applicability

There are hundreds of piezoelectric crystals that have been studied theoretically and experimentally over the years [38] but most are not applicable for high-temperature operation above a few hundred degrees celsius [2, 6, 32, 60, 101]. The most fundamental upper temperature limit is when the crystal melts or undergoes a phase change that alters the crystal structure such that the piezoelectric effect is eliminated or critically reduced. Piezoelectric crystals that are ferroelectric lose their ferroelectricity and piezoelectricity at the Curie temperature (T_c). Additionally Turner et al. recommend that the operating temperature be less than half the Curie temperature to avoid material degradation [1]. High-temperature losses, such as electrical conductivity and acoustic losses, can limit the operation temperature for many applications. Practical considerations of mechanical stability in harsh environments as well as the consistency, size, and cost of crystal growth factor into the selection of a suitable high-temperature piezoelectric substrate [6, 103]. An overview of the temperature limitations of some common piezoelectric materials is provided in this section with focus on common piezoelectric crystals that have been suggested for use at high temperatures.

Quartz (SiO_2) is the most common piezoelectric crystal to be used in frequency control and sensing applications. Quartz can be used for moderate temperature applications [7, 32, 104] but is typically limited by the transition from α -phase to β -phase quartz at 573°C [59, 105]. Whereas α -quartz has two independent piezoelectric coefficients, e_{11} and e_{14} , β -quartz only has one, e_{14} [105–107], therefore many α -quartz devices will cease to operate above the transition temperature, including the ST-X SAW orientation, Euler angles $(0^\circ, 132.75^\circ, 0^\circ)$ [7, 32]. When cooled below the transition temperature β -quartz will randomly form one of two electrical twins (Dauphiné twins) of α -quartz, which have opposite piezoelectric directions, and the

piezoelectric effect will tend to cancel [59, 105, 106]. However, the twin boundaries have some memory [59] so α -quartz heated over the transition temperature for a short time might recover with the electrical twins oriented primarily in a single direction thus retaining piezoelectricity; quartz devices have been heated up to 600°C for 1 h with only minor increases in loss after brought below the transition temperature [7, 32]. Also, the quality factor of α -quartz decreases above 300°C and when under high pressure because of a decrease in the tetrahedral tilt angle that indicates that the crystal structure is become closer to that of the β -phase [108]. Additionally, Quartz can react with platinum electrodes at temperatures as low as 400°C forming platinum-silicide and resulting in increased losses [7].

The use of β -quartz as a high-temperature piezoelectric material was proposed by White [106] but is not commonly used [105] for the reasons discussed next. A β -quartz device would be stable between the α - β transition at 573°C and the transition from β -quartz into β -cristobalite, a non-piezoelectric cubic crystal, around 1050°C [59, 106, 107]. However, if the quartz is not pure the β -phase will instead transition into the high-temperature, non-piezoelectric form of tridymite at 867°C [59, 105]. The usefulness β -quartz devices are limited since the piezoelectric constant e_{14} is below 0.07 C m^{-2} [107], which is about 2.4, 2.9, and 6.7 times smaller than e_{11} of α -quartz, GaPO_4 , and $\text{La}_3\text{Ga}_5\text{SiO}_{14}$, respectively [31, 107, 109].

A number of quartz homeotypes, such as berlinite, gallium arsenate, germanium dioxide, and gallium orthophosphate, have been investigated to replace quartz in room-temperature applications and for possible high-temperature operation. Berlinite (AlPO_4), a homeotype of quartz, had early potential to replace quartz in some applications [110], but suffered from the high difficulty of growing commercial-size, high-quality crystals [31]. Also, the temperature behavior of berlite is very similar to that of quartz with a β -phase transition at 583°C [111] and has a similar decrease in tetrahedral tilt angle as quartz and increasing losses with temperature,

as discussed for quartz [112]. Gallium arsenate (GaAsO_4) is an α -quartz homeotype with a piezoelectric coupling approximately 3 times that of α -quartz and 1.4 times that of GaPO_4 [113]. X-ray powder diffraction studies of the gallium arsenate crystalline axes indicate that the piezoelectric properties should remain until 925°C [113]. However, it is in early stages of development and has not been well characterized acoustically; boules of 8 mm in length were first grown by hydrostatic methods in 2003 [113, 114]. Germanium dioxide (GeO_2) is the closest analog of α -quartz [115] and, along with gallium arsenate, should have the highest piezoelectric coupling of α -quartz-type crystals based on their crystalline structures [112, 116]. The α -quartz structure of germanium dioxide is stable up to 1071°C , suggesting that piezoelectricity should exist up to that temperature [116]. However, α -quartz-type germanium oxide slowly changes to the more stable, non-piezoelectric rutile-type form at temperatures above 750°C and becomes approximately 30 % rutile-type around 1000°C . This transition to a rutile-type structure is faster as the gas pressure increases and can occur at temperatures as low as 200°C in the presence of water [112]. Germanium dioxide has the potential for use as a highly piezoelectric substrate for high-temperature operation but two main obstacles have been identified by Haines, et al. [112]: the crystal growth of α -quartz-type germanium oxide needs to be optimized and the transition to rutile-type structure must be inhibited.

Lithium tantalate (LiTaO_3) has higher piezoelectric coupling than quartz but is not suited for high-temperature application because the Curie temperature is about 610°C [117] and it has high conductivity and a strong pyroelectric effect at elevated temperatures [118]. Lithium tetraborate ($\text{Li}_2\text{B}_4\text{O}_7$) is another promising acoustic wave substrate around room temperature and has a melting point of 917°C but not suitable for use in high-temperature devices because of pyroelectricity and high ionic conductivity, which limit practical use to about 300°C [60, 118].

Tourmaline is a piezoelectric crystal with class 32 symmetry and is described by the chemical formula $(\text{Na,Ca})(\text{Mg,Fe})_3 \text{B}_3 \text{Al}_6 \text{Si}_6 (\text{O,OH,F})_{31}$ [105]. Tourmaline does not form twins and has no phase transitions below 900 °C so could be used in high temperature devices, but artificially grown crystals are too small for use and natural tourmaline is brittle and has high variability in composition and behavior between crystals [105].

Ceramic and ferroelectric piezoelectrics are generally not suitable for high-temperature operation since elevated temperatures can cause the poling to decrease, these ceramics are pyroelectric, typically have low resistivity, and are sensitive to temperature changes [105]. Additionally, the piezoelectric ceramics have limited applications in BAW and SAW devices operated at high frequencies (above ~ 100 MHz) due to scattering at grain boundaries [118]. Ferroelectric crystals lose their ferroelectric and piezoelectric properties at the Curie temperature, T_C , but should be used only up to about half of T_C to avoid aging [1, 15]. Lead zirconate titanate (PZT, $\text{Pb}(\text{Zr}_x\text{Ti}_{1-x})\text{O}_3$) is a commonly-used, high-coupling piezoelectric ceramic but has a Curie temperature (T_C) of 360 °C and is not suitable for elevated temperature applications [1]. Two perovskite layer structure ferroelectrics, $\text{Sr}_2\text{Nb}_2\text{O}_7$ and $\text{La}_2\text{Ti}_2\text{O}_7$, have potential for high temperature use due to Curie temperatures of 1342 °C and 1500 °C, respectively [105], and thus could be operated up to approximately half those temperatures [1]. Bismuth titanate ($\text{Bi}_4\text{Ti}_3\text{O}_{12}$) ceramics can have Curie temperatures above 800 °C and high resistivity when doped with Nb or Na [1, 119]. The piezoelectric properties of the W-doped $\text{Bi}_4\text{Ti}_3\text{O}_{12}$ was investigated up to 700 °C and was found to be usable up to 500 °C, which is higher than the expected half of the Curie temperature ($T_c = 655$ °C) [120].

Lithium niobate (LiNbO_3) has a high piezoelectric coupling compared to quartz but is a ferroelectric crystal with a Curie temperature of 1210 °C and the operating temperature is limited to about 650 °C, above which poor electrical resistivity and

oxygen loss that leads to crystal degradation are significant [15, 121]. Additionally, long term operation of lithium niobate at elevated temperatures leads to lithium evaporation and to the growth of Niobium-rich LiNb_3O_8 on the crystal surface and at defect sites [122]. This degradation limits the lifetime of lithium niobate SAW devices to several years if operated at 350°C , to less than 50 days if operated at 400°C , and less than a few hours above 500°C [6, 123]. Lithium niobate is brittle, pyroelectric, and prone to thermal shocking which necessitate stringent process control in device fabrication [15, 121, 123, 124]. Thermal shocking also limits the usefulness of LiNbO_3 to only sensor applications that do not experience rapid temperature changes. Composite materials and ceramic lithium niobate can extend the practical operating temperature range of the material for acoustic transducers [15, 121] but would not be usable for the higher frequencies of SAW devices or many BAW devices due to material boundaries.

Oxyborate single-crystals $\text{ReCa}_4\text{O}(\text{BO}_3)_3$ (Re=rare earth element, such as gadolinium, Gd, yttrium, Y, or lanthanum, La) have been mostly studied for their non-linear optical properties and have only recently been to have promise as high-temperature piezoelectric substrates for AW devices [125, 126]. These crystals belong to the monoclinic crystal symmetry class m, in Hermann-Mauguin notation, so are pyroelectric. Oxyborate crystals have no phase transition before their melting point around 1500°C , lower conductivity than langasite-type crystals and GaPO_4 , piezoelectric constants about equal to those of langanite and approximately 3 times larger than those of quartz, and have been grown with diameters of 7.5 cm (3 in). Recently $\text{YCa}_4\text{O}(\text{BO}_3)_3$ and $\text{GdCa}_4\text{O}(\text{BO}_3)_3$ have been used in BAW devices up to 1000°C , with the temperature limited by the failure of the platinum films [125, 126].

1.5.2 Piezoelectric Crystals for High-Temperature Operation

Few piezoelectric single-crystals can operate above 400 °C in a harsh environment for more than a few days. For this recent research in this area is mostly focused on either gallium orthophosphate or the langasite family of crystals [6, 60, 103, 127].

Gallium orthophosphate (the α -phase of GaPO_4) is a quartz homeotype that has received considerable attention for temperature-compensated orientations, higher coupling than quartz, and phase stability up to 930 °C [2, 11, 31, 34, 128–132]. Gallium orthophosphate is commercially available and has been considered for pressure sensors since 1994 [105, 130]. Piezoelectric devices made with gallium orthophosphate have been successfully operated at high temperatures and up to 700 °C [11, 62, 133–136]. The piezoelectric properties of gallium orthophosphate start to degrade at 750 °C due to disorder in the oxygen lattice causing a rapidly decreasing resonator quality factor [137]. The propagation attenuation of gallium orthophosphate is high, which limits the operation frequencies to below 1 GHz; this is partly due to the poor surface polishing available on current crystals [6]. Gallium orthophosphate has potential for high temperature applications up to 750 °C and is the subject of ongoing work but crystal quality, wafer size, and cost are limiting factors [6, 103, 127].

Crystals in the langasite family have the calcium gallium germanate ($\text{Ca}_3\text{Ga}_2\text{Ge}_4\text{O}_{14}$, CGG) structure and have received significant attention as new piezoelectric crystals for acoustic wave devices, with most of the research on the subgroup of langasite ($\text{La}_3\text{Ga}_5\text{SiO}_{14}$, LGS), langanite ($\text{La}_3\text{Ga}_{5.5}\text{Nb}_{0.5}\text{O}_{14}$, LGN) and langatate ($\text{La}_3\text{Ga}_{5.5}\text{Ta}_{0.5}\text{O}_{14}$, LGT), collectively called LGX. The over 60 CGG-type crystals have, in general, a number of potential advantages as acoustic wave materials: (i) they are not pyroelectric; (ii) they have no phase transitions below their melting points, which is 1470 °C for LGX crystals; and (iii) they typically have piezoelectric moduli approximately 3 times larger than those of quartz [31, 34, 105, 138]. Additionally, LGX crystals have been shown to have temperature-compensated orientations

for BAW, SAW, and vibrating beams [34, 139–146] and low-acoustic losses, with LGN and LGT achieving higher Q-f products (quality factor \times frequency) than AT-cut quartz [31, 147]. No deterioration of LGX substrates has been observed when heated in laboratory atmosphere to high temperatures up to 1200 °C [103, 148, 149]; however, gallium on the crystal surface is reduced when heating in a vacuum atmosphere above 800 °C [150, 151]. Wafers and boules of good quality LGS and LGT are commercially available with diameters up to 10 cm (4 in) and the quality of crystals is improving with time as the growth parameters are optimized [6, 38, 103, 152].

The CGG-type crystals do not naturally occur and belong to the trigonal crystal class 32 and space group P321, and similar to but not the same as the structure of quartz, which is also in crystal class 32 but is in space group P3₁21 or P3₂21 [42, 105]. The LGX family are single crystals with a disordered structure in which the element occupying one of the cation sites in the unit cell is not predictable on a microscopic level and can be filled by either gallium or, depending on the crystal, by silicon, tantalum, or niobium [31]. However, on a macroscopic level the site is shared equally between the species. The disordered structure may lead to higher acoustic losses and non-uniform material properties relative to a similar ordered structure [153]. New langasite isomorphs with an ordered structure are being investigated, such as Ca₃NbGa₃Si₂O₁₄, Ca₃TaGa₃Si₂O₁₄, Sr₃NbGa₃Si₂O₁₄, and Sr₃TaGa₃Si₂O₁₄, which have yielded promising growth and acoustic wave characteristics but are still being developed and investigated for temperature compensation [153–160].

The LGS, LGT, and LGN crystals have very similar structures and material properties but some significant differences exist. LGS was the first to be synthesized, is the most commercially available, and have been more thoroughly studied. The piezoelectric constants of LGN and LGT are larger than those of LGS; e_{11} of LGN and LGT are about equal and approximately 17% greater than that of LGS [31, 35, 41]. The acoustic losses of LGT and LGN are lower than those of LGS [161, 162], and

as a result LGT and LGN Y-cut BAW devices have achieved higher Q-f products than both LGS and AT-cut quartz [31, 147, 163]. Bulk acoustic wave Y-cut LGN and LGT devices have lower force-frequency coefficients than quartz, with LGT having the smallest of the pair, which indicates that LGT can potentially have lower acceleration sensitivity and resonators with lower noise than quartz [164]. Additionally, LGT has the best growth consistency of the three crystals [40, 43, 152].

Among high-temperature AW devices, LGS is more commonly used than LGT and LGN because it is more established than the other LGX crystals. There have been a number of LGS AW devices operated at high temperature; an overview is discussed next.

The feasibility of operating LGS at very high temperatures was demonstrated in 1997 by operating a SAW delay line up to 1070 °C for a short time before the electrodes and packaging deteriorated [60, 165–168]. Languisite SAW devices were developed with Pt electrodes and a coating of tungsten trioxide (WO_3) to detect ethylene (C_2H_4) in nitrogen (N_2) gas and also developed with palladium (Pd) electrodes that absorb and sense hydrogen (H_2) in N_2 [7, 12, 13, 32, 169, 170]. These LGS SAW devices successfully sensed the target gases at the optimal temperature range between 250 °C and 450 °C and were operated up to 750 °C [7], but electrode degradation was observed above 700 °C [171]. Alternatively, electrodes of co-deposited Pt/Rh/ ZrO_2 film were found to survive up to 1000 °C with little degradation and were used to fabricate LGS SAW devices that have operated at 800 °C for 5 ½ months with minimal change in frequency or loss [149, 171–174]. These electrodes have been characterized acoustically at room temperature [175] and SAW resonators have been designed for their use [176].

Languisite BAW resonators have been operated at high temperatures up to 1400 °C [177–179], and have been utilized as gas sensing nanobalances with TiO_2 and CeO_2 films at temperature as high as 1050 °C [180–184]. Micromachined resonant cantilevers or other microelectromechanical systems (MEMS) for high-temperature

operation have been fabricated utilizing the anisotropic etching of LGS, with experimental measurements up to 930 °C [185–188].

SAW delay lines with metallized and free surfaces were used to measure the temperature coefficient of frequency (TCF), piezoelectric coupling, and acoustic loss of LGS along select directions up to 500 °C [102, 189] and later up to 730 °C [178, 190–192]. LGS SAW delay lines were characterized up to 560 °C using a platinum-film heater on the LGS substrate thus allowing the SAW device to be connected with bond wires to standard SMA connectors, without the need for high-temperature cables or a furnace [193].

Wireless LGS SAW reflective delay lines have been reported to have been operated at high temperatures up 700 °C [100, 102]. A wireless LGS oxygen sensor was demonstrated up to 700 °C, with wired sensing up to 900 °C [194]

Reflective delay line, code-division multiple-access (CDMA) delay lines, and resonator LGS SAW devices have been operated wirelessly up to 925 °C, demonstrating the applicability of the use of SAW devices in a multiple-access wireless sensor system for harsh environments, such as turbine engines [96, 97].

Even though LGS has been utilized in high-temperature application there is no published full set of LGS AW constants and temperature coefficients at high temperature that can be used to calculate AW performance. The high-temperature LGS AW constants either have not all been reported with temperature coefficients at very high temperatures or are the data is only reported in a figure without the temperature coefficients nor assessments of the accuracy. The elastic and piezoelectric properties of LGS have been determined up to 900 °C from BAW and SAW measurements but are reported only graphically and the temperature coefficients or numerical values of the LGS AW constants are not given, which are needed for others to utilize the results [178, 190, 191, 195–197].

1.5.3 Langatate: State-of-the-Art

The latest developments in LGT research are described in this section. The topics have been divided into (i) the development and growth of LGT, (ii) LGT AW characterization at temperatures below 250 °C, and (iii) LGT AW characterization at temperatures above 250 °C.

1.5.3.1 Development and Growth of Langatate

Crystals with the calcium gallium germanate ($\text{Ca}_3\text{Ga}_2\text{Ge}_4\text{O}_{14}$, CGG) structure were first discovered and synthesized in the late 1970's and early 1980's in Russia [33, 36–38, 139, 198–201]. This early work included analysis of crystal structure and optical properties [33, 198–200] and electromechanical properties including temperature-compensated orientations at room temperature and low acoustic loss [139, 201]. Research on LGS for acoustic wave applications greatly increased after a pair of papers were presented in the 1991 Frequency Control Symposium showing that LGS had the potential replace quartz in some BAW and SAW applications due to its higher coupling, the absence of any phase transitions up to the melting point at 1470 °C, and a lower phase velocity than quartz [202, 203].

Langatate, in particular, was investigated as early as 1985 [204] but the initial studies focused on the LGT optical properties for laser applications. By 1997 the growth and atomic structure of LGT was considered for acoustic wave applications [205]. The next year two independent sets of room-temperature LGT elastic, piezoelectric, and dielectric constants were presented [206, 207]. Additionally, LGT was proven to have a zero-temperature-coefficient BAW orientation around room temperature [206], LGT resonators were fabricated with higher Q-f products than LGS [208], and LGT growth parameters were studied [39]. Further studies on LGT quality factors of AW resonators and growth studies were published soon after [40, 42, 147, 153, 163, 209, 210].

Langatate has also been investigated with various substitutions to improve the piezoelectric coupling and to decrease the conductivity. Langatate was grown with barium ion (Ba_2^+) substitutions, $\text{La}_{3-x}\text{Ba}_x\text{Ta}_{(0.5+x/2)}\text{Ga}_{(5.5-x/2)}\text{O}_{14}$, resulting in a 50 % increase in d_{14} but 5 % decrease in d_{11} [211]. The piezoelectric coefficient d_{11} of $\text{La}_{2.95}\text{Ba}_{0.05}\text{Ta}_{0.525}\text{Ga}_{5.475}\text{O}_{14}$ was measured up to 500 °C from the difference between the resonant and anti-resonant frequencies of a BAW resonator and was found to have very little variation with temperature, on the order of 5% and below the measurement repeatability [211]. Substituting aluminum into LGT ($\text{La}_3\text{Ta}_{0.5}\text{Ga}_{5.5-x}\text{Al}_x\text{O}_{14}$, $x=0.2$ to 0.5) decreases the conductivity by an order of magnitude relative to pure LGT, measured up to 700 °C, but causes the piezoelectricity to be smaller than that of pure LGT, measured up to 500 °C [212, 213]. Crystals based on total substitution of the gallium by aluminum have been grown ($\text{La}_3\text{Al}_{5.5}\text{Ta}_{0.5}\text{O}_{14}$) with the same structure as LGT. These crystals are less expensive than LGT but further research is needed on growth, material characterization, and high-temperature behavior [214].

Langatate is typically grown from a melt by Czochralski method, in which a starting crystal seed is slowly rotated and pulled from the molten components of LGT that coalesce on the seed [39, 40, 42, 205, 215]. Initially, LGT was grown using LGS at the seed crystal until single-crystal LGT could be used for future Czochralski growth [42, 205]. Czochralski growth requires careful selection of the melt composition, melt temperature, rate of pulling, and rotation rate to reduce crystal defects and maximize crystal boule size [39, 40, 42, 205, 215]. A consideration in the Czochralski growth of LGX crystals is that the congruent composition is not the same as the stoichiometric composition, so starting from a stoichiometric melt results in poor crystal homogeneity [216–218]. Striations, faceting, and inclusions can lead to a build of stress in the material, interfering with the SAW properties [43, 152, 216]. Growth striations on LGS and LGT wafers lead to inconsistent device parameters and degraded Q-values of devices that cover such striations [43, 152]. However, studies on

LGS and LGT uniformity [43, 152] found that the LGT wafers had “very low defect density” and SAW wafer mapping analysis found a standard deviation in resonant frequency of 210 ppm to 223 ppm for LGS and 156 ppm for LGT, indicating that the LGT wafer has better uniformity. The measured standard deviation in LGS and LGT SAW frequencies dropped from above > 100 ppm as low as 50 ppm from results reported between 2001 and 2003, indicating an improved growth process [43, 152].

Langatate crystals have also been grown using the floating zone method, with boule diameter of 5.5 mm (0.22 in) [219], and the vertical Bridgman method, with a boule diameter of 25.4 mm (1 in) [220], which are smaller than the 76.2 mm (3 in) or greater diameter achieved by Czochralski growth [152, 221]. It is also possible to grow LGX films with liquid phase epitaxy, forming a single-crystal LGX film a few micrometers thick on a substrate below the melting temperature by using the correct solvents. Crystal films of LGS, LGN, and LGT with lateral dimensions of $1.5\text{ cm} \times 1.5\text{ cm}$ and orientated along X, Y, and Z axes have been grown with high crystalline quality, as judged by optical microscopy, X-ray diffraction, and composition analysis [216, 222–226]. Further work is required to study the capability of growth along other orientations, repeatability, and AW parameters of the films.

Langatate crystals have been grown at a number of different locations, including the Moscow State University (Moscow, Russia) [198, 199], Fomos Materials (Moscow, Russia) [221], the Institute for Materials Research, Tohoku University (Sendai, Japan) [205, 213, 222], Freiberg University of Mining and Technology (Freiberg, Germany) [42], Crystal Photonics (Sanford, FL) [39], University of Central Florida (Orlando, FL) [224], Shandong University (Jinan, China) [227, 228], and the Chinese Academy of Sciences (Shanghai, China) [229].

The LGT crystal boules used in this work were purchased from Fomos Materials (Moscow, Russia). The purchased hexagonal prism boules were grown along the Z-axis, weighed up to 1.5 kg, had length up to 10 cm (3.9 in) and diameter of 6.35 cm

(2.5 in). The boules were purchased from Fomos because it has been growing LGS and LGT since the mid-1990's and sells wafers and large boules with up to 13 cm (5.1 in) diameter and 12 cm (4.7 in) length [221, 230, 231]. Langasite and langatate 3 in wafers produced by Fomos from Fomos were quoted to have “very low defect density” [43] and allowing SAW resonators with 50 ppm resonant frequency standard deviation [152]. Due to the observed quality and consistency of the Fomos crystal, it was judged that the extraction of the AW constants was relevant and that the constants could be reasonably utilized to predict performance of new LGT AW devices. Additionally, Russia is the largest supplier of LGS and LGT [39], so the extracted constants would be applicable to the widest audience of LGT device manufacturers. To the best of the author's knowledge, no other commercial crystal suppliers were selling LGT boules with dimensions greater than 5 cm (2 in) at the time of the initial crystal purchase in 2004.

1.5.3.2 Langatate Characterization Below 250 °C

At room temperature the LGT elastic, piezoelectric, and dielectric constants have been extracted by the BAW plate resonance, pulse echo, and resonant ultrasound (RUS) techniques [41, 138, 206, 207, 232–237]. The temperature coefficients of the LGT acoustic wave constants have been reported in the temperature range from -50°C to 150°C or less [35, 141, 210, 215, 236–239]. Most of the early data sets of LGT constants have not been sufficiently accurate to identify temperature-compensated orientations [141, 236]. However, recently extracted LGT constants up to 120°C from the University of Maine have been used to successfully predict temperature-compensated SAW orientations around room temperature [236, 237, 240].

In the late 1990's and early 2000's there were a number of studies investigating the application of LGT for BAW and SAW devices. The LGT BAW quality

factor, coupling, and temperature behavior has been investigated for different crystal orientations [147, 163, 208, 241–244]. The SAW and pseudo-SAW (PSAW) velocity, piezoelectric coupling, temperature coefficient of delay (TCD), and other SAW parameters of LGT were calculated from material constants and used to predict temperature compensated crystal orientations around room temperature [35, 141, 142, 238, 240, 245–253].

The LGT SAW phase velocity, piezoelectric coupling, temperature coefficient of delay (TCD), and power flow angle were calculated from room temperature to 200 °C and used to predict LGT high-coupling SAW temperature-compensated orientations around room temperature [141, 245, 247, 248, 251]. Soon after other groups published LGT temperature-compensated SAW orientations around room temperature [238, 246]. A number of patents have been filed for LGT SAW devices of select orientations [246, 251, 254, 255]. Other LGT SAW orientations were numerically identified with thermal stability from -60°C to 60°C but exhibited lower coupling than previously determined orientations [142]. Langatate SAW orientations have also been predicted for which the SAW velocities have either high or low sensitivity to mechanical rotation of the device around room temperature [256]. Recently extracted LGT constants and temperature coefficients were used to successfully predict new LGT temperature-compensated SAW orientations around room temperature [236, 237, 240, 253].

The piezoelectric coupling of LGT lateral-field excited (LFE) BAW orientations have been investigated to find singly-rotated cuts with LFE coupling of the slow shear mode as high as 0.19 and doubly-rotated cuts with LFE coupling to the slow shear mode around 0.15 and low coupling for the other modes (< 0.02) [241–243]. Doubly-rotated LGT BAW orientations have been found that are temperature-compensated around room temperature [244].

Langatate has also been considered towards commercial applications. Langatate resonators have been investigated regarding the influence of the excitation amplitude and the mounting stress on the device resonant frequency [164, 257–259]. Langatate from Fomos and the University of Central Florida were compared in [260, 261]. The effects of polishing and resonator designs were studied to increase the mode trapping and Q-f products of LGT resonators [260, 261]. Langatate resonators have been implemented to create “ultra-stable” crystal oscillators [260, 262–265]. Imbaud et al. suggest that LGT is a “serious candidate” for low-noise crystal oscillator applications due to a high Q-f product, low power spectral density noise floor, and low aging [264, 265].

There have been few studies into beneficial LGT orientations at temperatures above 25 °C. Temperature-compensated orientations for LGT vibrating beams with turn-over temperatures near room temperature and up to 250 °C have been theoretically and experimentally studied [144, 145, 266]. Ji et al. predicted and experimentally tested SAW orientations of LGS crystal for operation around 250 °C, reporting multiple LGS orientations with turn-over temperatures near 250 °C, but observed poor agreement between the theoretical and measured results [267] and the orientations were not investigated for LGT. Langatate SAW devices with multiple orientations were demonstrated to have turnover temperatures around 140 °C [141, 247, 268, 269] using AW constants determined up to 150 °C [247]. A full set of LGT high-temperature acoustic constants was needed to make accurate and useful predictions of AW orientations for high-temperature devices.

1.5.3.3 Langatate Characterization at Elevated Temperatures Above 250 °C

The high temperature (> 250 °C) characterization of LGT has been limited and no full set of LGT high temperature AW constants have been published. The LGT dielectric permittivity, conductivity, and piezoelectric constants or coupling have been

investigated in some studies, but, in general, either not all the tensor values are reported or the data is given only in a plot, as discussed below. Therefore the available data was both insufficient and inaccurate for the prediction and calculation of AW device behavior.

Researchers at the University of Maine, in cooperation with the High Temperature Materials Laboratory at the Oak Ridge National Laboratory, have previously extracted the LGT density, lattice vectors \vec{a} and \vec{c} , lattice expansion, and bulk crystal expansion up to 1200 °C and reported them along with third-order temperature coefficients [148, 270, 271]. The LGT density was extracted by hydrostatic weighing at room temperature and the bulk crystal thermal expansion coefficients were measured by dual push-rod dilatometry up to 1200 °C. X-ray powder diffraction was used to extract the lattice vectors and lattice expansion up to 1300 °C. The bulk and lattice expansion data agreed within measurement error ($< 2\%$) indicating both accurate results and the high quality of the LGT crystal used. Other groups have measured the LGT expansion at lower temperatures [227, 272–274] and studied the structure of LGT crystals [39, 42, 205, 215, 275–277].

Schreuer et al. described measuring the LGT elastic constants up to 525 °C with the RUS technique but did not list the temperature coefficients and only plotted all the elastic constants up to 350 °C [232, 273], with another three elastic constants shown up to 525 °C [278]. The temperature coefficients of the LGT dielectric permittivities are given up to 625 °C [273]. Schreuer et al. provided a complete set of room-temperature LGT elastic, piezoelectric, and dielectric constants measured at room temperature [232]; but the set cannot be used for accurate high-temperature LGT AW calculations.

Sakharov et al. described, in a technical report from Fomos Materials, measurements of the LGT d_{11} piezoelectric coefficient up to 550 °C, finding that the change in d_{11} between room temperature and 450 °C is small, about 5 % and on the order of the

measurement uncertainty, and is followed by a rapid increase in d_{11} at 500 °C [221]. The piezoelectric constant was extracted from the difference between the resonant and anti-resonant frequencies of a resonator and the authors noted difficulties in the measurement due to the effect of spurious resonant modes [221].

Kong et al. grew LGT crystal and measurement of the capacitance of XY-oriented, [110]-direction and Z-oriented, [001]-direction LGT plates up to 600 °C, but only report the data in a plot of the raw capacitance, in Farads, not the permittivities ϵ_{ij} and no equations are given for the curves, which are needed for others to utilize the results [227]. The capacitance was measured at a single frequency, 1 kHz, and it is not clear if the authors accounted for the effect of the LGT conductivity. Sehirlioglu et al. measured the LGT dielectric permittivity up to 600 °C from plates in the [100], [120], and [001] directions, reporting the room-temperature permittivities and loss tangent for each orientation and plotting their temperature behavior [279].

There has been a number of characterizations on the conductivity of langatate at high temperatures, which contributes to device losses, but is not needed to calculate the AW velocities. Since LGT is an insulator, the conductivity follows the Arrhenius behavior and is exponentially related to the negative of the activation energy, E_a , divided by the temperature. The activation energy was studied with conductivity measurements up to 1000 °C using crystals from multiple sources with different growth processes and atmospheres [42, 162, 219, 221, 279, 280].

Acoustic anelastic losses at high temperatures have been investigated and provides evidence that the movement of dislocations in the crystal structure causes acoustic losses [162, 278, 281–283]. These studies investigated the quality factor versus temperature, but did not report on the viscoelastic constants to describe the losses.

1.5.4 Thin-Film Piezoelectric Materials

Aluminum nitride (AlN) is a non-ferroelectric piezoelectric ceramic that can be epitaxially grown as a piezoelectric thin film but is not easy to grown as a bulk single crystal [1, 118]. Aluminum nitride has large potential for use in high-temperature acoustic devices due the low electrical conductivity when the crystal purity is high, high surface acoustic wave phase velocity ($\sim 5600 \text{ m s}^{-1}$), and absence of phase transitions between room temperature and its melting point, which is above 2000°C in a nitrogen atmosphere [1, 60, 118, 284]. In low-pressure environments, N_2 rapidly disassociates from AlN above 1040°C , with the rate increasing with temperature [285]. Aluminum nitride BAW devices using AlN deposited on fused quartz have been reported to maintain piezoelectric operation up to 1150°C [1]. However, AlN oxidizes rapidly in air at temperatures above 700°C , transforming the surface to non-piezoelectric alumina [103]. The surface changes are particularly important for AlN SAW devices and limit the lifetime in high-temperature oxygen environments; for example, AlN SAW devices were found to degrade in insertion loss by 2 dB after 30 minutes at 900°C in air [284, 286]. Aluminum nitride is more suitable for high-temperature operation in environments with low oxygen partial pressures, which cause oxygen reduction in oxide-based piezoelectric materials [118]. Gallium nitride (GaN) and different compositions of $\text{Al}_x\text{Ga}_{1-x}\text{N}$ are also piezoelectric and thermally stable thin films that have been considered for SAW applications [60].

Zinc oxide (ZnO) is a piezoelectric thin film that has been used for SAW devices [287–290] and has a melting point of about 1700°C [291]. However, the ZnO Z-axis rotation, which controls the piezoelectricity, degrades at high temperature, with this effect observed as low as 430°C [292], compromising the high-temperature capability.

1.5.5 Thin-Film Electrodes for High-Temperature Operation

For long-term reliable operation high-temperature BAW and SAW devices require thin-film electrodes that are both electrically conductive and high-temperature stable. The thickness of SAW thin-film electrodes is typically 1 % or less of the acoustic wavelength, on the order of 100 nm to 200 nm thick [25]. BAW and resonant beam devices can utilize somewhat thicker electrodes because less energy is concentrated at the surface and the frequencies are often lower than SAW devices [26].

Aluminum (Al) is the most commonly used metal for SAW electrodes but it melts at 660 °C and suffers from electro- and stress- migration at lower temperatures [60]. Noble metal elements have been considered for high-temperature applications, described next. The melting temperature of gold (Au) is 1063 °C, but gold films can be expected to deteriorate at lower temperatures [60, 103]. Iridium (Ir), ruthenium (Ru), and osmium (Os) are all noble metals with melting points above 2300 °C but form oxides above 700 °C to 800 °C that are volatile above 900 °C to 1000 °C. Rhodium (Rh) also oxidizes at high temperatures but the oxide is not as volatile [103]. Palladium (Pd) has a melting point of 1550 °C but easily absorbs hydrogen gas below around 250 °C and absorbs oxygen at high temperature [7, 103, 293]. Platinum (Pt) melts at 1770 °C but at high temperature a surface oxide forms, however, there is negligible mass variation in the platinum up to 1000 °C so it is the most applicable to high-temperature use among the elements listed [103, 293].

Platinum thin-film electrodes (≈ 100 nm thick), with zirconium (Zr) and tantalum (Ta) adhesion layers, start to de-wet above 700 °C, the film aggregates and becomes discontinuous due to the surface tension [103, 149, 171–173, 190, 294]. Platinum-rhodium (Pt with 10 % Rh) electrodes were found survive up to 950 °C for at least a few hours [171]. Films made from Pt and 10 % Rh alloy co-deposited with zirconium oxide (ZrO_2) survive temperatures up to 1000 °C with little degradation and have been demonstrated for long-term use by operating a SAW device with Pt/Rh/ ZrO_2

electrodes at 800 °C for 5 ½ months with minimal variation in frequency or loss [149, 171–173].

Platinum-based films on LGX and quartz require an adhesion layer to keep the metal on the substrate and prevent peeling. Typically, titanium (Ti), tantalum (Ta), or zirconium (Zr) are used as the adhesion layer [103, 295]. However, Ti migrates into the Pt at high temperature (above 500 °C) whereas Zr and Ta do not, so Zr and Ta are preferred for high-temperature platinum-based films [103, 172, 294, 295].

Conductive ceramics, such as CoSi_2 , TiN, and WC with melting temperatures of 1326 °C, 2950 °C, and 2800 °C, respectively, have been suggested for use as electrodes for AW devices [60]; however, the thin-film fabrication and the mechanical loading due to the mass, stiffness, and anisotropy of ceramic films has not been investigated. Langasite BAW devices fabricated with ceramic lanthanum strontium manganate (LSM, $(\text{La}_{0.8}\text{Sr}_{0.2})_{0.98}\text{MnO}_2$) electrodes have been operated up to 1350 °C [177]. Monolithic electrodes on langasite crystals can be produced by heavy strontium doping and have shown early success up to 800 °C for BAW devices [177, 187, 296], but it is not clear if patterned electrodes, required for SAW devices, are possible with this technique.

1.6 Crystal Acoustic Wave Properties Characterization Techniques for High Temperature

1.6.1 Fundamental Crystal Properties for Acoustic Wave Technology

The analysis and simulation of acoustic waves on piezoelectric crystals requires knowledge of the relevant acoustic properties of the substrate, namely the elastic stiffness (c_{ij}), piezoelectric constants (e_{ij}), permittivity (ϵ_{ij}), density (ρ), and thermal expansion, which in this work are referred to as the full set of AW constants. Crystals are anisotropic so most crystal properties are directionally dependent and must be represented as tensors. Additionally, the acoustic properties can be affected by the

conditions of the crystal, such as as temperature, pressure, and strain; thus these conditions must be accounted for in determining the acoustic wave constants. To analyze the behavior of an piezoelectric crystal in response to varying temperature the temperature coefficients of the elastic moduli, piezoelectric constants, permittivity, and density as well as the thermal expansion of the lattice parameters must be characterized. For certain crystals, other crystal properties may play a significant role in material performance, such as viscosity, dielectric losses, and conductivity, and thus need to be considered.

Using the matrix notation of tensor quantities, the elastic moduli can be described by a 6×6 matrix, the piezoelectric constants by a 3×6 matrix, the dielectric permittivity by a 3×3 matrix, and the density by a scalar [297]. For class 32 crystals, including LGT, LGS, and quartz, the elastic, piezoelectric, and dielectric constants matrices are given in Appendix A by (A.1), (A.2), and (A.3). All the elastic constants used in this work are assumed to be measured at constant electric field, c^E , whereas the permittivity is considered at both constant electric field, ϵ^E , and constant stress, ϵ^T , as will be discussed in Chapter 2.

The bulk density of a crystal crystal can be measured by hydrostatic weighing in a high purity liquid and using Archimedes' principle [148, 270, 271]. The lattice density can also be calculated from the lattice vectors, measured by X-ray diffraction, the crystal structure, chemical composition, and atomic masses of the component elements. The calculated lattice, or X-ray, density will agree with the measured bulk density for a pure crystal; disagreements can be caused by measurement errors or crystal defects that affect the density, such as vacancies and impurities [148]. Thermal expansion of the lattice vectors is measured by X-ray diffraction of a heated sample, and bulk expansion can be determined from dual-push rod dilatometry or optical differential dilatometry. Again, lattice and bulk thermal expansion are equal for high quality crystals [148, 270, 271]. Further discussion on the measurement techniques

used for the extraction of density, crystal lattice vectors, and thermal expansion and measurement data for LGT can be found in [35, 148, 227, 270, 271, 273, 274].

A review of the measurement techniques used to extract the high-temperature AW constants is given in the following sections, focusing on the extraction of the elastic, piezoelectric, and dielectric constants, the targets of this dissertation.

1.6.2 Extraction Techniques for High-Temperatures Elastic and Piezoelectric Constants

The elastic stiffness and piezoelectric constants of piezoelectric crystals are typically extracted from the acoustic velocity from a few AW devices with different crystal orientations [297]. Velocity measurements along multiple directions are required to extract the elastic and piezoelectric constants of crystals due to anisotropy. The elastic and piezoelectric constants can be extracted from the same acoustic velocity measurements, relying on the overdetermined set of equations to separate the elastic and piezoelectric effects [298].

The piezoelectric constants can be measured independently by determining the effective piezoelectric coupling of resonators from the difference between the series and parallel resonant frequencies of a resonator [297], but this method is inaccurate because it does not consider the non-uniform distribution of motion of the vibration [131, 236, 298, 299]. The piezoelectric constants can also be measured under static conditions directly from the piezoelectric effect by applying a known force to the crystal and measuring the charge built up on the faces. However, static tests are often inaccurate and rarely used even around room temperature because the electric boundary conditions are complicated to control [297]. As early as 1927 this technique was used up to 600 °C to investigate the piezoelectric effect of quartz [300] but gave inaccurate results due to the increasing conductivity of quartz at elevated temperature [301].

Time-of-flight (TOF) techniques measure the time it takes an acoustic wave to travel a predetermined distance through the crystal under test, thus determining the acoustic wave velocity, which can be used to extract the elastic stiffness and piezoelectric constants. One method for TOF measurement is transmission mode, in which a transmitting piezoelectric transducer generates the acoustic wave that travels through the crystal under study and into the receive transducer. Another TOF method is pulse echo, where there is a single transducer that generates the acoustic wave and receives the returned echo after it reflects off the back of the crystal sample [302].

A buffer rod is used to physically separate the crystal sample from the transducer, allowing a more accurate determination of the time delay of the returned pulses [236, 237, 299, 303–305]. The buffer rods for TOF measurements require the use of an ultrasonic couplant to transmit the acoustic energy between the sample and the buffer rod or transducer. The time delay due to the couplant thickness and acoustic velocity can lead to relative errors in the crystal sample velocity on the order of 10^{-3} of the crystal velocity and correcting for the couplant requires knowing the couplant acoustic impedance and thickness [236, 305]. The effect of temperature on the couplant is significantly larger than the velocity variation of the crystal thus preventing accurate measurements at elevated temperatures, even at moderate temperatures up to 120 °C [236]. Additionally, the selection of couplant material for elevated temperatures is not obvious because it needs to withstand high temperatures while acoustically bonding the crystal to the buffer rod. It also needs to be easily removable so that the same buffer rod can be reused and have repeatable acoustic properties and thickness so that the time delay can be corrected. Air-coupled transmission is typically weak unless the parts are pressed together, which affects the measurement due to the added stress, and could add an unknown and non-repeatable time delay because of the gap between the samples.

The crystal acoustic velocity can be measured using BAW resonators since the BAW resonant frequency is $f = n v / (2h)$, neglecting second-order effects, where n is the mode number of the harmonic, v is the phase velocity of the resonator's acoustic mode and h is the crystal wafer thickness. The bulk waves are generated electrically either through the piezoelectricity of the crystal, an attached piezoelectric transducer, or electromagnetic transduction (EMAT). For piezoelectric crystal resonators an electric field is applied to the crystal either with electrodes attached to or near the crystal and either in the thickness or lateral direction. Electrodes attached to the crystal alter the resonant frequency due to mass loading and non-uniform distribution of motion. Electrode-less techniques, in which the crystal is not metallized and rests directly on top of or very close to separate electrodes, allow for these mass effects to be mitigated, producing a more accurate measurement [131, 236, 298]. Non-piezoelectric crystals could be characterized using a second piezoelectric transducer that generates the acoustic resonance, but the mass and stiffness of transducer would also affect the crystal under test and these effects would need to be separated. Bulk waves can also be excited using electromagnetic transduction (EMAT) for crystal constant extraction by using Lorentz forces acting on moving charges in a static magnetic field [306, 307]; however, high-temperature application would require a small heated zone within the magnetic field or generating the magnetic field within the high-temperature furnace.

The velocities of multiple modes are measured in order to extract the elastic and piezoelectric constants of crystals; for example, class 32 crystals, like quartz, GaPO_4 , and LGT, require the measurement of 13 mode velocities and using 5 different wafer orientations [236]. Extension of this technique to high temperature necessitates the measurement of the each of the acoustic modes in separate heating cycles because each requires a different wafer crystal orientation and placement with respect to the electrodes. Resonator techniques typically rely on the piezoelectric coupling of the mode being measured, which can be small even at room temperature and often

decrease with temperature. Additionally, the increased resistivity of the electrodes with temperature reduces the received signal diminishing the signal level and measurement precision. The electrodes also need to be made of a metal that can survive the high-temperature environment, as discussed in Section 1.5.5. BAW resonators have been used at high temperature to extract material constants of LGS but metal electrodes were directly deposited on the resonator [195, 308].

Surface acoustic wave (SAW) resonator and delay-line devices can be used to measure the SAW phase velocity for extraction of the elastic and piezoelectric constants [178, 309, 310]. For a general orientation, the SAW velocity of class 32 crystals cannot be calculated analytically and must be determined numerically. The extraction of acoustic constants requires the measurement of multiple devices and a minimization technique to find the best set of constants, as well as a accurate set of AW constants for the starting SAW calculations. The SAW velocity is only able to accurately indicate the value of the AW constants that most affect it [253, 309, 310]. Therefore, the extraction of elastic and piezoelectric constants from SAW measurements requires the selection of a set of SAW orientations such that each AW constant of interest has a significant effect on the velocity of multiple devices.

The thin-film interdigitated (IDT) electrodes of SAW devices, with thicknesses typically on the order of 1% of the acoustic wavelength, about 100 nm [25], have electrode mass and stiffness that changes the SAW velocity away from the free velocity and can cause spurious resonant modes [25, 176]. As discussed in Section 1.5.5, high-temperature-stable thin-film electrodes are typically Pt, Ir, and Pt/Rh/ZrO₂, which are more dense and less conductive compared to aluminum. The resistivity of these electrodes can be significant at high temperature because metal resistivity increases with temperature. The electrodes that are made thicker have lower resistance but the resultant high-temperature electrodes are more dense and thicker than those used at

low temperature so have a larger effect on the SAW velocity. Design of SAW devices can reduce the spurious modes caused by the dense electrodes [176]. Delay-line SAW devices with an unmetallized delay path are less affected by the mass loading of the electrodes than resonator devices because the delay path is a significant portion of the device and the velocity in the path is the free velocity; however, the acoustic losses typically increase with temperature and will attenuate the signal of the long delay lines more than for other techniques.

The piezoelectric constants are typically extracted simultaneously with the elastic constants in the minimization fitting of the calculated and measured SAW velocities. Alternatively, the piezoelectric constants can be extracted from the SAW coupling determined from the difference between metallized and free SAW velocities, specifically by measuring the SAW velocity using delay lines with metallized or free delay paths [25, 190, 191]. However, this technique typically assumes that the metal is perfectly conducting and massless, but the electrodes are not ideal and the SAW velocity is affected by the mass, stiffness, and finite conductivity of metal layer [25]. High-temperature measurements require noble metal based electrodes [103, 172] that have non-negligible density and resistivity. Therefore, for high-temperature SAW coupling extraction the loading effects and resistive losses are significant and reduce the measurement accuracy [190, 191]. Additionally, the differences in thermal expansions of the metal film and the substrate will cause stresses that can alter the SAW velocity and temperature behavior [311–313].

Laser ultrasonics techniques could potentially be applied to the extraction of the high-temperature elastic and piezoelectric constants of piezoelectric crystals. As discussed above in Section 1.3, surface acoustic waves can be excited by a pulsed laser and their velocity measured with a heterodyne interferometer and this technique has been applied to metals and cubic crystals at temperatures as high as 1600 °C [81, 88–92]. This process avoids the mass loading and loss effects of

SAW electrodes but still requires accurate starting constants for the minimization technique and may require multiple orientations accurately extract all the elastic and piezoelectric constants. A similar technique utilizing an IDT to generate the SAW and a laser probe has been utilized to extract LiNbO_3 elastic and piezoelectric constants at room temperature [309, 310, 314, 315].

Resonant ultrasound spectroscopy (RUS) can be used to extract the elastic and piezoelectric constants of crystals in harsh environments by recording the spectrum of acoustic resonant frequencies of a crystal sample and utilizing minimization fitting to determine the constants [316]. RUS has the advantage that it can measure all of the elastic and piezoelectric constants of a crystal from a single small sample because many acoustic resonance modes are used, each dependent on several different constants. The precision of RUS is comparable with that of the most carefully executed time-of-flight measurements, achieving approximately 10^{-4} relative measurement uncertainty, which is typically an order of magnitude better than BAW and SAW resonator techniques [316, 317].

In an RUS measurement, a crystal sample with a well-defined shape, such as cube, sphere, or rectangular parallelepiped, is contacted by multiple acoustic transducers that probe the crystal. One transducer generates a continuous-wave acoustic wave that vibrates the crystal sample and a second receiving transducer will measure increased vibration amplitude when the input frequency matches the frequency of a resonant mode of the crystal sample. The inverse problem of extracting the acoustic parameters directly from the resonant frequencies is not analytically manageable so a fitting technique is used to determine the set of constants that creates the best agreement between the measured and predicted frequency spectrum. The resonant frequencies of a piezoelectric crystal sample are calculated from the shape, orientation, density, elastic stiffness, piezoelectric constants, and dielectric permittivity of the material under investigation. Typically the sample size, orientation with

respect to crystalline axes, density, and dielectric constants are determined by separate measurement techniques and held constant for the RUS fitting so that the elastic and piezoelectric constants can be determined. However, other material parameters can often be extracted if the system is sufficiently overdetermined and the initial guesses for the constants are accurate [316]. The piezoelectric and permittivity of piezoelectric crystals cannot be separated because they appear as a ratio [318].

RUS is applicable to LGT and has been used to determine the elastic and piezoelectric constants of quartz and other trigonal crystals in [318–325] and, in recent years, to LGS and LGT crystals [232, 273, 278, 281, 283, 326–334].

Starting in the late 1970’s RUS has been adapted to high-temperature material measurement, initially focusing on the thermodynamic behavior of materials relevant to geophysics [335, 336]. Long buffer rods are added between the transducers and the sample to extend the measurement temperatures to 1550 °C and higher without exposing the transducers to excess heat [337–342]. The piezoelectric transducers used in RUS are typically PZT or a similar material that doesn’t survive above 100 °C or 200 °C so must be external to the heating area. The crystal sample and the buffer rods are the only components of the RUS system exposed to the hot environment and, for correctly designed system buffer rods with overlapping low-quality-factor modes, the measured changes in the resonant spectra are only due to the change in sample temperature. In order to extract the temperature dependence of the elastic stiffness and piezoelectric constants the density, thermal expansion, and temperature-dependent permittivity must be used in the fitting.

The crystal sample is not metallized and is only contacted by the buffer rods, simplifying the measurement and diminishing sources of error. Typically the sample rests on top of three buffer rods that form a tripod, in which one of the transducers is a transmitter and the other two are receivers [316]. When the crystal is placed on the transducer tripod the force is only that of the crystal weight, which is negligible for

most practical sample sizes [316]. The buffer rods contact the sample directly and no couplant material is needed because the weaker air-coupled interaction is sufficient to measure the resonant frequencies due to the larger vibrations during resonance. The crystal sample is not constrained and can freely expand as the temperature increases. Additionally, RUS utilizes frequency domain measurements so it is not affected by any time delay caused by an air gap between the buffer rod and the sample.

The RUS technique was selected to extract the LGT high-temperature elastic and piezoelectric constants in this work because of the high accuracy, ability to extract all constants from each crystal sample tested, and the applicability of high-temperature measurements without the complications due to mass loading, thermal expansion constraints, or acoustic couplant.

1.6.3 Extraction Techniques for High-Temperature Permittivity and Conductivity

The permittivity of a piezoelectric crystal is fundamental to the calculation of the piezoelectric effect and the design of acoustic wave devices. Additionally, the imaginary part of complex permittivity and the conductivity describe the electrical losses and should also be investigated at high temperature because the conductivity increases with temperature and the dielectric response can change with temperature.

The complex permittivity, $\epsilon_{ij} = \epsilon'_{ij} + \epsilon''_{ij}$, for a crystal is represented by a 3 by 3 tensor relating the electric field magnitude vector to the electric flux magnitude vector. The permittivity is frequency dependent, especially at and above optical frequencies but is often constant for the acoustic wave frequencies of interest, approximately from 1 MHz to a few GHz.

For piezoelectric crystals the permittivity should not be extracted at the natural acoustic resonant frequencies of the sample because the resonance will affect the extracted permittivity [297]. For example, a parallel-plate capacitor fabricated on

a piezoelectric crystal can excite BAW modes, which will absorb energy, if there is piezoelectric coupling in the thickness direction. Permittivity extracted at frequencies below 1 % of the fundamental BAW resonant frequency are extracted under constant stress and is denoted $\epsilon_{ij}^{\mathcal{T}}$, the free permittivity. Conversely, dielectric measurements made above the resonant frequencies yield the permittivity extracted under constant strain, denoted is ϵ_{ij}^S , called the clamped permittivity [297]. The free and clamped permittivities are related by [297]

$$\epsilon_{ij}^{\mathcal{T}} - \epsilon_{ij}^S = d_{iq}e_{jq} = e_{qip}s_{pq}^E e_{jq}, \quad (1.1)$$

where s_{pq}^E is the elastic compliance. Typically, $\epsilon_{ij}^{\mathcal{T}}$ can be found with more accuracy than ϵ_{ij}^S so $\epsilon_{ij}^{\mathcal{T}}$ usually measured and used to calculate ϵ_{ij}^S [297].

The permittivity at sub-optical wavelengths can be extracted from capacitor, resonant cavity, waveguide, or microstrip structures, but each has benefits and limitations in terms of applicable frequency range, accuracy, complexity, and adaptability to high temperature measurement [343, 344]. Total characterization of a dielectric material requires dielectric spectroscopy, utilizing a number of different measurement systems to characterize the permittivity over a wide range of frequencies, a few kHz to a few GHz for consideration with acoustic wave devices. However, this full spectrum characterization would require significant resources and time to acquire and validate the measurements at the high temperatures and is beyond the scope of this dissertation.

The permittivity of a crystal sample could be extracted from the resonant frequency of an electromagnetic resonant cavity containing the material. These measurements are typically in the range of hundreds of MHz to tens of GHz [344]. For solid samples, such as crystals, the cavity would be mostly filled with air or other gas and have the sample inside the cavity, perturbing the resonant frequency [343–345]. The sample dimensions and placement within the fixture need to be accurately known at all measurement temperatures for the sample permittivity to be extracted from the resonance in an inverse fitting process. Crystals with

anisotropic permittivity require more measurements and better modeling to extract the dielectric constants. Care must be taken to avoid disturbing the resonant cavity with the sample heating and temperature measure [344].

The reflection coefficient of an open-ended coaxial line can be used to determine the high-temperature dielectric properties of a sample placed at the end of the coaxial line because the changing sample permittivity alters load at the end of the cable. The coaxial reflection technique is a relatively easy method to measure high-temperature dielectric properties over a wide frequency range, about 500 MHz to 5 GHz, and at temperatures up to around 1200 °C, depending on the construction of the fixture [344]. Thermal expansion is a significant problem because it can make the sample lose contact with the center and outer conductors causing measurement errors; additionally, the expansion changes the phase shift of the coaxial line, requiring a complicated high-temperature calibration process [344, 346]. Open-ended coaxial probes have been fabricated out of metallized alumina to reduce the thermal expansion for dielectric measurements up to 1000 °C [346, 347]. Similarly, at higher frequencies open-ended waveguides can be used to extract the dielectric behavior of a sample at the high temperatures up to 1000 °C. Accounting for the sample waveguide expansion, heating the sample, and keeping the external measurement system at low temperature are the major problems in such waveguide measurements [344]. A similar technique utilizes a dielectric sample can be placed in free space and the electromagnetic wave transmission through the sample can be measured with a transmitting and a receiving antenna, and then correlated to the sample permittivity. This free-space method is applicable to frequencies in the range of 5 GHz to about 110 GHz, but requires samples $5\text{ cm} \times 5\text{ cm}$ to $15\text{ cm} \times 15\text{ cm}$ [344].

More recently, transmission coefficient measurement techniques using a platinum-coated ceramic coaxial have been demonstrated for complex permittivity measurements at frequencies from 0.3 MHz to 3000 MHz at temperatures up to 900 °C [348, 349].

The above techniques require careful sample alignment, precise fabrication, and accurate calibration across the entire temperature range and the use with anisotropic samples adds complexity that has not been demonstrated. Therefore, it is preferable to use parallel-plate capacitors to extract the permittivity of piezoelectric crystals because they typically are measured below the acoustic resonance, as specified by the IEEE Standard on Piezoelectricity [297], require simple measurements and calculations, adapt easily to high temperature, and can also be used directly to also determine the electrical conductivity [344, 350].

In this work, the dielectric constants are extracted from parallel plate capacitors because it allows for the simultaneous extraction of ϵ' , ϵ'' , and σ at relatively low frequencies. Capacitor measurements are the preferred method of dielectric extraction for piezoelectric materials [297].

1.7 Objective and Dissertation Organization

The primary objective of this dissertation research was to characterize the langatate acoustic wave constants at high temperatures up to 900 °C and use them to determine useful high-coupling temperature-compensated and temperature-sensitive orientations for BAW and SAW operation in harsh environments.

The first component of this work, discussed in Chapter 2, was the measurement of the LGT dielectric constants up to 900 °C. Capacitor measurements on LGT wafers were used to determine the permittivity and conductivity along the X, Y, and Z directions.

In Chapter 3 the measurement of the LGT elastic and piezoelectric constants up to 900 °C using resonance ultrasound spectroscopy (RUS) is discussed. The resonant spectra of LGT parallelepiped samples were measured and the acoustic constants were extracted using the dielectric constants from Chapter 2, the material dimensions, and the previously measured thermal expansion and density.

The extracted LGT constants were validated, in Chapter 4, by comparing predicted and measured SAW device thermal behavior up to 900 °C. Langatate delay line SAW devices were fabricated on wafers cut from a crystal boule, ground and polished to an optical-quality finish, and had high-temperature electrodes deposited on them. The LGT devices were characterized at high temperature to determine the operation frequency, velocity, temperature coefficient of delay, and the temperature dependence of each. The predicted and experimental behaviors were compared and used to validate the extracted high-temperature LGT constants.

The high-temperature LGT AW constants were used in Chapter 5 to predict SAW behavior at high temperatures and to search for SAW orientations optimized for high-temperature operation. High-temperature orientations were investigated using SAW calculations for high piezoelectric coupling and either low dependence on temperature or high sensitivity to temperature. Temperature-compensated orientations with a turnover temperature at high temperatures find application as frequency-control devices, identity tags, or sensors for pressure, strain, vibration, gas species, or among other measurands. Conversely, orientations with a large dependence on temperature are relevant for temperature sensors.

In Chapter 6 the extracted high-temperature LGT constants were used to identify orientations to use for BAW devices with high temperature operation. The temperature coefficient of frequency (TCF) and coupling were calculated to identify temperature-compensated orientations at elevated temperatures.

Chapter 7 concludes the dissertation with a summary of the work, statement of the contribution, and suggestion for future work.

Additional details of the work are included in the appendices. Appendix A contains the elastic, piezoelectric, and dielectric constants matrices for class 32 crystals. Additional details on the dielectric permittivity fitting calculations from Chapter 2 are described in Appendix B. Appendix C provides further detail of the RUS calculations, RUS sample fabrication, and constants extraction used in Chapter 3.

Chapter 2

DIELECTRIC PERMITTIVITY AND CONDUCTIVITY

2.1 Dielectric Permittivity and Conductivity Extraction Method

2.1.1 Complex Permittivity and Losses

The dielectric extraction process in this work considers the effect of the dielectric permittivity as well as polarization and conductivity losses because of the expected increase in losses at high temperatures [345, 351, 352]. The polarization and conductivity losses are both temperature dependent and are material dependent so for any particular crystal being investigated it is difficult to determine a priori at which temperatures these losses would become significant. For some insulators the losses are not significant below a few hundred degrees Celsius, but for others the losses are relevant at room temperature [345, 352]. For a complete study of a new crystal, it is better to consider both forms of loss relevant to the measurement of the real dielectric permittivity.

Prior studies of LGT conductivity indicate that the conductive losses do increase with temperature [42, 162, 219, 221, 279, 280] and should be included in the dielectric extraction above around 350 °C [279]. The LGT and LGS polarization losses are typically not separated from the conductivity losses [178, 279], so it was not known before hand if the polarization of LGT would be measurable. For the measurement process in this work, described in the following sections, the consideration of both the polarization losses and conductivity required no modification of the measurement equipment and are included in the modeling and constant extraction, described in Section 2.1.2.

The electrical losses from conductivity and polarization originate from different physical phenomena. Conductivity losses are caused by energy lost to the flow of mobile charge carriers, such as electrons, holes, and ions. The imaginary component

of permittivity describes losses in the polarization process of the reorientation of induced or built-in dipoles.

The dielectric permittivity and polarization losses are caused by the creation of a charge separation when an external electric field is applied. The total polarization of a non-ferroelectric medium is the sum of polarization due the physical phenomena relevant for that material; specifically the electronic, ionic, orientational, and space charged polarizations [352], each discussed below. The electronic, ionic, and orientational polarizations are caused by positive and negative charges that are bound together, whereas the hopping and space charge polarizations are due to the movement of charge carriers better sites in the crystal lattice.

The electronic polarization is caused by the displacement of the electron orbit offsetting the average electron orbit from the nucleus and occurs in all atoms. The ionic polarization occurs when the atoms forming an ionic bond experience a displacement from the equilibrium positions. The orientational or dipolar polarization arises from the orientation of permanent dipoles in the medium. This process typically occurs only in gases, liquids, and some solids in which the dipoles are capable of reorienting. In most solids the dipoles are frozen below the melting point and have a fixed orientation [352].

Polarization due to the hopping of charge carriers, such as electrons, holes, or ions, occurs when the carrier moves between neighboring sites and can be approximated by movement in a double potential well. Polarization also occurs when carriers are located at the interface between materials, such as in layered dielectrics. The space charge polarization is caused by mobile or trapped charge carriers and occurs mostly in polycrystalline or amorphous solids or solids in which the carriers are trapped at defects or internal barriers.

Each polarization effect responds with a different time-constant so are relevant at different frequencies. The most common polarization types in solids will be detailed

here, starting from the ones with the fastest response. In response to a step-function electric field, the electric polarization reaches steady state first, followed by the ionic, orientational, hopping, and space charge polarizations. When an AC electric field is applied to a dielectric, the frequency affects which polarization phenomena are significant. At low frequencies, all the polarizations are relevant but as the frequency increases the contributions of some of the polarization mechanisms are reduced. For example, orientation polarization is caused by built-in dipoles reorientating to the electric field but has sufficiently high frequencies (above a few GHz) the dipoles lag the electric field and at optical frequencies the dipoles can be considered stationary with respect to the electric field and do not contribute to the polarization.

The types of polarization can be classified as either resonance type or relaxation type. The electronic and ionic polarizations are resonance-type and the crystal electrons experience a physical resonance when excitation signal frequency matches a natural oscillation. The relaxation-type polarizations, such as orientational and space charge contributions, require time for the dipoles to respond to an electric field and have a characteristic relaxation time in which the polarization decays due to thermal agitation after the field is removed. Since the ionic polarization resonances occur at high frequency, only the losses due to the dielectric relaxations need to be considered at frequencies below about 10^{12} Hz, ie. below the near-infrared frequencies [352].

The real and imaginary permittivity are related to each other by the the Kramers-Kronig relationship, in which one can be found from the other quantity integrating over frequency due to linearity and causality [351–354]. Specifically, the imaginary permittivity has a peak or spike in loss at a given frequencies for each of the separate polarization mechanisms described above. The real permittivity has a flat response to frequency except around the loss peak. For relaxation-type polarization mechanisms, the real permittivity decreases around the loss frequencies, then becomes flat until the next loss peak. The resonance-type loss mechanisms at higher frequencies cause

the real permittivity have a resonance behavior with an apex followed by a dip before returning to the starting value before the loss peak.

This work targets the extraction of permittivity at low frequencies, <1 MHz, rather than at high frequencies, >1 GHz, for use in the prediction of BAW and SAW device performance, which are typically expected to operate between 100 kHz and 1 GHz. This is because the real permittivity, the primary focus of this work, decreases as the frequency increases such that relaxation mechanisms are no longer significant, as described above. For most crystals, the real permittivity is flat with frequency until the orientational dipole polarization loss increases around a few GHz [352]. The extracted low-frequency permittivity is an upper bound on the actual permittivity at the AW operation frequency and thus the calculated piezoelectric coupling of the AW device, which is inversely related to permittivity, is the lower bound coupling [297]. If the permittivity is only measured at higher frequencies, where the permittivity could be smaller than at the acoustic frequency, the calculated coupling could over estimate the coupling for a fabricated acoustic device. Additionally, the difference between the LGT permittivity in GHz-range and low-frequency is expected to be small, following the behavior of LGS, which has permittivities measured at 4.4 GHz and 6.7 GHz [355] that were found to be less than 2.1 % different from the average low-frequency permittivities reported in the literature [356].

2.1.2 Dielectric Extraction with Parallel-Plate Capacitors

The LGT dielectric measurements at high temperature are modeled with the dielectric permittivity and losses from both the polarization and conductivity losses, as detailed below.

The dielectric permittivity is treated as a complex number [352]

$$\epsilon = \epsilon' - j\epsilon'' \quad (2.1)$$

where $j = \sqrt{-1}$, ϵ' accounts for the energy storage effect, and ϵ'' describes the polarization losses.

Additionally, the permittivity can be represented in terms of a relative permittivity

$$\epsilon_R = \frac{\epsilon}{\epsilon_0} \quad (2.2)$$

where $\epsilon_0 = 8.854 \times 10^{-12} \text{ F m}^{-1}$ is the permittivity of free space.

The electrical conductivity, σ , is included in the dielectric analysis through the total current density, \vec{J} , considering both conduction and displacement currents as given by

$$\begin{aligned} \vec{J} &= \sigma \vec{E} + j\omega (\epsilon' - j\epsilon'') \vec{E} \\ \vec{J} &= j\omega\epsilon_0 \left(\epsilon'_R - j \left(\epsilon''_R + \frac{\sigma}{\omega\epsilon_0} \right) \right) \vec{E} \end{aligned} \quad (2.3)$$

where $\omega = 2\pi f$ and f = frequency.

The conductivity, σ , is treated as a frequency-independent real number for the frequencies used in this work ($< 100 \text{ MHz}$). The relaxation time of carriers in high-resistivity materials is typically very small ($< 1 \times 10^{-8} \text{ s}$) [352], so for the frequencies in this work the carriers will respond to the applied electric field with negligible delay and can be considered to be frequency independent.

The loss tangent, $\tan \delta$, is often used to quantify the electrical losses in a material and is calculated from (2.3) by the losses divided by the energy storage, namely

$$\tan \delta = \frac{\omega\epsilon''_R\epsilon_0 + \sigma}{\omega\epsilon'_R\epsilon_0} \quad (2.4)$$

In this work, the dielectric parameters ϵ' , ϵ'' , and σ , are extracted through admittance measurements of parallel-plate capacitors. The measurement details, including compensation for the measurement fixture and cables, are described in Section 2.2. The admittance, Y , of a parallel-plate capacitor, neglecting electric field fringing until

Section 2.1.3, is given by

$$Y = \frac{I}{V} = \frac{J \cdot A}{E \cdot h} = (\sigma + \omega\epsilon_R''\epsilon_0 + j\omega\epsilon_R'\epsilon_0) \frac{A}{h} \quad (2.5)$$

where A is the electrode area and h is the dielectric thickness and Eq. (2.3) is used. Equation (2.5) will be referred to as the ideal parallel-plate relation because it assumes that there is no fringing of electric field at the edges of the electrodes, i.e. the electric field is assumed to be normal to the wafer surface and only exist below the electrode. The electric field fringing can be a significant effect for actual samples depending on the dimensions and the effect will be included in the analysis in Section 2.1.3.

By measuring the complex admittance for a range of frequencies, the ϵ_R' is extracted from the imaginary part of Y and the real part is fit to a function of frequency to extract ϵ'' and σ . The permittivity and conductivity constants are assumed to be independent of frequency over the range of frequencies used in the capacitor measurements, which is 20 Hz to 1 MHz for the measurement setup described in Section 2.2.2.

Capacitance measurements of piezoelectric crystals require additional care because the capacitor structure can excite thickness mode bulk acoustic wave vibration in the crystal. The dielectric permittivity under constant-stress, ϵ^T , were extracted from admittance measurements made at frequencies more than a decade below the acoustic resonance of the samples [297]. The dielectric permittivity under constant-strain, ϵ^S , is related to ϵ^T by the relation [297]

$$\epsilon_{ij}^S = \epsilon_{ij}^T - e_{ip}s_{pq}^E e_{jq}, \quad (2.6)$$

where $c_{pr}^E s_{pq}^E = \delta_{pq}$, s_{pq}^E is the elastic compliance matrix at constant electric field, c_{pr}^E is the elastic constant matrix at constant electric field, δ_{pq} is the Kronecker delta or identity tensor, and the subscript indices are $i, j = 1, 2, 3$ and $p, q = 1, 2, 3, 4, 5, 6$. In the dielectric extraction process describe in the rest of the chapter the superscript T will

be dropped for convenience and reference is made to the constant-stress permittivities, $\epsilon^{\mathcal{T}}$, unless otherwise noted.

Langatate and other class 32 crystals have two independent dielectric constants, ϵ_{11} and ϵ_{33} , given by the dielectric constant matrix (A.3). Measurements of X-axis and Y-axis plates yield ϵ_{11} , whereas Z-axis plates are used to extract ϵ_{33} . For LGT and other class 32 crystals, (2.6) is evaluated using the elastic and piezoelectric matrices resulting in [297]

$$\begin{aligned}\epsilon_{11}^S &= \epsilon_{11}^{\mathcal{T}} - \left(\frac{c_{44}^E e_{11}^2 - 2c_{14}^E e_{11} e_{14} + c_{66}^E e_{14}^2}{c_{44}^E c_{66}^E - c_{14}^E{}^2} \right) \\ \epsilon_{33}^S &= \epsilon_{33}^{\mathcal{T}}.\end{aligned}\tag{2.7}$$

In this work, the elastic and piezoelectric constants extracted in Chapter 3 and the extracted $\epsilon^{\mathcal{T}}$ are used to calculate ϵ^S .

2.1.3 Compensating for Electric Field Fringing

In parallel-plate capacitors the electric field undergoes fringing at the edges of the electrodes where it is not normal to the sample surface and it extends out beyond the electrodes [357]. For an infinitely wide capacitor there is no fringing and the admittance is given by (2.5). For finite capacitors, the fringing has a negligible effect if the length and width are much greater than the dielectric thickness. However, the diameter of the wafers are limited by the boule dimensions and material availability, and the thickness should not be so thin that the samples are fragile and have a larger relative error in the thickness measurement. The effect of the fringing field had to be considered in this work since the sample thickness could not be considered negligible with respect to the electrode diameter.

For electrodes with circular electrodes the fringing is proportional to the electrode radius, allowing measurements of capacitors of various electrode sizes to be used to remove the fringing [110, 357–359]. The backside of each capacitor is completely

coated with a ground plane and the top side has a round electrode, as shown in Fig. 2.1. The radius of the top electrode, r , was increased in subsequent fabrications on the same sample, allowing multiple measurements with decreasing ratios of thickness to radius, h/r . A curve can be fit to the data and the permittivity data extrapolated to $h/r = 0$, thus removing the fringing effect.

The total measured capacitance, C_{meas} of a circular parallel-plate capacitor is [110, 357]

$$C_{meas} = \frac{\epsilon'_R \epsilon_0 \pi r^2}{h} + 2\pi r \alpha' \quad (2.8)$$

where α' is the electric field fringing parameter for the real permittivity and has units F m^{-1} .

A measured permittivity, ϵ'_{meas} , is defined to be directly calculated from the capacitance by

$$C_{meas} = \frac{\epsilon'_{meas} \epsilon_0 \pi r^2}{h} \quad (2.9)$$

where ϵ'_{meas} is the true relative permittivity plus the fringing effect, given by

$$\epsilon'_{meas} = \epsilon'_R + \frac{2\alpha'}{\epsilon_0} \left(\frac{h}{r} \right). \quad (2.10)$$

The dielectric losses are also affected by the fringing of the electric field which increases the effective area of the capacitor. The measured imaginary permittivity, ϵ''_{meas} , is extracted from the admittance in (2.5) and given by

$$\epsilon''_{meas} = \epsilon''_R + \frac{2\alpha''}{\epsilon_0} \left(\frac{h}{r} \right), \quad (2.11)$$

where α'' is the fringing parameter for the imaginary permittivity.

The electrical current is be increased by the fringing electric field and the measured conductivity is

$$\sigma_{meas} = \sigma + 2\alpha_\sigma \left(\frac{h}{r} \right). \quad (2.12)$$

where α_σ is the fringing parameter for the conductivity.

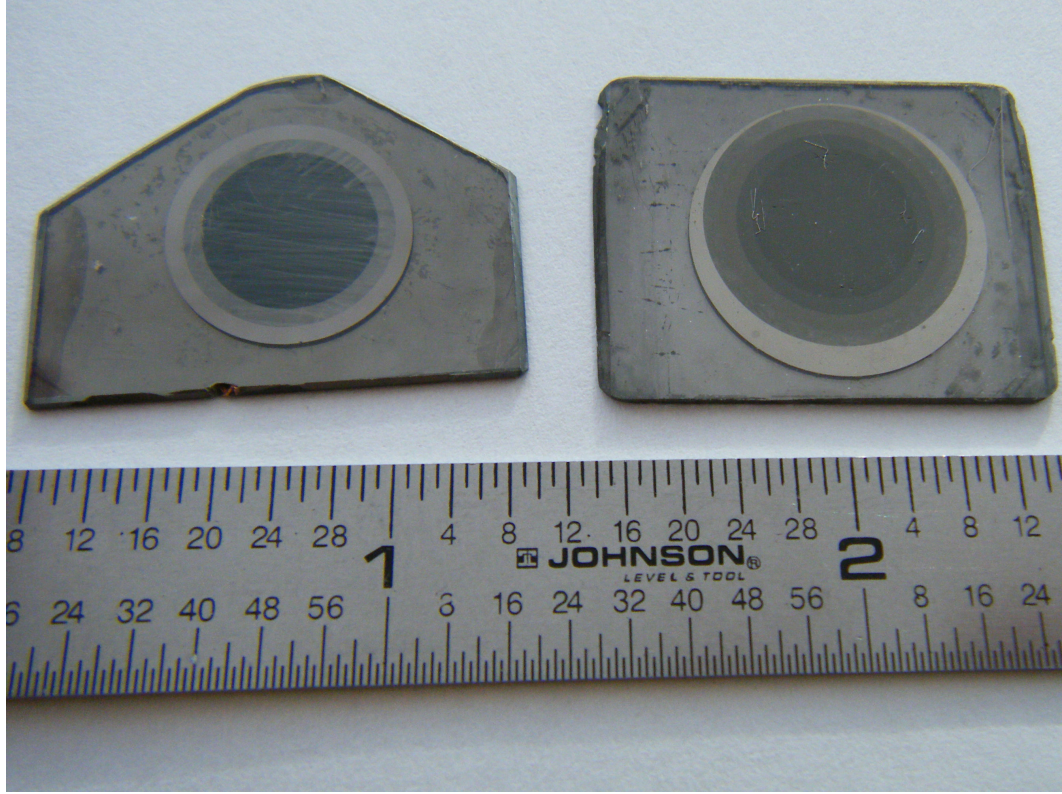


Figure 2.1. Fabricated LGT capacitors. Multiple depositions of the top electrode with increase radius can be seen. The units of shown ruler are inches.

2.1.4 Temperature Dependence and Curve Fitting Process

The dielectric properties ϵ' , ϵ'' , and σ are temperature dependent and the extraction process needs to reflect the appropriate temperature functions for each parameter. The fringing parameter, α , is assumed to be independent of temperature, this assumption was tested and is verified in Section 2.3.

The measured permittivity is temperature dependent due to the permittivity itself and also due to the thermal expansion of the sample thickness and electrode radius. The measured permittivity (2.10) is modified to include the effects of temperature on the permittivity, wafer thickness, and electrode radius by the inclusion of the

temperature coefficients, TC (3.33), and becomes

$$\epsilon'_{meas}(T) = \epsilon'_R \left[1 + \sum_n TC_{\epsilon'}^{(n)} (T - T_0)^n \right] + \dots$$

$$\frac{2\alpha'}{\epsilon_0} \left(\frac{h \left[1 + \sum_n TC_h^{(n)} (T - T_0)^n \right]}{r \left[1 + \sum_n TC_r^{(n)} (T - T_0)^n \right]} \right) \quad (2.13)$$

where ϵ'_R , h , and r are the previously defined quantities at the reference temperature T_0 .

The LGT permittivity ϵ'_{R33} was described using third-order temperature coefficients because the measured permittivity was found to decrease monotonically with temperature from 25 °C to 900 °C and could be accurately fit with the third-order polynomial. However, the LGT ϵ'_{R11} was found to increase with temperature until around 650 °C before decreasing and did not follow the shape of a third-order polynomial with $T_0=25$ °C. The data for ϵ'_{R11} was split into two temperature regions, 25 °C to 500 °C and 500 °C to 900 °C, each fit with separate temperature coefficients. The extracted temperature coefficients and fit quality will be discussed in Section 2.3.

The sample thickness and electrode radius both increase with temperature due to the thermal expansion of the LGT. The thin-film electrode is assumed to be compliant enough such that r expands with the substrate. For LGT the total linear expansion from 25 °C to 900 °C is as high as 0.73 % [148, 271] and for LGT wafers normal to the X, Y, or Z crystalline axes h/r increases by 0.2 % or less over the temperature range from 25 °C to 900 °C. The thickness and radius expansions partially cancel each other out in the ratio, with incomplete cancellation due to the anisotropy of LGT. The circular electrodes become slightly elliptical when the lateral sample dimensions have different expansion coefficients: for LGT the expansion along the Z axis is 0.53 % compared to 0.73 % expansion in the X and Y directions. The eccentricity of the ellipse remains low, <0.07 , close to zero eccentricity for a circle, even at 900 °C and therefore can be approximated by a circle with a radius equal to the mean of the

two expansions. The approximation leads to a relative calculation error of less than 1×10^{-6} of the electrode area and circumference for LGT at 900 °C, which is less than the effect of the uncertainty in the expansion measurement [148, 271]. The LGT thermal expansion and temperature variation of h/r are utilized in the data extraction calculations for completeness but are not written in the following analysis for simplicity.

The measured permittivity is given by a two-dimensional function of the capacitor h/r ratio and temperature, T . By fabricating samples with multiple h/r ratios and measuring them over the high temperature range there will be data points across the surface and a fitting process can be used to extract the unknowns ϵ'_R and $TC_{\epsilon'}^{(n)}$. The fitting process and data extraction for the LGT dielectric measurements are discussed in Section 2.2.3.

The dielectric polarization losses, ϵ''_R , are also functions of temperature and are characterized by increased losses at particular temperatures and frequencies so are not described temperature coefficients [352]. The temperature behavior of the LGT ϵ''_R in the range 25 °C to 900 °C was found to display a single loss peak over the measured temperature and frequency range and was described by a Gaussian curve given by

$$\epsilon''_R(T) = a \exp \left(- \left(\frac{T - b}{c} \right)^2 \right) + d \quad (2.14)$$

where a is the unitless amplitude parameter, b is the center of the loss peak in °C, c has units °C and is the full width at half maximum (FWHM) divided by $2(\ln 2)^{1/2}$, and d is the unitless temperature-independent loss.

The effect of electric field fringing on the dielectric loss parameters from (2.11) is combined with the temperature dependence from (2.14), and the imaginary permittivity is extracted from the measurements using

$$\epsilon''_{meas}(T) = a \exp \left(- \left(\frac{T - b}{c} \right)^2 \right) + d + 2\alpha'' \left(\frac{h}{r} \right) \quad (2.15)$$

The electrical conductivity, σ , of insulators has temperature dependence described by the Arrhenius relationship [351, 352] with the added fringing effect

$$\sigma(T) = \frac{A}{T} \exp\left(\frac{-E_a}{kT}\right) + 2\alpha_\sigma \left(\frac{h}{r}\right) \quad (2.16)$$

where A is the pre-exponential factor with units $\text{K } \Omega^{-1} \text{ m}^{-1}$, E_a is the conduction activation energy in eV, $k = 8.61733 \times 10^{-5} \text{ eV K}^{-1}$ is the Boltzmann constant, and T is the temperature in Kelvin. In general, the term AT^{-1} multiplying the exponential can be replaced by a constant or other slowly-varying functions of temperature, depending on the carrier mobility and concentration temperature behavior for the dominant conduction mechanisms [351, 352].

The conduction in LGT and LGS crystals is caused by a movement of electrons and ions, where the dominant conduction mechanism depends on the temperature regime, doping, contamination, and oxygen concentration during heating [162, 219, 360, 361]. Research on the physical conduction mechanisms is on-going in the literature and is beyond the scope of this work.

Most of the literature indicates that the conductivity of undoped LGT and LGS annealed in air is modeled using an Arrhenius curve with a pre-exponential term of T^{-1} , and shown in (2.16) [162, 219, 280, 360, 361], although a constant temperature-independent pre-exponential factor has also been used in a few studies [42, 362]. In this work, the pre-exponential term AT^n with $n = -1$ and $n = 0$ were both explored to fit the data to the Arrhenius equation (2.16) since both are reported in the literature.

2.2 LGT Dielectric Permittivity Extraction Process

2.2.1 LGT Capacitor Fabrication

The LGT samples used in this study were X-ray aligned, cut, ground, and polished at the University of Maine from LGT boules purchased from Fomos (Fomos-Materials,

Moscow, Russia). The samples were aligned to the normals of the X and Y crystalline axes for the extraction of $(\epsilon'_{R11}, \epsilon''_{R11}, \sigma_{11})$ and normal to the Z crystalline axis for the extraction of $(\epsilon'_{R33}, \epsilon''_{R33}, \sigma_{33})$. The X-axis and Y-axis oriented plates should yield the same permittivity results due to crystal symmetry and their data were combined together; this assumption is validated in Section 2.3. The process at UMaine of wafer alignment with a PANalytical X'Pert Pro MRD X-ray diffractometer (PANalytical Inc., Natick, Corp., Waltham, MA) and cutting with an inner diameter saw (Meyer-Berger, Steffisberg, Switzerland) was shown to have achieved wafer orientations within 6 arcminutes [240]. The wafers were rectangular in shape with lateral dimensions larger than 20 mm and thicknesses between 0.4 mm and 0.7 mm. The thicknesses were measured with a Heidenhain-Metro precision length gauge (Heidenhain Corp., Schaumburg, IL).

The capacitor electrodes were made with co-deposited Pt/Rh/ZrO₂ thin-film metal with thickness of 200 nm or more and a Zr adhesion layer, which provide stable high-temperature performance [149, 171, 173]. One side of each wafer was covered in a ground electrode and the other has a round electrode with a radius from 5 mm to 10 mm, which is defined through photolithography. Successive round electrodes of increasing diameter were fabricated on the same wafer following each measurement, as shown in Fig. 2.1, thus allowing the usage of the same sample for multiple h/r ratios.

2.2.2 Capacitance Measurement Setup

The capacitors were heated in laboratory air in a Thermolyne furnace (Thermolyne, Dubuque, IA) and connected through high-temperature and room-temperature cables to a Precision LCR Meter (Agilent 4284A, Santa Clara, CA), shown in Fig. 2.2a. Although the impedances were measured between 500 Hz and 1 MHz, the data for the X and Y plates above 100 kHz was not used to ensure that

ϵ_{11}^T is extracted at frequencies at least a decade below any acoustic resonances, as discussed in Section 2.1.3. The measured frequency range is relatively narrow in terms of dielectric characterization [344, 352] and the extracted parameters are considered frequency independent in the measured range, as discussed in Section 2.1.1.

The capacitors were loosely held in a fixture so that there was no stress on the wafers, and the electrodes were bonded to two high-temperature coaxial cables using 1-mil platinum wire, shown in Fig. 2.3. At least four bonds were made from each of the top electrode to the center conductor of one of the cables and four bonds from the ground electrode to the center conductor of the other cable. The bonds were physically separated to evenly cover the electrodes. Room-temperature coaxial cables extended from the LCR meter to the high-temperature cables, enabling the system calibration and the four-wire measurement of the combined high-temperature cable and capacitor circuit. The impedances were measured at 25 °C and from 100 °C to 900 °C, in steps of 50 °C, and at 925 °C so that the extracted constants would be valid in the temperature range from 25 °C to 900 °C.

The capacitance measurement setup required multiple stages of calibration, shown in Fig. 2.2b, because no set of calibration terminations were available that could be operated up to 900 °C. The LCR meter and the four room-temperature cables were calibrated up to plane B' using open and short coaxial standards prior to each test using an internal LCR procedure. The high-temperature cables were calibrated up to the DUT at place C', utilizing open and short circuits inside the furnace. The effect of the high-temperature cables on the capacitor impedance was modeled with parasitic circuit elements, specifically a series resistance, series inductance, and parallel capacitance, without the need of transmission line theory because the measurement frequencies are below 1 MHz and the guided wavelength in the cable is 100 m or more and the high-temperature cables are less than 1 m long. The series resistive and inductive parasitic elements were found by measuring the capacitance fixture shorted with

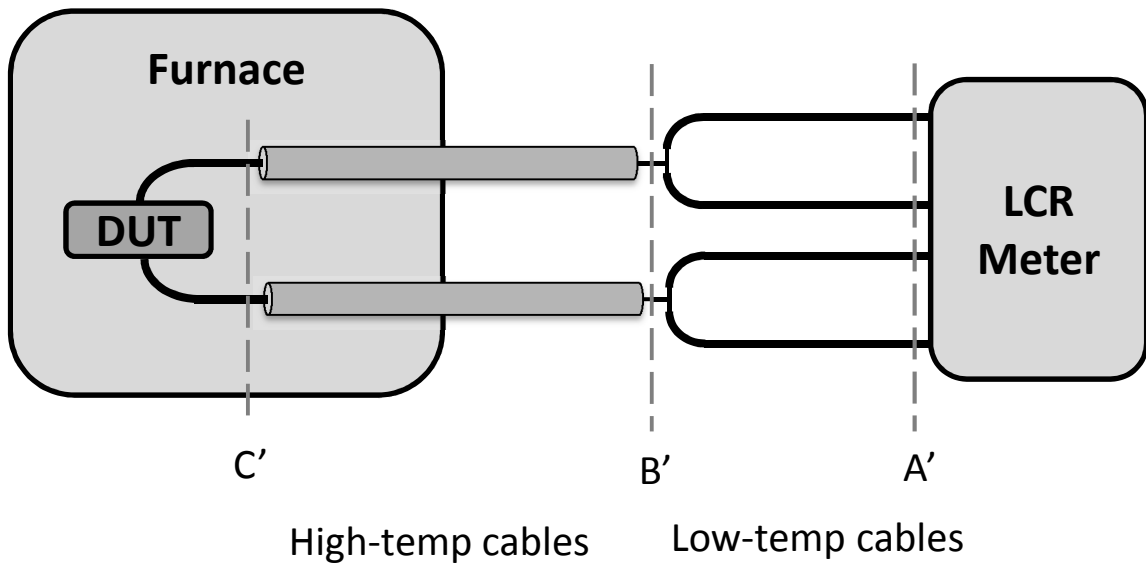


Figure 2.2. UMaine capacitance measurement setup. (a) high-temperature furnace and LCR meter used in capacitance measurement, (b) capacitance measurement schematic with calibration planes A',B',C'. DUT is device under test, either LGT capacitor or calibration circuit.

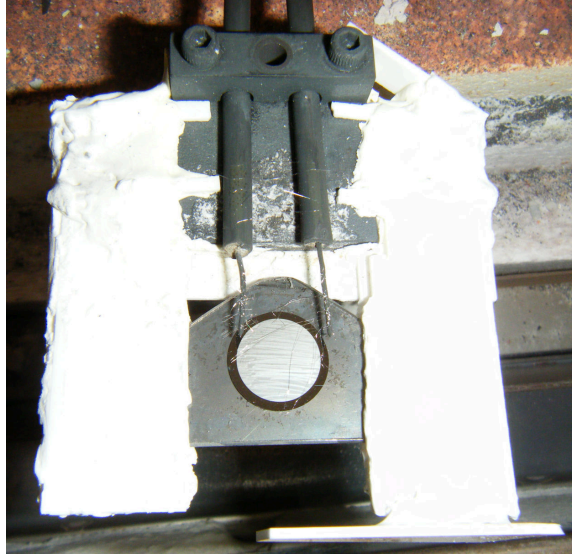


Figure 2.3. High-temperature capacitance measurement fixture with high-temperature cables.

platinum wires and the parasitic capacitance was found from open circuit measurements. The parasitics of the high-temperature fixture were measured from 25 °C to 900 °C and used to post-process the impedance measurements of the LGT capacitors to remove the cable and fixture effects.

2.2.3 Dielectric Extraction Calculations

Custom MATLAB functions were written to extract ϵ'_R , ϵ''_R , and σ from the high-temperature impedance measurements for the X, Y, and Z oriented capacitors. First, the parasitic circuit elements due to the the high-temperature cable and fixture were numerically removed from the impedance measurement data. The ϵ'_{meas} , ϵ''_{meas} , and σ_{meas} were extracted from the admittance measured at each temperature using the capacitor dimensions and LGT thermal expansion.

The extraction of the permittivity constants and respective temperature coefficients was accomplished by fitting a surface to ϵ'_{meas} with T and h/r as the independent variables. The uncertainty from the measurements was utilized in the fitting process by using the Total Least Squares (TLS) technique [363–365], in contrast the

ordinary least squares (OLS) method only includes uncertainty in the dependent variables, which is not the case in this work. In the fitting the temperature and h/r ratio are the independent variables and are measured with a non-negligible uncertainty, necessitating TLS for accurate fitting. The uncertainty was calculated from the measurement uncertainty of the impedance [366] and the Jacobian matrix from the fitting [367, 368]. The dielectric extraction method and calculation are detailed in Appendix B. The extracted relative permittivities, temperature coefficients, and fringing parameter from the surface fitting are given in Section 2.3 with respective standard deviation uncertainty values.

The permittivity under constants stress, ϵ^T , was extracted from the dielectric measurements and (2.7) was used to calculate the permittivity under constant strain, ϵ^S , with the extracted high-temperature piezoelectric and dielectric constants, which will be presented in Chapter 3. The ϵ^S curve was then fit to temperature coefficient polynomials.

The imaginary permittivity was extracted from a surface that was fit to a Gaussian peak, given by (2.15), using the Curve Fitting Toolbox in MATLAB (Mathworks, Natick, MA). The fitting function was nonlinear and was not easily linearized so would require modification of the TLS algorithm [364, 369, 370]. The usage of OLS instead of TLS may increase the systematic error in the ϵ'' fitting [364, 371], but was assumed to be acceptable for the dielectric losses in this work.

The conductivity parameters were extracted from the Arrhenius equation (2.16) fit to the measured conductivity. The conductivity was fit both with and without the fringing parameter, α_σ , using the Curve Fitting Toolbox in MATLAB to determine if electric field fringing is significant in the conductivity. Weighted TLS was also used when the fringing effect in the conductivity is ignored, $\alpha = 0$, because the Arrhenius equation can be linearized by taking the natural logarithm of it. The weighted TLS fitting was able to include the temperature measurement uncertainty in the

conductivity extraction, improving the fit accuracy. As mentioned in Section 2.1.4, the conductivity best-fit curve was determined using pre-exponential terms of A/T and A since both are consistently utilized in the literature.

2.3 LGT Dielectric Permittivity Results

The LGT dielectric properties ϵ'_{R11} , ϵ'_{R33} , ϵ''_{R11} , ϵ''_{R33} , σ_{11} , and σ_{33} were extracted from 25 °C to 900 °C using X-, Y-, and Z-oriented wafers and fit to their respective functions of temperature and h/r , as described in Section 2.1.

The admittance of the LGT capacitors was used in the extraction process and example representative admittance measurements for the LGT capacitors are displayed in Fig. 2.4 for visualization of the frequency and temperature dependence.

The LGT ϵ'_{meas} data, best-fit surface, and extracted fringe-free permittivity are shown for the combined X and Y wafers in Fig. 2.5a and for the Z wafer in Fig. 2.5b. The ϵ'_{meas11} data was fit to a surface utilizing a linear relationship for h/r and 2 sets of third-order temperature coefficients, the first is valid from 25 °C to 500 °C and the second is valid from 500 °C to 900 °C. As discussed in Section 2.1.4, it was necessary to break the polynomial fitting of ϵ'_{meas11} into multiple regions to improve the fitting accuracy. For ϵ'_{meas33} a single set of third-order temperature coefficients is sufficient to describe the temperature curve from 25 °C to 900 °C.

The ϵ'_{meas11} fit data agrees with the measured data with a root mean square error (RSME) of 0.397 and a correlation coefficient (R^2) of 0.978 and the ϵ'_{meas33} fit achieved an RSME of 0.587 and R^2 of 0.997. The high correlation between the measured data and the fitting confirms the assumption that the fringing effect is not strongly dependent on temperature, i.e., α' can be assumed constant with temperature in this work, as mentioned in Section 2.1.4. The ϵ'_{11} permittivities determined independently from X-axis and Y-axis oriented plates agree with each other by 1.1 % on average, which is within the experimental uncertainty of the results

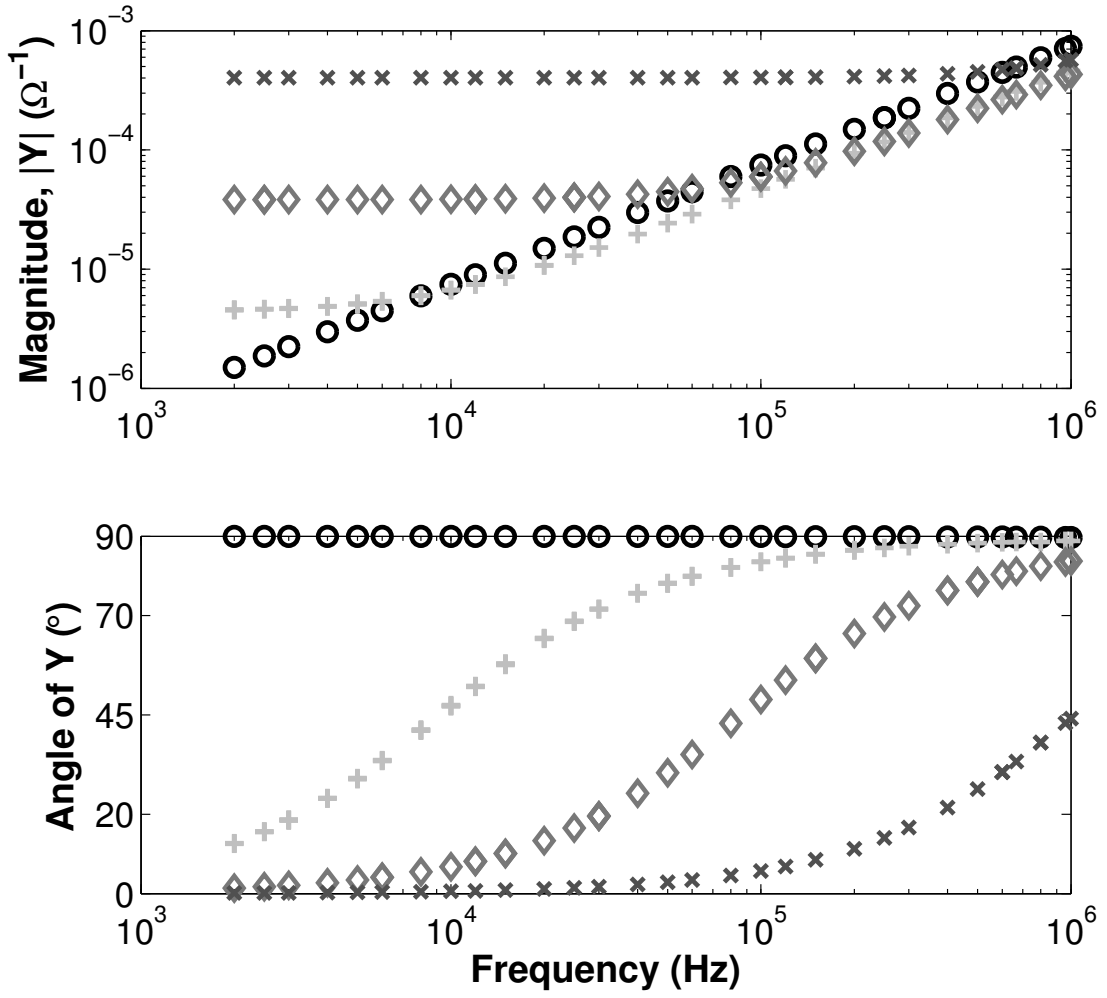


Figure 2.4. Example LGT measured capacitor admittances. For a Z-oriented wafer with a 6 mm radius electrode at 23 °C (o), 500 °C (+), 650 °C (\diamond), and 900 °C (\times)

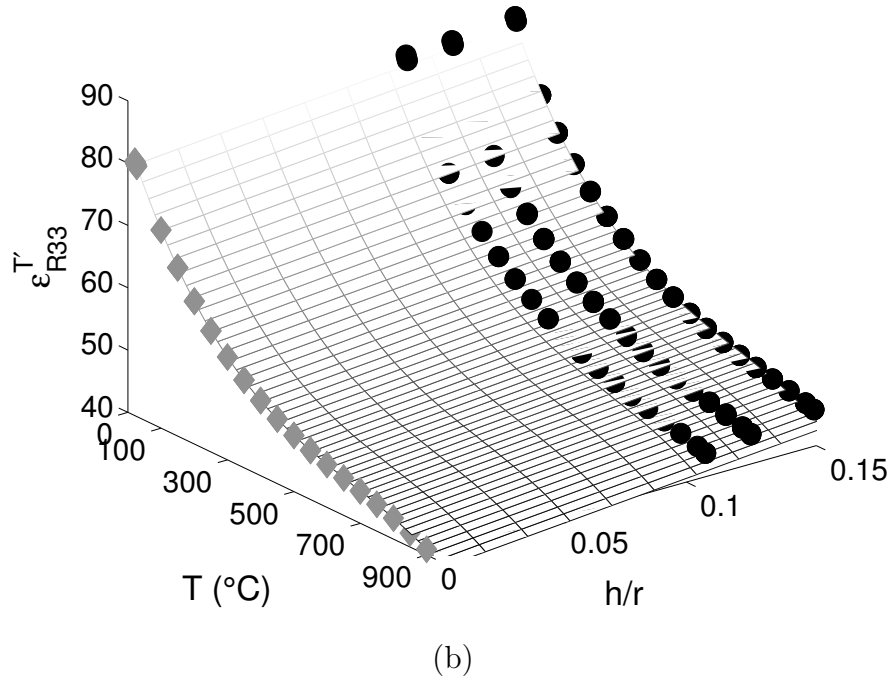
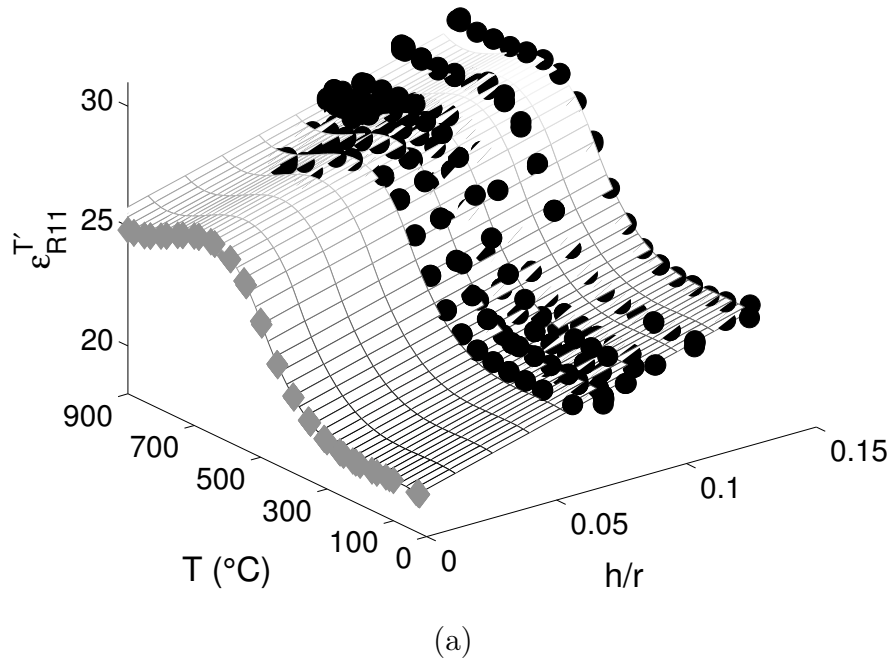


Figure 2.5. LGT measured permittivity and best-fit surface. (a) 11-direction from combined X and Y wafer data and (b) 33-direction from Z wafer data; with ϵ'_{meas} (●), best-fit surface (gray mesh), and extracted permittivity (◇).

of each orientation. The X-axis and Y-axis data are combined and used together in the ϵ'_{11} fitting and extraction due to the agreement between the data sets and due to crystal symmetry. The fringing parameters the from ϵ'_{meas11} and ϵ'_{meas33} data fitting were found to be $\alpha'_{11} = (1.29 \times 10^{10} \pm 0.05 \times 10^{-10}) \text{ F m}^{-1} = (14.5 \pm 0.6)\epsilon_0$ and $\alpha'_{33} = (1.57 \times 10^{-10} \pm 0.17 \times 10^{-10}) \text{ F m}^{-1} = (17.7 \pm 1.9) \epsilon_0$. The fringing electric field contributed between 4 % and 16 % of the total capacitance and was smaller when the h/r ration was smaller and decreased with temperature. The impact of the fringing on the LGT permittivity indicates the importance of the fringing analysis.

The fringing effect was removed to extract $\epsilon'^{\mathcal{T}}_{R11}$, ϵ'^S_{R11} , and ϵ'_{R33} up to 900 °C, where the ϵ'^S_{R11} was calculated with (2.7) using the extracted LGT stiffness and piezoelectric constants found in Chapter 3. The permittivities $\epsilon'^{\mathcal{T}}_{R11}$, ϵ'^S_{R11} and ϵ'_{R33} are shown in Figures 2.6 and 2.7 and are given with their temperature coefficients in Table 2.1. The one-standard-deviation uncertainty of each parameter is reported along with the nominal value.

The extracted ϵ'^S_{R11} increases from its room temperature value by 38 % at around 650 °C and slowly decreases at higher temperatures. The value of ϵ'^S_{R33} decreases by 49 % from 25 °C to 900 °C. The uncertainty in extracted permittivity $\epsilon'^{\mathcal{T}}_{R11}$ is better than 1.4 % at temperatures less than 875 °C and increases to 1.9 % at 925 °C. The uncertainty of ϵ'^S_{R11} is less than 1.5 % up to 400 °C and has the highest uncertainty, 2 %, at 900 °C. Note that the uncertainty in ϵ'^S_{R11} is slightly larger than for $\epsilon'^{\mathcal{T}}_{R11}$ because of the added uncertainty due to the elastic and piezoelectric constants used in the calculation. The uncertainty in $\epsilon'^{\mathcal{T}}_{R33}$ and ϵ'^S_{R33} is less than 1.1 % up to 525 °C and less than 1.6 % up to 925 °C. The RMS uncertainties over the measurement temperature range for $\epsilon'^{\mathcal{T}}_{R11}$, ϵ'^S_{R11} , and ϵ'^S_{R33} are 1.2 %, 1.5 %, and 1.1 %, respectively.

The extracted LGT room-temperature permittivities are given in Table 2.2 along with the values available in the literature [36, 41, 141, 206, 207, 227, 232, 233, 238, 279, 358]. The room temperature $\epsilon'^{\mathcal{T}}_{R11}$, ϵ'^S_{R11} , and ϵ'^S_{R33} found in this work are 4.0 %, 279, 358].

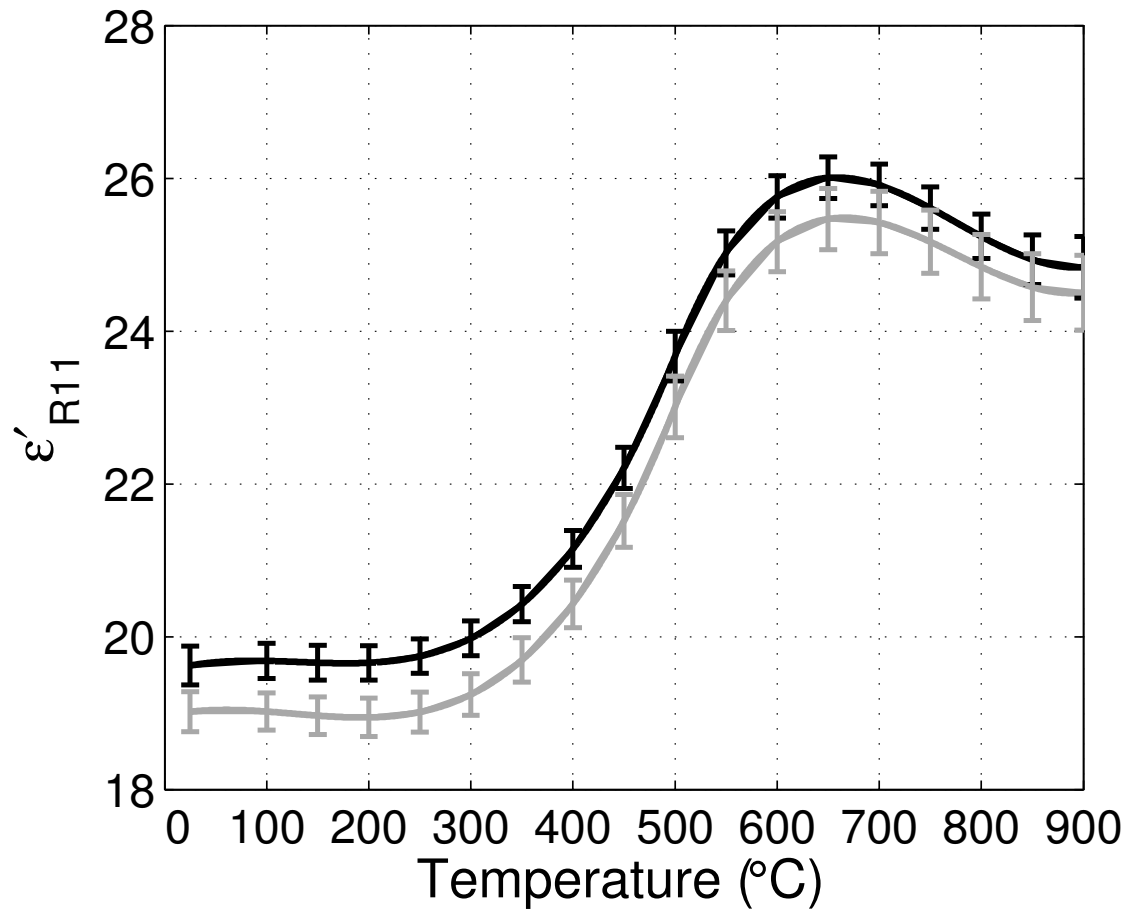


Figure 2.6. Extracted LGT real permittivity ϵ'_{R11} . Extracted under constant stress ϵ'^T_{R11} (black) and under constant strain ϵ'^S_{R11} (gray).

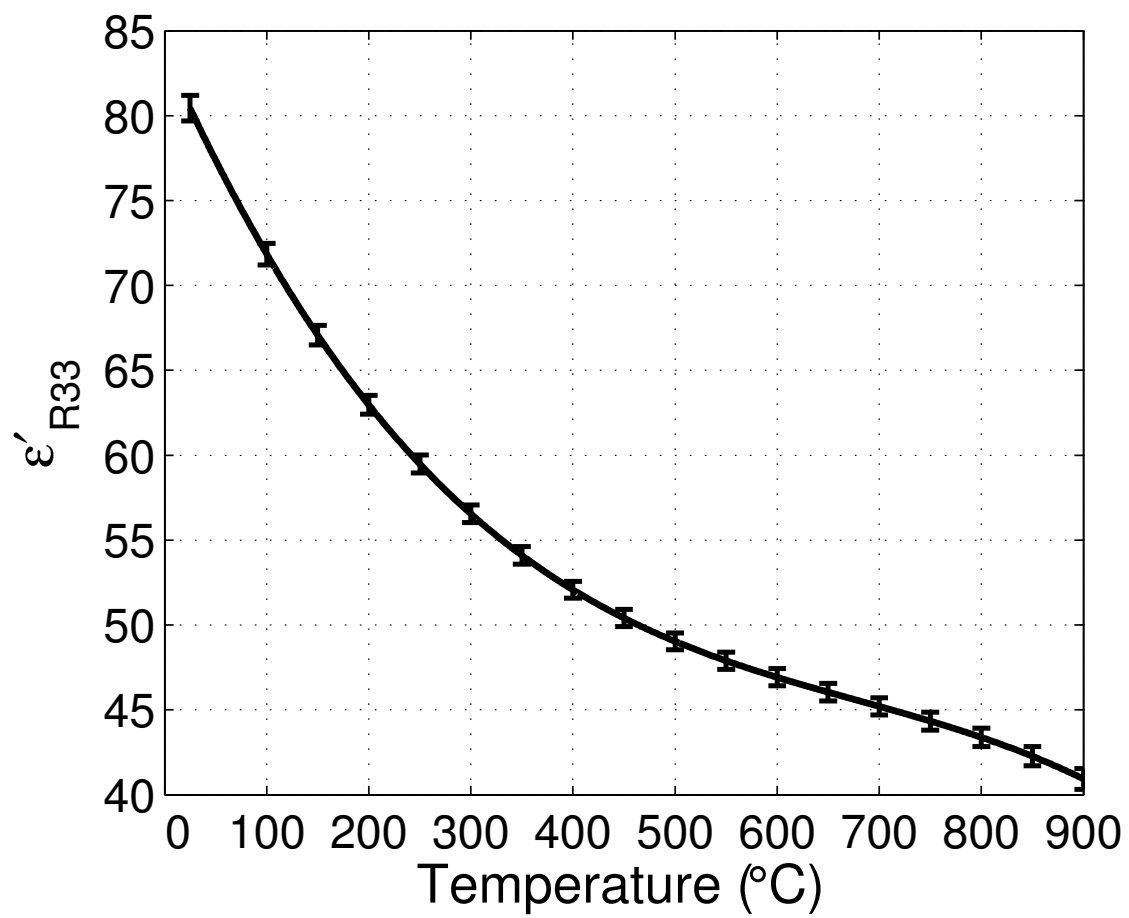


Figure 2.7. Extracted LGT real permittivity ϵ'_{R33} . Note $\epsilon'_{R33}^{\mathcal{T}} = \epsilon_{R33}^{S'}$.

	Temp. Range (°C)	$\epsilon'_R(T_{\text{ref}})$ (-)	TC ⁽¹⁾ (10 ⁻³ °C ⁻¹)	TC ⁽²⁾ (10 ⁻⁶ °C ⁻²)	TC ⁽³⁾ (10 ⁻⁹ °C ⁻³)
ϵ'_{R11}	25 to 500	19.62 ± 0.21	0.12 ± 0.05	-1.38 ± 0.19	4.30 ± 0.26
	500 to 900	23.67 ± 1.14	1.44 ± 0.06	-6.39 ± 0.26	7.73 ± 0.46
ϵ'_{R11}	25 to 500	19.02 ± 0.27	0.08 ± 0.06	-1.35 ± 0.22	4.46 ± 0.31
	500 to 900	23.01 ± 1.31	1.51 ± 0.09	-6.48 ± 0.37	7.79 ± 0.64
ϵ'_{R33}	25 to 900	80.44 ± 0.97	-1.57 ± 0.05	2.09 ± 0.08	-1.07 ± 0.05
ϵ'_{R33}					

Table 2.1. High-temperature LGT real dielectric permittivities and temperature coefficients from 25 °C to 900 °C. The reference temperature, T_{ref} , for each curve is given by the starting temperature for the respective temperature range.

2.7 %, and 4.3 % of the literature averages, respectively. When outliers more than two standard deviations from the average are removed, the difference from the literature average at room temperature improves to within 2.8 %, which is less than one standard deviation of the literature data.

The LGT dielectric losses, ϵ''_{R11} and ϵ''_{R33} , were extracted from 25 °C to 900 °C, shown in Fig. 2.8, and the fitting parameters indicated in (2.15) are given in Table 2.3. The curve fitting achieved an RSME of 0.19 with an R^2 of 0.93 for ϵ''_{R11} and an RSME of 0.067 with an R^2 of 0.97 for ϵ''_{R33} . The loss peaks are centered at 523 °C for ϵ''_{R11} and 718 °C for ϵ''_{R33} . At temperatures below 200 °C, the dielectric losses ϵ''_{R11} and ϵ''_{R33} are too small to be measured accurately, as indicated in Fig. 2.8. The fringing parameter α'' was found to be $(6.71 \pm 0.62) \times 10^{-12} \text{ F m}^{-1}$ for the 11-direction. and $(4.22 \pm 1.17) \times 10^{-12} \text{ F m}^{-1}$ for the 33-direction. For both directions the fringing effect accounts for 0.5 % to 1 % of ϵ''_{meas} at the loss peaks.

The fringing electric field effect on the conductivity was investigated by fitting the measured data with and without the fringing parameter, α_σ , using the MATLAB curve fitting toolbox. The fringing parameter was $3 \times 10^{-12} \Omega^{-1} \text{ m}$ or less for both the σ_{11} and σ_{33} data and pre-exponential terms with $n = 0$ or $n = -1$. The fringing contributed 1.4 % of the conductivity at 350 °C, 0.4 % at 400 °C, and decreased exponentially with temperature at higher temperatures, where it is below the experimental uncertainty. Therefore the fringing effect on the conductivity was considered to be negligible and was not included in further analysis, allowing the use of the weighted TLS fitting.

The LGT conductivities, σ_{11} and σ_{33} , were found to agree with the Arrhenius relationship in (2.16) using both $n = -1$ and $n = 0$ in the pre-exponential term. The best-fit parameters extracted using weighted TLS are given in Table 2.4. Both the AT^{-1} and A pre-exponential terms lead to good agreement between the best-fit curves and the data, as observed by their R^2 and RSME values, so neither equation

Reference	$\epsilon_{R11}^{\mathcal{T}}$	ϵ_{R11}^S	ϵ_{R33}^S
This work	19.62 ± 0.21	19.02 ± 0.27	80.44 ± 0.97
Fukuda et al. [207]	19.97	17.80 ^a	78.42
Pisarevsky et al. [206]	18.5	17.53 ^a	60.9
Bohm et al. [41]	20.42 ^a	19.6 ± 0.5	76.5 ± 1.3
Mill and Pisarevsky [36]	19.8	18.97 ^a	79.9
Onozato et al. [238]	20.02 ^a	19.3	80.3
Pereira da Cunha et al. [141]	18.98 ^a	18.25	78.95
Schreuer [232]	19.9 ± 0.2	19.1 ± 0.2	77.2 ± 0.4
Stade et al. [233]	19.9 ± 0.3		78.1
Kong et al. [227]	26.22		81.9
Davulis et al. [358]	18.57 ± 0.30	17.69 ± 0.30	70.73 ± 1.24
Sehirlioglu et al. [279]	24 ^b		84
Literature Average ^c	20.44 ± 2.31	18.50 ± 0.76	77.15 ± 6.04
Average removing outliers ^d	19.51 ± 0.68	18.50 ± 0.76	78.91 ± 1.64

^aCalculated using (2.6) and the constants given in the respective reference

^bAverage of X and Y axis values used for ϵ_{11}

^cUncertainty of the averages is the sample standard deviation of the data

^dOutliers removed if more than two standard deviations from the average

Table 2.2. Room-temperature LGT relative dielectric permittivities from the literature.

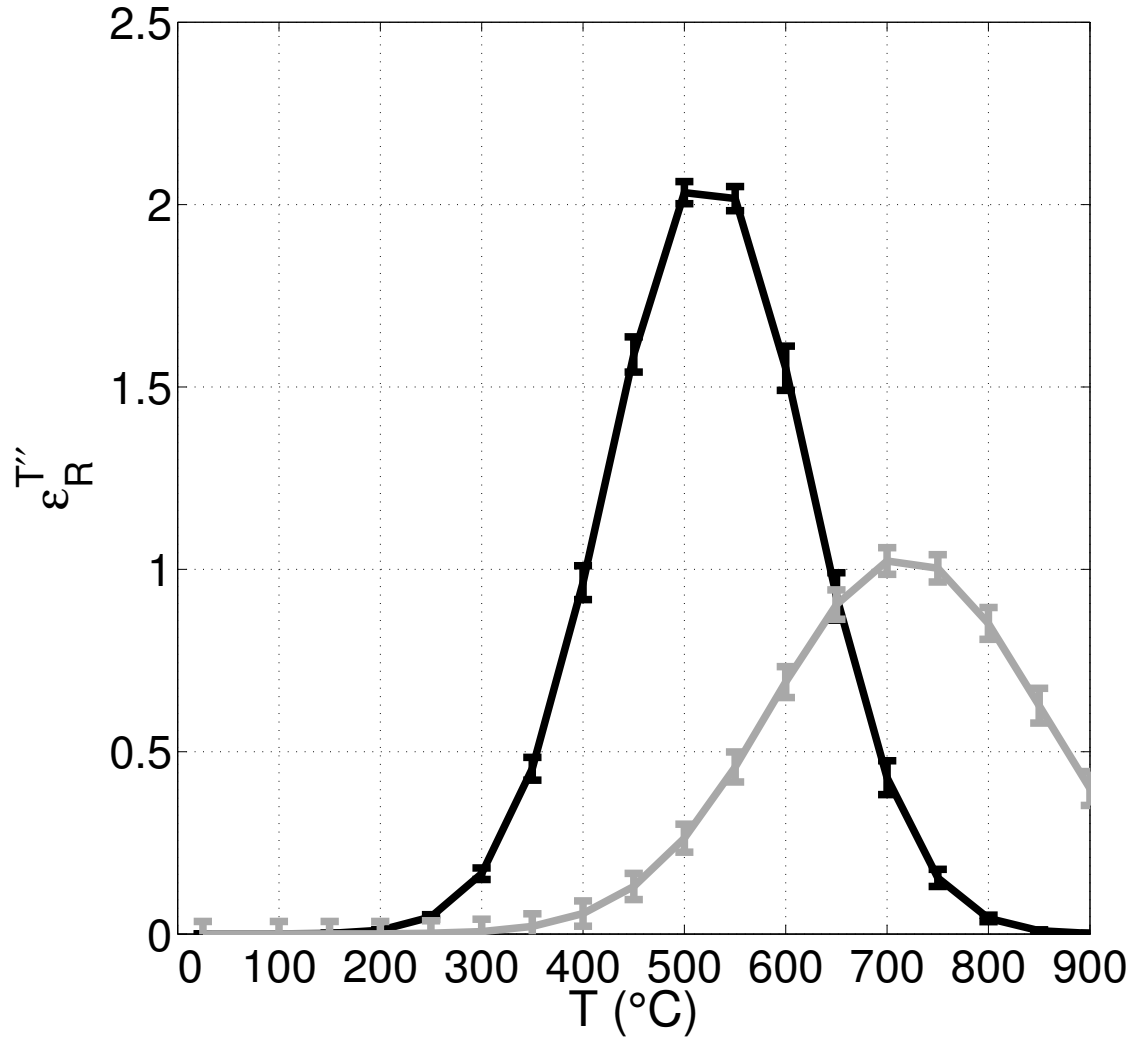


Figure 2.8. Extracted LGT imaginary permittivities. ϵ''_{11} (black line) and ϵ''_{33} (gray line).

	a	b	c	d
	(-)	(°C)	(°C)	(-)
ϵ''_{R11}	2.091 ± 0.024	523.4 ± 1.2	140.3 ± 2.1	0
ϵ''_{R33}	1.032 ± 0.012	718.2 ± 1.5	186.5 ± 2.8	$1.9 \times 10^{-7} \pm 3.4 \times 10^{-2}$

Table 2.3. High-temperature LGT imaginary dielectric permittivity. Extracted using temperature fitting parameters for (2.15) from 25 °C to 900 °C.

could be ruled out by the quality of the fitting. However, the pre-exponential term AT^{-1} will be used in this work to be consistent with the majority of the literature on LGT and LGS, as discussed in Section 2.1.4.

The measured LGT σ_{11} and σ_{33} data and the Arrhenius best-fit curves from (2.16) with AT^{-1} are shown in Fig. 2.9. The LGT conductivity at temperatures below 350 °C was too small to be measured with the equipment and technique used, which could not accurately resolve conductivities below $1 \times 10^{-6} \Omega^{-1} \text{ m}$. Although the measured data was kept in Fig. 2.9, the data was not considered for the curve fitting for extraction of A and E_a . Due to the class 32 crystal symmetry, the X and Y wafers should both measure the same conductivity, σ_{11} , [31]. The measured X and Y wafer conductivity data overlapped across the temperature range, confirming the symmetry relation, and the wafer measurements are combined into a single data set.

The LGT conductivities σ_{11} and σ_{33} increase with temperature and are $1.2 \times 10^{-2} \Omega^{-1} \text{ m}$ and $3.1 \times 10^{-3} \Omega^{-1} \text{ m}$, respectively, at 900 °C. The extracted activation energy, E_a , is $(1.0358 \pm 0.0019) \text{ eV}$ along the X- and Y-axes and $(0.9526 \pm 0.0023) \text{ eV}$ along the Z-axis. The measured values are within the range expected from the literature using the A/T pre-exponential factor, which range from 0.82 eV to 1.15 eV [162, 219, 280]. Additionally, the crystal growth atmosphere, growth method, and high-temperature annealing have been found to have an effect of up to 0.2 eV and can explain the discrepancy [219, 280].

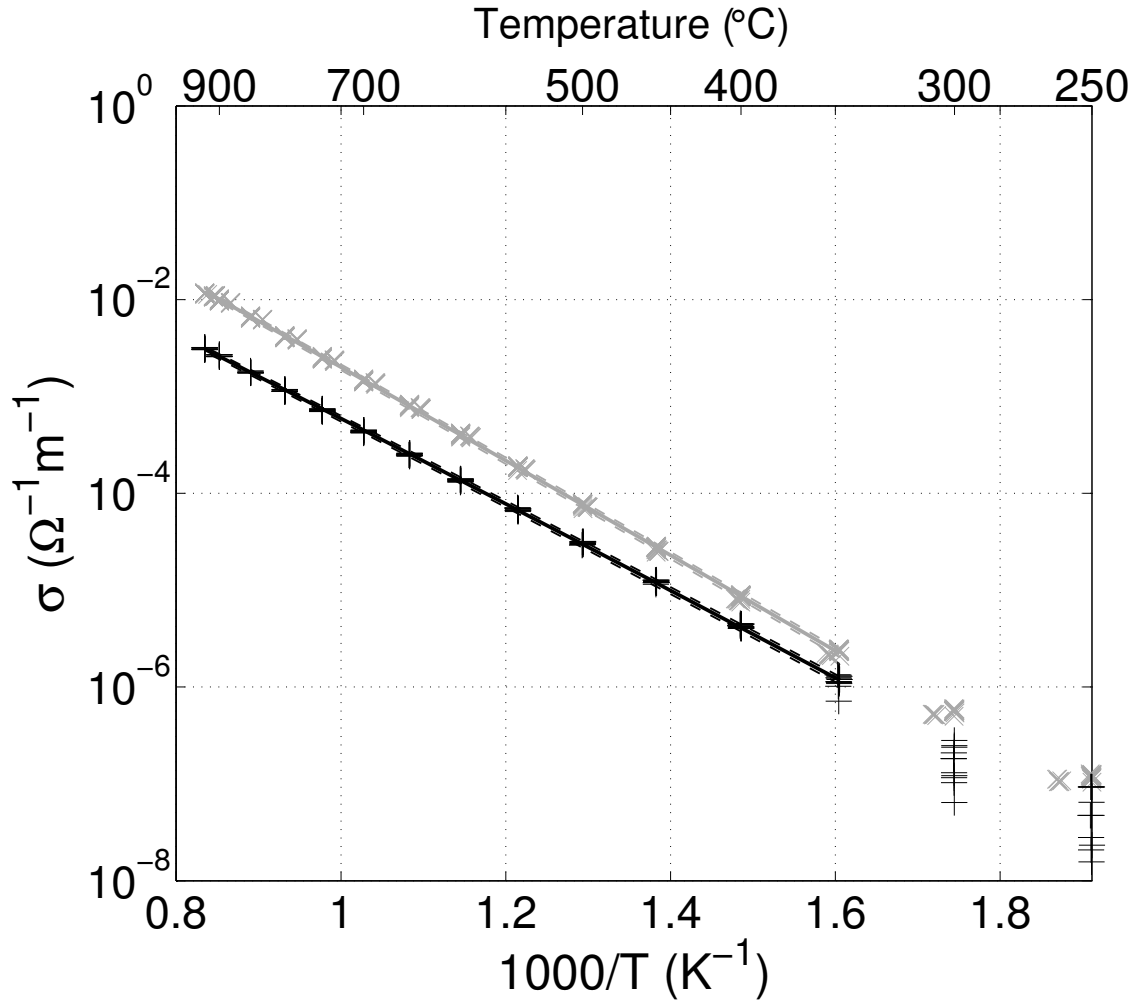


Figure 2.9. High-temperature LGT conductivity. Measured σ_{11} (gray \times), extracted σ_{11} (gray solid line) with uncertainty (gray dashed line), measured σ_{33} (black $+$), and extracted σ_{33} (black solid line) with uncertainty (black dashed line).

$A e^{-E_a/(k_b T)}$		A	E _a	R ²	RMSE
		(Ω ⁻¹ m)	(eV)	(-)	(Ω ⁻¹ m)
	σ ₁₁	138.8 ± 1.6	0.9612 ± 0.0009	0.9952	2.59 × 10 ⁻⁴
	σ ₃₃	15.32 ± 0.20	0.8766 ± 0.0010	0.9992	2.92 × 10 ⁻⁵
$AT^{-1} e^{-E_a/(k_b T)}$		A	E _a	R ²	RMSE
		(10 ³ K Ω ⁻¹ m)	(eV)	(-)	(Ω ⁻¹ m)
	σ ₁₁	333.3 ± 7.8	1.0358 ± 0.0019	0.9974	1.90 × 10 ⁻⁴
	σ ₃₃	37.39 ± 1.1	0.9526 ± 0.0023	0.9989	3.45 × 10 ⁻⁵

Table 2.4. High-temperature LGT conductivity parameters. Arrhenius curve parameters determined for two pre-exponential terms from 350 °C to 900 °C.

The loss tangent, $\tan \delta$, calculated by (2.4), is a more appropriate way to analyze the electrical losses of an insulator material, since it considers both conductivity and polarization effects and is a function of temperature and frequency. The LGT $\tan \delta$ is calculated up to 900 °C for the 11- and 33-directions from the extracted losses and is shown in Fig. 2.10 for 1 kHz and 1 MHz to reflect the frequency range of the dielectric measurements.

For LGT the loss tangent at 900 °C and at a representative BAW device frequency of 10 MHz is 0.88 for the X and Y directions and 0.15 for the Z direction. Between 100 MHz and 1 GHz, which is a typical LGT SAW device frequency range, the relevance of the σ component for the material losses diminishes in comparison to the ϵ'' , resulting in loss tangent values smaller than 0.088 for the X and Y directions and 0.026 for the Z direction over the entire temperature range. These results reveal that by increasing the frequency, SAW devices can better cope with the LGT electrical losses than BAW devices.

2.4 Conclusions

This chapter reported on the extraction of langatate real and imaginary permittivity and conductivity up to 900 °C. The dielectric properties were determined from

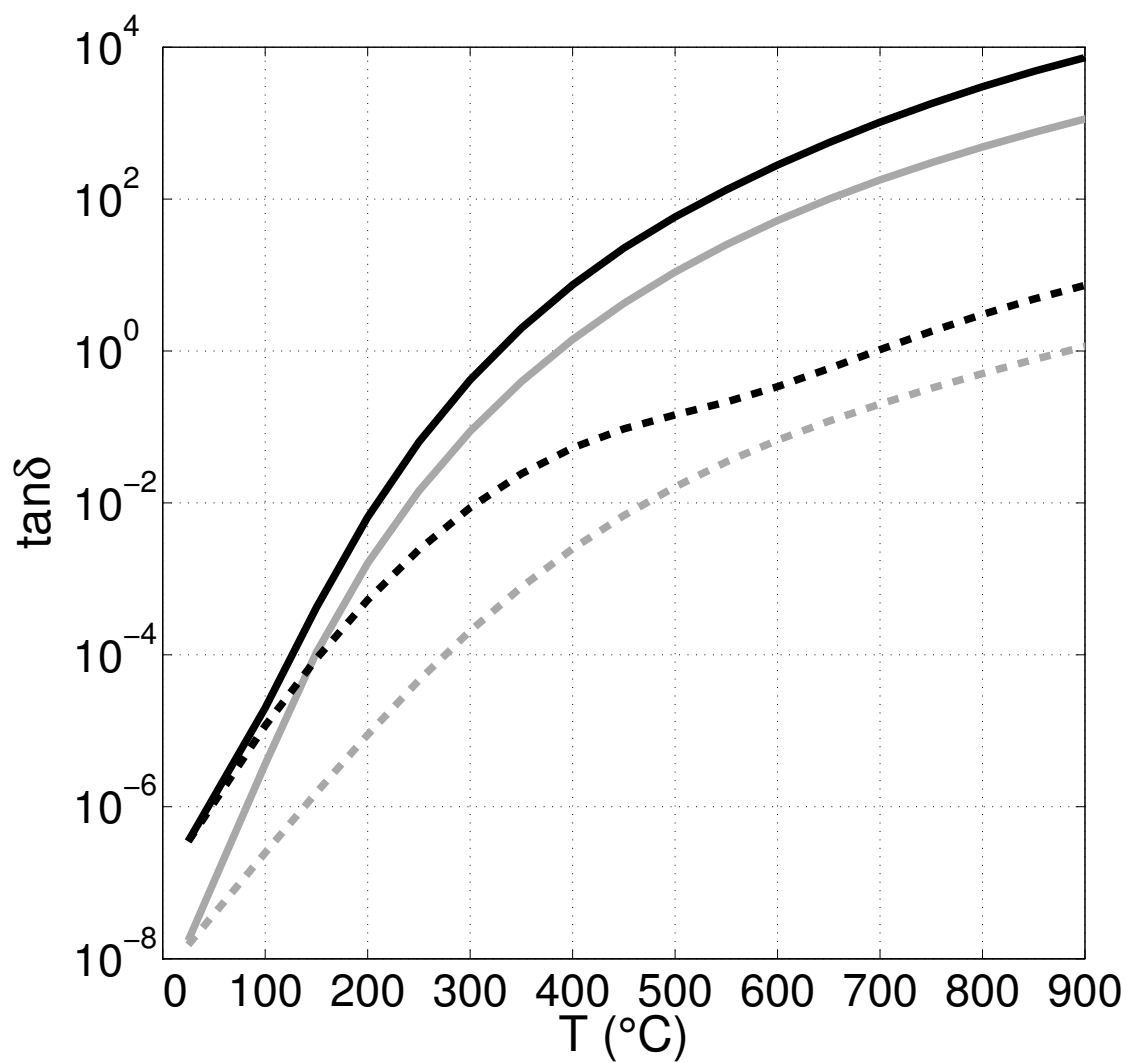


Figure 2.10. LGT loss tangent, $\tan \delta$. For the 11-direction at 1 kHz (solid black) and 1 MHz (dashed black), and for the 33-direction at 1 kHz (solid gray) and 1 MHz (dashed gray).

admittance measurements of parallel-plate capacitors fabricated on LGT X, Y, and Z axes. The electric field fringing was corrected for by measuring the capacitors with circular electrodes of successively increasing diameters and fitting the results to a surface plane with the dependent variables of temperature and the ratio of the wafer thickness to the electrode radius.

It was found that the extracted permittivity ϵ'_{R11} increases from its room temperature value by 38 % at around 650 °C then slowly decreases at higher temperatures. The value of ϵ'_{R33} was found to decrease by 49 % from 25 °C to 900 °C. The uncertainties for ϵ'_{R11} and ϵ'_{R33} over the measurement range are less than 2 % and 1.6 %, respectively. The dielectric losses ϵ''_{R11} and ϵ''_{R33} exhibit maximum peaks at 525 °C and 721 °C, respectively. The conductivity of LGT increases with temperature, as expected for an insulator, with activations energies of 1.0358 eV along the X- and Y-axes and 0.9526 eV along the Z-axis.

Chapter 3

RESONANT ULTRASOUND SPECTROSCOPY

The resonant ultrasound spectroscopy (RUS) technique for the extraction of the LGT elastic and piezoelectric constants at high temperatures is detailed in this chapter. The RUS technique is summarized in Section 3.1, including a brief history, description of some measurement constraints, and an overview of the constant extraction process. Section 3.2 presents the mathematical derivation of the RUS technique and how it was implemented numerically. The RUS sample preparation and measurement system assembled at UMaine are discussed in Section 3.3. The RUS fitting calculations and constants extraction process is presented in Section 3.3.3. Section 3.4 gives the verification of the implemented RUS system and calculation tools, discusses the high-temperature LGT spectra measurements, and presents the extracted high-temperature elastic and piezoelectric LGT constants.

3.1 Background

Resonant ultrasound spectroscopy (RUS) can be used to extract the elastic and piezoelectric constants of crystals in harsh environments by recording the spectrum of acoustic resonant frequencies of a crystal sample with a well-defined geometry and utilizing minimization fitting to determine the constants [316]. RUS and related techniques originated in the 1960's as the "resonant sphere technique," in which the resonant spectra of spheres was theoretically determined [372]. Initial applications included material characterization of small moon rock samples and characterization of the components of the Earth's crust for geophysics [316, 373, 374]. The Rayleigh-Ritz variation technique utilizing Lagrangian minimization extended the technique to be able to calculate and fit the resonances of cube and rectangular parallelepiped samples of crystals with isotropic and cubic symmetries [375–377] and with orthorhombic and trigonal symmetries [319, 378]; this technique was termed rectangular parallelepiped

resonance (RPR). Group theory was applied to RUS techniques, simplifying mode calculation and mode matching [379]. The RUS theory was extended to apply to trigonal crystals and to include piezoelectricity; quartz was used to validate the additions [318, 319]. With the development of improved calculation methods and increased computing power, RUS could be applied to more complicated shapes, such as cylinders, eggs, sandwiches, cones, composite materials, and layered structures [380–384]. Laser-doppler interferometry can be added to the RUS technique to map vibration displacements and achieve complete mode identification [326, 385]. RUS has been applied trigonal crystals in [318–325] and, in recent years, to langasite-type crystals [232, 273, 278, 281, 283, 326, 327]. A detailed history of the RUS technique can be found in Chapter 10 of Migliori and Sarrao’s book [316].

Resonant ultrasound spectroscopy (RUS) measures the spectrum of acoustic resonant frequencies of a crystal sample with well defined dimensions to extract the acoustic properties of the sample through a minimization fitting. The sample must be prepared with a well-defined shape, such as cube, sphere, or rectangular parallelepiped, and used to extract all the elastic stiffness and piezoelectric constants. A transducer generates a continuous-wave acoustic wave and a large vibration amplitude is measured at a receiving transducer when the input frequency matches the frequency of a resonant mode of the crystal sample. The resonant frequencies of a piezoelectric crystal sample can be calculated from the shape, orientation, density, elastic stiffness, piezoelectric constants, and dielectric permittivity of the material under investigation. The inverse problem of extracting the acoustic parameters directly from the resonant frequencies is not analytically manageable so a fitting technique is used to determine the set of constants that creates the best agreement between the measured and predicted frequency spectrum. Typically the sample size, orientation with respect to crystalline axes, density, and dielectric constants are determined by separate measurement techniques and held constant for the RUS fitting so that

the elastic and piezoelectric constants can be determined. However, other material parameters can often be extracted if the system is sufficiently overdetermined and the initial guesses for the constants are accurate [316]; however, the piezoelectric and permittivity of piezoelectric crystals cannot be separated because they appear as a ratio [318]. The precision of RUS is comparable with that of the most carefully executed time-of-flight measurements, achieving approximately 10^{-4} relative measurement uncertainty, which is typically an order of magnitude better than BAW and SAW resonator techniques [316, 317].

There are two principal methods used in the literature to contact the sample with the buffer rods in RUS: the sample can be held between two transducers with a small force, one transmitter and one receiver, see Fig. 3.1a; or the sample can rest on top of three transducers that form a tripod, in which one of the transducers is a transmitter and the other two are receivers, shown in Fig. 3.1b. The first method has a stronger signal because of the increased coupling caused by pressing the sample and the buffer rod together but the force causes the resonant frequencies to shift from the free resonant frequencies [316, 318]. When the crystal is placed on the transducer tripod the force is only that of the crystal weight, which is negligible for most practical sample sizes [316]. The buffer rods contact the sample directly and no couplant material is needed because the weaker air-coupled interaction is sufficient to measure the resonant frequencies due to the larger vibrations during resonance. Additionally, RUS utilizes frequency domain measurements so it is not affected by any time delay caused by an air gap between the buffer rod and the sample. The buffer rod might contact the sample at a vibration null of one or more of the resonant modes, causing a little or no signal from this mode to be measured. When two transducers are used to hold a parallelepiped sample at the corners, for example, few modes will be missed because the corners have the fewest vibration nulls. For the tripod method the number of modes missed can be reduced by averaging the signals from the two

receive transducers. Also, the constant extraction technique will still be accurate if less than 10 % of the resonant frequencies are not measured [316].

Acoustic resonance spectra can also be generated and captured using non-contacting electromagnetic-acoustic resonance (EMAR) electrodes, which uses the same Lorentz force transduction principle as EMAT, described in Section 1.6.2. Once the acoustic spectrum is acquired, the standard RUS constant extraction minimization process is used. The EMAR electrode orientation, crystal symmetry, and sample shape determine which acoustic modes are excited. This allows for selective mode excitation and, thus, simpler mode identification and more robust calculations than traditional RUS, but EMAR excites fewer modes [325, 383, 386]. EMAR has been used for quartz and can be applied to other trigonal crystals [325] and has been used up to at least 125 °C to investigate the cubic crystal BaTiO₃ [387].

Starting in the late 1970's RUS has been adapted to high-temperature measurement, initially focusing on the thermodynamic behavior of materials relevant to geophysics [335, 336]. Long buffer rods between the transducers and the sample were added to extend the measurement temperatures to 1550 °C and higher without exposing the transducers to excess heat [337–342]. The piezoelectric transducers used in RUS are typically PZT or a similar material that doesn't survive above 100 °C or 200 °C so must be external to the heating area. RUS can be adapted to high temperature measurement by using long buffer rods attached to the piezoelectric transducers, at room temperature, to probe a sample contained inside a furnace, as shown in Fig. 3.2 [273, 316, 337, 340, 342]. The crystal sample and the buffer rods are the only components of the RUS system exposed to the hot environment and, for correctly designed system buffer rods described in the next paragraph, the measured changes in the resonant spectra are only due to the change in sample temperature. In order to extract the temperature dependence of the elastic stiffness and piezoelectric

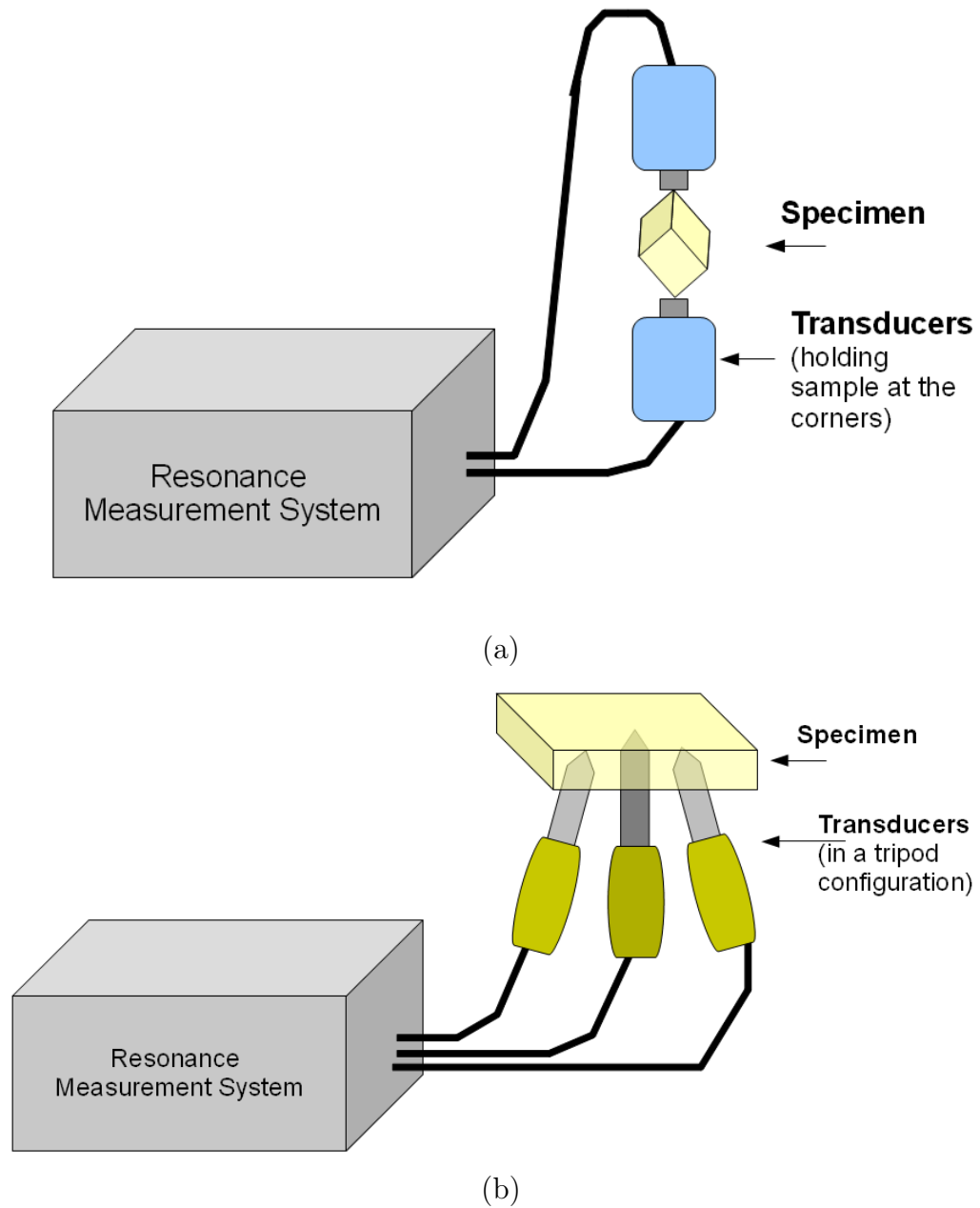


Figure 3.1. RUS measurement system types. (a)RUS System with two transducers. The sample is clamped between the transducers. (b) RUS system with transducer tripod. The sample rest on the transducers with only the force of gravity.

constants the density, thermal expansion, and temperature-dependent permittivity must be used in the fitting.

The long buffer rods have acoustic resonances that can interfere with the measurement; however, a number of factors mitigate this problem. The buffer rods are designed to have a large density of modes with low enough quality factor such that the modes overlap and reach the reverberation limit such that the high-Q sample resonances to be easily separated from the background signal [316]. This allows the rods transmit acoustic energy over the entire spectra of the sample under test, but with an frequency-dependent amplitude and phase. The receiver is not affected by the phase and the buffer rods are designed to have modes with quality factors and amplitudes that are less than the sample modes [316].

The material constants of a given sample cannot be found directly the resonant spectra, instead an inverse fitting technique is required. The process extracting material constants entails (i) measuring the natural resonant frequencies of a sample, (ii) using a set of best-guess material constants to calculate the resonant spectra, (iii) comparing the measured and predicted resonant frequencies, (iv) using the result to improve the trial set of material constants, and (v) repeating steps ii through iv until a stopping condition is met [316]. The unknown material properties, such as the elastic and piezoelectric constants, are allowed to vary in the fitting technique to find extract a new set of material constants. The fixed sample properties are inputs and need to be known, typically they are the crystal symmetry, sample geometry, dimensions, and dielectric permittivity. At elevated temperatures, extraction of the elastic stiffness and piezoelectric constants temperature functions requires the density, thermal expansion, and dielectric permittivity to be previously measured at the temperatures of interest.

The forward RUS calculation of the resonant frequency spectra for a sample with known dimensions and acoustic properties has no analytic solution and there are two standard methods of computation: Lagrangian minimization and finite-element

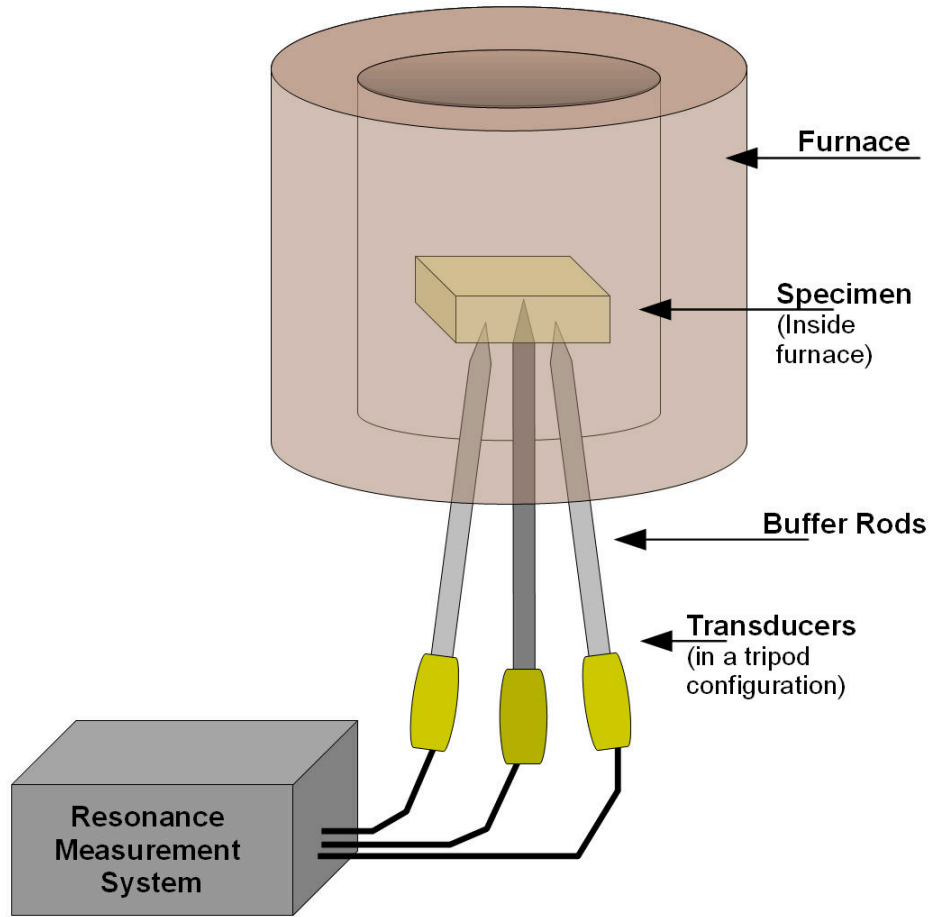


Figure 3.2. RUS system with high-temperature buffer rods. The long buffer rods reaching from room-temperature transducers to the sample under test in the hot zone of the furnace.

modeling [316]. The Lagrangian technique utilizes Hamilton's principle to determine the free-vibrations of a solid by finding the frequencies at which the action is stationary and the Lagrangian, the kinetic minus the potential energy of the solid, is at not affected by a differential change in the vibration. The finite-element method (FEM) involves dividing the solid into small elements and balancing the forces interacting between them.

Calculating the Lagrangian involves integrating sets of basis functions over the sample geometry is only easily applied to simple sample shapes, such as rectangular parallelepipeds, cylinders, and spheres, [316, 380] but can be expanded to complex

geometries using numerical integration [388]. The FEM is more complicated and computationally intensive but is capable of simulating arbitrary samples geometries and symmetries [389]. The Lagrangian method is quicker so is better suited for acoustic parameter extraction when the sample shape can be controlled [316] and is implemented in this work.

3.2 Resonant Spectra Calculation

The RUS calculation and extraction process will be described in the following sections; first the mathematical formulation of the forward calculation of resonant spectrum of a known sample is presented. Then the numerical implementation of the forward calculation is described. Finally the minimization or optimization process used to fit the acoustic constants to a measured resonant spectrum is given.

3.2.1 Mathematical Formulation

The resonance spectrum of a sample with known dimensions and material constants can be calculated using a technique called Lagrangian minimization. This process utilizes the fact that the free vibrations or resonant frequencies of a body are the same as the stationary points of the Lagrangian [316]. According to Hamilton's principle a system that is conservative and holonomic (the variables depend on position and time) can be described using the Lagrangian function, L , and the system dynamics can be described by the equation [390, 391]

$$\delta \int_{t_0}^t L \, dt = 0 \quad (3.1)$$

where the differential, δ , indicates the variation in the Lagrangian due to small variations in the generalized coordinates and velocities, which for a piezoelectric medium are given by the displacements and electric potential [390, 391]. The set of the displacements and potentials that satisfy (3.1) are the natural resonance mode

of the dynamical system and by convention the Lagrangian is said to be minimized and stationary [316, 390].

The Lagrangian density function for a piezoelectric media was independently derived by Tiersten [390, 391] and by Holland and Eer Nisse [375, 376, 392–394]; the derivation the Lagrangian is given in Appendix C.1. The Lagrangian for the free piezoelectric medium is

$$L = \iiint_V \left[\frac{1}{2} \rho v_j^2 - \frac{1}{2} S_{ij} c_{ijkl}^E S_{kl} + E_i e_{ijk} S_{jk} + \frac{1}{2} E_i \epsilon_{ij}^S E_j \right] dV \quad (3.2)$$

where

v_j = particle velocity tensor

S_{ij} = strain tensor

E_i = electric field tensor

ρ = mass density

c_{ijkl}^E = elastic stiffness tensor at constant electric field

e_{ijk} = piezoelectric tensor

ϵ_{ij}^S = dielectric tensor at constant strain.

Tensor notation is used where the subscripts are 1, 2, or 3 and refer to the Cartesian coordinates (x_1, x_2, x_3) , i.e. E_i is the electric field along x_i . Standard Einstein and Tensor operation notation is used, where the repeated indices represent a summation over the index, time derivatives are given dotted variables ($\dot{E} = \partial E / \partial t$, $\ddot{E} = \partial^2 E / \partial t^2$), and partial derivatives with respect to the spacial coordinate x_j is given by a subscript comma followed by the index of the coordinate being integrated over, i.e. $E_{i,j} = \partial E_i / \partial x_j$.

The steady-state forced vibrations are assumed to have a harmonic $e^{j\omega t}$ time dependence, where $\omega = 2\pi f$, f is the frequency, and t is time. The velocity becomes

$$v_i = \dot{u}_i = \omega u_i, \quad (3.3)$$

where u_j is the particle displacement. Then the kinetic energy, the first term of the Lagrangian, becomes

$$\frac{1}{2}\rho v_j^2 = \frac{1}{2}\rho\omega^2 u_j u_j. \quad (3.4)$$

The stress and electric fields can be replaced by the displacement and electric scalar potential, ϕ , or voltage, using

$$S_{ij} = \frac{1}{2}(u_{i,j} + u_{j,i}) \quad (3.5)$$

$$E_i = -\phi_{,i}. \quad (3.6)$$

note that $\phi_{,i}$ is the gradient of the potential.

Combining (3.2), (3.4), (3.5), and (3.6), the Lagrangian becomes [316, 376, 391]

$$\begin{aligned} L = \frac{1}{2} \iiint_V \left[\rho\omega^2 u_j u_j - \frac{1}{4} (u_{i,j} + u_{j,i}) c_{ijkl}^E (u_{k,l} + u_{l,k}) \cdots \right. \\ \left. - \phi_{,i} e_{ijk} (u_{j,k} + u_{k,j}) + \phi_{,i} \epsilon_{ij}^S \phi_{,j} \right] dV \end{aligned} \quad (3.7)$$

The natural modes of the piezoelectric sample are found by determining the set of displacements and potentials that minimize the Lagrangian function in (3.1). The Rayleigh-Ritz methods can be used to find approximate solutions by replacing the displacement and potential with summation of orthogonal basis functions [316, 318, 319, 376, 378, 380, 392, 394]. The displacement vector and potential are expanded in terms of the basis functions Ψ by

$$\vec{u} = \sum_p a^{(p)} \Psi^{(p)} \hat{x}^{(p)} \quad (3.8)$$

$$\phi = \sum_r b^{(r)} \Psi^{(r)} \quad (3.9)$$

where $\Psi^{(p)}$ is the p -th basis function, a and b are multiplication factors, and $\hat{x}^{(p)}$ is the \hat{x}_i unit vector, for $i = 1, 2, 3$ given by the index p .

There are primarily two types of orthogonal basis functions used in the RUS literature: (i) the powers of Cartesian coordinates in (3.10) [316, 380, 395] and (ii) Legendre polynomials in (3.11) [319, 377]. The powers of Cartesian coordinates are defined as:

$$\Psi^{(k)} = x_1^\alpha x_2^\beta x_3^\gamma \quad (3.10)$$

where k represents either the p or r index of the set of non-negative integers (α, β, γ) .

The Legendre polynomial basis functions for a rectangular parallelepiped with edge lengths $(2l_1, 2l_2, 2l_3)$ are defined as:

$$\Psi^{(k)} = (l_1 l_2 l_3)^{-1/2} \bar{P}_\alpha(x_1/l_1) \bar{P}_\beta(x_2/l_2) \bar{P}_\gamma(x_3/l_3) \quad (3.11)$$

where $\bar{P}_\alpha(x)$ is the normalized Legendre polynomial with degree α . The normalization is $\bar{P}_\alpha(x) = \sqrt{(2\alpha+1)/(2)} P_\alpha$. The interaction matrices, Γ , Ω , and Λ , are expanded using Legendre polynomials in Appendix C. The Legendre polynomial basis functions have been normalized by the sample size and their orthogonality is given by

$$\iiint_V \Psi^{(k)} \Psi^{(k')} dV = \delta_{kk'} \quad (3.12)$$

where $\delta_{kk'}$ is the Kronecker delta function, $\delta_{kk'} = 1$ when $k = k'$ and 0 otherwise.

In this work, the Legendre polynomial basis functions are selected for use, as discussed in Section 3.2.2.

A finite number of basis functions are used to approximate the displacements and the potential from (3.8) and (3.6), respectively. The basis functions are truncated by selecting the order of the individual functions such that [316]

$$\alpha + \beta + \gamma \leq N \quad (3.13)$$

where N is the truncation criteria and is chosen to balance accuracy and computation time. The number of basis functions used to approximate the potential and each

displacement component is chosen to be the same for convenience but is not necessary. For a particular N , the number of basis functions for each parameter, u_j or ψ , is given by the binomial coefficient $\binom{N+3}{3} = (N+1)(N+2)(N+3)/6$ because three natural numbers are selected from the set of N with repetitions allowed [316].

The Lagrangian integration can be solved numerically but analytical solution is preferred for speed and accuracy [316, 380]; however, analytic solutions only exist for certain samples geometries for a given set of basis functions. The Legendre polynomials have analytic solutions for rectangular parallelepipeds, whereas the Cartesian coordinate powers can be applied to a number of different shapes, including rectangular parallelepipeds, cylinders, and spheres [316, 380]. The Legendre polynomials are more computationally efficient when applied to rectangular parallelepipeds than the coordinate powers are [316, 380].

Combining (3.7), (3.8), and (3.12), the Lagrangian becomes

$$L = \frac{1}{2} \left[\sum_p \sum_{p'} a^{(p)} a^{(p')} (\Gamma_{pp'} - \rho \omega^2 \delta_{pp'}) \cdots \right. \\ \left. + 2 \sum_p \sum_r a^{(p)} b^{(r)} \Omega_{pr} - \sum_r \sum_{r'} b^{(r)} b^{(r')} \Lambda_{rr'} \right] \quad (3.14)$$

where the elastic, piezoelectric, and dielectric interaction matrices, respectively Γ , Ω , and Λ , are given by [318, 392]

$$\Gamma_{pp'} = \iiint_V S_{ij}(\Psi^{(p)}) c_{ijkl} S_{kl}(\Psi^{(p')}) dV \quad (3.15)$$

$$\Omega_{pr} = \iiint_V \Psi_{,i}^{(r)} e_{ikl} S_{kl}(\Psi^{(p)}) dV \quad (3.16)$$

$$\Lambda_{rr'} = \iiint_V \Psi_{,i}^{(r)} \epsilon_{ij} \Psi_{,j}^{(r')} dV \quad (3.17)$$

and the strain for the p th basis function is

$$S_{ij}(\Psi^{(p)}) = (\Psi_{i,j}^{(p)} + \Psi_{j,i}^{(p)})/2 \quad (3.18)$$

As discussed previously, the natural vibration modes are found by solving (3.1) for the stationary points of the Lagrangian, at which the Lagrangian is not affected

by differential changes in the displacements and the electric potential. In the basis function approximations (3.8) the variations in u and ϕ are given by the changes in the coefficients $a^{(p)}$ and $b^{(r)}$ and (3.1) becomes

$$\partial L / \partial a^{(p)} = 0 \quad (3.19)$$

$$\partial L / \partial b^{(r)} = 0. \quad (3.20)$$

Solving for the stationary points of (3.14) yields

$$\partial L / \partial a^{(p)} = \frac{1}{2} (2 (\Gamma_{pp'} - \rho\omega^2 \delta_{pp'}) a^{(p)} + 2\Omega_{pr} b^{(r)}) \quad (3.21)$$

$$\partial L / \partial b^{(r)} = \frac{1}{2} (2\Omega_{rp} a^{(p)} - 2\Lambda_{rr'} b^{(r)}) \quad (3.22)$$

Rearranging yields

$$\rho\omega^2 \delta_{pp'} a^{(p)} = \Gamma_{pp'} a^{(p)} + \Omega_{pr} b^{(r)} \quad (3.23)$$

$$\Lambda_{rr'} b^{(r)} = \Omega_{rp} a^{(p)} \quad (3.24)$$

If the sets of $a^{(p)}$ and $b^{(r)}$ are replaced with the vectors \mathbf{a} and \mathbf{b} , the indices on the matrices Γ , Ω , and Λ removed, and the identity matrix is indicated by I , then \mathbf{b} is solved for with (3.24) and substituted into (3.23).

$$\rho\omega^2 I \mathbf{a} = (\Gamma + \Omega \Lambda^{-1} \Omega^t) \mathbf{a} \quad (3.25)$$

$$\mathbf{b} = \Lambda^{-1} \Omega^t \mathbf{a} \quad (3.26)$$

Equation (3.25) is an eigenvalue problem where $\rho\omega^2$ are the eigenvalues and \mathbf{a} are the eigenvectors of the matrix $(\Gamma + \Omega \Lambda^{-1} \Omega^t)$.

Group theory has been applied to RUS to separate the eigenvalue problem into separate orthogonal problems [316, 318, 319, 377–380, 395]. When the RUS sample shape and crystal lattice have common symmetries the basis functions can be grouped into smaller orthogonal sets. This splits the eigenvalue problem into separate smaller

matrices and reduces calculation time because the computational cost scales with the cube of the matrix rank [316, 318, 319, 377–380, 395]. The separate matrices are solved independently to determine the resonant modes that belong to the particular group and are combined to determine the resonant modes of the RUS sample.

For a rectangular parallelepiped fabricated from a class 32 crystal, such as LGT, the basis functions and resultant vibration modes can be divided into four groups if the sample faces are aligned along the crystalline axes [318, 319, 379]. The resonant modes can be separated into the different groups by the parity (even or odd about the origin) of the basis functions and the calculation of the mode groups for an LGT rectangular parallelepiped is detailed in Appendix C.3.

3.2.2 Numerical Implementation

The mathematical RUS formulation presented in the previous section is implemented in MATLAB (Mathworks, Natick, MA) to numerically calculate the resonant spectra for the samples being tested. The RUS program first calculates the resonant spectra of a given sample using assumed acoustic constants, then compares the calculated frequencies to measured ones, and minimizes the difference by varying the material constants to determine the best-fit constants.

The resonant spectra for the crystal sample is calculated by first determining the basis functions, using the basis functions and their integrals to construct the eigenvalue problem in (3.25), and then calculating the resonant modes from the eigenvalues.

In this work, both Legendre polynomials and powers of Cartesian coordinates basis functions were initially implemented. For the code written in this work, the Legendre polynomials were found to result in faster calculations than the coordinate powers, as reported for rectangular parallelepipeds [316, 380]. Additionally, when using the coordinate powers, the interaction matrices for the implemented code were often rank

deficient when the piezoelectric effect was included, which has not been reported in the literature. For all the results reported in this work, Legendre polynomials were utilized. The accuracy of the RUS resonant mode calculations were verified by comparing the results with published spectra in Section 3.4.1.

The basis functions are determined, as shown in (3.11) from the master function, e.g. Legendre polynomials, and their indices: and (α, β, γ) , which are non-negative integers and are selected such that (3.13) holds. Increasing N increases the accuracy of the solution but results in a larger problem size that slows down the calculation and requires more memory. Migliori and Sarrao found that $N=10$ was sufficient for their work when using up to the first 50 resonant modes [316] and Ohno et al. used $N=11$ to calculate 40 modes [319]. In this work, up to about 100 modes were used in the LGT RUS measurement process, when available, and the larger number of modes required the use of a higher value of N than suggested in the literature. In order to determine which value of N to use in this work, the RUS resonance modes of LGT samples were calculating using N ranging from 12 to 22 and the resonance frequencies for the first 100 modes were found to converge with increasing N . For the fitting calculations in this work, $N=20$ was selected because all of the 100 modes had a fractional discrepancy less than 1×10^{-4} with respect to the $N=22$ modes, which is within the recommendation of Ohno to select N such that the fractional frequency difference is less than 2×10^{-4} .

The eigenvalue problem, (3.25), includes the inverse of the matrix Λ but numerically calculating the inverse of a matrix should be avoided if possible because it typically has lower accuracy than the starting matrix [396]. For improved stability \mathbf{b} in (3.24) is instead solved for using $\Lambda \backslash \Omega^t \mathbf{a}$, where \backslash denotes the matrix left divide operator. In the numerical implementation of the term $\Lambda^{-1} \Omega^t$ is replaced with $\Lambda \backslash \Omega^t$ wherever it is used in the RUS formulation.

The basis functions are divided into four orthogonal groups based on the parity of the indices, as described in Section 3.2.1 and Appendix C.3[318, 319, 379]. The basis functions are used in the calculation of the elastic, piezoelectric, and dielectric interaction matrices, Γ , Ω , and Λ as shown in (3.15), (3.16), and (3.17), for each group. The interaction matrices are further simplified into separate matrices that multiply each acoustic constant, the G matrices consisting of integrated Legendre basis functions defined in Appendix C when utilizing Legendre basis functions [318]. The basis functions, the interaction matrices, and their derivatives are calculated once for a particular size sample at a given temperature and used to calculate the resonant spectra with the current set of the varying optimized acoustic constants used in the fitting process.

The eigenvalues and eigenvectors found according to (3.25) for each of the four groups individually, as discussed in Section 3.2.1 and Appendix C.3, and then the results are combined to form the resonant spectra. The resonant mode frequencies are calculated from the eigenvalues and the group and order within the group is saved for mode identification. The eigenvectors are the basis functions multipliers and can be used to reconstruct the displacements or electric potential but are not needed in the constants extraction process.

The acoustic constants c , e , and ϵ for most crystals have great differences in scale, ranging from 10^{-11} to 10^{11} when in the International System of Units (SI), and are all used in the calculation of the (3.25). The multiplication of matrices with large differences in magnitude is numerically unstable so the acoustic constants are pre-scaled before the RUS calculations. The length, mass, and current units are each scaled, as shown in Table 3.1, so that the acoustic constants and the integrated Legendre polynomial matrices are approximately the same scale. This scale leaves the calculated frequency values unaffected so they can be directly compared to the measured frequencies. The scaling would cause the density to be very small but it

doesn't need to be scaled because the density is only used in the scalar calculation of the frequencies from the eigenvalues, as shown in (3.25).

The condition number of a matrix is used to quantify the sensitivity of the matrix to small errors in the elements and thus the accuracy of the calculations using the matrix, where the condition number is equal to or greater than 1 and the lower the number the better conditioned and more stable the matrix is [396]. The sensitivity of the eigenvalues to errors in the eigenmatrix is given by the condition number of the matrix of eigenvectors, not the condition of the matrix being solved [397]. In the LGT RUS calculations the eigenvector matrices of each orthogonal mode group had a condition number of 1, indicating a well-conditioned eigenvalue problem. The uncertainty in the extracted constants is estimated using the curvature of the fitting function and is discussed in Section 3.3.3.

3.3 RUS Experimental Process

The RUS measurement process is used to calculate the elastic and piezoelectric constants from a LGT crystal sample heated in a furnace, the process is described in the following sections and in [328, 330, 331]. The first step in the experimental process is the fabrication of a rectangular parallelepiped crystal sample. Then the sample is heated in a custom furnace that allows for the access of the acoustic resonance by high-temperature capable buffer rods connected to the RUS transducers outside the furnace. The resonance frequencies are determined from the RUS spectrum and used in the minimization calculations to extract the elastic and piezoelectric constants of the crystal at the measurement temperature.

3.3.1 RUS Sample Preparation

Six LGT parallelepiped samples were fabricated at the University of Maine (UMaine) Microwave Acoustic Material Laboratory from a boule purchased from

Quantity	Unit	Scale Factor	Scale Implemented
length	[m]	S_l	10^3
mass	[kg]	S_m	10^{-6}
current	[A]	S_c	10^7
Elastic Stiffness	[Pa]=[N m ⁻²]	$S_l^{-1} S_m$	10^{-9}
Piezoelectricity	[C m ⁻²]	$S_l^{-2} S_c$	10
Permittivity	[F m ⁻¹]	$S_l^{-3} S_m^{-1} S_c^2$	10^{11}
Density	[kg m ⁻³]	$S_l^{-3} S_m$	10^{-15}
Frequency	[Hz]	1	1

Table 3.1. Unit scaling used for RUS calculations.

Fomos (Fomos-Materials, Moscow, Russia). Rectangular parallelepiped samples were selected to allow for simple analytic integration of both Legendre polynomial and powers of Cartesian coordinate basis function sets. Migliori and Sarrao suggest that the sample orientation be within a degree or two of the crystal axes [316], so X-ray diffraction (XRD) alignment along with precise dicing and polishing is required for RUS sample preparation. The UMaine LGT sample preparation, described further in Appendix C.4, includes crystal alignment with a PANalytical X’Pert Pro MRD X-ray diffractometer (PANalytical Inc., Natick, Corp., Waltham, MA), cutting with an inner diameter saw (Meyer-Berger, Steffisberg, Switzerland), grinding, and polishing with an abrasive alumina slurry (Micro Abrasives Corporation, Westfield, MA) using automatic rotating polishing machines (R. Howard Strasbaugh 6U, Lynwood, Ca). The sample preparation process process (alignment, cutting, grinding, and polishing) at UMaine was shown to have achieved wafer orientations within 6 arcminutes [240]. Extra care was taken in the RUS sample handling and fabrication to preserve the sharp corners and parallelism, since an ideal parallelepiped shape is assumed in the spectra calculation. Any deviation from the ideal shape would alter the measured resonant spectra and lead to errors in the extracted constants [316].

Two different parallelepiped sample types were fabricated with nominal dimensions of (2.9 mm, 12.6 mm, 18.6 mm): the first type with the corresponding dimensions along the XYZ crystalline axes and the other with corresponding dimensions along the XZY axes. Of the samples fabricated, two were of the first orientation and four were of the second orientation mentioned. Any samples with different size or orientation will have different resonance spectra and thus increase the robustness of the measurement against errors induced by resonance frequencies that are close or overlapping [316]. The sample dimensions were chosen to be at least a few mm long on two sides in order to be large enough to be placed on the RUS transducer tripod. The amount of LGT material available was limited so the size of each sample was limited in order to ensure that six samples could be fabricated to ensure measurement redundancy in case of sample breakage.

The dimensions of the completed samples were measured with a Heidenhain-Metro precision length gage (Heidenhain Corp., Schaumburg, IL), the results are shown in Table 3.2. The measurements on each side of the sample were repeated 6 to 8 times so that the random error could be reduced.

3.3.2 RUS Measurement System

The RUS measurement system consists of a transceiver unit, three acoustic transducers, a high-temperature furnace, and a furnace control system. The transceiver unit (RU Spec, Magnaflux Quasar, Albuquerque, NM) generates frequency modulated output voltage applied to one of the transducers, which produces a vibration in the sample under test. Two receive transducers generate charge due to the sample vibration, which is measured by the RUS transceiver. The transceiver sweeps frequencies from 1 kHz to 500 kHz and measures the strength of the received signal, saving the signal magnitude as a function of frequency. The extraction of resonance peaks

Sample name	X dimension (mm) ^a	Y dimension (mm)	Z dimension (mm)
LGT 3	2.877 ± 0.011	12.591 ± 0.009	18.573 ± 0.005
LGT 4	2.913 ± 0.005	12.588 ± 0.009	18.559 ± 0.003
LGT 7	2.899 ± 0.003	18.542 ± 0.010	12.587 ± 0.008
LGT 8	2.895 ± 0.007	18.593 ± 0.003	12.590 ± 0.008
LGT 9	2.896 ± 0.004	18.527 ± 0.005	12.584 ± 0.009
LGT 10	2.898 ± 0.004	18.605 ± 0.003	12.593 ± 0.007

^aUncertainty given by measurement standard deviation

Table 3.2. LGT RUS sample dimensions.

from the spectra is not performed by the RU Spec software and must be performed by the user, as described in the next section (3.3.3).

The high-temperature furnace, transducer holders, and enclosure were custom designed and are shown in Fig. 3.3. The system was fabricated based on the RUS system of the High Temperature Materials Laboratory at the Oak Ridge National Laboratory (Oak Ridge, TN) with modifications to meet the needs of this work. The transducer holders and furnace support at UMaine was constructed to have increased manipulation of the transducer orientation such that various samples sizes could be measured and the buffer rod placement could be easily adjusted for sample leveling, preventing the samples from slipping off the tripod. The Oak Ridge system required a gas tight chamber for high-temperature gas testing, which was not needed at UMaine. The UMaine furnace and transducers are surrounded by an aluminum enclosure to protect the RUS system from accidental damage and to protect the user from the high temperatures during testing.

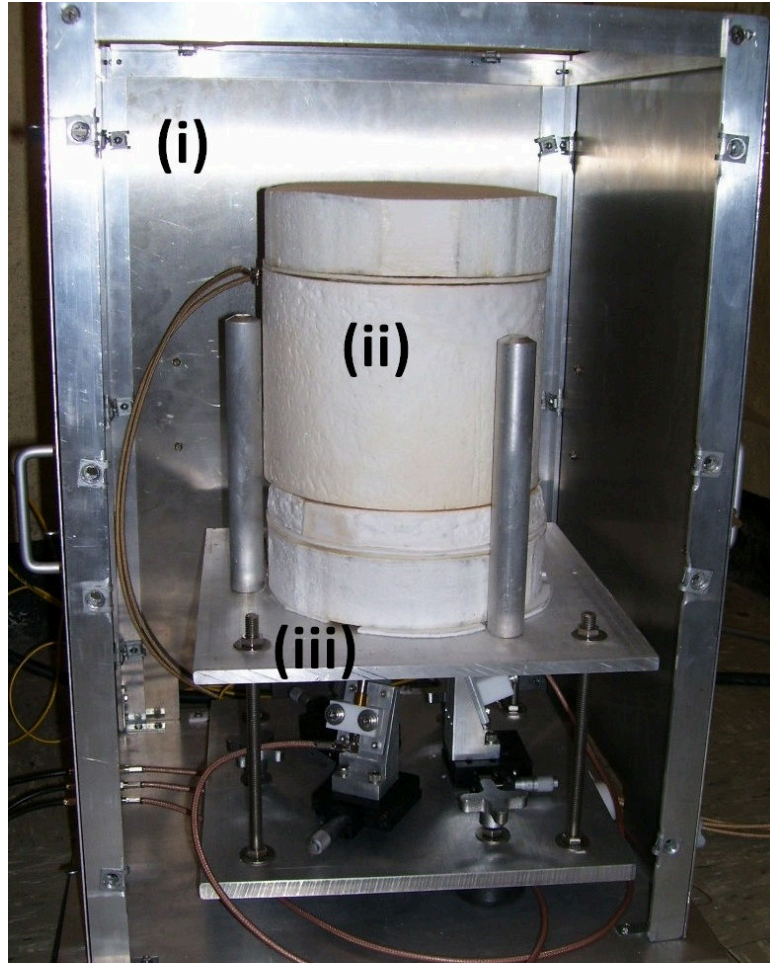
The furnace was constructed in parts to allow for simple removal and easy access to the sample. The furnace was assembled from a cylindrical ceramic fiber heater with embedded coils, which can heat to 1100 °C, and separate ceramic fiber spacers and caps (Watlow, St. Louis Missouri). A tripod was formed by the three

high-temperature 15.2 cm (6 in) silicon carbide buffer rods (Magnaflux Quasar, Albuquerque, NM) that extend into the hot zone of the furnace to support the sample and transmit the acoustic vibrations between the transducers and the crystal sample. The transducers must be kept below 55 °C (130 °F) to ensure that there is no damage to the lead zirconate titanate (PZT) transducer or the glue holding the buffer rod to transducer. It was found to be necessary to blow air across the transducers to ensure that they did not overheat due to heat transfer from the furnace.

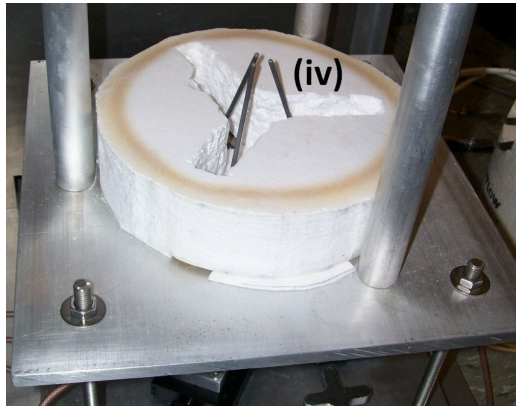
The furnace temperature is measured using two exposed-junction k-type thermocouples, suitable for use above 1200 °C (Omega Engineering, Stamford, CT). The furnace temperature is controlled and recorded by a programmable temperature controller, alarm over-temperature controller, and solid state relay, which communicates with a computer via serial cable (Omega Engineering, Stamford, CT).

While the heaters were off and the furnace was at room temperature, the temperature settled to approximately 0.1 °C variation with time, the resolution of the temperature monitor. When the furnace was heating, the temperature took between 20 minutes to 1 hour for the temperature to stabilize and even then the temperature would alternate by up to 3 °C over time due to the furnace controller. This variation increases the temperature measurement uncertainty and is included in the uncertainty analysis discussed at the end of Section 3.3.3. At each temperature, multiple spectrum measurements, typically six, are made and averaged to reduce the effect of random errors.

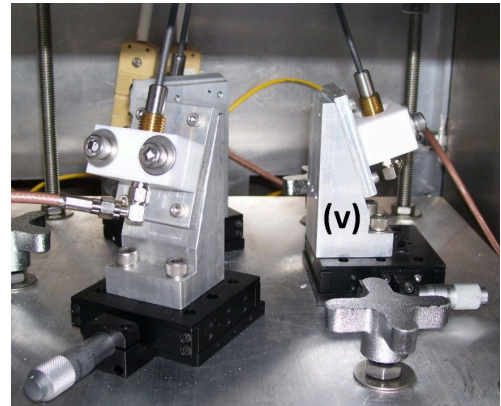
The resonance spectra of the buffer rods is measured without the sample and used to remove the ‘background noise’ peaks introduced by the buffer rods from the measured sample spectra. As the crystal sample is heated, its modes will shift in frequency and reduce in strength; however, the acoustic buffer rod peaks are minimally affected by the furnace temperature. It was found that for the measurement system in this work, the largest buffer rod interfering peaks typically occurred below



(a)



(b)



(c)

Figure 3.3. RUS high-temperature furnace assembly at UMaine. (a) Furnace in enclosure (i) with heater section (ii) in place on stand (iii), (b) heater removed to show transducer tripod (iv), (c) transducer holders (v) with adjustable angles and positions.

50 kHz, with only a few significant peaks at higher frequencies, whereas the LGT RUS samples in this work had only two peaks below 50 kHz and almost 100 peaks below 500 kHz.

The RUS measurement process, frequency determination, and mode identification are given in more detail in Appendix C.5.

3.3.3 RUS Fitting and Constants Extraction Process

The acoustic parameters of a sample are extracted by finding a best-fit set of constants to minimize the difference between the calculated, Section 3.2, and measured resonance frequencies, Section 3.3.2. The fitting and constants extraction process, described in this section, involves the calculation of the resonant frequencies of the sample for a best-guess set of constants, matching the modes with the measured frequencies, and varying the constants until difference between the calculated and measured frequencies is minimized. The entire process is repeated at each of the measurement temperatures.

The difference between the measured frequencies, g_i , and the calculated frequencies, f_i , is quantified by the objective function or figure of merit, F , given by

$$F = \sum_i \frac{1}{g_i^2} (f_i - g_i)^2. \quad (3.27)$$

Here i is the frequency index and represents the modes selected by the user to be included in the fitting.

The minimization calculation utilizes non-linear least-squares fitting, implemented with the MATLAB `lsqnonlin` function, to extract a best-fit set of acoustic constants that minimizes (3.27) for a resonant spectra measurement. A large-scale trust-region algorithm is used and returns a solution when F or the parameters change by less than the tolerance of 1×10^{-23} , which was reduced from the MATLAB default of 1×10^{-6} to ensure that a minimum is found.

The Jacobian matrix, which is derived in Appendix C.6, is used by the `lsqnonlin` function to determine how modifying the optimized parameters will change the error between the calculated and measured frequencies. The (m, n) element of the Jacobian matrix is partial derivative of the m^{th} resonant frequency with respect to the n^{th} optimized parameter, which are the elastic and piezoelectric constants. The minimization program uses the Jacobian to find an improved constants set to reduce the difference between the measured and calculated resonance frequencies.

The acoustic constants fit to the measurements in this work could be either the elastic constants only or both the elastic and piezoelectric constants together. The non-fit constants are the sample dimensions, dielectric constants, and thermal expansion, which are included as fixed values in the minimization process along with their respective measurement uncertainties.

The piezoelectric RUS calculations require dielectric permittivity at constant strain, ϵ^S , as discussed in Section 3.2, but the capacitor measurements in Chapter 2 resulted in the the permittivity for constant stress, ϵ^T . The RUS process in this work was extended from the process described in the literature [316, 318] to calculate ϵ^S at each step in the minimization process utilizing ϵ^T and the trial set of elastic and piezoelectric constants with (2.6). The extracted elastic constants from RUS are the constant electric field constants, c^E .

Consideration of the electrical losses, represented by σ and ϵ'' , in the dielectric extraction discussed in Chapter 2 was fundamental to extract the proper value of the real part of the permittivity, ϵ' . For the RUS elastic and piezoelectric extraction performed in this section only ϵ' was used, since the losses due to σ , ϵ'' , and viscoelastic losses are not of first-order importance to the behavior of the resonance modes analyzed [398], would add significant complexity to the data extraction [323, 399] and a careful analysis of the relative importance of the losses mechanisms for device performance in such environment is beyond the scope of this work.

In the minimization process, the elastic constants were only constrained to be positive, as required for positive energy density [297] but are otherwise allowed to vary freely to achieve the best fit of measured and calculated modes. The sign of the piezoelectric constants are not set by the energy requirements [297] but the convention from the 1949 Standards on Piezoelectric Crystals [400] is followed, which specifies that for right-handed class 32 crystals e_{11} is negative and e_{14} is positive.

The root-mean-square of the residual error (RMSE) of (3.27) is used to judge the quality of the best-fit set of constants determined by the minimization. The RSME allows comparison of the quality of fit for different sets of resonant frequencies. From experience with room-temperature LGT spectra fitting in this work, it was found that good quality fits, with results similar to reported room-temperature LGT constants [236], typically have RSME less than 2×10^{-3} , agreeing with the suggested RSME from [316]. When some of the calculated and measured modes were mismatched in this work, the minimization was found to take more iterations to converge and the RSME was found be around 5×10^{-3} to 1×10^{-2} , thus a fitting with $\text{RSME} > 5 \times 10^{-3}$ was investigated for incorrect mode identification.

Uncertainty in the extracted constants is estimated using the curvature of the objective function (3.27) at the best fit solution. As recommended in [316], the error in each of the fit constants is calculated as the variation of the constant that produces a 2% change in F using the process described next. Thus constants that have a strong effect on the objective function have a steeper curvature and less error, where as constants that only weakly affect F have lower curvature and increased uncertainty.

The uncertainty covariance matrix for the RUS minimization problem is $1/(2G)$, where G is calculated from the Jacobian matrix, J , by [316, 368]

$$G = (J'J)^{-1}. \quad (3.28)$$

The eigenvalues, σ_μ^2 , and eigenvectors, \hat{y}_μ of the covariance matrix are the principal axes of curvature and are found by

$$G\hat{y} = 2\sigma^2\hat{y}. \quad (3.29)$$

The variation of parameter p_μ in the \hat{y}_μ direction is

$$\delta p_\mu = \delta \vec{p}_\mu \cdot \hat{y}_\mu = \sigma_\mu \sqrt{2\delta F} \quad (3.30)$$

where $\delta F = 0.02F$ is the allowed change in the objective function residual. The uncertainty in a particular parameter is the combined variation along each principal axis,

$$Up_\alpha = \sqrt{\sum_\mu \delta p_\mu^2}. \quad (3.31)$$

According to Migliori and Sarrao [316], a good quality fit with RMSE below 2×10^{-3} also has predicted uncertainty in the elastic constants between 0.1 % and 3 %, where only non-piezoelectric materials were considered. In this work, for LGT fitting at room temperature with RSME $\leq 2 \times 10^{-3}$ the elastic constants typically had less than 1.5 % uncertainty and the piezoelectric constants e_{11} and e_{14} had around 7% and 20% relative uncertainty, respectively, reflecting their reduced effect on the resonance spectra compared to the elastic constants.

In the literature [316], the calculated and measured modes are typically matched and compared only by looking at the mode order; however, this method will confuse modes that are close in frequency to each other and may switch order during the fitting process as new sets of constants are tried, creating a mode mismatch that cannot be corrected by the user. In this work, mode identification utilizes group theory and matches modes based on the order within group. By including the mode groups, the mode switching is much less common because the modes are spaced further apart. This reduces the sensitivity of the fit constants to the start values. The inclusion of group identification is very important to the extraction of constants at elevated

temperature where the actual constants may be quite different from the previous temperature constants used to start the minimization.

The mode identification can be improved by using the temperature behaviors of the resonances modes since modes that are close in frequency may be separated if their measured and calculated temperature behaviors can also be compared. This requires resonance measurements that are close enough in temperature to be able to observe mode crossing and temperature coefficients of the fit constants that are accurate to calculate the direction and relative magnitude of the temperature derivatives. In this work, the low-temperature ($\leq 120^\circ\text{C}$) LGT constants temperature derivatives from [236] were used to calculate the temperature derivatives of the resonance modes and help to confirm the low-temperature mode identification. At elevated temperatures, above $\sim 150^\circ\text{C}$, the LGT elastic and piezoelectric temperature coefficients are not available so the RUS constants extracted at each temperature are used to approximate the temperature behavior of the resonance modes at the next highest measured temperature. This process aids in mode establishment, especially at higher temperatures where not all the modes are measured and thus the order with respect to the missed modes cannot be determined.

The extraction process starts at room temperature and progressively moves to the next temperatures after a set of constants is found that has low RSME ($\leq 2 \times 10^{-3}$) and matches most of the measured modes. After the constants have been fit to the measurements at each temperature to a satisfactory level, they are used together to determine the temperature behavior of the extracted constants.

The constants from multiple temperature tests and redundant crystal samples are combined into a single data set and a polynomial function of temperature is fit to the data. Total least squares regression is used to find the best-fit polynomial with the inclusion of uncertainty in the constants and in the temperature, since traditional least squares fitting ignores the errors in the independent variable [364, 368]. The

uncertainty in the temperature coefficients is propagated from the curve fitting using standard error propagation [367].

The standard practice is to report acoustic constants by their value at a reference temperature with a set of temperature coefficients defined by [297]

$$TC^{(n)} = \frac{1}{x(T_0) n!} \left(\frac{\partial^n x}{\partial T^n} \right)_{T=T_0} \quad (3.32)$$

where the x is the quantity being expanded, T is the temperature, T_0 is the reference temperature, often room temperature, and $TC^{(n)}$ is the n^{th} -order temperature coefficient.

The value of the material constant x at temperature T is given by

$$x(T) = x(T_0) \left[1 + \sum_n TC^{(n)} (T - T_0)^n \right]. \quad (3.33)$$

3.4 RUS Results

3.4.1 Validation of RUS Technique

The custom RUS software, written in this work and described in the previous sections, was validated by comparing the forward calculation and reverse constant extraction with RUS calculations published by Ohno [318]. The forward calculation of the UMaine RUS software was validated by comparing the calculate resonant frequencies for a parallelepiped of quartz, which has the same crystal class as LGT, measured by Ohno in [318]. Ohno listed 36 measured modes of a quartz sample and the calculated RUS spectra, found using Lagrangian minimization with Legendre polynomial basis functions [318]. For verification, the frequency spectrum was calculated using the UMaine RUS software using the quartz constants and sample dimensions reported by Ohno. The calculated frequencies had the same mode groups as Ohno and had a relative room-mean-square-error (RSME) of 2.2×10^{-4} from Ohno's calculated frequencies, this difference could be explained by the rounding of the listed frequencies modes and the elastic constants. Additionally, the UMaine

RUS software was used to extract the elastic constants from Ohno’s measured resonance spectrum using the UMaine software. The quartz constants extracted by the UMaine software had a 9.7×10^{-3} RMS discrepancy with the constants extracted by Ohno and agreed within the estimated uncertainty for this fitting. Thus, both that forward and reverse RUS calculations of the UMaine software were found to be accurate and satisfactory for the extraction of LGT acoustic constants.

To validate the RUS experimental setup implemented at UMaine, including the RU Spec transceiver unit (Magnaflux Quasar, Albuquerque, NM), LGT crystal spectra were compared to measurements of the same samples with the RUS system at the High Temperature Materials Laboratory (HTML) of the Oak Ridge National Laboratories. A fabricated LGT sample was measured at room temperature at the University of Maine and at the HTML using fixtures for high-temperature and room-temperature measurements. The UMaine fixture measured all the modes that were measured by the HTML fixtures. The fractional disagreement between the UMaine and HTML spectra of measured resonant frequencies was on average 0.014%. The discrepancy is on average less than twice the frequency resolution of the measurements. The worst mode had a disagreement of 0.33% and the other 92 modes measured at both UMaine and the HTML had a maximum difference of 0.072% and is smaller than the recommended frequency measurement accuracy of 0.1% [316]. The compared spectra measurements are the result of the measurements with the background spectrum of each fixture numerically removed. The average frequency discrepancy of 0.014% is assumed to be the spectra measurement repeatability of the UMaine system

3.4.2 LGT High-Temperature Resonant Spectra

The resonant spectra of the fabricated LGT samples were measured from 25 to 1100 °C, with measurements at UMaine and at the HTML. The HTML and UMaine spectra were used together for the initial RUS constants extractions but only UMaine

spectra were selected for the final extracted constants in order to use consistent temperatures for the extraction process. The resonant modes were identified from the amplitude spectra at each temperature and tracked as they moved to help identify modes as described in Section 3.3.2. An example measured spectra of an LGT sample at room temperature is presented in Fig. 3.4.

For the fabricated LGT samples, the measured spectra typically contained 40 to 100 measurable resonance modes, depending on the temperature. At room temperature, commonly 80 to 100 modes were used in the fitting technique. For temperatures from 100 °C to 400 °C approximately 60 to 95 modes were used in the fitting. In this temperature range, fewer resonance peaks were measured and more modes were ignored in the fitting due to ambiguity in the mode selection when multiple resonance peaks are close in frequency or cross over each other. For temperatures in the range 500 °C to 750 °C, there were only about 45 to 65 modes that could be utilized in the fitting, due to the resonance peaks' decrease in magnitude and quality factor. The increased acoustic losses in this temperature range has been observed for LGT, LGS, and other CGG-type crystals and is speculated to be caused by oxygen defects [161, 162, 278, 281–283, 401]. For the measured LGT RUS spectra, in the temperature range from 800 °C to 1100 °C, the magnitudes of the resonance peaks increase, raising the number of measured modes to 65-95. This higher number of resonance peaks improves the fitting process accuracy again, in spite of some difficulties in selecting the modes and determining the starting values for the constants for the fitting. The losses observed in the RUS modes are not explained by the LGT dielectric losses, given in Section 2.3, due to the relatively low effect of the electrical properties on the mechanical vibrations because the piezoelectric coupling of LGT being on the order of 5 %.

The number of modes used in the RUS fitting should be at least 5 times the number of constants being extracted for an accurate least-squares fitting according

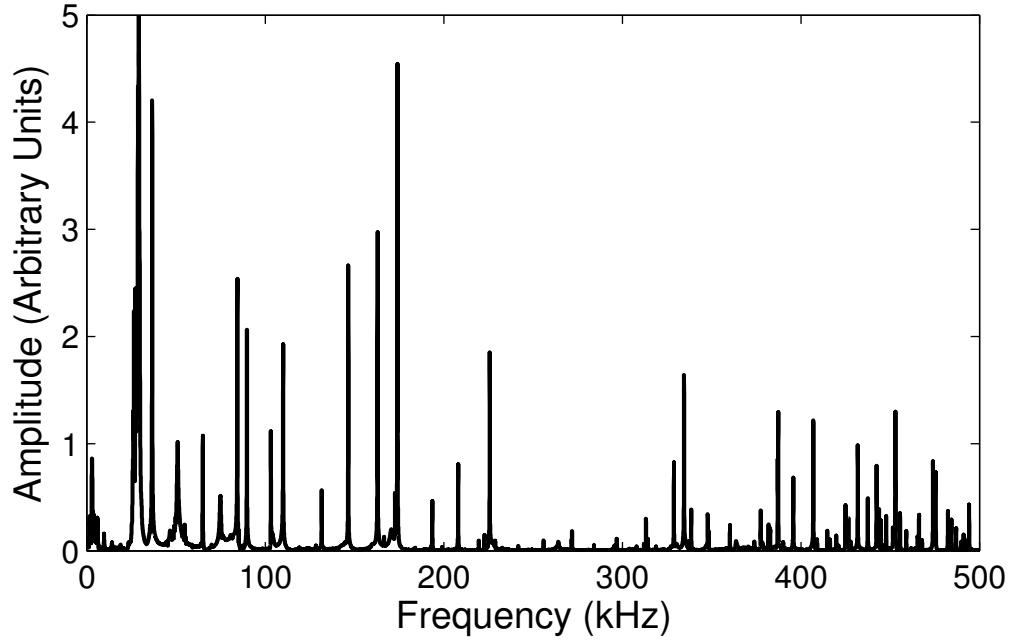


Figure 3.4. Example LGT RUS spectrum at 25 °C of LGT10 sample

to the suggested RUS guidelines in [316]. Langatate has 6 elastic and 2 piezoelectric constants, so there should be at least 30 measured modes for the elastic-only fitting and 40 modes for the extraction including piezoelectricity. For this reason, the extracted constants in temperature range of 500 °C to 775 °C are expected to have additional systematic error not accounted for in the estimated measurement uncertainty and typically were not used in the determining the LGT temperature behavior results, as discussed in Sections 3.4.3 and 3.4.4. The mode matching process used in this work is detailed in Appendix C.5

3.4.3 LGT Extracted Stiffened Elastic Constants

Two sets of high-temperature LGT elastic, piezoelectric, and dielectric constants were extracted in this work; the first set utilized the temperature coefficients on the elastic constants only with the piezoelectric and dielectric constants treated as unchanged with temperature (described in this section)[328–330], and the second set

extracted the elastic, piezoelectric, and dielectric all with temperature dependencies (described in Section 3.4.4)[331, 334].

The first set of LGT acoustic constants in this work were determined from temperature coefficients of extracted high-temperature piezoelectrically stiffened elastic constants (SEC) and room-temperature unstiffened elastic constants (UEC) with the piezoelectric and dielectric constants treated as not being affected by temperature. The SEC were extracted using RUS without the piezoelectric or dielectric constants because the high-temperature dielectric constants had not been measured at the time. The room-temperature LGT elastic and piezoelectric constants were extracted from RUS measurements at 25 °C and using the dielectric constants from [236, 358].

For the second and final set of extracted high-temperature LGT in this work, the UEC and piezoelectric constants were simultaneously extracted from the RUS data using the high-temperature dielectric constants given in Section 2.3.. The two data sets were compared and the impact of ignoring the temperature behavior of the piezoelectric and dielectric constants will be analyzed in Sections 3.4.4 and 4.4.

The values for the UEC and piezoelectric constants extracted from room-temperature RUS measurements were averaged for the six LGT samples tested and are listed in Table 3.3. The SEC are also extracted at room temperature and shown in Table 3.3 along with their temperature coefficients up to 1075 °C.

The UEC extracted from the four RUS samples oriented along the XZY axes (samples described in 3.3.1) were found to be larger than those extracted from the two samples oriented along the XYZ axes by an RMS difference of 3 %. The XZY oriented samples yielded values for e_{11} and e_{14} which were 22 % smaller and 23 % larger in magnitude, respectively, than those found using the XYZ oriented samples. There was no reason to believe that either sample orientation was preferable to the other and so the constants determined from all of the samples were averaged together to reduce effects of variation in sample preparation.

	Value at 25 °C		TC ⁽¹⁾	TC ⁽²⁾
	Piezo. Included	No Piezo.	No Piezo.	No Piezo.
Elastic constants				
	(10 ⁹ Pa)	(10 ⁹ Pa)	(10 ⁻⁶ °C ⁻¹)	(10 ⁻⁹ °C ⁻²)
c_{11}	193.0 ± 4.1	218.1 ± 9.9	5.0 ± 107.1	-161.7 ± 102.0
c_{12}	112.8 ± 3.9	137.7 ± 11.0	—	—
c_{13}	104.3 ± 3.2	121.5 ± 7.5	80.9 ± 131.2	-275.3 ± 125.1
c_{14}	14.06 ± 0.08	13.15 ± 0.47	-390.0 ± 68.3	250.9 ± 65.0
c_{33}	265.1 ± 2.4	276.4 ± 5.1	-49.7 ± 40.0	-115.1 ± 38.1
c_{44}	51.01 ± 0.06	50.92 ± 0.44	-23.0 ± 10.3	-23.2 ± 9.9
c_{66}	40.12 ± 0.15	40.28 ± 0.60	-42.7 ± 30.3	-23.1 ± 28.9
Piezoelectric constants				
	(C m ⁻²)	—	—	—
e_{11}	-0.462 ± 0.060	—	—	—
e_{14}	0.224 ± 0.030	—	—	—

Table 3.3. Preliminary LGT elastic, piezoelectric, and stiffened elastic constants extracted by RUS. Given at 25 °C with stiffened-elastic temperature coefficients (TC) up to 1075 °C

The LGT SEC are extracted at high temperatures to determine the temperature coefficients of the elastic constants. Only some of the LGT samples were completely measured at high temperature because LGT7 was damaged and LGT9 was used for a destructive test. For the SEC extraction, the RUS spectra of the remaining samples were measured up to 1100 °C and separated by at most 200 °C. The extracted constants from the crystals were combined and analyzed together. A second-order polynomial was fit to the constants and used to extract the two temperature coefficients of each elastic constant, as defined in (3.32).

It was found that the extracted constants in the temperature range from 500 °C to 775 °C were outliers from the best-fit curves and were removed from the data set. At these temperatures the resonant modes were weaker and there were a reduced number

of measured modes, as discussed in Section 3.4.2, which reduces the accuracy of the extracted constants. Additionally, the extracted constants at 1100 °C were excluded from the fit because they were outliers from the best fit, mostly do to increased measurement error due to increased difficulty in frequency determination and mode identification. The data and best fit curves for the six LGT SEC are shown in Fig 3.5.

The standard deviation uncertainty in the elastic constants and temperature coefficients, included in Table 3.3, were calculated using the error from the curve fitting as discussed in [367]. It is worth noting that the uncertainties in the temperature coefficients, typically not reported in the literature regarding AW crystal characterization, are important to access the quality and applicability of the high-temperature SAW propagation predictions based on those constants and coefficients; this topic will be discussed Section 4.4. The uncertainties in the elastic constants at room temperature range from 0.1 % to 3.1 % relative to the constants. The stiffened elastic constants the uncertainties increase with temperature and at 500 °C are between 0.6 % and 7.7 %, and at 1100 °C they range from 1.7 % to 26 % with respect to the elastic constants at those respective temperatures. The uncertainty in the elastic constants was reduced once the piezoelectricity and dielectric constants were included, as will be discussed in Section 3.4.4

3.4.4 LGT Extracted Elastic and Piezoelectric Constants

The high-temperature LGT elastic and piezoelectric constants were simultaneously extracted from the RUS data using the high-temperature dielectric constants from Chapter 2 and the process described in Section 3.3.3. This allowed the inclusion of the temperature behavior of the LGT piezoelectric and dielectric constants in the second set of constants extracted in this work.

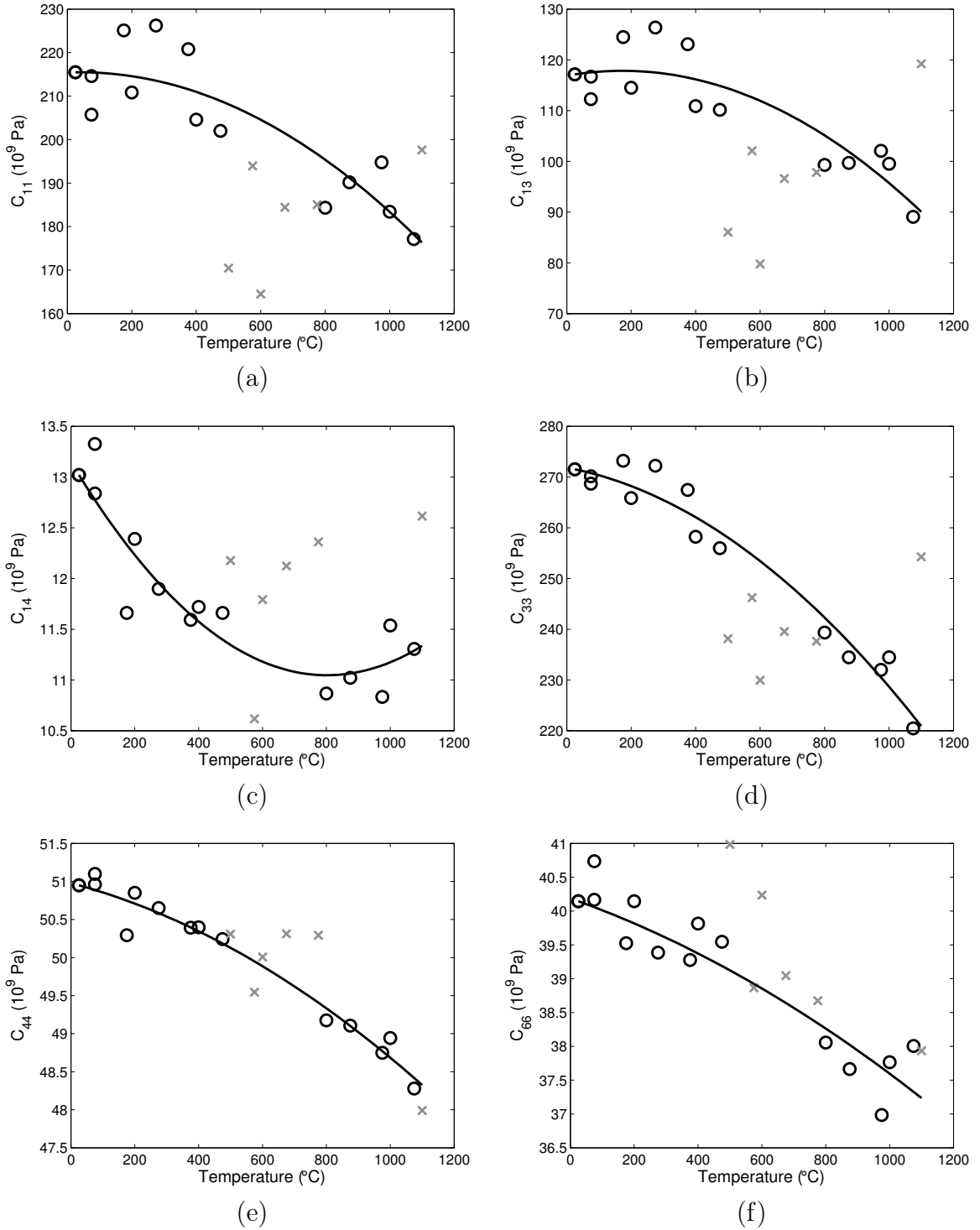


Figure 3.5. Extracted high-temperature LGT stiffened elastic constants. Included data (o), excluded data (x), second-order best-fit curve (black line). For the constants (a) c_{11} , (b) c_{13} , (c) c_{14} , (d) c_{33} , (e) c_{44} , (f) c_{66} .

The inclusion of piezoelectricity in the RUS fitting allows for more accurate agreement between predicted and measured resonance modes [318]. In this work, it was found that this allowed for the inclusion of more measured modes in the LGT fitting when compared with the non-piezoelectric SEC fitting. In the previous non-piezoelectric fitting, the difference between some consecutive modes was on the order of the agreement between the measured and calculated modes so could not be identified reliably; this would occur mostly with higher frequency modes above the 70th mode, > 425 kHz. The improved accuracy of the considering the piezoelectric constants in the RUS extraction enabled these modes to be matched with the measurements, increasing the number of modes used at high temperatures and, correspondingly, the accuracy of the extracted constants.

The mode matching at high temperatures was also improved by using the extracted results from the previous temperatures to predict the temperature behavior of the resonance modes. The preliminary elastic and piezoelectric constants were fit to a second-order polynomial and extrapolated to higher temperatures and used to calculate the resonance spectra for comparison with the measurements. This enabled modes that are close in frequency at a given temperature to be identified by their temperature dependency. The extraction using the piezoelectric theory was able to utilize more modes because of the improved mode matching techniques and new resonance spectrum measurements from 25 °C to 925 °C with measurements every 100 °C.

New measurements with finer temperature resolution, measuring at least every 100 °C, improved mode matching, preliminary temperature data (up to 400 °C) was used to calculate temperature curves and anticipate temperature behavior of each mode to better identify modes that are close in frequency or become lost in the temperature range of 500 °C to 800 °C. The UEC and piezoelectric RUS fitting included 95 to 100 modes at room temperature, 85 to 95 modes up to 450 °C, 45

to 65 modes from 500 °C to 750 °C, and 65 to 85 modes from 800 °C to 925 °C. In comparison, the SEC only fitting was only able to utilize ~ 75 modes up to 500 °C and ~ 50 modes at higher temperatures. For the UEC and piezoelectric fitting, at all temperatures the number of modes is greater than the minimum 40 modes, five modes for each of the eight LGT constants being determined for RUS, as suggested in [316].

A new set of room-temperature and high-temperature LGT elastic and piezoelectric parameters were extracted up to 925 °C. The respective second-order polynomial temperature coefficients are listed in Table 3.4. The extracted RUS constants in the temperature range from 600 °C to 800 °C were found to have uncertainties about twice as high with respect to other measured temperatures and up to 3 times higher departure from the best-fit curve due to the higher losses and fewer number of resonance modes measured in this temperature region, as discussed Section 3.4.2. For this reason some of the data points in the temperature range 600 °C to 800 °C were excluded from the best-fit. At these temperatures, resonance modes measured for RUS have significantly weakened responses, causing many modes to vanish below noise level and others to be measured with less accuracy. At 800 °C and higher temperatures the magnitude of the resonance peaks increase, improving the RUS fitting and allowing the consideration of the data for the extraction of elastic constants.

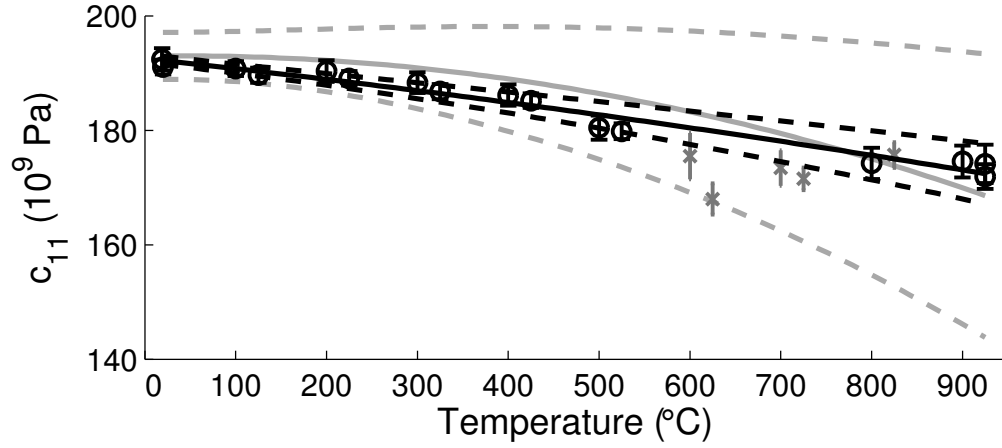
The unstiffened elastic constants (UEC) determined in this work considering the temperature behavior of the piezoelectric and dielectric constants are compared in Fig. 3.6 to the stiffened elastic constants (SEC) from Table 3.3, which were determined from the temperature coefficients of the piezoelectrically-stiffened elastic constants at elevated temperatures and the room temperature elastic constants extracted with piezoelectricity. As can be seen from Fig. 3.6, there is a significant reduction in the uncertainty for the UEC when compared to the uncertainty of the SEC from [328, 330], also included in the plots. For example, the difference between the SEC and UEC c_{11}

	Value at 25 °C	TC ⁽¹⁾	TC ⁽²⁾
Elastic constants			
	(10 ⁹ Pa)	(10 ⁻⁶ °C ⁻¹)	(10 ⁻⁹ °C ⁻²)
c_{11}	192.1 ± 0.7	-91.2 ± 21.7	-25.2 ± 23.4
c_{12}	111.1 ± 0.7	—	—
c_{13}	102.9 ± 0.5	-119.7 ± 29.6	8.9 ± 32.0
c_{14}	13.81 ± 0.02	-243.4 ± 10.3	0.9 ± 11.9
c_{33}	264.1 ± 0.5	-106.6 ± 10.0	-20.7 ± 10.9
c_{44}	50.99 ± 0.02	3.4 ± 2.3	-70.8 ± 2.7
c_{66}	40.51 ± 0.02	5.5 ± 2.9	-73.7 ± 3.1
Piezoelectric constants			
	(C m ⁻²)	(10 ⁻⁶ °C ⁻¹)	(10 ⁻⁹ °C ⁻²)
e_{11}	-0.377 ± 0.023	1339 ± 392	-2341 ± 500
e_{14}	0.165 ± 0.009	-1741 ± 330	2991 ± 375

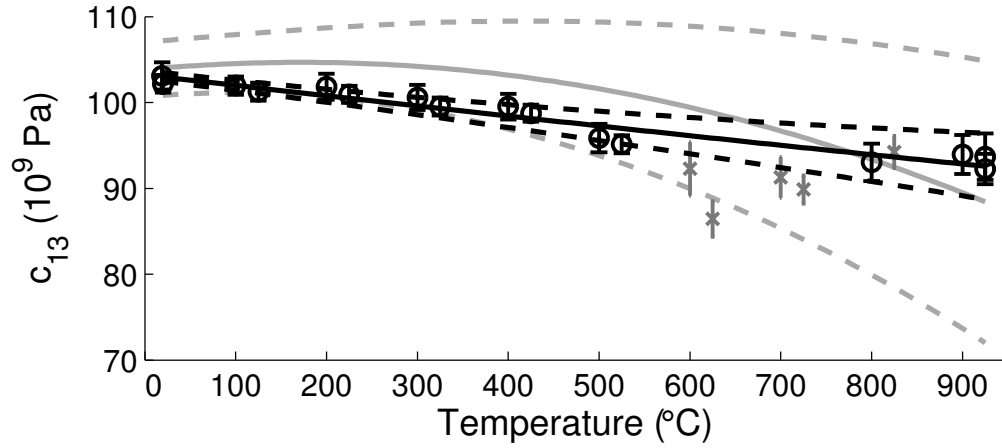
Table 3.4. LGT elastic and piezoelectric constants and temperature coefficients from 25 °C to 900 °C.

starts at 0.4 % at 25 °C and increases to the largest difference of 2.2 % around 400 °C, which indicates the relevance to consider the temperature dependence of ϵ and e in the extraction of the elastics constants. The difference between the SEC and UEC of c_{44} was the smallest as a percentage of the UEC, the SEC and UEC were within 0.5 % up to 700 °C and disagreed by 1.5 % at 900 °C. The largest difference between the SEC and UEC was 10 % for c_{14} at 900 °C.

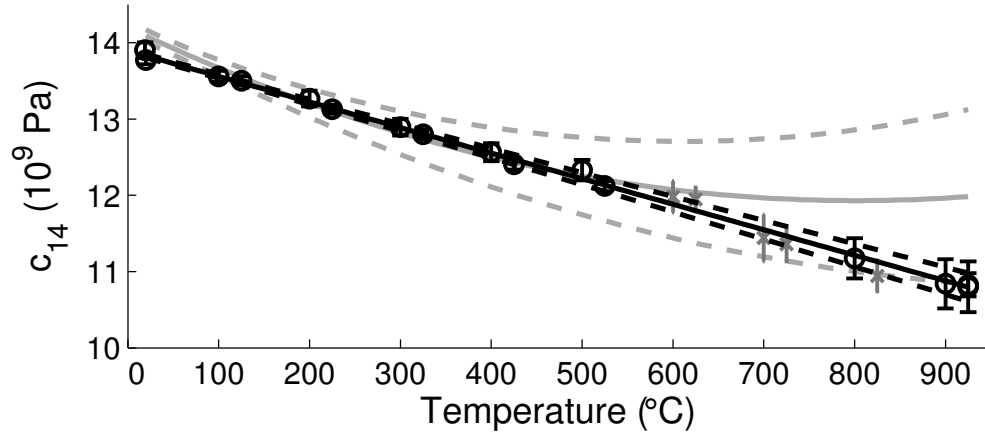
The extracted LGT piezoelectric parameters up to 900 °C are shown in Fig. 3.7. It is found that the magnitude of e_{11} increases by up to 20 % of its room temperature value until 450 °C before starting to decrease with temperature and is reduced by 62 % at 900 °C. On the other hand, e_{14} follows an opposite trend, first decreasing with temperature until 350 °C and then increasing by 77 % of the room temperature value at 900 °C.



(a)

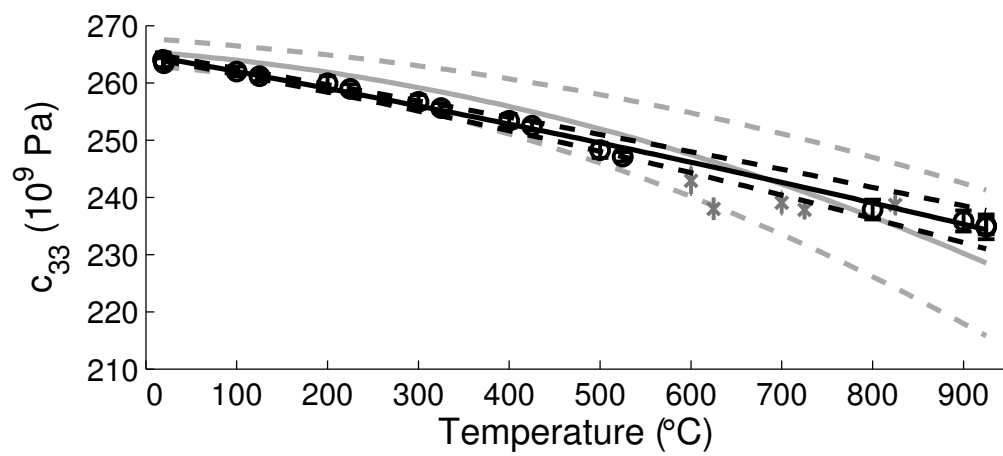


(b)

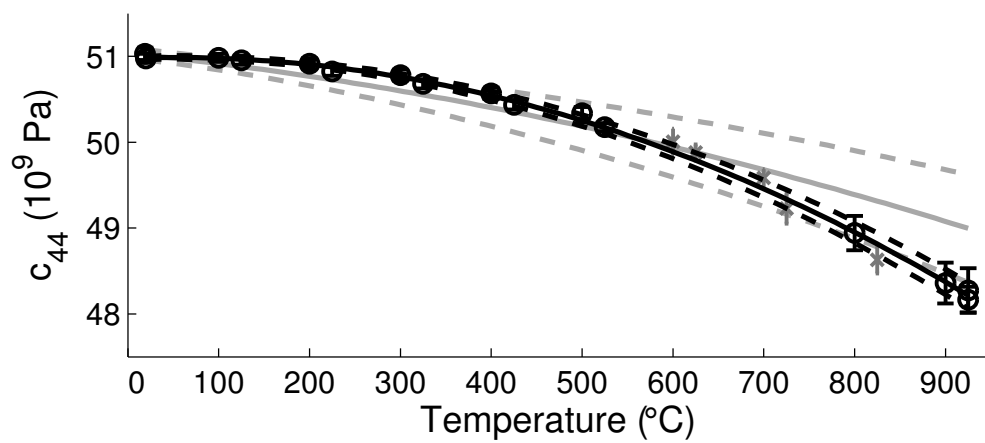


(c)

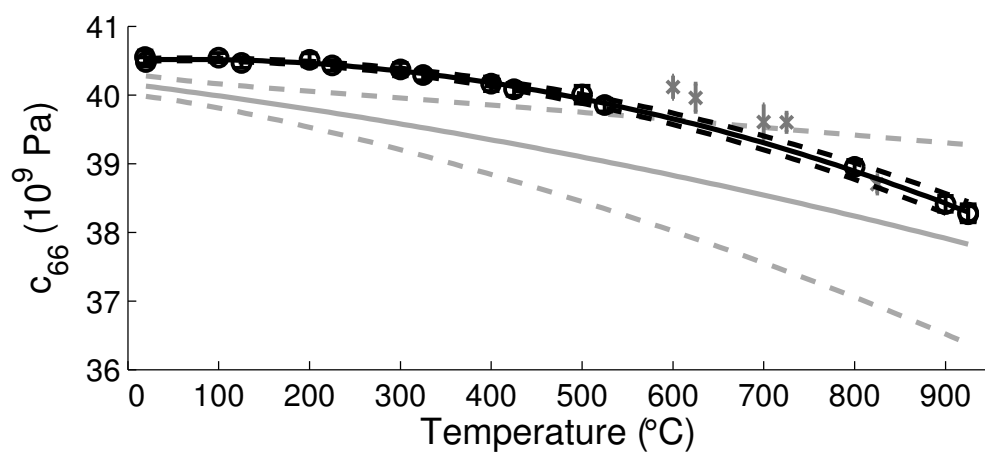
Figure 3.6. Extracted high-temperature LGT elastic constants. Included data (black o), excluded data (gray x), second-order best-fit curve (black line), stiffened elastic constants (gray line). Uncertainty given by dashed lines. For the constants (a) c_{11} , (b) c_{13} , (c) c_{14} , (d) c_{33} , (e) c_{44} , (f) c_{66} .



(d)



(e)



(f)

Figure 3.6. Continued.

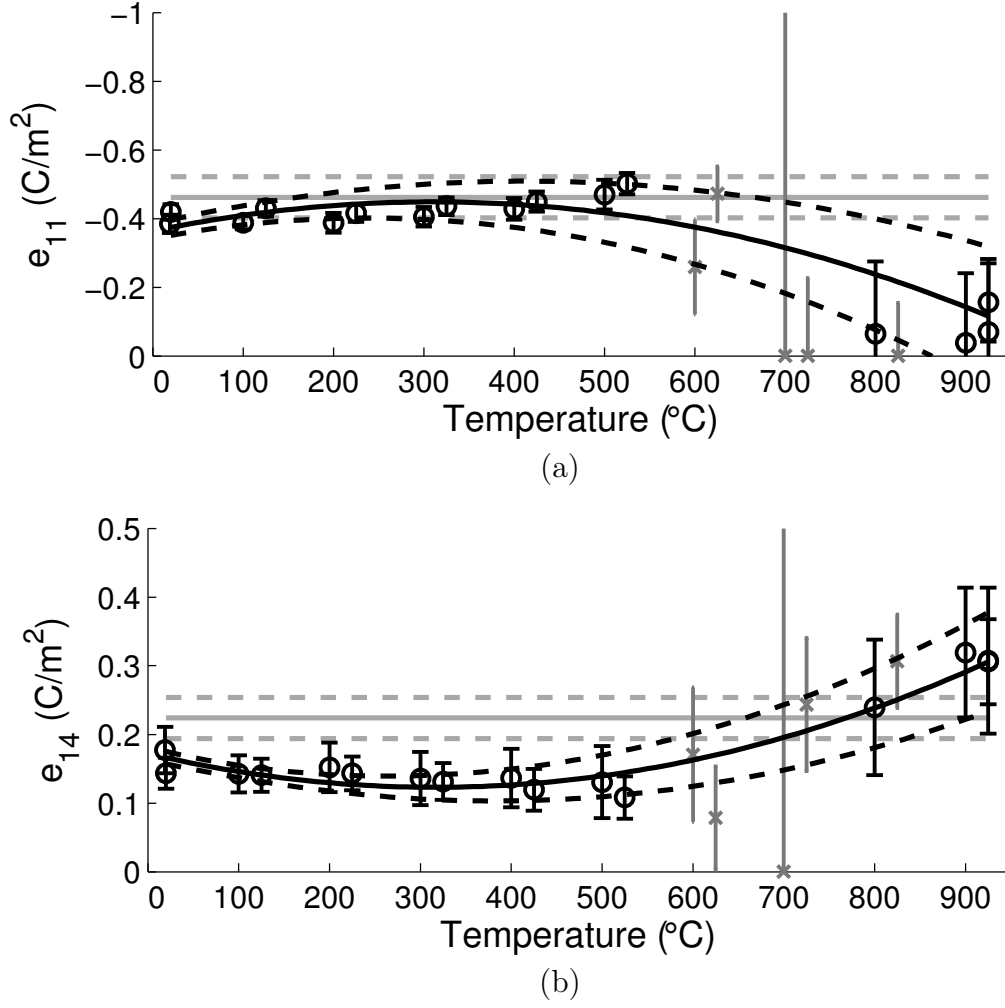


Figure 3.7. Extracted high-temperature LGT piezoelectric constants. Included data (black \circ), excluded data (gray \times), second-order best-fit curve (black line), previous room temperature constants (gray line). Uncertainty given by dashed lines. For the constants (a) e_{11} , (b) e_{14} .

The fitting correlation coefficient, R^2 , was greater than 0.99 for c_{14} , c_{33} , c_{44} , and c_{66} , $R^2 = 0.95$ for c_{11} , and is lowest for c_{13} , $R^2 = 0.91$. The piezoelectric constants, e_{11} and e_{14} , were fit with R^2 values of 0.65 and 0.88, respectively; reflecting the larger variation in these constants with temperature. At room temperature the 6 extracted elastic constants have uncertainty ranging from 0.05 % to 0.52 % and were calculated using the curve fit of the parameter data over the entire temperature range from 25 $^{\circ}\text{C}$ to 900 $^{\circ}\text{C}$. These uncertainty values at room temperature are consistent with the

uncertainty range of 0.01 % to 0.79 % for LGT elastic constants previously reported by the authors using pulse echo and combined resonance techniques up to 120 °C [236]. Still at room temperature, the relative uncertainty of e_{11} and e_{14} are 6.2 % and 5.5 %, respectively, reflecting their reduced effect on the LGT resonance spectra compared to the elastic constants. Up to 900 °C the uncertainty in the extracted elastic constants is lowest for c_{44} , and c_{66} which have less than 0.4 % relative uncertainty. The elastic constants c_{33} , c_{14} , c_{11} , and c_{13} , have higher uncertainty: the worst case uncertainty, respectively, 1.4 %, 1.6 %, 2.9 %, and 4.0 % at 900 °C. For the piezoelectric constants, the uncertainties increase significantly above 600 °C, as shown in Fig. 3.7, reflecting the previously discussed increase in LGT losses over the 600 °C to 800 °C temperature range and the consequent loss of measured modes for the RUS technique.

The extracted LGT room-temperature elastic and piezoelectric constants are compared in Table 3.5 with published values from [36, 41, 141, 206, 207, 232, 234–236, 238, 239, 402]. The room-temperature elastic constants determined in this work are within 1.5 % of the average of the literature values, which had their signs corrected to match the IEEE standard [297]. The constants c_{13} , c_{33} , c_{44} , and c_{66} had the closest agreement with the literature, ranging from -0.15 % to -0.65 %, and were smaller than the average; whereas c_{11} , c_{12} , and c_{14} were larger than the average and had slightly more disagreement, ranging from 0.7 % to 1.5 %. The extracted piezoelectric constant e_{11} is 31 % lower than the literature average and e_{14} is 62 % above the average. All of the room temperature constants except for e_{11} were within one standard deviation of the literature average, indicating fairly good agreement with the published values. While the room-temperature agreement with the literature helps validate the extraction process and crystal quality, the primary concern of this work is the applicability of the constants to accurately predict the temperature behavior of acoustic wave devices in particular at elevated temperatures up to 900 °C, which will be discussed in Chapter 4.

Reference	c_{11} (10^9 Pa)	c_{12} (10^9 Pa)	c_{13} (10^9 Pa)	c_{14} (10^9 Pa)	c_{33} (10^9 Pa)	c_{44} (10^9 Pa)	c_{66} (10^9 Pa)	e_{11} (C m^{-2})	e_{14} (C m^{-2})
This work	192.1 ± 0.7	111.1 ± 0.7	102.9 ± 0.5	13.81 ± 0.02	264.1 ± 0.5	50.99 ± 0.02	40.51 ± 0.02	-0.377 ± 0.023	0.165 ± 0.009
Fukuda et al. [207]	192	108	98.7	-13	264	51	42 ^a	-0.867 ^b	0.520 ^b
Pisarevsky et al. [206]	189.4	108.4	132.0	13.7	262.9	51.25	40.52	-0.54	0.07
Bohm et al. [41]	188.9	108.6	104.4	13.74	264.5	51.29	40.17	0.508	-0.028
Mill and Pisarevsky [36]	190.9	107.9	73.9	13.7	263.2	51.2	40.5	-0.514 ^b	0.0519 ^b
Onozato et al. [238]	202	120	125	13.3	288	49.7	40.7	-0.468	0.0632
Pereira da Cunha et al. [141]	188.62	107.94 ^a	103.44	13.51	261.88	51.10	40.34	-0.456	0.094
Schreuer [232]	188.81 ± 0.28	107.84 ± 0.31	100.15 ± 0.32	13.5 ± 0.02	261.05 ± 0.50	50.95 ± 0.07	40.485 ^a -	-0.478 ± 0.3	0.043 ± 0.5
Hubert et al. [234, 402] ^c	191.0	113.4	103.5	13.7	265.5	51.4	38.8	-0.6	-0.07
Straube et al. [235]	188.94	108.13	100.86	13.91	264.44	51.25	40.41 ^a	0.51	-0.025
Bourquin and Dulmet [239]	188.5	104.1	96.88	14.15	261.68	53.71	42.21	-	-
Sturtevant et al. [236]	189.41 ± 0.04	109.06 ± 0.1	100.63 ± 0.8	13.6 ± 0.1	262.29 ± 0.07	51.12 ± 0.01	40.17 ± 0.03	-0.518 ± 0.2	0.051 ± 0.278
Average ^d	190.77 ± 3.90	109.40 ± 4.11	103.59 ± 14.98	13.62 ± 0.30	265.40 ± 7.62	51.27 ± 0.93	40.57 ± 0.91	-0.546 ± 0.120	0.102 ± 0.148

^aCalculated using $c_{12}=c_{11}-2c_{66}$ and the constants given in the respective reference

^bCalculated using [297, (Eq. 43)] and the constants given in the respective reference

^cElastic constants from [402] and piezoelectric constants from [234]

^dAverage of literature values with signs corrected

Table 3.5. LGT elastic and piezoelectric constants from the literature at room temperature.

3.5 Conclusions

This chapter presented the resonant ultrasound spectroscopy (RUS) measurement technique for high-temperature material characterization, which was used to extract the LGT elastic and piezoelectric constants up to 900 °C. The RUS equations used to calculate the resonant spectrum of a crystal sample using Lagrangian minimization was detailed, along with the numerical process used to extract the crystal constants.

Langatate parallelepiped samples were fabricated and had their spectra measured in a custom high-temperature furnace. Initially the LGT stiffened-elastic constants was extracted up to 1100 °C ignoring the piezoelectric effect. A full set of the LGT elastic and piezoelectric constants was then determined up to 900 °C utilizing the dielectric constants from Chapter 2. The uncertainty in the extracted elastic constants was 1.5% or better at room temperature and remain below 3% over the entire temperature range. The piezoelectric constants e_{11} and e_{14} have relative uncertainties of 6.8% and 19.1% at room temperature.

Chapter 4

VERIFICATION OF HIGH-TEMPERATURE LGT CONSTANTS

4.1 Verification Methodology

The extracted high-temperature LGT elastic, piezoelectric, and dielectric constants should be independently verified with acoustic wave device measurements in order to provide confidence in the constants. High-temperature characterization of SAW or BAW devices allows for the comparison of measured behavior with that calculated using the set of AW constants. Bulk acoustic wave devices are fabricated along a single orientation determined by the cut and have three acoustic modes. Surface acoustic wave devices can be fabricated along any orientation in the crystal cut plane with sufficiently strong SAW electromechanical coupling and therefore allow the exploration of multiple orientations from a single prepared wafer. Additionally, SAW devices require only one polished surface, whereas BAW devices require both faces to be polished and parallel to each other. For these reasons, SAW devices are used in this work to verify the high-temperature LGT acoustic properties.

The propagation direction of a SAW device can be defined by the Euler angles (Φ, Θ, Ψ) [297]. The first two Euler angles define the SAW cut plane and the third angle, Ψ , is the SAW in-plane rotation. A single cut wafer can be used to simultaneously fabricate multiple SAW devices with different values of Ψ that will have different dependence on the acoustic constants.

The LGT SAW devices, fabricated at UMaine, used for the AW validation were made from a single crystal cut in order to minimize the cutting, polishing, and processing work. In this work the selection of a crystal cut was aimed at the following properties: (i) singly rotated or having a first rotation aligned along major axes for accurate orientation cutting; (ii) SAW electromechanical coupling, K^2 , larger than 0.1% over most of the plane to allow the practical excitation of SAW along

diverse orientations using the same wafer; (iii) significant variation of TCD around the plane to allow for the verification of the predicted temperature behavior using the high-temperature constants described in Chapter 3. Orientations with Euler angles $(0^\circ, \Theta, \Psi)$, $(90^\circ, \Theta, \Psi)$, and $(\Phi, 90^\circ, \Psi)$ have surface normals in the planes defined by the Y-Z, X-Z, and X-Y axes, respectively, and can be cut from a crystal boule by rotating a single time from a major axis [237, 240, 329, 331–334].

The LGT cut plane $(90^\circ, 23^\circ, \Psi)$ was selected to verify LGT AW constants both up to 120°C by Sturtevant, et al. [237, 240, 253] and for the verification of the high-temperature LGT constants determined in this work [329, 330]. Multiple wafers of the cut were fabricated at the same time for use in both studies.

The LGT $(90^\circ, 23^\circ, \Psi)$ cut offers interesting characteristics, namely: coupling $0.1\% < K^2 < 0.4\%$ for much of the plane; TCD values ranging from -80 to $5\text{ ppm}/^\circ\text{C}$ at room temperature, thus indicating the existence of temperature-compensated orientations around room temperature; phase velocities $> 2700\text{ m s}^{-1}$; and orientations of reduced diffraction [237, 240, 253]. For this study, six orientations with $0.1\% < K^2 < 0.4\%$ were chosen for SAW device fabrication on the $(90^\circ, 23^\circ, \Psi)$ plane, namely $\Psi=0^\circ$, $\Psi=13^\circ$, $\Psi=48^\circ$, $\Psi=77^\circ$, $\Psi=119^\circ$, and $\Psi=123^\circ$. These orientations were selected because they were predicted to have a range of TCD between $-64\text{ ppm }^\circ\text{C}^{-1}$ and $4\text{ ppm }^\circ\text{C}^{-1}$ at room temperature [240, 253] and thus could be used to validate the extracted acoustic constants and temperature coefficients.

The SAW coupling between 25°C and 900°C for the SAW plane $(90^\circ, 23^\circ, \Psi)$, shown in Fig. 4.1, is predicted using the LGT high-temperature constants including the piezoelectric and dielectric temperature behavior from Table 3.4. As can be seen, K^2 rapidly decreases for temperatures above 400°C ; however, all the six tested devices had sufficient coupling to be measured up to 900°C , which will be discussed in Section 4.3.

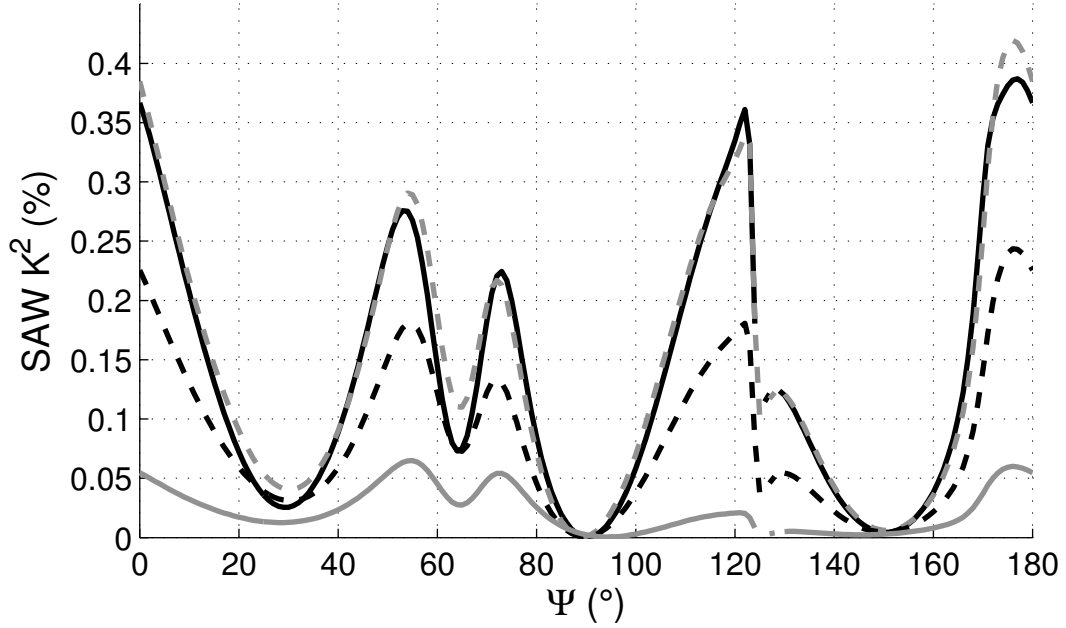


Figure 4.1. LGT SAW coupling, K^2 , along plane (90° , 23° , Ψ) at high temperature. 25°C (solid-black), 400°C (dashed-gray), 600°C (dashed-black), 900°C (solid-gray).

4.2 Calculation of SAW Propagation Properties

The high-temperature LGT SAW properties are calculated using the extracted LGT dielectric permittivity from Chapter 2 [331, 334, 359], the elastic and piezoelectric constants from Chapter 3 [331, 334], and the LGT density and thermal expansion from [148, 271]. Additionally, the stiffened-elastic constants (SEC) from Chapter 3 [328, 331], determined with RUS neglecting the piezoelectricity and dielectric constants, were also used to calculate the SAW propagation properties and compare results including and neglecting the temperature behavior of the piezoelectric and dielectric constants.

The LGT SAW phase velocity (v_p), fractional frequency variation ($\Delta f/f_0$), and temperature coefficient of delay, (TCD) were calculated from 25°C to 900°C in increments of 10°C and are reported in Section 4.4. The predictions were calculated along the fabricated SAW orientations $\Psi = 0^\circ, 13^\circ, 48^\circ, 77^\circ, 119^\circ, 123^\circ$ in the plane ($90^\circ, 23^\circ, \Psi$), described in Section 4.1.

The SAW phase velocity for a particular orientation and temperature was calculated from the LGT acoustic wave constants using the matrix method [403], in which the SAW free-surface velocity was found by minimizing the determinant of the boundary condition matrix of the piezoelectric half-space [403, eq. (21)]. The SAW properties calculations using the matrix method were implemented in a custom program written for MATLAB (The MathWorks, Natick, MA, USA) [245, 404].

The SAW frequency variation was determined from the calculated SAW velocity and thermal expansion and was normalized to the initial frequency so that it was independent of the choice of wavelength. The fractional frequency variation quantifies the percent change in the device frequency at a given temperature has varied from the room temperature frequency, $f_0 = f(25^\circ\text{C})$, and is defined as

$$\frac{\Delta f}{f_0} = \frac{f(T) - f(25^\circ\text{C})}{f(25^\circ\text{C})}. \quad (4.1)$$

The TCD is defined as the fractional temperature change in the electrical delay, $\tau = l/v_p$, of a SAW delay line of length l , and is given by [405, 406]:

$$TCD = \frac{1}{\tau} \frac{\partial \tau}{\partial T} = \frac{v_p}{l} \frac{\partial \left(\frac{l}{v_p} \right)}{\partial T} = \frac{v_p}{l} \left(\frac{v_p \frac{\partial l}{\partial T} - l \frac{\partial v_p}{\partial T}}{v_p^2} \right) = \frac{1}{l} \frac{\partial l}{\partial T} - \frac{1}{v_p} \frac{\partial v_p}{\partial T} \quad (4.2a)$$

$$TCD = TCE - TCV \quad (4.2b)$$

where the thermal expansion coefficient (TCE) of the acoustic medium along the propagation direction is defined by

$$TCE = \frac{1}{l} \frac{\partial l}{\partial T} \quad (4.3)$$

and the thermal expansion velocity (TCV) of the acoustic medium along the propagation direction is defined by

$$TCV = \frac{1}{v_p} \frac{\partial v_p}{\partial T}. \quad (4.4)$$

The derivatives are evaluated around the device operation temperature T .

The TCD is calculated using the TCV and TCE determined in this work by the central-difference discrete derivatives of v_p and expansion evaluated at 5 °C above and below the target temperature.

For particular crystal orientations, if there is a temperature at which $TCD = 0$, also called the turnover temperature, then the SAW device is insensitive to temperature variation at that operation temperature. The accurate prediction of turnover temperature requires accurate AW constants and temperature coefficients [356], and the identified LGT turnover temperatures of the measured orientations are used to validate the extracted high-temperature LGT AW constants.

The temperature coefficient of frequency (TCF) is similarly defined by

$$TCF = \frac{1}{f} \frac{\partial f}{\partial T} = \frac{l}{v_p} \frac{\partial \left(\frac{v_p}{l} \right)}{\partial T} = \frac{l}{v_p} \left(\frac{l \frac{\partial v_p}{\partial T} - v_p \frac{\partial l}{\partial T}}{l^2} \right) = \frac{1}{v_p} \frac{\partial v_p}{\partial T} - \frac{1}{l} \frac{\partial l}{\partial T} \quad (4.5a)$$

$$TCF = TCV - TCE \quad (4.5b)$$

$$TCF = -TCD. \quad (4.5c)$$

The TCD and TCF are the normalized slopes of the delay or frequency around the operating temperature and, in general, are also functions of temperature. The TCD and TCF define how the delay and frequency, respectively, of a SAW device will change with temperature.

The uncertainty in the predicted v_p cannot be analytically determined since it is numerically calculated, instead the velocity uncertainty was determined from the uncertainties in the elastic constants, temperature coefficients, density, and thermal expansion and the partial derivative of each constant using standard error propagation techniques [367, 368, 407]. The piezoelectric and dielectric constants were ignored in the calculation of the velocity uncertainty due their relatively small contribution when compared to the elastic constants and density. The partial derivatives of the constants with respect to the velocity were approximated by the discrete derivative, determined by perturbing each of the input constants individually and observing the

velocity change at room temperature [237, 240, 253]. For the uncertainty calculation, the v_p partial derivatives were assumed to not change significantly over temperature since v_p changed by less than 3 % up to 900 °C. The v_p uncertainty was calculated at each temperature by squaring the sum of the uncertainties of each extracted constant (estimated at the measurement temperature) multiplied by the v_p partial derivative (determined at room temperature) then taking the square root.

4.3 High-Temperature SAW Fabrication and Characterization

4.3.1 SAW Device Fabrication

The LGT SAW devices using in work were fabricated at UMaine. Due to the small batch size, the research focus of this work, and the desired precision and control over the wafer preparation process, the decision was made to prepare the samples at UMaine.

The LGT SAW devices were fabricated from a single Z-axis grown langatate crystal boule purchased from Fomos Materials (Moscow, Russia). This hexagonal prism boule, shown in Figure 4.2a, had a length of 6 cm (2.36 in) and a diagonal distance of 6.35 cm (2.5 in). This LGT boule was not the same boule as the one used to fabricate the samples for the RUS and dielectric measurements, which also purchased from Fomos Materials.

The LGT samples were aligned with a PANalytical X’Pert Pro MRD X-ray diffractometer (PANalytical Inc., Natick, Corp., Waltham, MA) and cut with an inner diameter saw (Meyer-Berger, Steffisberg, Switzerland), displayed in Figure 4.2b. The process starts by epoxying the crystal boule to the chuck on the saw and manually aligning the cut to the faces of the boules, which correspond to the crystal axes. A thin crystal wafer is cut and the orientation is determined by XRD. The misalignment from the desired orientation is precisely determined and corrected on the inner diameter saw, which has two degrees of freedom to correct rotation without removing the

samples from the chuck [408, 409]. The alignment and cutting process at UMaine was shown to have achieved wafer orientations within 6 arcminutes [240]. Multiple wafers were diced from the boule with the same thickness but different lateral dimensions due to the rotation of the boule necessary to obtain the desired orientation.

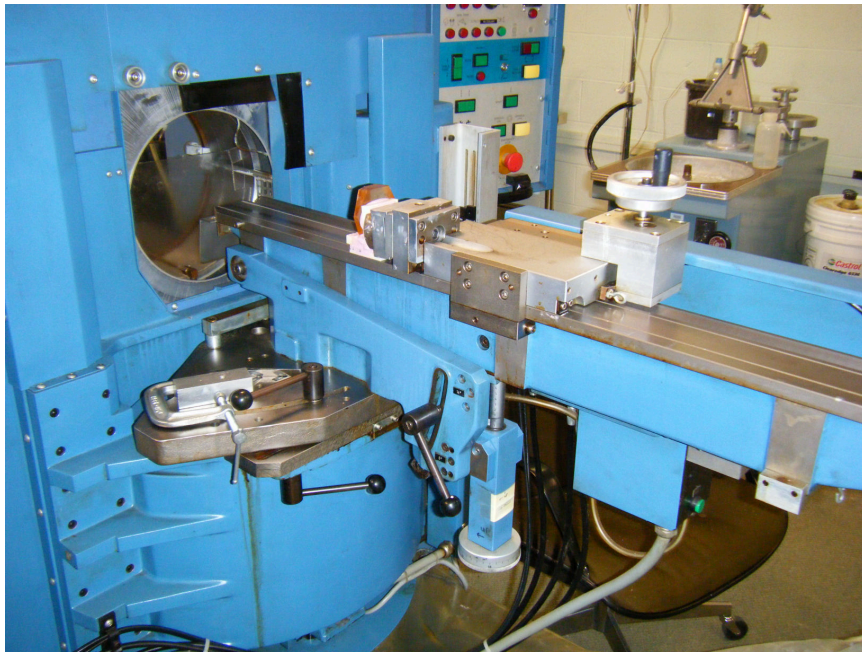
The edges and corners of the final wafers were beveled to remove any damaged crystal and prevent chipping during the polishing process. The wafers were then attached to an aluminum plate with melted wax, then placed sample face down so that the samples are aligned together and planar once the wax has cooled. The LGT wafers are ground to a uniform roughness then polished to optical quality with an abrasive slurry using automatic rotating in polishing machines (R. Howard Strasbaugh 6U, Lynwood, Ca), as shown in Figure 4.3. Alumina abrasives are used successively with progressively smaller diameters, from $30\text{ }\mu\text{m}$ to $1\text{ }\mu\text{m}$ (Micro Abrasives Corporation, Westfield, MA), and the final polishing step utilizes colloidal silica (Universal Photonics, Hicksville, NY).

The surface quality of the wafers was measured with a surface profilometer (Alpha-Step 500, Tencor Instruments, Mountain View, CA), the root-mean-square roughness was 0.67 nm and the average waviness was 9.59 nm . The surface quality is more than adequate for the SAW fabrication in this work and is within the average roughness $< 0.7\text{ nm}$ specification of commercially available langasite wafers [230].

SAW delay lines were designed and fabricated along Euler angles $(90^\circ, 23^\circ, \Psi)$ with $\Psi = 0^\circ, 13^\circ, 48^\circ, 77^\circ, 119^\circ, 123^\circ$, as discussed in Section 4.1. The SAW power flow angle (PFA) was considered in the design of the SAW devices along each propagation direction. Split-finger 500-electrode interdigital transducers (IDTs) were used, with $4\text{ }\mu\text{m}$ wide fingers and apertures equal to 2.56 mm on one IDT of the delay line and 4.21 mm for the other IDT in the delay line (about 80 and 130 wavelengths). These variations in the IDT apertures aimed at accounting for possible uncertainties in



(a)



(b)

Figure 4.2. Cutting of LGT boule for SAW devices. (a) LGT boule mounted to chuck for wafer dicing with the inner-diameter saw, (b) Meyer Berger inner-diameter saw



Figure 4.3. Polishing LGT wafers with an alumina slurry

the PFA calculations and to accommodate variations of the PFA within the large temperature range. The delay lines have a free region path of approximately 10.6 mm.

The size of the wafer was constrained by the co-deposition chamber. For this reason, two different SAW wafers were fabricated, one with delay lines along $\Psi=0^\circ$, $\Psi=48^\circ$, and $\Psi=123^\circ$ (shown in Figure 4.4) and another along $\Psi=13^\circ$, $\Psi=77^\circ$, and $\Psi=119^\circ$. The SAW delay lines were fabricated using 105 nm to 108 nm thick ($h/\lambda=0.3\%$) co-deposited platinum-rhodium-zirconia (Pt/Rh/ZrO₂) electrodes and were annealed prior to SAW characterization above 900 °C [149]. These electrodes have been tested for long term operation up to 800 °C and short term operation up

to 1000 °C [149]. In this work, we set the upper temperature limit to 900 °C to avoid compromising the electrode quality. In fact, after repeated cycles up to 900 °C, no measurable permanent device degradation was observed.

4.3.2 High-Temperature SAW Characterization

The fabricated LGT wafers were attached to a measurement fixture for SAW characterization using a small amount of epoxy and were loosely wrapped with bond wires as a safety precaution in case the epoxy released from the fixture, as shown in Figure 4.5a. The epoxy was applied in minimal amounts at a single location to avoid breaking the LGT wafer because of the different thermal expansion with respect to the alumina insulating base of the fixture. The delay lines were electrically connected to high-temperature coaxial lines using platinum bond wires with an Unitek parallel gap welder (Miyachi Unitek, Monrovia, CA). Platinum wire with a 25.4 μm (1 mil) diameter were required to bond to the 105 nm thin electrode and which were then connected to the high-temperature coaxial cable with 101.6 μm (4 mil) diameter platinum wire to reduce the resistance and increase the mechanical stability. The high-temperature tests were performed in laboratory air at atmospheric pressure inside a Thermolyne furnace (Thermolyne, Dubuque, IA), as shown in Figure 4.5b.

The SAW delay line type of structure was selected for the verification of the SAW propagation properties and the device frequency was used to extract the phase velocity. The delay lines have one input interdigitated transducer (IDT), a bare LGT delay path, and an output IDT. The transmitted signal from one port to the other, S_{21} , allows for the measurement of the SAW response even if the acoustic signal is relatively weak because the electrical feedthrough was relatively small, around -65 dB for the fabricated LGT devices.

The SAW S_{21} was converted to the time domain with the inverse Fourier transform, time gated to exclude responses not corresponding to the delay pulse, and then

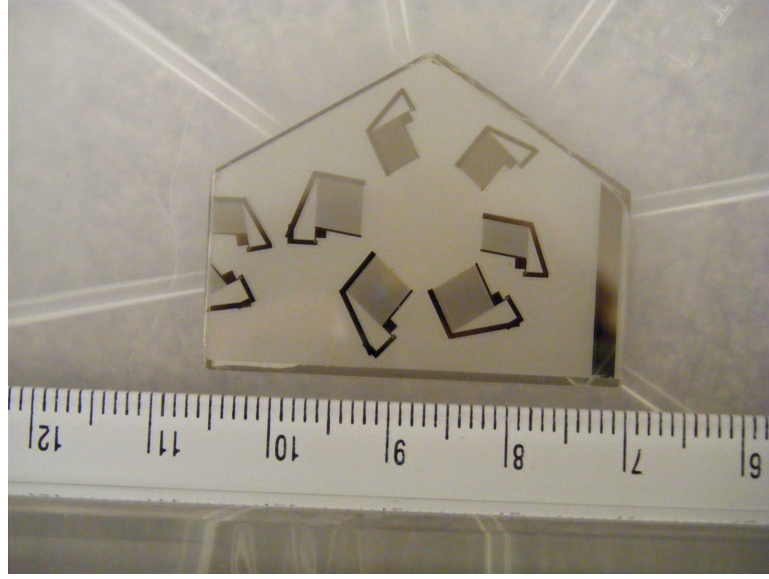


Figure 4.4. Fabricated LGT SAW delay lines. Units of ruler are cm.



Figure 4.5. High-temperature LGT SAW device fixture. (a) SAW device mounted to fixture with platinum bond wires, (b) measurement fixture inside the furnace.

converted back to the frequency domain, shown as an example for $(90^\circ, 23^\circ, 119^\circ)$ at 25°C in Fig. 4.6. This time gating filters out the electrical feedthrough, IDT electrical responses, triple transit, and other acoustic modes because they have little or no energy in the time window of the delay line pulse. This smooths the ripples in the delay line S_{21} peak for the determination of the frequency with the minimum return loss, which is taken as the SAW device center frequency in the calculations. The device

frequency is utilized instead of the phase to extract the SAW propagation velocity for simplicity; typically multiple delay lines of different along a single orientation are required to extract v_p from the device phase response [175, 410]. The effect of the IDT electrode mass loading and stiffness on the device frequency was neglected in this work for simplicity because the density and elastic properties of the electrodes are not known.

The transmission (S_{21}) responses of the delay lines were measured with an Agilent 8753ES network analyzer (Agilent Technologies, Santa Clara, CA). These delay line responses were time-gated by windowing the inverse Fourier transform of the signal to remove the effect of electromagnetic feed through, SAW triple transit, and other acoustic spurious reflections. The SAW phase velocities were extracted from the measured center frequencies of the delay lines and the variations on the IDT periodicity determined using the LGT thermal expansion coefficients from [148, 271].

The TCD was calculated from the frequency measurements using the relation (4.5a). Small temperature steps were not adequate given the targeted large temperature range and the time it takes for the high-temperature furnace used in this work to reach an equilibrium temperature. The adopted temperature step in this work was $\Delta T=50^\circ\text{C}$, and the frequency data points were obtained at least twice along each orientation. However, the temperature step was decreased to $\Delta T=10^\circ\text{C}$ in the vicinity of $\text{TCD}=0$ in order to improve the TCD calculation. Polynomial fitting was used to calculate the frequency derivative with respect to temperature by extracting the slope from the fitted curve. A fourth-order polynomial was used to provide a good correlation over the large temperature range (25°C to 900°C). The discrete difference TCD was also calculated and used to verify the TCD obtained from the curve fitting.

The uncertainty in the device temperature, U_T , considered both the thermocouple precision and the furnace fluctuations due to the limitations of the furnace controller

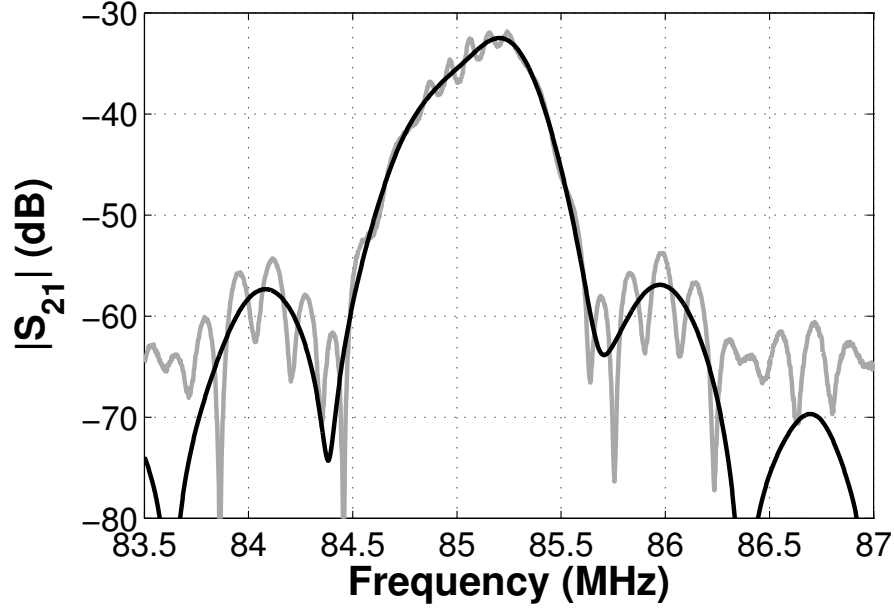


Figure 4.6. Example LGT SAW S_{21} response for $(90^\circ, 23^\circ, 119^\circ)$ at 25°C / Raw frequency response (gray), time-gated frequency response (black).

as independent errors. The uncertainty in the frequency, U_F , was calculated based on the discrepancies in the fitting and is given by [367]

$$U_F = \sqrt{\frac{1}{N - O_p - 1} \sum_{i=1}^N (F_i - F_i^P)^2} \quad (4.6)$$

where N is the number of data points, F_i is the i^{th} measured frequency, F_i^P is the frequency calculated from the polynomial fitting at the i^{th} temperature data point, and O_p is the polynomial order. The frequency uncertainty due to the fitting was larger than the uncertainty in the frequency measurement by the network analyzer, which was neglected. The uncertainty in the measured TCD was calculated by propagating U_T , U_F , and the uncertainty $U_{\Delta F} = U(\partial F^P / \partial T)$, where F^P is a fourth-order polynomial fit of the measured frequencies, using standard error propagation as described in [367]. These uncertainties are quantified in Section 4.4.

4.4 Comparison of Predicted and Measured SAW Properties Results

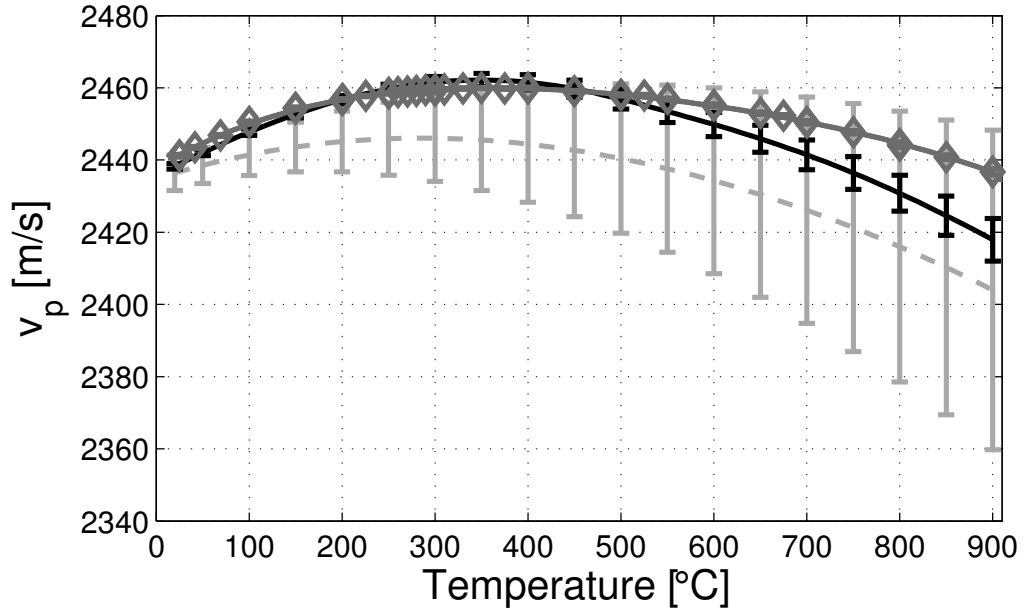
The predicted SAW v_p , $\Delta f/f_0$, and TCD were calculated with the process described in Section 4.2 using two sets of extracted LGT constants with and without considering the temperature dependence of the piezoelectric and dielectric constants. The initial LGT constants set, Table 3.3, utilizes the high-temperature stiffened elastic constants to determine the temperature coefficients of the elastic constants determined at room temperature along with the room temperature piezoelectric and dielectric constants. The updated constants include the temperature behavior of the piezoelectric and dielectric constants, given in Table 3.4.

Comparison of calculated and measured SAW phase velocity allowed the verification of the accuracy of the acoustic wave constants. The fractional frequency change, $\Delta f/f_0 = (f_T - f_{25^\circ\text{C}})/f_{25^\circ\text{C}}$, is calculated to compare the net frequency change of a device over temperature. The TCD allows the constants to be assessed on the accuracy of determining the slope of the temperature response at any individual point.

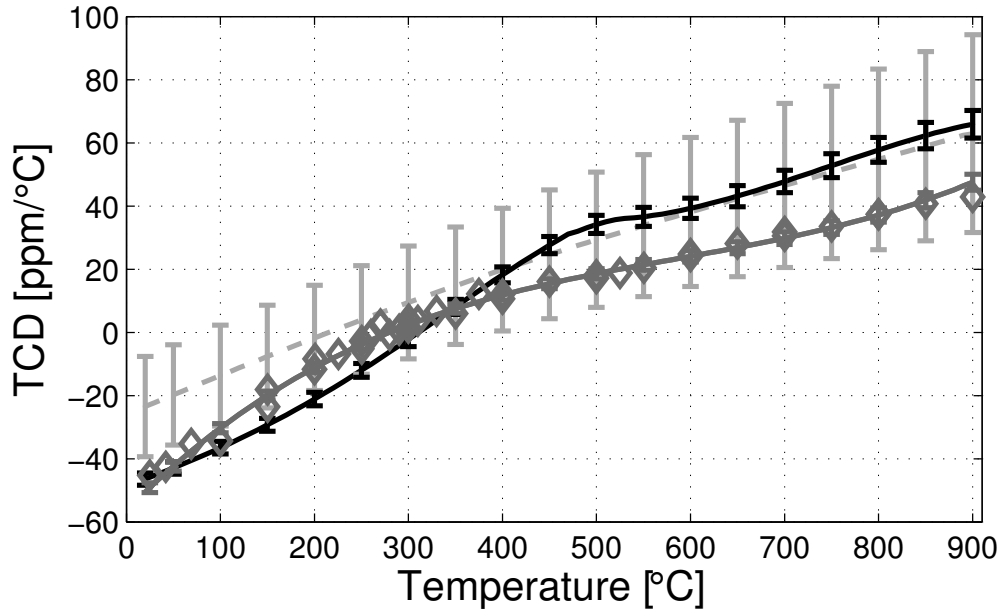
The predicted SAW v_p and TCD are compared to measured SAW data for the orientations $(90^\circ, 23^\circ, \Psi)$ where $\Psi = 0^\circ, 13^\circ, 48^\circ, 77^\circ, 119^\circ$, and 123° in Figs. 4.7, 4.8, 4.9, 4.10, 4.11, and 4.12, respectively. The measured TCD along $(90^\circ, 23^\circ, \Psi)$ are additionally shown together in Fig. 4.13 to convey the different temperature behaviors between the orientations.

The root-mean-square error and max absolute error of the SAW v_p , $\Delta f/f_0$, and TCD predictions with respect to the measurements are given in Table 4.1, where the velocity error is given as a percentage of the measured velocity and the $\Delta f/f_0$ and TCD errors are given as absolute quantities instead of percentages because they are zero at certain temperatures so any discrepancy would be an infinite error and would obscure the comparison between the measures and predictions.

The final LGT constants that considered the temperature behavior of the piezoelectric constants has improved accuracy with respect to the SAW measurements

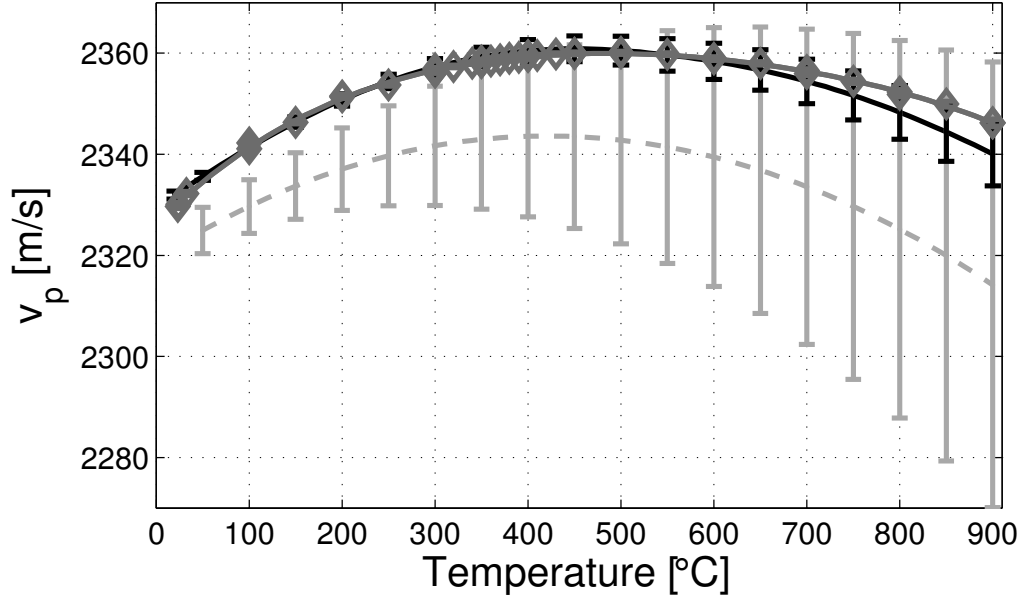


(a)

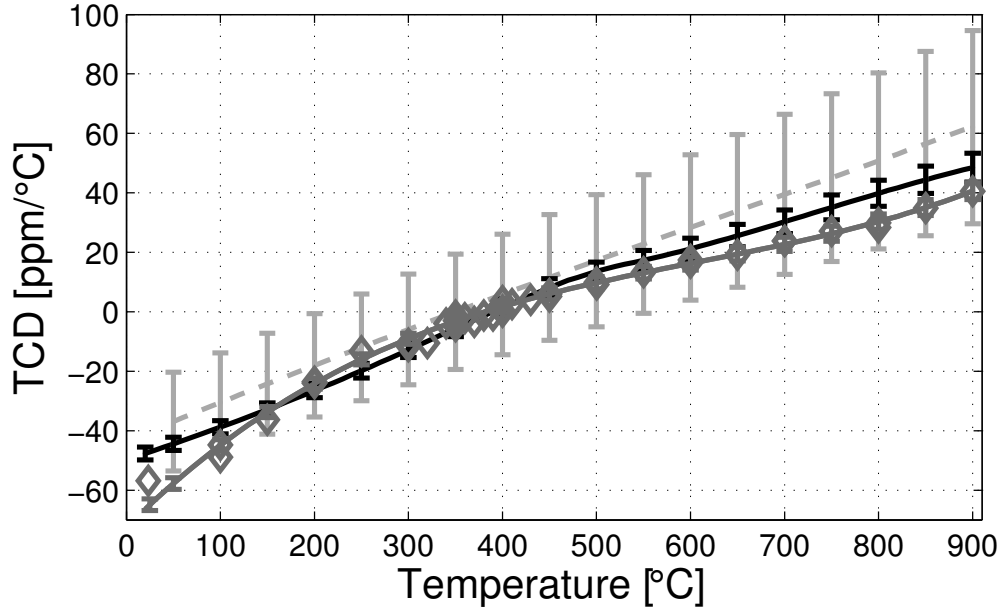


(b)

Figure 4.7. Comparison of measured and predicted v_p and TCD for LGT SAW orientation (90° , 23° , 0°). (a) v_p , (b) TCD. Measured SAW data (dark gray, diamonds); predicted using extracted constants with temperature behavior of the piezoelectric and dielectric constants (black line); and predicted using preliminary constants neglecting temperature behavior of the piezoelectric and dielectric constants (light gray dashed line).

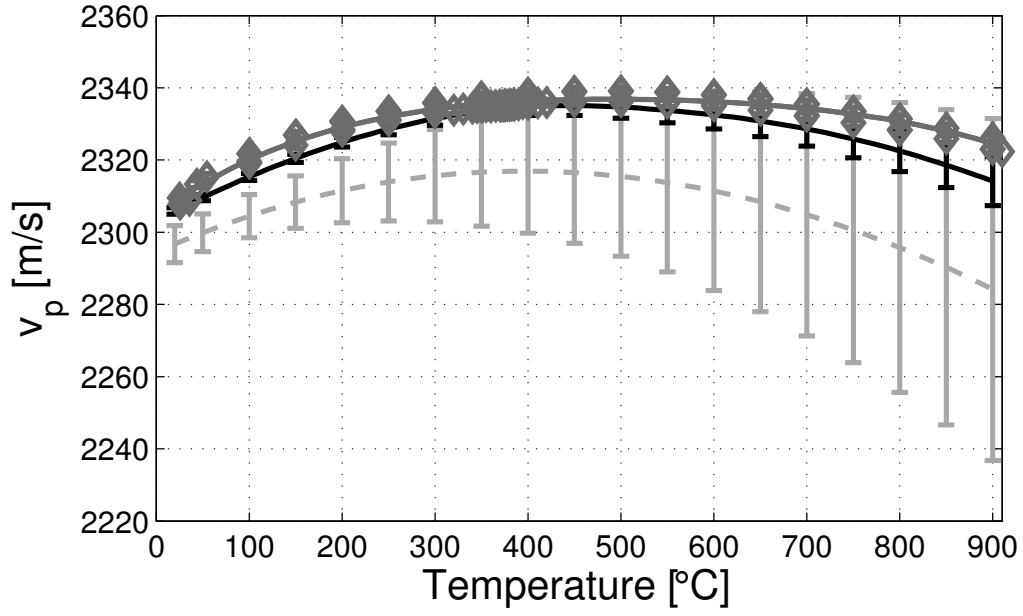


(a)

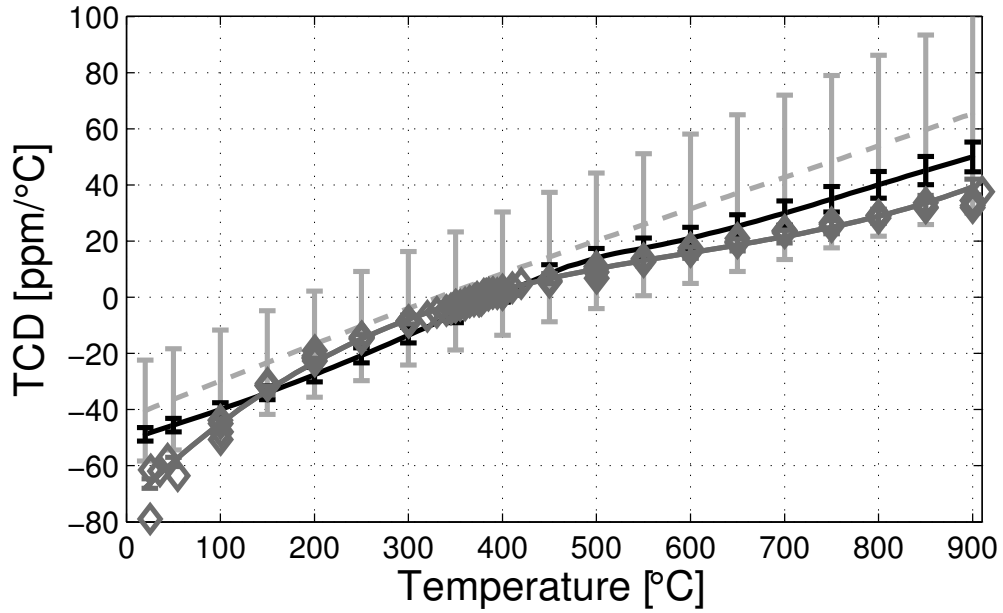


(b)

Figure 4.8. Comparison of measured and predicted v_p and TCD for LGT SAW orientation (90° , 23° , 13°). (a) v_p , (b) TCD. Measured SAW data (dark gray, diamonds); predicted using extracted constants with temperature behavior of the piezoelectric and dielectric constants (black line); and predicted using preliminary constants neglecting temperature behavior of the piezoelectric and dielectric constants (light gray dashed line).

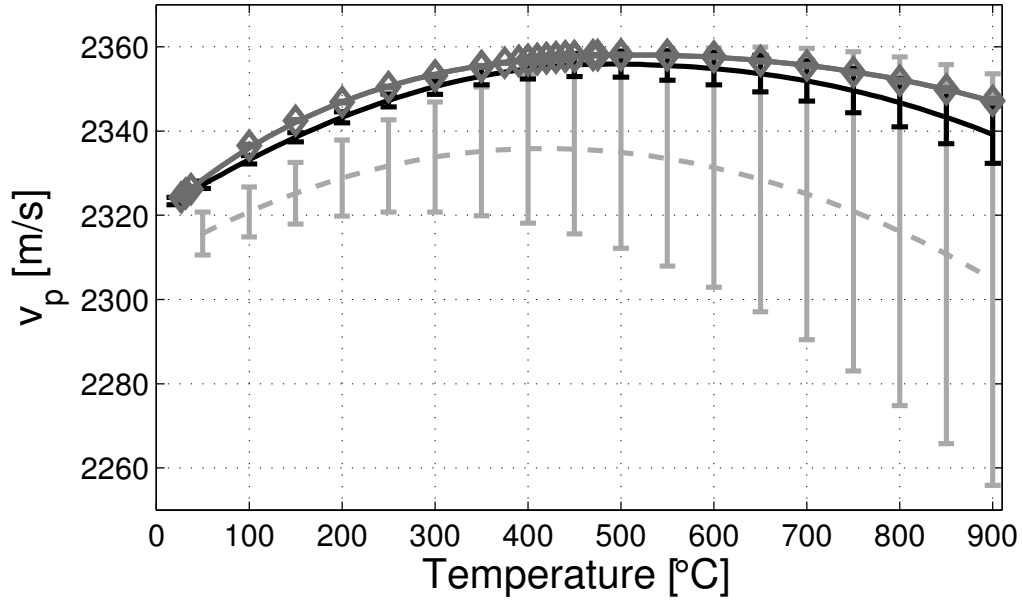


(a)

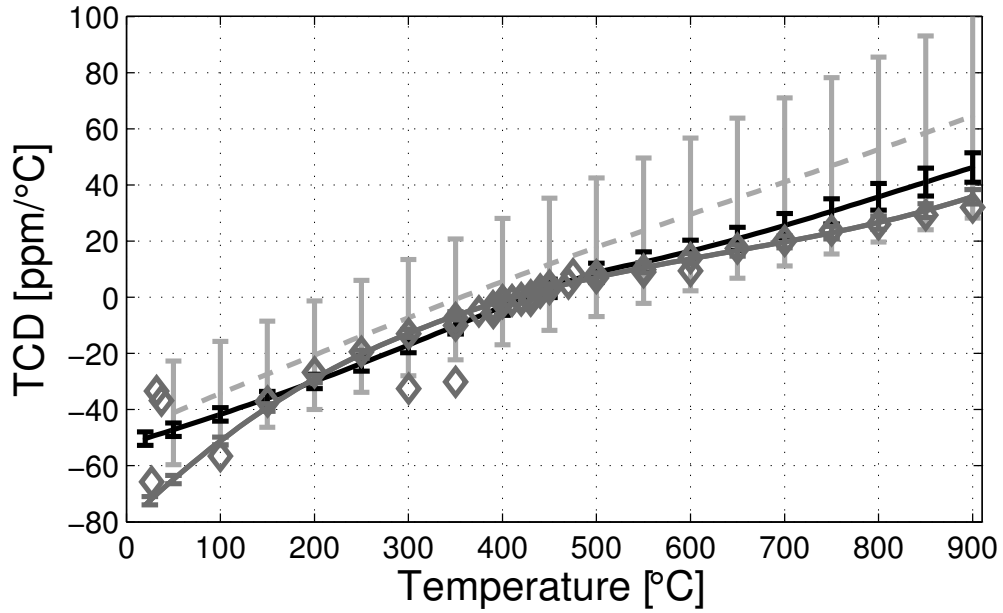


(b)

Figure 4.9. Comparison of measured and predicted v_p and TCD for LGT SAW orientation (90° , 23° , 48°). (a) v_p , (b) TCD. Measured SAW data (dark gray, diamonds); predicted using extracted constants with temperature behavior of the piezoelectric and dielectric constants (black line); and predicted using preliminary constants neglecting temperature behavior of the piezoelectric and dielectric constants (light gray dashed line).

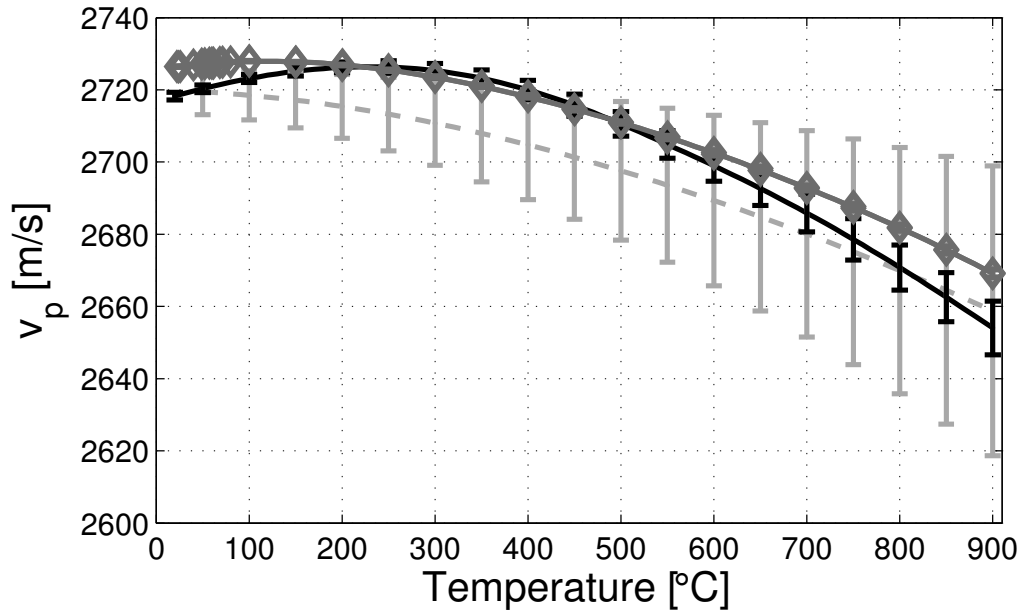


(a)

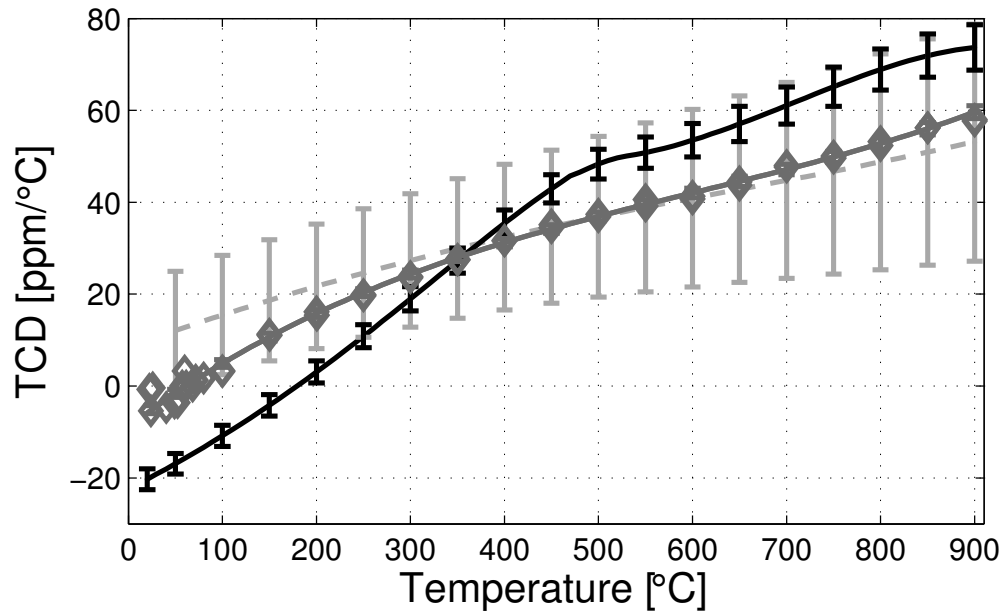


(b)

Figure 4.10. Comparison of measured and predicted v_p and TCD for LGT SAW orientation (90° , 23° , 77°). (a) v_p , (b) TCD. Measured SAW data (dark gray, diamonds); predicted using extracted constants with temperature behavior of the piezoelectric and dielectric constants (black line); and predicted using preliminary constants neglecting temperature behavior of the piezoelectric and dielectric constants (light gray dashed line).

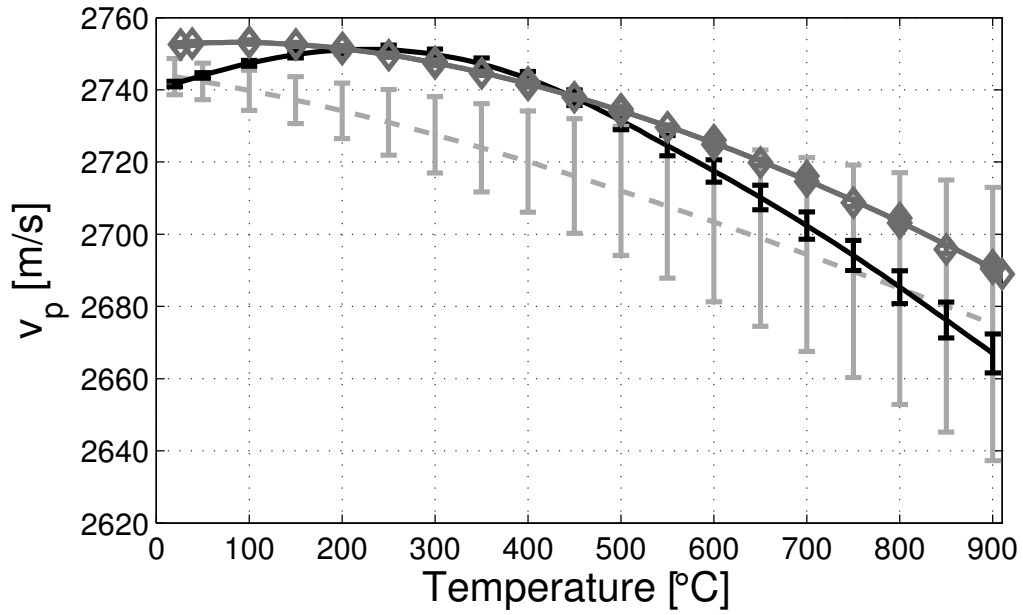


(a)

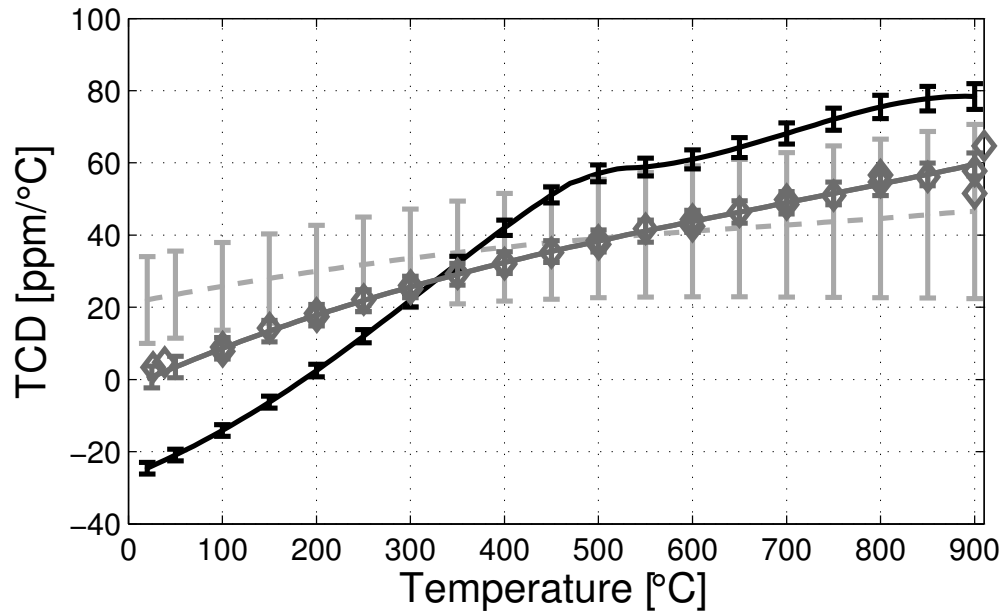


(b)

Figure 4.11. Comparison of measured and predicted v_p and TCD for LGT SAW orientation (90° , 23° , 119°). (a) v_p , (b) TCD. Measured SAW data (dark gray, diamonds); predicted using extracted constants with temperature behavior of the piezoelectric and dielectric constants (black line); and predicted using preliminary constants neglecting temperature behavior of the piezoelectric and dielectric constants (light gray dashed line).



(a)



(b)

Figure 4.12. Comparison of measured and predicted v_p and TCD for LGT SAW orientation (90° , 23° , 123°). (a) v_p , (b) TCD. Measured SAW data (dark gray, diamonds); predicted using extracted constants with temperature behavior of the piezoelectric and dielectric constants (black line); and predicted using preliminary constants neglecting temperature behavior of the piezoelectric and dielectric constants (light gray dashed line).

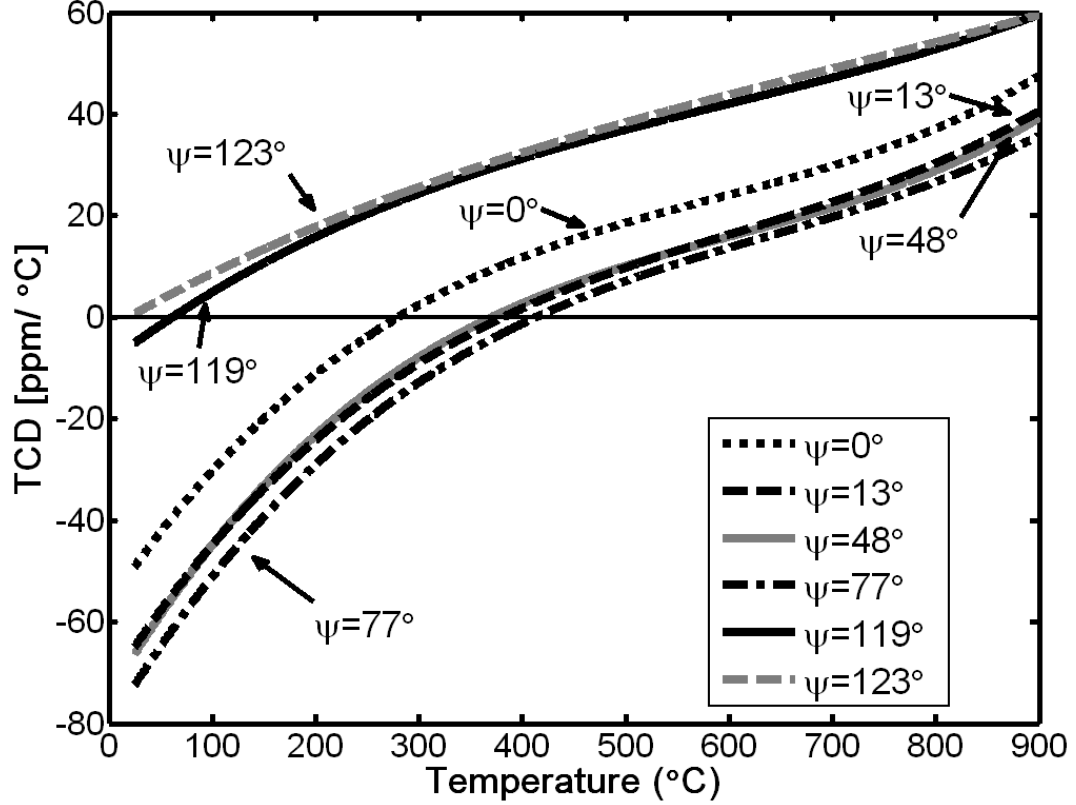


Figure 4.13. Measured TCD for LGT SAW orientations (90° , 23° , Ψ). $\Psi=0^\circ$, 13° , 48° , 77° , 119° , and 123° .

than the constants that ignored the temperature behavior. The RMS error with respect to the measured velocity is less for all six measured SAW orientations when the temperature dependence of the piezoelectric and dielectric constants are used. The predicted velocity for the set with the high-temperature piezoelectric constants have an RMSE for the temperature range 25°C to 900°C that averages 0.23% for the six measured orientations and is 3.5 times better than the average RMSE of 0.82% for the constants without the piezoelectric temperature behavior. Similarly, the final constants predict $\Delta f/f_0$ and TCD with an average RSME 58% and 14% lower than the constants without the piezoelectric temperature behavior. However, for the orientations $(90^\circ, 23^\circ, 119^\circ)$ and $(90^\circ, 23^\circ, 123^\circ)$ the final constants, which including the temperature behavior of the piezoelectric and dielectric constants, did not predict the TCD as accurately as the previous constants without the temperature dependence.

Ψ	Calculation	v_p (%)		$\Delta f/f_0$ (Unitless)		TCD (ppm °C ⁻¹)	
	Constants	Max ^a	RSME ^b	Max	RSME	Max	RSME
0°	HT piezo ^c	0.77%	0.31%	0.0065	0.0025	20.7	13.5
	No HT piezo ^d	1.34%	0.79%	0.0114	0.0062	27.1	14.1
13°	HT piezo	0.26%	0.09%	0.0034	0.0014	18.8	6.7
	No HT piezo	1.37%	0.83%	0.0102	0.0051	21.8	13.1
48°	HT piezo	0.45%	0.22%	0.0031	0.0012	19.1	7.5
	No HT piezo	1.74%	1.05%	0.0122	0.0058	27.6	16.3
77°	HT piezo	0.33%	0.16%	0.0032	0.0015	23.7	7.4
	No HT piezo	1.80%	1.10%	0.0133	0.0066	28.6	16.8
119°	HT piezo	0.57%	0.23%	0.0037	0.0023	16.2	12.4
	No HT piezo	0.49%	0.45%	0.0024	0.0020	13.7	5.0
123°	HT piezo	0.87%	0.37%	0.0048	0.0031	24.7	17.6
	No HT piezo	0.81%	0.70%	0.0047	0.0037	21.9	10.1
Max	HT piezo	0.87%	0.37%	0.0065	0.0031	24.7	17.6
all Ψ	No HT piezo	1.80%	1.10%	0.0133	0.0066	28.6	16.8
Average	HT piezo	0.54%	0.23%	0.0041	0.0020	20.5	10.8
all Ψ	No HT piezo	1.26%	0.82%	0.0090	0.0049	23.4	12.6

^aMaximum error is largest disagreement over the temperature range

^bRMSE is the root-mean-square error of the entire temperature range

^cHT piezo indicates data set using temperature behavior of piezoelectric and dielectric constants

^dNo HT piezo indicates data set that ignored temperature behavior of the piezoelectric and dielectric constants

Table 4.1. Disagreement between predicted and measured LGT SAW properties for plane (90°, 23°, Ψ) from 25 °C to 900 °C

The constants including the piezoelectric constants predict v_p for (90°, 23°, 119°) and (90°, 23°, 123°) that had a larger curvature than the measured v_p and have the best agreement in the temperature range between 150 °C and 500 °C. The SAW velocities along (90°, 23°, 119°) and (90°, 23°, 123°) are 3 to 50 times less dependent on c_{14} and about 2 time more dependent on c_{11} and c_{13} as the other 4 measured modes, based on the partial derivatives of v_p [237]. This might indicate that the temperature coefficients of the c_{11} and c_{13} constants are not as accurate as those for the other elastic constants

The turnover temperature, where $\text{TCD}=0$, of the tested SAW orientations have been predicted and measured for the orientations in which they exist in the temperature range 25 °C to 900 °C and are given in Table 4.2. The orientations (90°, 23°, 119°) and (90°, 23°, 123°) have low turnover temperature, below 100 °C, and neither of the sets of high-temperature LGT constants could accurately predict their turnover temperature. However, the predictions are better for the four orientations with turnover temperatures above 100 °C ($\Psi=0^\circ$, 13°, 48°, and 77°). The final LGT constants with the piezoelectric and dielectric temperature behavior predicted these four turnover temperatures within an average of 18 °C or 5 % of the turnover, which is a 62.5 % improvement over the predictions made using the constants ignoring the temperature behavior of the piezoelectric and dielectric constants.

4.5 Conclusions

The accuracy of the extracted set of high-temperature (up to 900 °C) LGT acoustic wave elastic, piezoelectric, and dielectric constants was verified by comparing calculated and measured SAW device propagation properties at high temperature. For the 6 tested orientations the measured and predicted SAW v_p agree with an average RMS error of 0.2 % of the measured v_p for the temperature range of 25 °C to 900 °C and are within 0.9 % in the worst case. The calculated TCD has an average RMS error of 10.8 ppm °C⁻¹ from the measured value for the tested orientations over the entire investigation temperature range. Additionally, the new set of constants that considered the temperature variations of the permittivity and piezoelectric constants resulted in the reduction of the average RMSE discrepancies between predicted and measured SAW v_p by 72 %, TCD by 14 %, and the turnover temperature by 63 %. The reported results verify the accuracy of the high-temperature LGT AW constants

Ψ (°)	Measured (°C)	Calculated, HT Piezo ^a Error from Meas.			Calculated, No HT Piezo ^b Error from Meas.		
		(°C)	(°C)	(%)	(°C)	(°C)	(%)
0°	280	215	-65	-30.2%	311	31	10.0%
13°	382	350	-32	-9.1%	390	8	2.1%
48°	370	332	-38	-11.4%	391	21	5.4%
77°	413	356	-57	-16.0%	425	12	2.8%
119°	62	- -	- -	- -	179	117	65.4%
123°	- - ^c	- -	- -	- -	186	- -	- -
Average of $\Psi =$ 0°, 13°, 48°, 77°		-48 -16.7%			18 5.1%		

^aNo HT piezo indicates data set that ignored temperature behavior of the piezoelectric and dielectric constants

^bHT piezo indicates data set using temperature behavior of piezoelectric and dielectric constants

^cDashed Lines indicate that the turnover temperature was either not measured or calculated in the temperature range

Table 4.2. Disagreement between predicted and measured LGT SAW turnover temperatures for plane (90°, 23°, Ψ)

by comparison with SAW measured properties as well as the importance of including the dielectric and piezoelectric temperature behavior for accurate acoustic wave property predictions and device design at high temperatures.

Chapter 5

HIGH-TEMPERATURE SAW ORIENTATIONS ON LANGATATE

5.1 Introduction

The prediction, determination, and selection of LGT SAW orientations for high-temperature SAW devices is enabled by the measured and validated LGT AW constants discussed in the previous chapters. Langatate and langasite have been used as materials for high-temperature sensors but there has been very limited published on high-temperature LGT or LGS SAW orientations. Langasite SAW orientations were investigated up to 1000 °C in [267, 411] and up to 700 °C in [412], but the constants and temperature coefficients employed, taken from [413], were measured around at room temperature. Langatate bulk acoustic wave orientations have also been studied up to 400 °C [228, 414]. Several modern high-temperature frequency control and sensing applications require operation beyond 400 °C. For example, sensors are desired for high-temperature fuel cells, which operate in the 600 °C to 1000 °C range [10], and for gas turbine engines in the compressor, combustor, and exhaust engine sections, which can typically reach temperatures around 450 °C to 750 °C, 900 °C to 1500 °C, and 650 °C, respectively [9, 10].

The major reason for that lack of high-temperature orientation data for LGT is the absence of elastic constants and temperature coefficients measured at high temperature, which could then provide meaningful orientation searches. With recent publications of high-temperature LGT acoustic wave constants and temperature coefficients reported in this work and in [148, 330, 331, 334], this deficiency has been overcome, and meaningful high-temperature LGT orientation searches up to 900 °C can be performed.

The prediction of high-temperature SAW propagation properties can be used to characterize the temperature sensitivity of specific orientations and to identify

temperature-compensated orientations. The LGT SAW propagation properties are analyzed in this chapter at high temperature with the goal to identify potential orientations for high-temperature operation.

The LGT SAW propagation properties searched for potential high-temperature orientations for three different conditions: (i) operation at a specific temperature; (ii) wide range of temperature operation, i.e. 400 °C to 800 °C; and (iii) operation of several orientations in the same plane (variation of the third Euler angle, Ψ).

For the case (i), SAW orientations were searched for zero, low, or high TCD at a specific temperature in between 400 °C and 900 °C. Orientations with zero or low TCD could be using in SAW devices that operate around a particular temperature and require relatively low sensitivity to temperature. Alternatively, orientations with larger TCD could be used as temperature sensors.

There is also a need for SAW devices with a broader operation range, which are addressed in case (ii) of the LGT orientation search that investigates the changes in the SAW frequency response from 400 °C to 800 °C to identify orientations. The temperature range of 400 °C to 800 °C was selected for the implementation of SAW sensors and frequency control devices in applications such as turbine engines and fuel cells.

In the case (iii), SAW cuts are investigated for multiple high-temperature orientations belonging to case (i) or (ii) that are in the same plane so that they can be fabricated on the same crystal wafer. In particular, SAW devices fabricated on the same wafer along different orientations (variation of the third Euler angle, Ψ), with different frequency dependencies on temperature, can be used in sensor applications where differential measurements are used to reduce correlated errors such as the effect of frequency offset and sensor drift [27, 415, 416].

5.2 High-Temperature SAW Properties Calculation

The LGT SAW calculations up to 900 °C were performed by employing the determined LGT elastic, piezoelectric, and constant-strain dielectric constants from Tables 3.4 and 2.1, respectively. The LGT density and thermal expansion measured up to 1200 °C [148, 271] were also utilized.

The SAW phase velocity, TCD, coupling, and operation frequency are computed using the matrix method, as discussed in Section 4.2. The calculations are repeated at numerous orientations and are swept across three regions of Euler angles: Region A = (0°, Θ , Ψ), Region B = (90°, Θ , Ψ), and Region C = (Φ , 90°, Ψ), in which the two variable Euler angles are swept. The angle ranges for the three regions are (0°, 0° → 180°, 0° → 90°), (90°, 0° → 90°, 0° → 180°), and (0° → 30°, 90°, 0° → 180°), respectively, and were selected based on crystal symmetry to avoid redundant orientations [237]. These sweeps were selected because they represent cut planes with surface normals in the planes defined by the main crystalline axis Y-Z, X-Z, and X-Y, as discussed in Chapter 4.

The LGT SAW velocity and TCD were predicted over the Regions A, B, and C at 400 °C, 500 °C, 600 °C, 700 °C, 800 °C, and 900 °C. These were used to identify SAW orientations that: (i) have zero, low, or high TCD, (ii) have either low or high frequency change from 400 °C to 800 °C, or (iii) exist on a single SAW cut planes with other such orientations as (i) and (ii).

In particular, for case (ii) the SAW frequency change $\Delta f/f_{400} = (f_{800^\circ\text{C}} - f_{400^\circ\text{C}})/f_{400^\circ\text{C}}$ was calculated. This metric was selected because it is easily calculated for each of the orientations in the three searched regions and is used to identify regions with either low or high temperature dependence. The $\Delta f/f_{400}$ calculation does not include the increased frequency variation for orientations with turnover temperatures between 400 °C and 800 °C. However, for LGT this does not lead to a significant deviation because only a few orientations have turnover temperatures

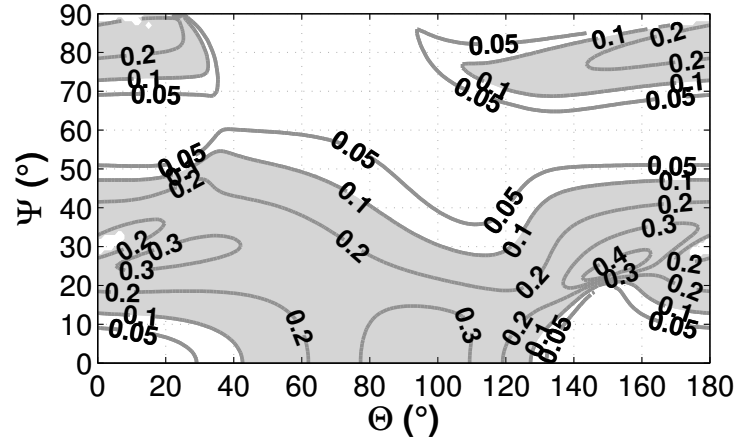
above 400 °C, which will be presented in Section 5.3.2. The end user of the selected orientations should simulate the SAW propagation properties along the orientation for the temperatures of interest, as was performed in Chapter 4 for the orientations in the LGT plane (90°, 23°, Ψ).

The SAW electromechanical coupling (K^2) was calculated at room temperature and every 100 °C up to 900 °C for Regions A, B, and C in order to select piezoelectrically excitable orientations. Only orientations with values of $K^2 \geq 0.1\%$ were considered for use at high temperature, since LGT SAW delay lines fabricated on orientations with $K^2 \geq 0.1\%$ at 25 °C were shown to operate up to at least 900 °C [329, 330]. Other SAW parameters, such as diffraction, power flow angle, and propagation losses, are not analyzed in this work because they are assumed to not prevent the utilization of any particular SAW device only possibly degrade the performance.

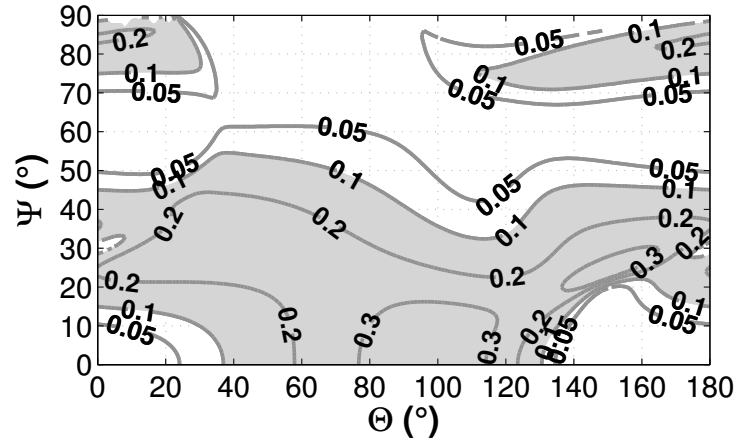
5.3 High-Temperature LGT SAW Properties and Orientations

5.3.1 LGT SAW Electromechanical Coupling

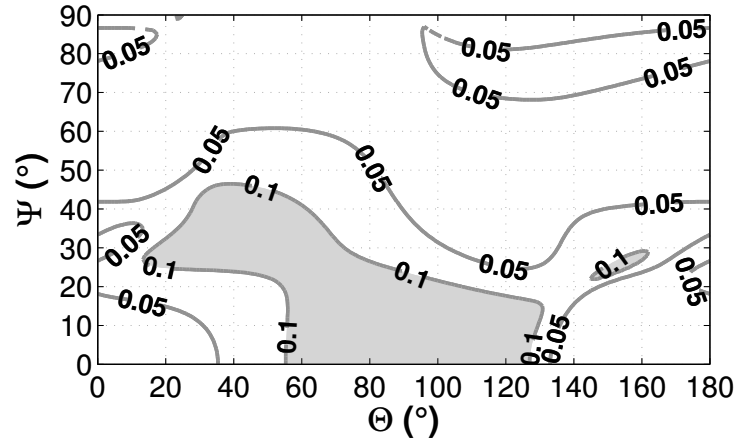
The SAW electromechanical coupling coefficients, K^2 , are calculated using the extracted LGT constants at high temperature and are plotted in Figs. 5.1, 5.2, and 5.3 for Regions A, B, and C, respectively, and at representative temperatures of 25 °C, 500 °C, and 800 °C. Orientations with $K^2 \geq 0.1\%$ are shaded in gray for easier identification. The K^2 contour plots at room temperature agree well with shape of the contour plots calculated with LGT constants extracted up to 120 °C in [237, Figs. 3.1a, C.1, C.3]. The maximum coupling values for each of for Regions A, B, and C was predicted in this work to be 0.4 % for each region, which is smaller than the values of 0.7 %, 0.7 %, and 0.6 % calculated in [237].



(a)

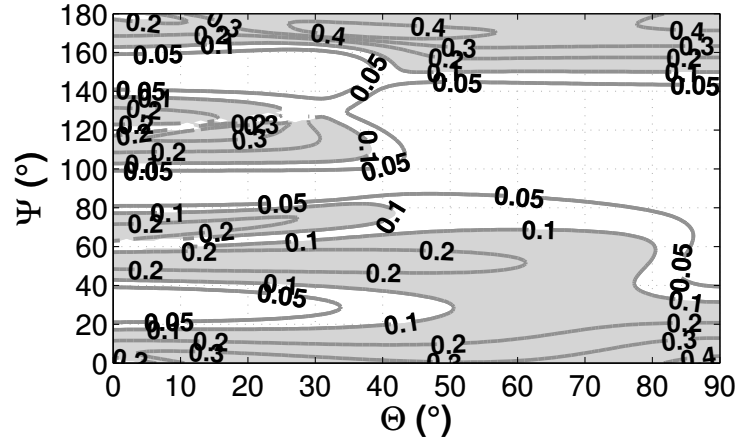


(b)

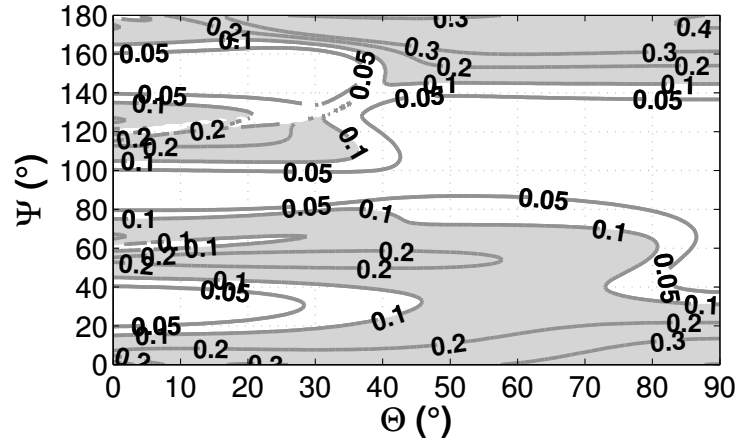


(c)

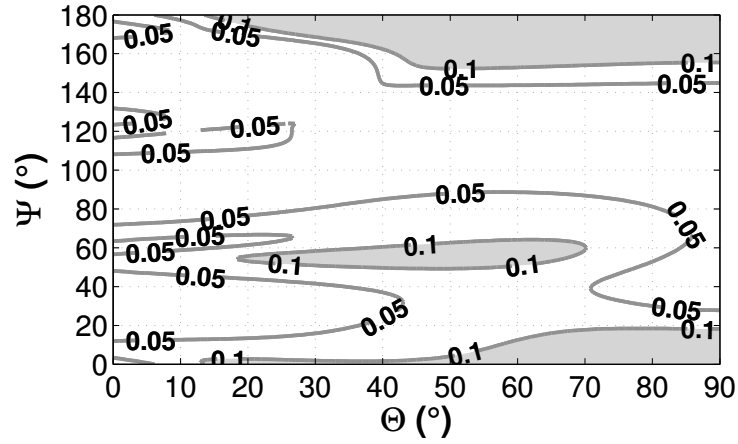
Figure 5.1. Contour plots of predicted LGT SAW K^2 for Region A, Euler angles (0° , Θ , Ψ). Given in %, at (a) 25°C , (b) 500°C , and (c) 800°C . Orientations with $K^2 \geq 0.1\%$ are shaded in gray.



(a)

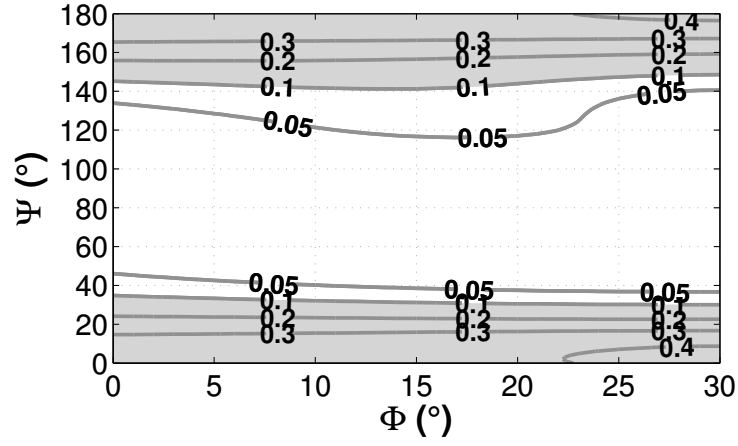


(b)

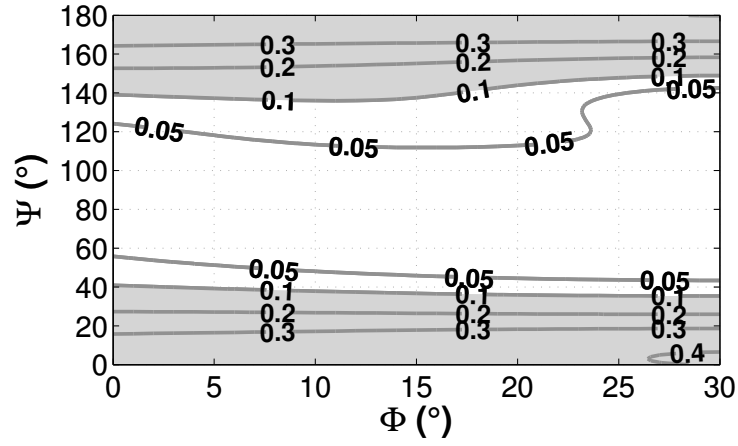


(c)

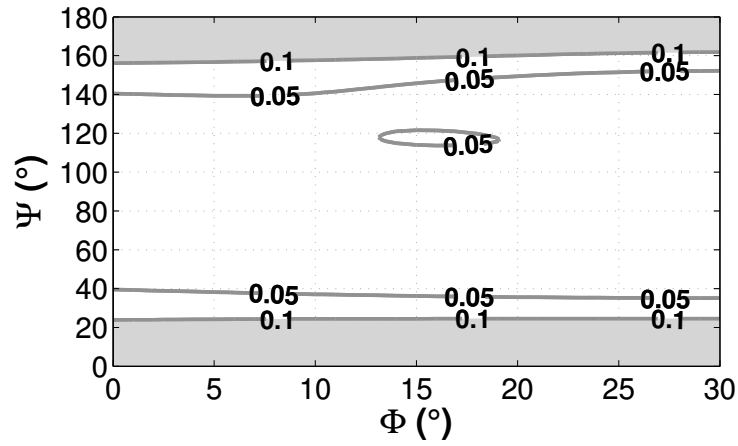
Figure 5.2. Contour plots of predicted LGT SAW K^2 for Region B, Euler angles (90° , Θ , Ψ). Given in %, at (a) 25°C , (b) 500°C , and (c) 800°C . Orientations with $K^2 \geq 0.1\%$ are shaded in gray.



(a)



(b)



(c)

Figure 5.3. Contour plots of predicted LGT SAW K^2 for Region C, Euler angles (Φ , 90° , Ψ). Given in %, at (a) 25°C , (b) 500°C , and (c) 800°C . Orientations with $K^2 \geq 0.1\%$ are shaded in gray.

5.3.2 LGT SAW TCD at High Temperature

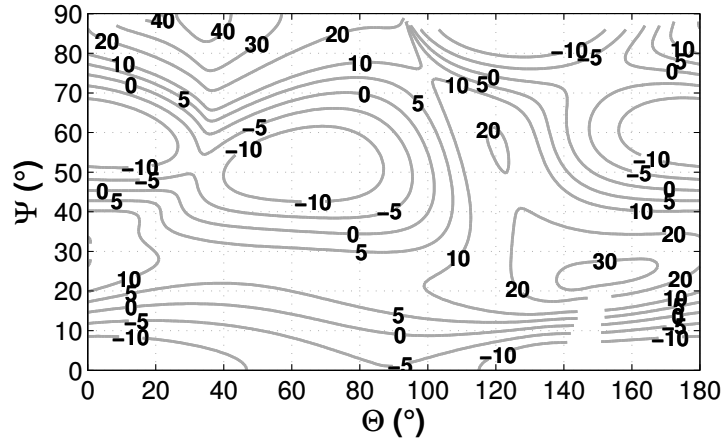
The LGT SAW TCD for Region A, the Euler angles $(0^\circ, \Theta, \Psi)$, are calculated from 400°C to 900°C in 100°C steps and are displayed as contour plots in Fig. 5.4. The LGT SAW TCD calculated for the Region B, $(90^\circ, \Theta, \Psi)$, and Region C, $(\Phi, 90^\circ, \Psi)$, are shown in Fig. 5.5 and Fig. 5.6, respectively, for the same temperature range and step.

The multiple LGT SAW orientations were identified to have close to zero or zero TCD at 400°C , given in Table 5.1, and 500°C , given in Table 5.2, and to have coupling $K^2 \geq 0.1\%$. For the three regions swept, A, B, and C, orientations with TCD=0 were found at 400°C and 500°C but none were found above 600°C . However, multiple orientations have negative TCD at 500°C indicating the existence of turn-over temperatures between 500°C and 600°C , which were the highest turnover temperatures identified for LGT orientations. In particular, as shown in Fig. 5.4, $\text{TCD} \approx -5 \text{ ppm } ^\circ\text{C}^{-1}$ at 500°C and $\text{TCD} \approx 5 \text{ ppm } ^\circ\text{C}^{-1}$ at 600°C are observed for LGT SAW orientations with Euler angles $(0^\circ, 130^\circ \rightarrow 130^\circ, 0^\circ \rightarrow 4^\circ)$ with $K^2 \approx 0.1\%$ (Fig. 5.1). Additionally, LGT orientations $(90^\circ, 48^\circ \rightarrow 68^\circ, 66^\circ \rightarrow 75^\circ)$ has $\text{TCD} \approx -5 \text{ ppm } ^\circ\text{C}^{-1}$ at 500°C and $\text{TCD} \approx 5 \text{ ppm } ^\circ\text{C}^{-1}$ at 600°C with $0.05\% \leq K^2 \leq 0.2\%$ (Fig. 5.2).

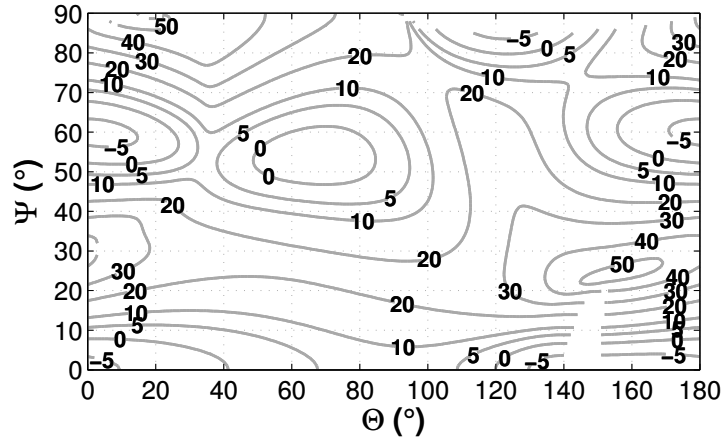
In contrast, LGT SAW orientations with the largest TCD at 500°C of the identified orientations are given in Table 5.3 and have TCD as high as $50 \text{ ppm } ^\circ\text{C}^{-1}$. At 900°C all the LGT orientations studied in this work are predicted to have TCD between 40 and $70 \text{ ppm } ^\circ\text{C}^{-1}$.

5.3.3 LGT SAW Frequency Change at High Temperature

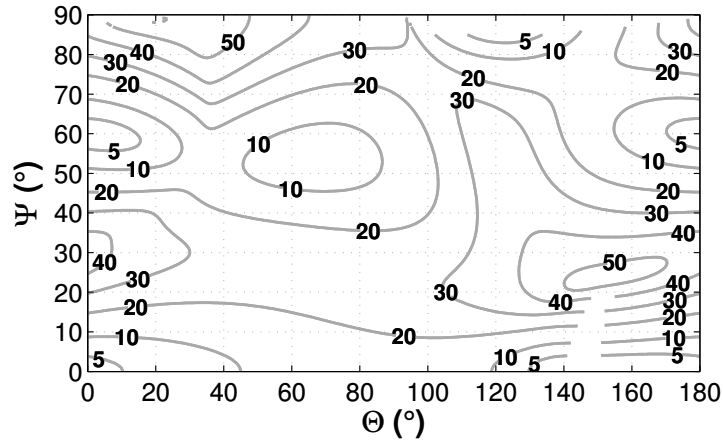
The LGT SAW behavior for a large temperature span was qualitatively estimated by calculating the SAW frequency change from 400°C to 800°C , namely $\Delta f/f_{400} = (f_{800^\circ\text{C}} - f_{400^\circ\text{C}})/f_{400^\circ\text{C}}$, which is shown in Fig. 5.7 for the Regions A,



(a)

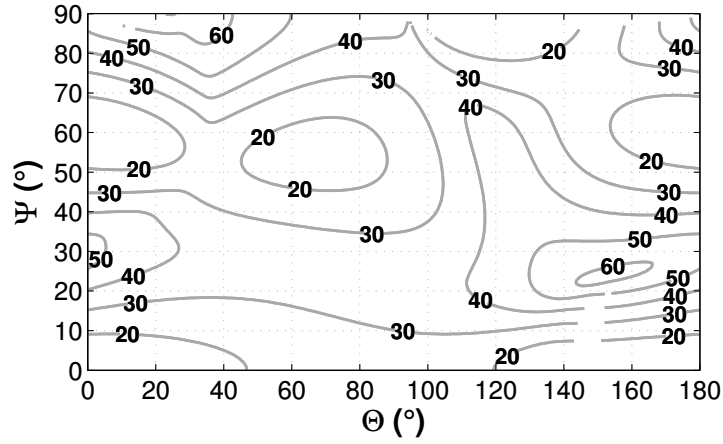


(b)

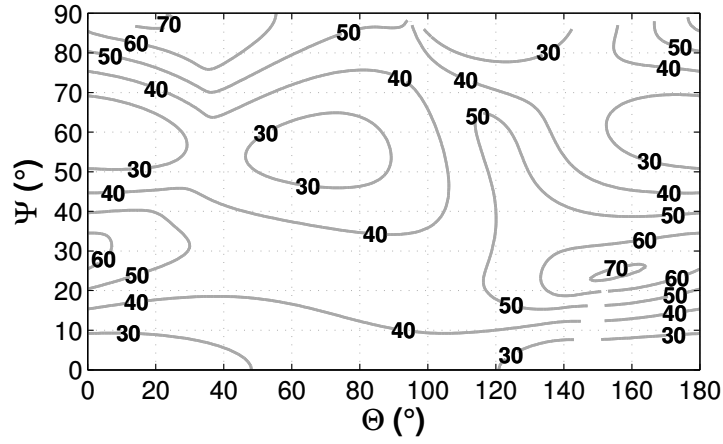


(c)

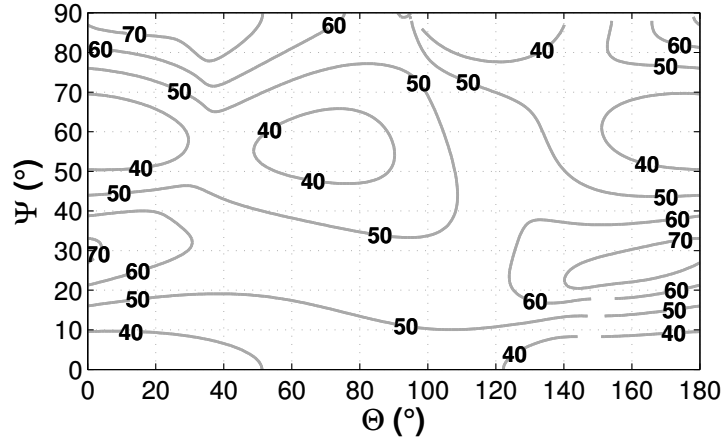
Figure 5.4. Contour plots of predicted LGT SAW TCD for Region A, Euler angles (0° , Θ , Ψ) in $\text{ppm } ^\circ\text{C}^{-1}$. (a) at 400°C , (b) at 500°C , (c) at 600°C , (d) at 700°C , (e) at 800°C , (f) at 900°C



(d)

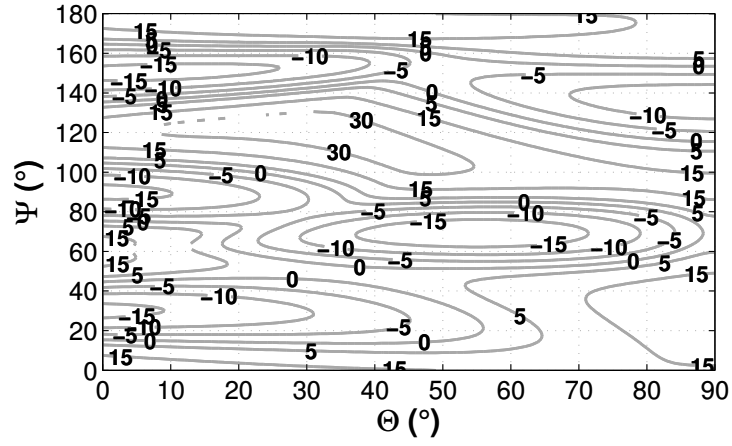


(e)

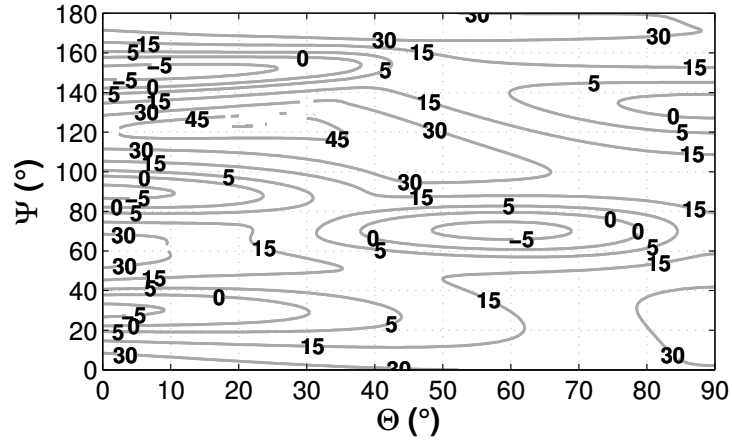


(f)

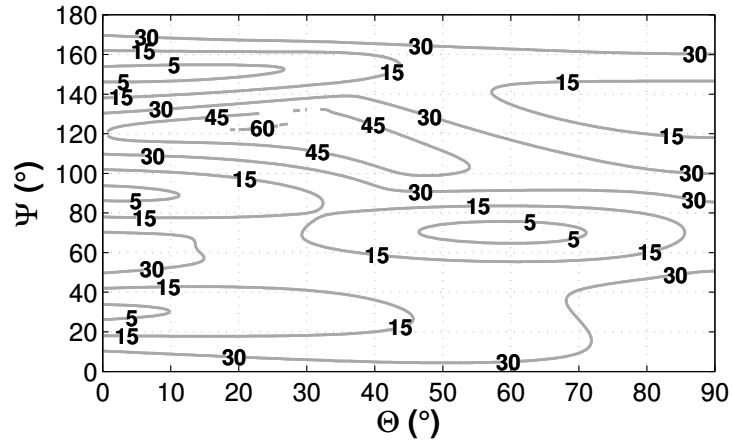
Figure 5.4. (Cont.) Contour plots of predicted LGT SAW TCD for Region A, Euler angles (0° , Θ , Ψ) in $\text{ppm } ^\circ\text{C}^{-1}$. (a) at 400°C , (b) at 500°C , (c) at 600°C , (d) at 700°C , (e) at 800°C , (f) at 900°C



(a)

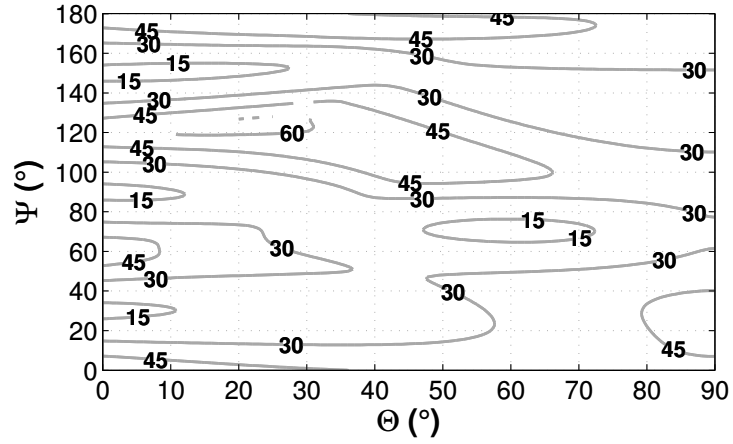


(b)

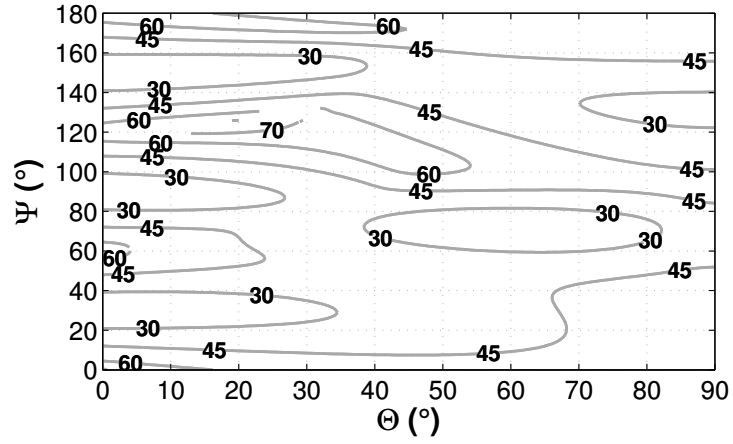


(c)

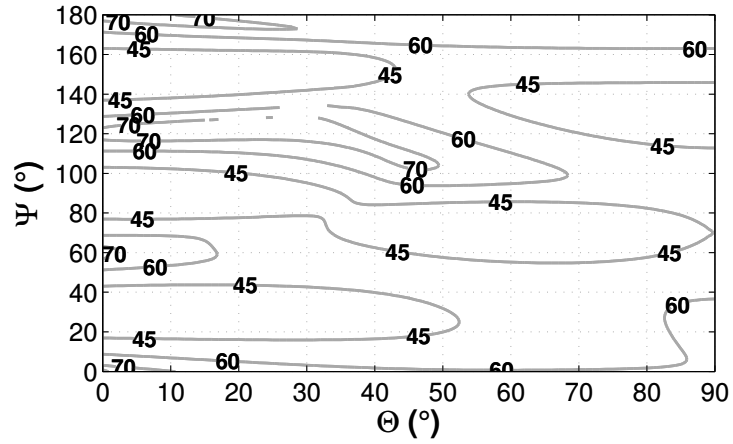
Figure 5.5. Contour plots of predicted LGT SAW TCD for Region B, Euler angles $(90^\circ, \Theta, \Psi)$ in $\text{ppm}^\circ\text{C}^{-1}$. (a) at 400°C , (b) at 500°C , (c) at 600°C , (d) at 700°C , (e) at 800°C , (f) at 900°C



(d)

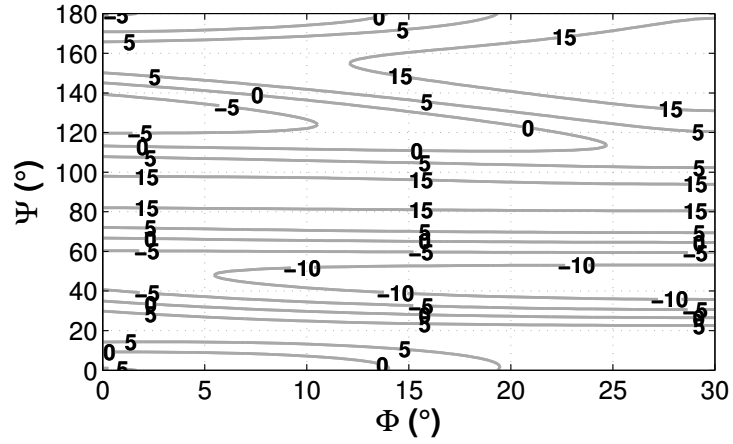


(e)

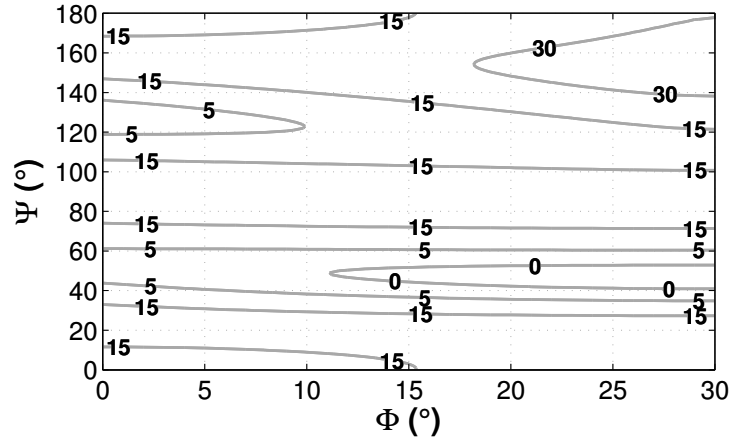


(f)

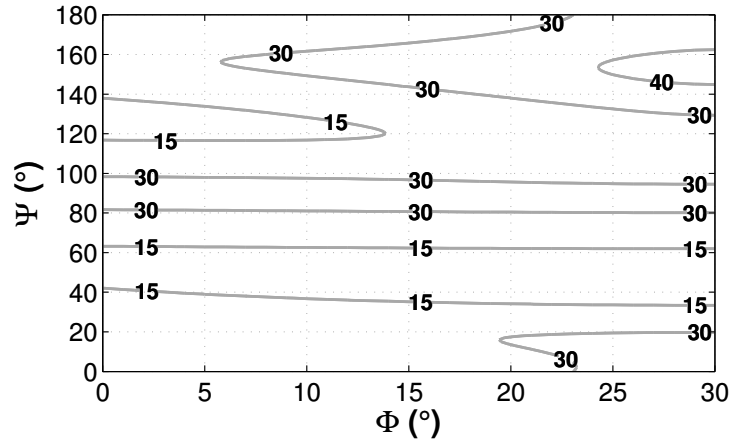
Figure 5.5. (Cont.) Contour plots of predicted LGT SAW TCD for Region B, Euler angles (90° , Θ , Ψ) in $\text{ppm}^\circ\text{C}^{-1}$. (a) at 400°C , (b) at 500°C , (c) at 600°C , (d) at 700°C , (e) at 800°C , (f) at 900°C



(a)

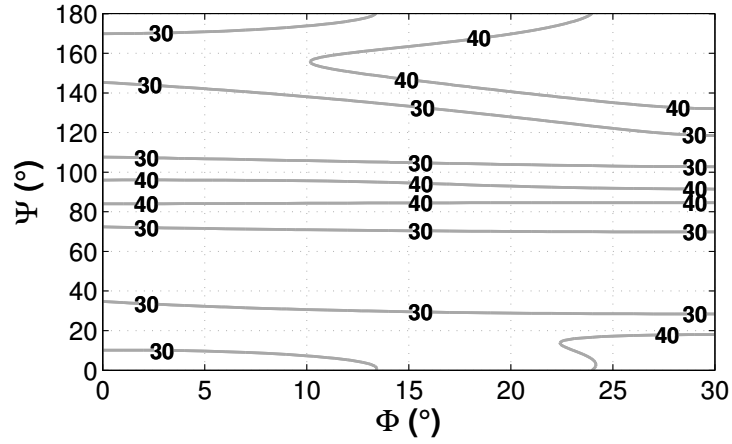


(b)

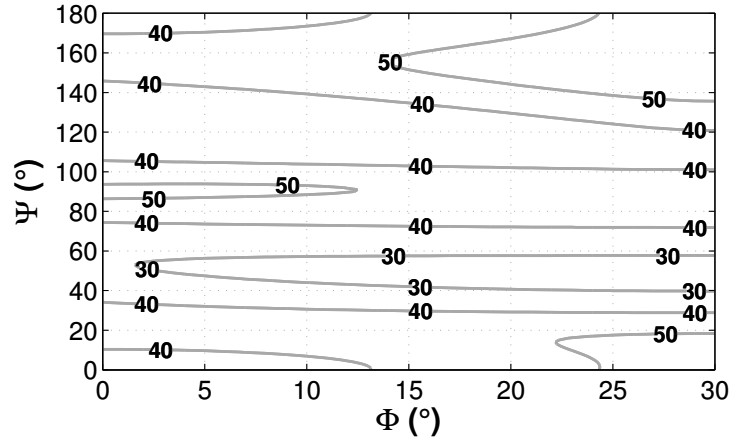


(c)

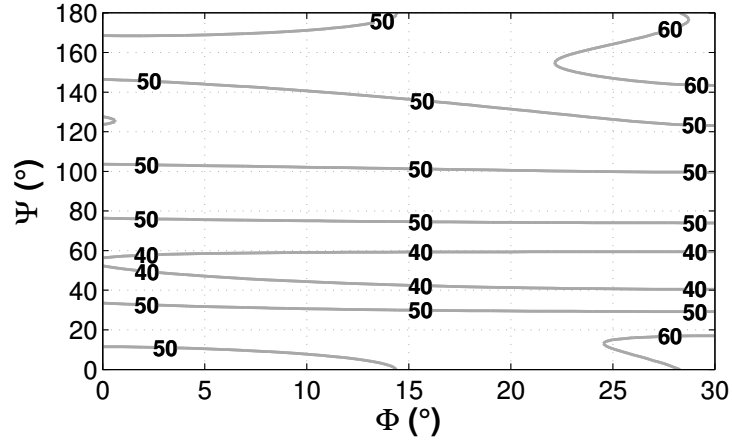
Figure 5.6. Contour plots of predicted LGT SAW TCD for Region C, Euler angles $(\Phi, 90^\circ, \Psi)$ in $\text{ppm}^\circ\text{C}^{-1}$. (a) at 400 °C, (b) at 500 °C, (c) at 600 °C, (d) at 700 °C, (e) at 800 °C, (f) at 900 °C



(d)



(e)



(f)

Figure 5.6. (Cont.) Contour plots of predicted LGT SAW TCD for Region C, Euler angles (Φ , 90° , Ψ) in $\text{ppm } ^\circ\text{C}^{-1}$. (a) at 400°C , (b) at 500°C , (c) at 600°C , (d) at 700°C , (e) at 800°C , (f) at 900°C

Euler Angle Sweep	Orientation Euler Angles (\circ)	TCD at 400 °C (ppm °C ⁻¹)	K^2 at 400 °C (%)
(0°, Θ , Ψ)	(0°, 0° → 130°, 0° → 22°)	-15 to 5	0.1 to 0.5
Region A	(0°, 166° → 180°, 13° → 17°)	0 to 5	0.1 to 0.2
	(0°, 0° → 105°, 30° → 55°)	-15 to 5	0.1 to 0.4
	(0°, 144° → 180°, 43° → 48°)	0 to 5	0.1 to 0.2
	(0°, 0° → 9°, 73° → 75°)	≈ 0	≈ 0.1
	(0°, 106° → 180°, 70° → 87°)	-10 to 10	0.1 to 0.3
(90°, Θ , Ψ)	(90°, 0° → 56°, 14° → 47°)	-5 to 0	≤ 0.2
Region B	(90°, 0° → 18°, 74° → 76°)	≈ 0	0.1 to 0.2
	(90°, 18° → 82°, 51° → 81°)	-15 to 0	0.1 to 0.3
	(90°, 0° → 14°, 103° → 105°)	≈ 0	≈ 0.1
	(90°, 0° → 7°, 135° → 137°)	≈ 0	≈ 0.1
	(90°, 35° → 90°, 148° → 165°)	-5 to 5	0.1 to 0.4
	(90°, 0° → 10°, 164° → 165°)	≈ 0	≈ 0.1
(Φ , 90°, Ψ)	(0° → 18°, 90°, 0° → 14°)	-5 to 5	0.3 to 05
Region C	(0° → 30°, 90°, 23° → 40°)	-10 to 5	≤ 0.3
	(0° → 14°, 90°, 132° → 150°)	-5 to 5	≤ 0.2
	(0° → 18°, 90°, 166° → 180°)	-5 to 5	0.3 to 05

Table 5.1. LGT SAW orientations with low or zero TCD at 400 °C

B, and C. Both low and high frequency variation regions have been identified and are discussed below. The orientations are selected to have $K^2 \geq 0.1\%$ at 400 °C.

As can be seen from Figs. 5.7a and 5.7b, the SAW orientations with the lowest identified $\Delta f/f_{400}$ and $K^2 \geq 0.1\%$ were (0°, 130° → 180°, 0° → 4°), with $K^2 \approx 0.1\%$, and (90°, 46° → 71°, 65° → 76°), with $K^2 \leq 0.2\%$. Orientations in the range (0°, 54° → 79°, 59° → 49°) also have low frequency change, namely $\Delta f/f_{400} = -0.3\%$, and have $K^2 \leq 0.2\%$. The lowest $\Delta f/f_{400}$ found in Region C, Fig. 5.7c, is -0.4% was in (7° → 30°, 90°, 39° → 55°) and had $K^2 \approx 0.1\%$.

Euler Angle Sweep	Orientation Euler Angles (\circ)	TCD at 500 °C (ppm °C ⁻¹)	K^2 at 500 °C (%)
(0°, Θ , Ψ)	(0°, 27° → 68°, 0° → 11°)	0 to 5	0.1 to 0.3
Region A	(0°, 108° → 130°, 0° → 9°)	-5 to 5	0.1 to 0.4
	(0°, 38° → 87°, 42° → 55°)	0 to 5	0.1 to 0.2
	(0°, 119° → 148°, 76° → 84°)	0 to 5	0.1 to 0.2
(90°, Θ , Ψ)	(90°, 31° → 81°, 57° → 79°)	-5 to 5	0.1 to 0.2
Region B	(90°, 72° → 90°, 144° → 146°)	≈ 5	≈ 0.1
	(90°, 38° → 43°, 150° → 159°)	≈ 5	≈ 0.1
	(90°, 34° → 44°, 20° → 28°)	≈ 5	≈ 0.1
(Φ , 90°, Ψ)	(16° → 30°, 90°, 35° → 37°)	≈ 5	≈ 0.1
Region C			

Table 5.2. LGT SAW orientations with low or zero TCD at 500 °C

Euler Angle Sweep	Orientation Euler Angles (\circ)	TCD at 500 °C (ppm °C ⁻¹)	K^2 at 500 °C (%)
(0°, Θ , Ψ)	(0°, 145° → 170°, 21° → 28°)	50	≈ 0.3
Region A			
(90°, Θ , Ψ)	(90°, 8° → 28°, 118° → 128°)	50	0.1 to 0.3
Region B			
(Φ , 90°, Ψ)	(12° → 30°, 90°, 145° → 180°)	30	0.1 to 0.3
Region C			

Table 5.3. LGT SAW orientations with largest TCD at 500 °C

The SAW orientations (0°, 40° → 90°, 40° → 50°) and (90°, 25° → 80°, 55° → 65°) have relatively small frequency variations from 400 °C to 800 °C, as can be seen from Figs. 5.7a and 5.7b, namely $\Delta f/f_{400} \approx -0.8\%$ with $0.1\% \leq K^2 \leq 0.3\%$ (Figs. 5.1 and 5.2). From Fig. 5.7b, one can see that LGT SAW orientations in the range (90°, 55° → 75°, 55° → 80°) have the lowest temperature sensitivity from 400 °C to 800 °C, $\Delta f/f_{400} = -0.6\%$, with coupling coefficients values with $0.1\% \leq K^2 \leq 0.3\%$

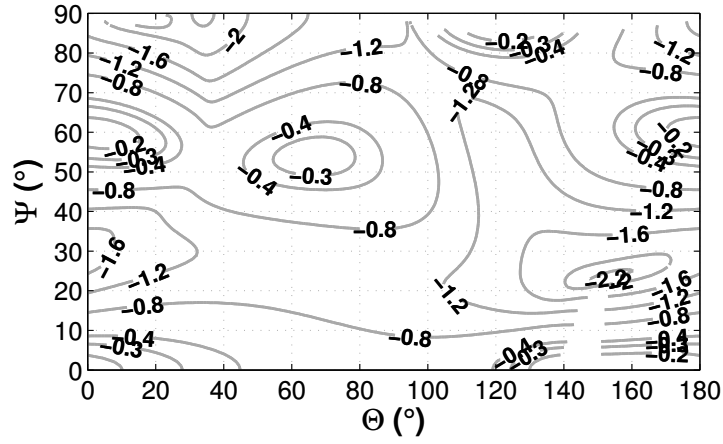
(Fig. 5.2). From Fig. 5.7c and Fig. 5.3, one can notice that the orientations in the range ($15^\circ \rightarrow 30^\circ$, 90° , $32^\circ \rightarrow 40^\circ$) have the lowest temperature sensitivity from 400°C to 800°C in Region C, but modest values of coupling coefficients, in the range $0.1\% \leq K^2 \leq 0.2\%$. The moderate frequency change for the orientations discussed in this paragraph for such a wide temperature range is partly due to the fact that most of these orientations have turnover temperatures between 400°C and 500°C , which would slightly increase the total frequency variation because of the brief increase in frequency until the turnover temperature is reached and the frequency decreases.

Conversely, other LGT orientations have larger temperature dependencies in the 400°C to 800°C span. The orientations (90° , $10^\circ \rightarrow 40^\circ$, $110^\circ \rightarrow 130^\circ$) have $\Delta f/f_{400}$ of -2% to -2.3% and coupling of $0.1\% \leq K^2 \leq 0.4\%$ (Fig. 5.1). Also, orientations in the ranges (0° , $5^\circ \rightarrow 30^\circ$, $82^\circ \rightarrow 90^\circ$) and (0° , $140^\circ \rightarrow 175^\circ$, $20^\circ \rightarrow 30^\circ$) have $\Delta f/f_{400}$ between -2% and -2.2% with $0.2\% \leq K^2 \leq 0.5\%$ (Fig. 5.1). These orientations have high TCD throughout the temperature range: $20 \text{ ppm } ^\circ\text{C}^{-1}$ to $40 \text{ ppm } ^\circ\text{C}^{-1}$ at 400°C and $60 \text{ ppm } ^\circ\text{C}^{-1}$ to $70 \text{ ppm } ^\circ\text{C}^{-1}$ at 800°C .

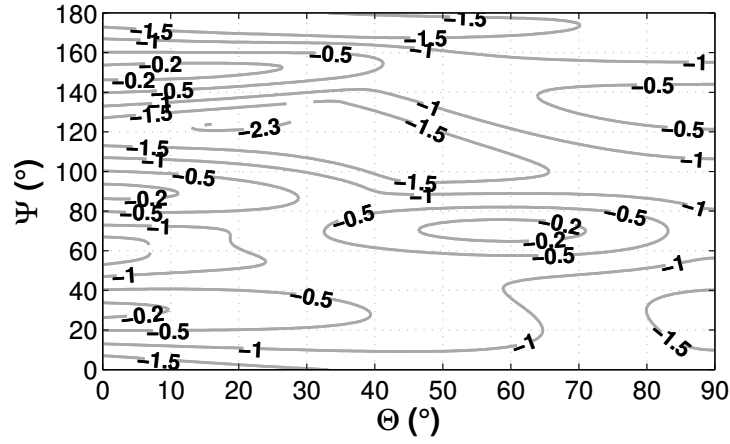
5.3.4 LGT SAW Planes for High-Temperature Sensor Suites

Multiple regions of LGT SAW planes have been identified as desirable for fabricating a suite of devices on the same wafer with $K^2 \geq 0.1\%$ and a variety of temperature sensitivities, useful for sensor applications, as discussed in Section 5.1. Analysis of Fig. 5.1 together with Fig. 5.7a reveals that LGT Region A planes in the range (0° , $120^\circ \rightarrow 150^\circ$, Ψ) contain SAW orientations with both relatively low and high temperature sensitivities, $\Delta f/f_{400}$ ranging from -0.3% to -1.6% in one plane and -0.8% to -2.2% in another, and K^2 ranging from 0.1% to 0.5% at 400°C .

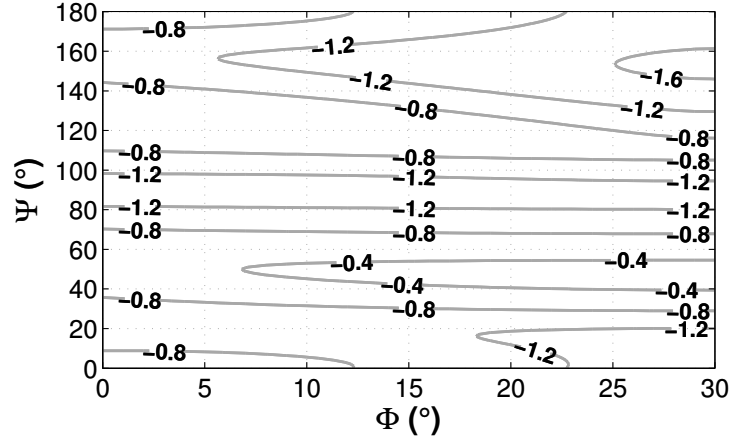
In Region B, LGT cuts in the range (90° , $20^\circ \rightarrow 30^\circ$, Ψ), Fig. 5.2, also have planes in which there are SAW orientations with small temperature sensitivity, $\Delta f/f_{400} = -0.5\%$, and others with large temperature sensitivity, $\Delta f/f_{400} = -2.3\%$, and K^2



(a)



(b)



(c)

Figure 5.7. Contour plots of predicted LGT SAW frequency change from 400 °C to 800 °C. $\Delta f/f_{400} = (f_{800^\circ\text{C}} - f_{400^\circ\text{C}})/f_{400^\circ\text{C}}$, in units %, for orientation sweeps (a) Region A, Euler angles (0° , Θ , Ψ), (b) Region B, Euler angles (90° , Θ , Ψ), and (c) Region C, Euler angles (Φ , 90° , Ψ).

varying between 0.1% and 0.4% (Fig. 5.2). Additionally, there are a number of cuts in this range that also have orientations with $\Delta f/f_{400} = -1.0\%$ widely spaced over the plane, with potential for multiple measurand sensor applications because the separate orientations have similar temperature dependencies but could have different sensitivity to pressure or strain.

5.3.5 Demonstration of LGT Differential SAW Sensors on a Single Wafer

The LGT SAW plane ($90^\circ, 23^\circ, \Psi$) that was selected for the SAW verification in Chapter 4 is within the range of planes identified for use as substrate for sensor suites. In fact, multiple SAW delay lines were fabricated on the same wafer, which enabled a demonstration of the simultaneous differential SAW sensors at high temperature.

In order to verify that the ($90^\circ, 23^\circ, \Psi$) plane can be used in the fabrication of a suite of SAW sensors, the differential response of a pair of SAW devices was measured as a function of temperature. Delay line SAW devices with orientations ($90^\circ, 23^\circ, 0^\circ$) and ($90^\circ, 23^\circ, 48^\circ$) were fabricated, Fig. 4.4, on the same LGT wafer with intersecting delay paths, discussed in Section 4.3.1, and were operated concurrently while the sensor was heated in a box furnace up to 900°C in 50°C intervals. The frequency difference $\Delta f_{\Psi=0^\circ, 48^\circ} = f_{\Psi=0^\circ} - f_{\Psi=48^\circ}$ was determined at each measured temperature.

The experimentally obtained temperature is plotted in Fig. 5.8 versus frequency difference ($\Delta f_{\Psi=0^\circ, 48^\circ}$) translation function for the sensor pair used. It was found that the relationship between $\Delta f_{\Psi=0^\circ, 48^\circ}$ and the measured temperature is approximately linear, with correlation coefficient $\rho = -0.9957$, in the region between 25°C and 900°C . A quadratic polynomial can be used to describe the frequency difference behavior with temperature to increase the accuracy relative to a linear curve, achieving a root-mean-square relative error of 7.15×10^{-2} with respect to the measured temperature. The temperature sensitivity of $\Delta f_{\Psi=0^\circ, 48^\circ}$ is $-706.1 \text{ Hz } ^\circ\text{C}^{-1}$ for the range

25 °C to 900 °C and the fractional sensitivity starts as $-172 \text{ ppm } ^\circ\text{C}^{-1}$ at 25 °C and becomes $-205 \text{ ppm } ^\circ\text{C}^{-1}$ at 900 °C. The frequency difference $\Delta f_{\Psi=0^\circ, 48^\circ}$ drops by a total of 16.0% from 25 °C to 900 °C and by 6.7% from 400 °C to 800 °C. The percent change in the differential response is 3 times that of the largest change $\Delta f/f_{400} = -2.3 \%$ predicted for any single LGT orientation identified in Section 5.3.3, demonstrating another benefit of the differential sensor pair, in addition to compensating for the common frequency drift or aging variation of both devices.

5.4 Conclusions

This chapter has investigated the high-temperature SAW phase velocity, frequency change, and TCD properties behavior of LGT up to 900 °C for three regions in space, namely, $(0^\circ, \Theta, \Psi)$, $(90^\circ, \Theta, \Psi)$, and $(\Phi, 90^\circ, \Psi)$. New LGT SAW orientations have been identified with zero TCD at 400 °C and 500 °C and with low TCD up to 900 °C, which have potential applications for frequency control, sensing, and signal processing. Alternatively, temperature-sensitive orientations of interest to temperature sensing have been identified.

Orientations have been identified for high-temperature sensing and frequency control applications with: (i) a narrow temperature range of operation; (ii) large temperature range of operation (400 °C to 800 °C); and (iii) multiple high-temperature applicable orientations in a same plane.

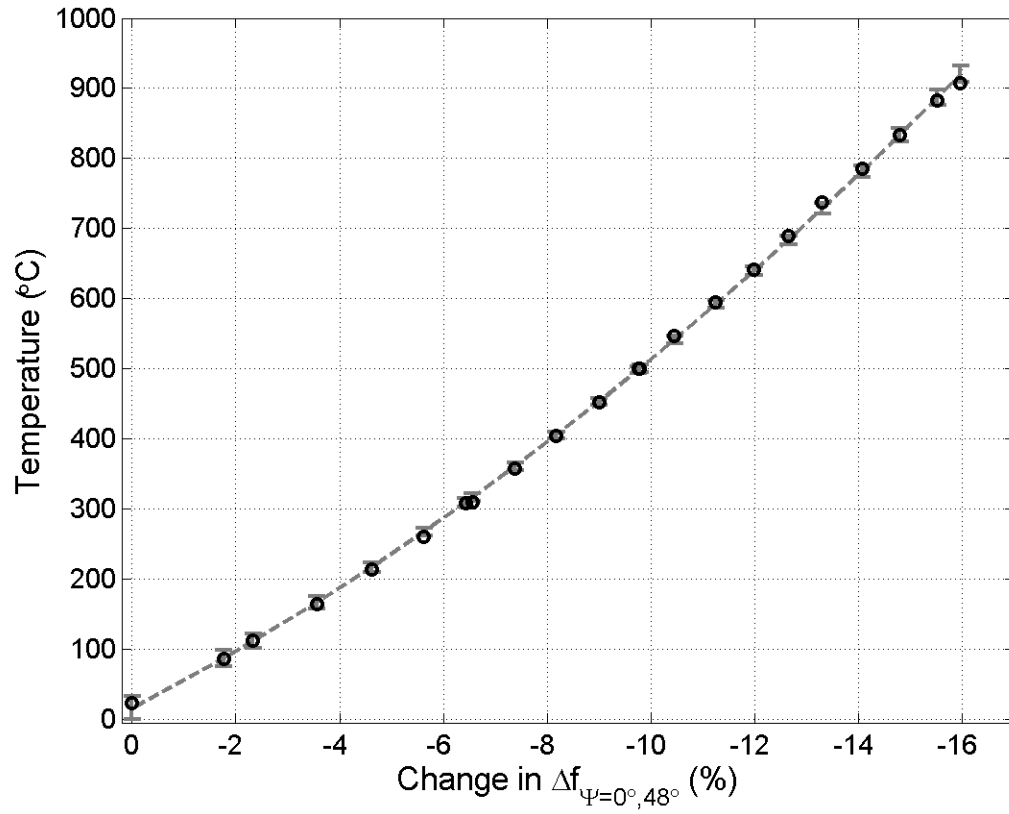


Figure 5.8. Measured differential frequency for LGT delay line sensor pair (90°, 23°, 0°) and (90°, 23°, 48°) up to 900 °C. Where $\Delta f_{\Psi=0^\circ, 48^\circ} = f_{\Psi=0^\circ} - f_{\Psi=48^\circ}$. Gray dashed line: quadratic fit of percent change in $\Delta f_{\Psi=0^\circ, 48^\circ}$, $(\Delta f_{\Psi=0^\circ, 48^\circ}(t) - \Delta f_{\Psi=0^\circ, 48^\circ}(25^\circ\text{C})) / \Delta f_{\Psi=0^\circ, 48^\circ}(25^\circ\text{C})$; black circle: measured temperature.

Chapter 6

HIGH-TEMPERATURE BAW ORIENTATIONS ON LANGATATE

6.1 Introduction

In addition to the high-temperature SAW orientations identified and discussed in the previous chapter, the extracted LGT acoustic constants up to 900 °C were used in this chapter to identify BAW orientations for high-temperature operation. Bulk acoustic wave devices that are temperature compensated at elevated temperatures could be employed in high-temperature applications, such as gas or chemical sensors and deposition rate monitors, and in frequency control devices for elevated temperature wireless systems in oil well and industrial settings, where further integration of sensors and wireless networks is desired to increase production efficiency and enable intelligent maintenance.

While LGS BAW orientations temperature compensated at 500 °C, 600 °C, and 700 °C have been reported using extracted LGS constants up to 900 °C [195, 417], no such study has been reported on LGT because of the absence of high-temperature constants. Langatate orientations were investigated in [144, 145] for temperature-compensated length extensional, flexural, and torsional cylinder resonators up to 250 °C but the study utilized constants extracted below 150 °C from [35, 239] for their predictions. Temperature-compensated thickness shear BAW orientations were similarly predicted in [414] using constants extracted below 150 °C [35]. Selected rotated Y-cut BAW orientations were fabricated using LGT crystals grown by Yu, et al. and experimentally identified turnover temperatures as high as 350 °C [228, 414].

In this chapter, langatate temperature-compensated BAW orientations were identified up to 550 °C from BAW predictions utilizing the extracted LGT elastic, piezoelectric, and dielectric constants up to 900 °C discussed in Chapters 2 and 3. Additionally, high-temperature density and thermal expansion constants from [148, 271]

were used. The BAW temperature coefficient of frequency (TCF) and piezoelectric coupling were calculated for selected orientations. A set of new LGT BAW orientations were found with turnover temperatures between 100 °C and 550 °C enabling their use in a variety of high-temperature applications. Both transversal and lateral field piezoelectric coupling of the identified orientations were investigated to determine the preferred cuts for high-temperature operation. Orientations were identified that have transverse-shear modes (TSM) with turnover temperatures as high as 550 °C.

6.2 Bulk Acoustic Wave Calculation Method

The identification of BAW orientations for high-temperature operation involved the calculation and analysis of the phase velocity, thermal expansion, temperature coefficient of frequency (TCF), and thickness-excitation piezoelectric coupling (k_{TE}) using the process described in [418, 419]. Additionally, the lateral-excitation piezoelectric coupling (k_{LE}) was also determined using the equations in [24].

The BAW properties were calculated for each of the BAW modes: (QL) quasi-longitudinal, ($QS1$) quasi-shear 1, and ($QS2$) quasi-shear 2, where in general the modes are denoted as quasi modes unless the mode displacement occurs only along a single direction, for which the Q will be dropped.

The modes are ordered in this work not by velocity, as done in [420], but instead the modes are organized by the mode eigenvectors, as used in [419] and the calculation software [418]. Typically, the $QS1$ mode was found to be the fast shear mode with higher velocity than that of the $QS2$, slow shear, mode, but not always because the mode identity is kept consistent with the eigenvectors when the mode velocities cross after mode degeneracy.

The extracted LGT elastic, piezoelectric, and dielectric constants up to 900 °C from Chapters 2 and 3 were used to predict the high-temperature properties of BAW

devices. These constants were validated by high-temperature SAW device measurement in Chapter 4 and therefore it was anticipated that these constants would also provide adequate prediction of the BAW properties including turnover temperatures.

The BAW orientations can be given by $(\text{YXwl})\phi, \theta$ in the BAW rotated plate nomenclature [297, 420] or by $(\Phi, \Theta, \Psi) = (\Phi, \Theta, 90^\circ)$ in Euler angle notation [297]. The BAW properties were calculated in this work for a range of orientations by sweeping the angles $0^\circ \leq \phi \leq 60^\circ$ and $-90^\circ \leq \theta \leq 90^\circ$. The orientation sweep was calculated at least every 100°C between 100°C and 900°C and orientations where $\text{TCF}=0$ at a particular temperature were highlighted. The TCF was determined from the discrete derivatives calculated 5°C above and below the target temperature.

The BAW piezoelectric coupling coefficients k_{TE} and k_{LE} were analyzed at high-temperatures to identify how the modes can be piezoelectrically excited. For each mode there is a single k_{TE} but k_{LE} depends on the angle of the lateral electric field [24], therefore the lateral-excitation coupling is calculated by rotating the electric field around the cut plane. The angle of the lateral electric field, $\Psi_E=0^\circ$, is defined as coincident with the rotated Y''' axis and increased with counter-clockwise orientations are the X''' axis, shown in Fig. 6.1, where the X''' axis is the propagation direction of the orientation given by Euler angle notation. In this work, unless otherwise specified, the k_{LE} given for a particular mode is the maximum lateral field coupling for the orientation found by sweeping Ψ_E .

6.3 High-Temperature LGT BAW Properties and Orientations

The BAW v_p , TCF, k_{TE} , and k_{LE} for LGT orientations $(\Phi, \Theta, 90^\circ)$ were calculated up to 900°C for the three BAW modes. The velocities of the three BAW modes are shown at 900°C in Fig. 6.2. The TCF ranges for the three modes are given in Table 6.1 at the representative temperatures of 100°C , 550°C , and 900°C . Temperature-compensated orientations have been identified above 100°C for modes

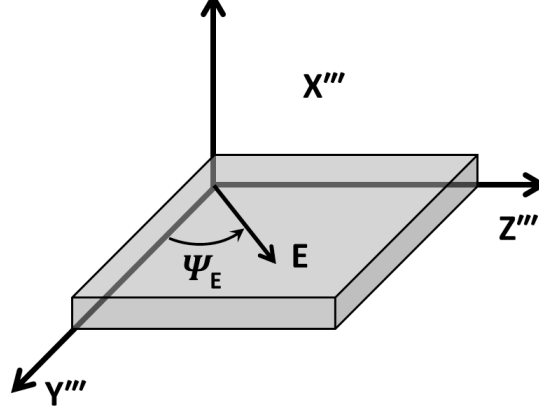


Figure 6.1. Definition of electric field, ψ_E , angle for lateral-field excitation

$QS1$ and $QS2$ but not for the QL mode. The $QS2$ mode was found to have $TCF=0$ orientations as high as 550°C and the $QS1$ mode had $TCF=0$ orientations up to 150°C .

6.3.1 LGT BAW Orientations with Zero TCF at High Temperature

Langatate orientations have been identified for both the QS modes that have turnover temperatures above 100°C and they will be presented here for each mode separately.

The k_{TE} and k_{LE} coupling are plotted for the $QS2$ mode at 100°C and 550°C in Fig. 6.3. The $QS2$ -mode TCF is shown at 100°C , 200°C , 300°C , 400°C , 500°C , and 550°C in Fig. 6.4. Note that in LGT orientations around $\phi = 0^\circ$, $\theta \geq 60^\circ$ and $\phi = 60^\circ$, $\theta \geq -20^\circ$ the $QS1$ mode and $QS2$ modes were exchanged in this region by the BAW calculation routines due to degenerate velocities, which lead to abrupt variations in the TCF values at the edges of the plots.

Langatate orientations have been identified that have $QS2$ -mode $TCF=0$ with k_{TE} of 0.04 to 0.14 and k_{LE} up to 0.1 for each temperature investigated between 100°C and 550°C . Fig. 6.5 plots contours of the LGT $QS2$ -mode orientations with turnover temperatures at every 100°C from 100°C to 500°C and 550°C . This particular plot can be used to select orientations for a desired turnover temperature.

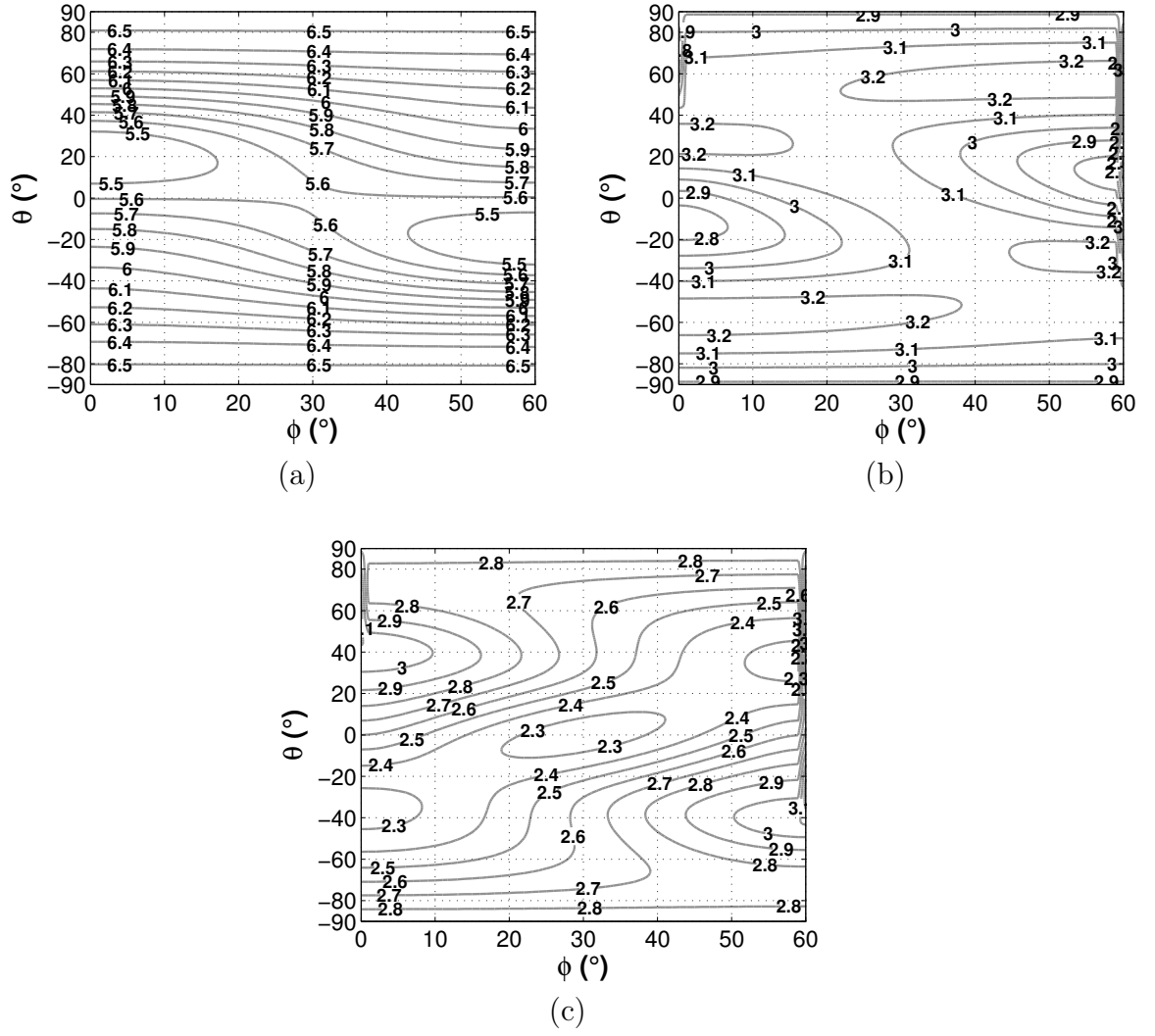


Figure 6.2. Contour plots of predicted LGT BAW Velocity at 100°C. Velocity in km s^{-1} for mode (a) *QL* (b) *QS1*, (c) *QS2*.

Temperature (°C)	TCF range ($\text{ppm } ^\circ\text{C}^{-1}$)		
	<i>QL</i> mode	<i>QS1</i> mode	<i>QS2</i> mode
100	−51 to −31	−44 to 8.0	−34 to 59
550	−64 to −46	−69 to −26	−64 to 3.3
900	−75 to −58	−91 to −54	−86 to −32

Table 6.1. LGT BAW mode TCF ranges at selected temperatures

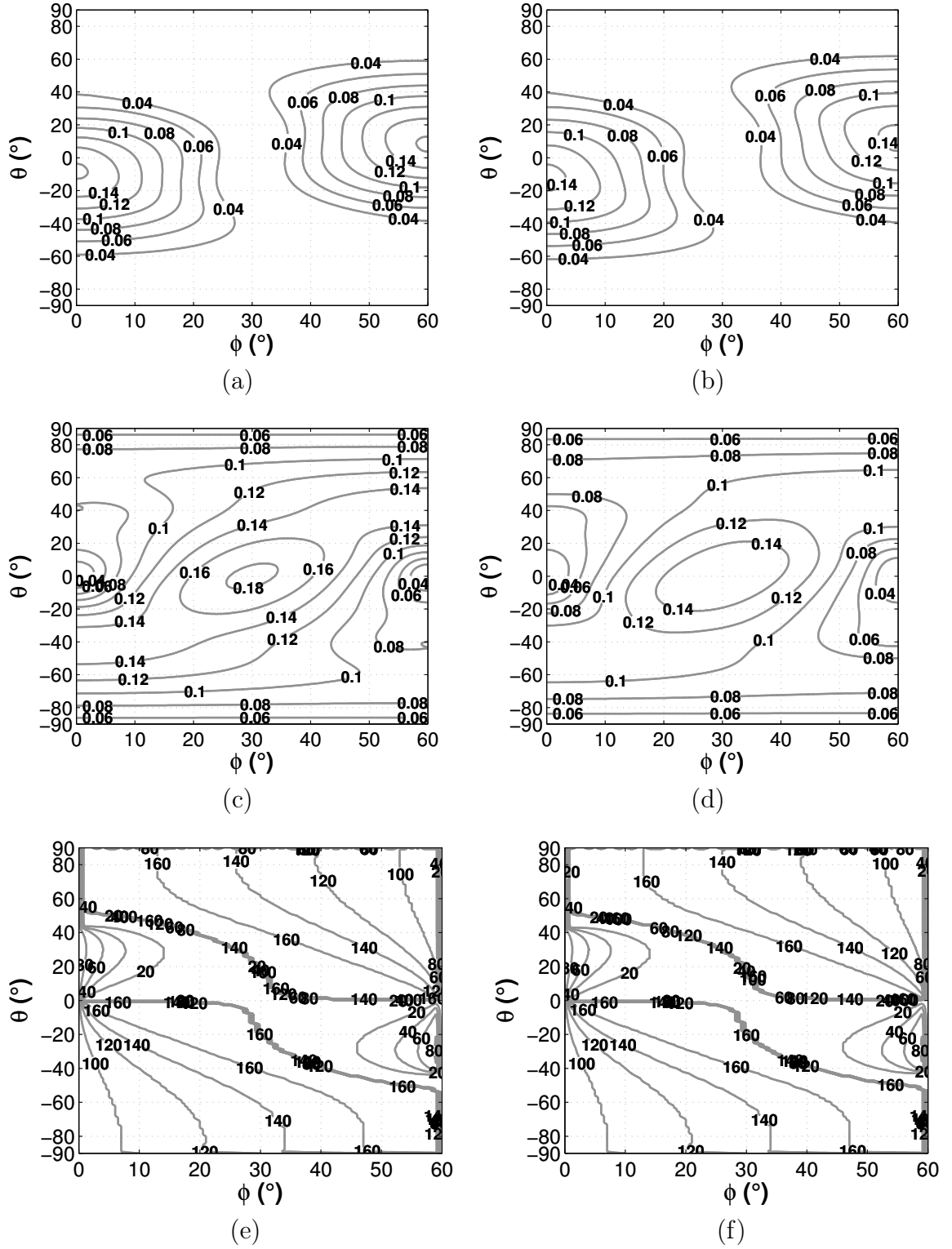


Figure 6.3. Contour plots of predicted LGT BAW QS2-mode coupling. (a) k_{TE} at 100°C, (b) k_{TE} at 550°C, (c) k_{LE} at 100°C, (d) k_{LE} at 550°C, (e) Ψ_E for maximal k_{LE} at 100°C, and (f) Ψ_E for maximal k_{LE} at 550°C.

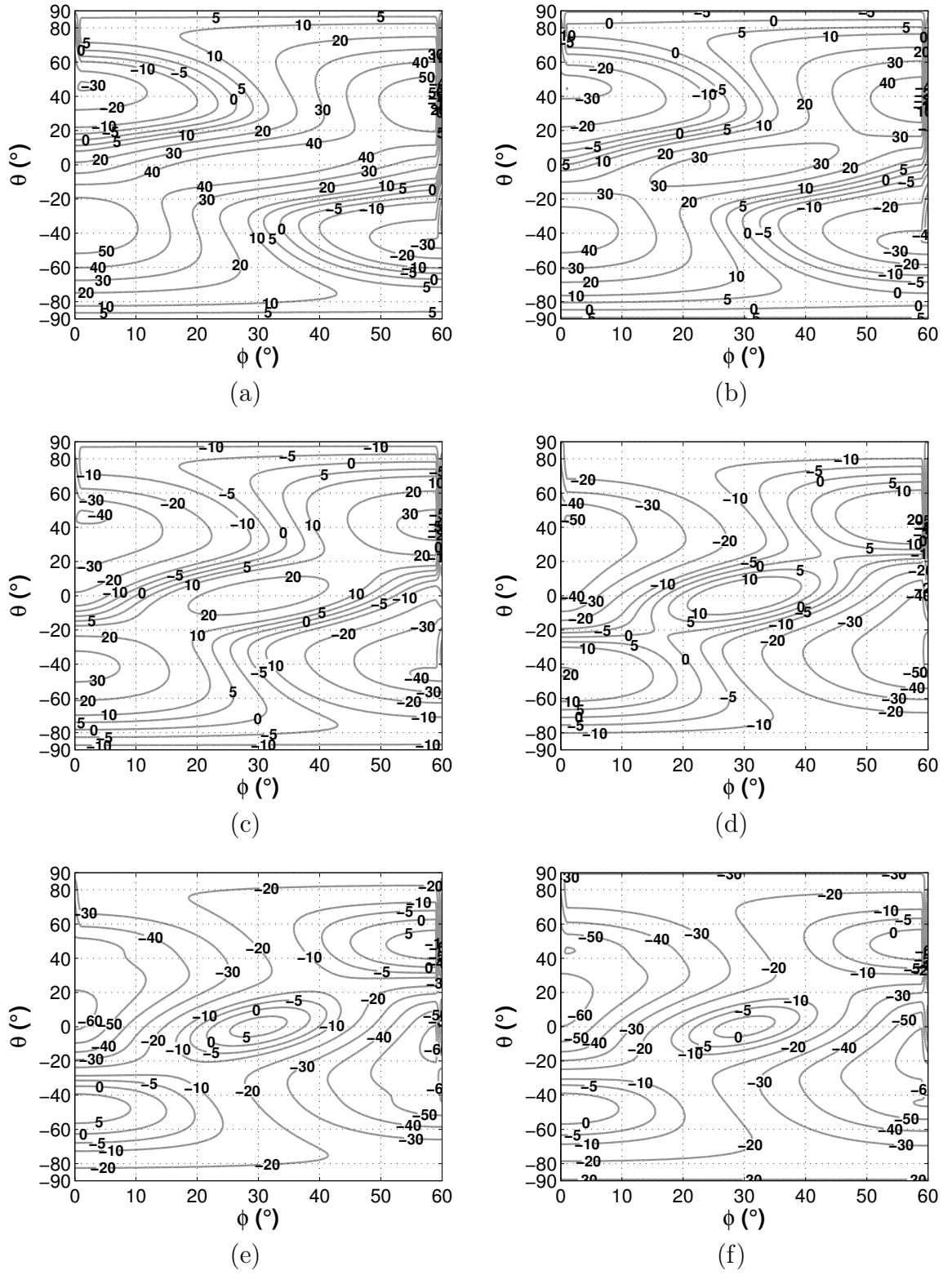


Figure 6.4. Predicted LGT BAW *QS2*-mode high-temperature TCF ($\text{ppm } ^\circ\text{C}^{-1}$).
Shown at (a) 100°C , (b) 200°C , (c) 300°C , (d) 400°C , (e) 500°C , (f) 550°C .

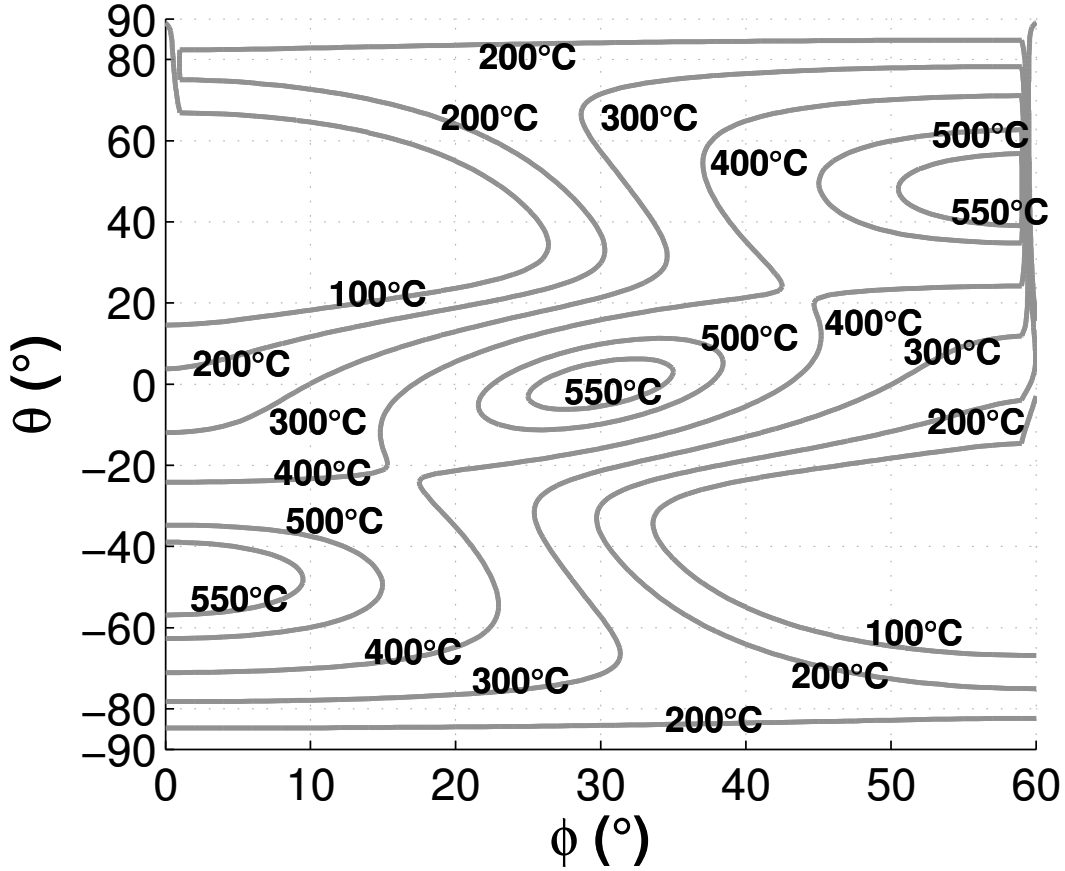


Figure 6.5. Predicted LGT BAW *QS2*-mode turnover temperatures between 100 °C and 550 °C

For the *QS2* mode, LGT orientations in the range $0^\circ \leq \phi \leq 10^\circ$ and $-58^\circ \leq \theta \leq -40^\circ$ and the range $50^\circ \leq \phi \leq 60^\circ$ and $40^\circ \leq \theta \leq 58^\circ$ were identified with $\text{TCF}=0$ at 550 °C. These orientations have coupling $0.04 \leq k_{TE} \leq 0.1$ and $k_{LE} \approx 0.1$; for comparison, SC-cut quartz has coupling of $k_{TE} = 0.051$ and AT-cut quartz can coupling of 0.063 [418, 421]. There are also 550 °C turnover temperature orientations in the range $25^\circ \leq \phi \leq 35^\circ$ and $-5^\circ \leq \theta \leq 5^\circ$ with coupling $k_{LE} \approx 0.14$ and $k_{TE} \leq 0.02$.

Experimentally-identified temperature-compensated *QS2*-mode orientations on (YXl) θ plates, reported in [228, 414], were also numerically predicted in this work. The BAW plates were fabricated from LGT boules of a few centimeters in diameter grown by Yu, et al. using the Czochralski method [228, 414]. In [228] measurements

of a LGT (YXl)–30° plate, Euler angle (0°, –30°, 90°), found a turnover temperature of about 350 °C, which is lower than turnover temperature of ~ 450 °C predicted in this work (Fig. 6.5). While these experimental results confirm the existence of high-temperature TCF=0 orientations, the turnover temperature is somewhat different than was predicted in this work. More study on LGT BAW devices would be required to identify the source of this discrepancy; possible causes include inaccurate constants, crystal differences due to different suppliers, crystals or wafers being under stress, miscut orientations used in device fabrication, and measurement errors.

Next, the $QS1$ -mode TCF and coupling are shown in Fig. 6.6. For the $QS1$ mode, LGT orientations in the range $0^\circ \leq \phi \leq 5^\circ$ and $-15^\circ \leq \theta \leq 0^\circ$ and the range $55^\circ \leq \phi \leq 60^\circ$ and $0^\circ \leq \theta \leq 15^\circ$ were identified with TCF=0 at 150 °C, which is the highest turnover temperature identified for this mode. The thickness-field coupling for these modes is less than 0.04; however, the lateral-field coupling of 0.06 to 0.08 in this region enables their use in lateral-excitation devices.

6.3.2 LGT BAW Orientations with Transverse-Shear Modes

Bulk acoustic wave devices that utilize transverse-shear modes (TSM) are useful in certain sensing applications, in particular liquid sensors, because there is no longitudinal displacement. Specifically, [421] indicated the desire for sensor substrates in which the TSM: (i) has purely shear displacements, (ii) can be selectively excited without exciting the other modes, (iii) is temperature compensated, and (iv) has piezoelectric coupling larger than that of AT-cut quartz (0.063).

For the LGT BAW orientations (0°, –58° → 10°, 90°), the $S2$ mode (quasi dropped for the pure mode) was identified to be a TSM with the all of the above mentioned TSM properties at high temperature. Orientations along this plane can be selected with turnover temperatures between 100 °C and 550 °C, as observed in Figs. 6.4 and 6.5. This BAW plane represents singly-rotated orientations that can be written in

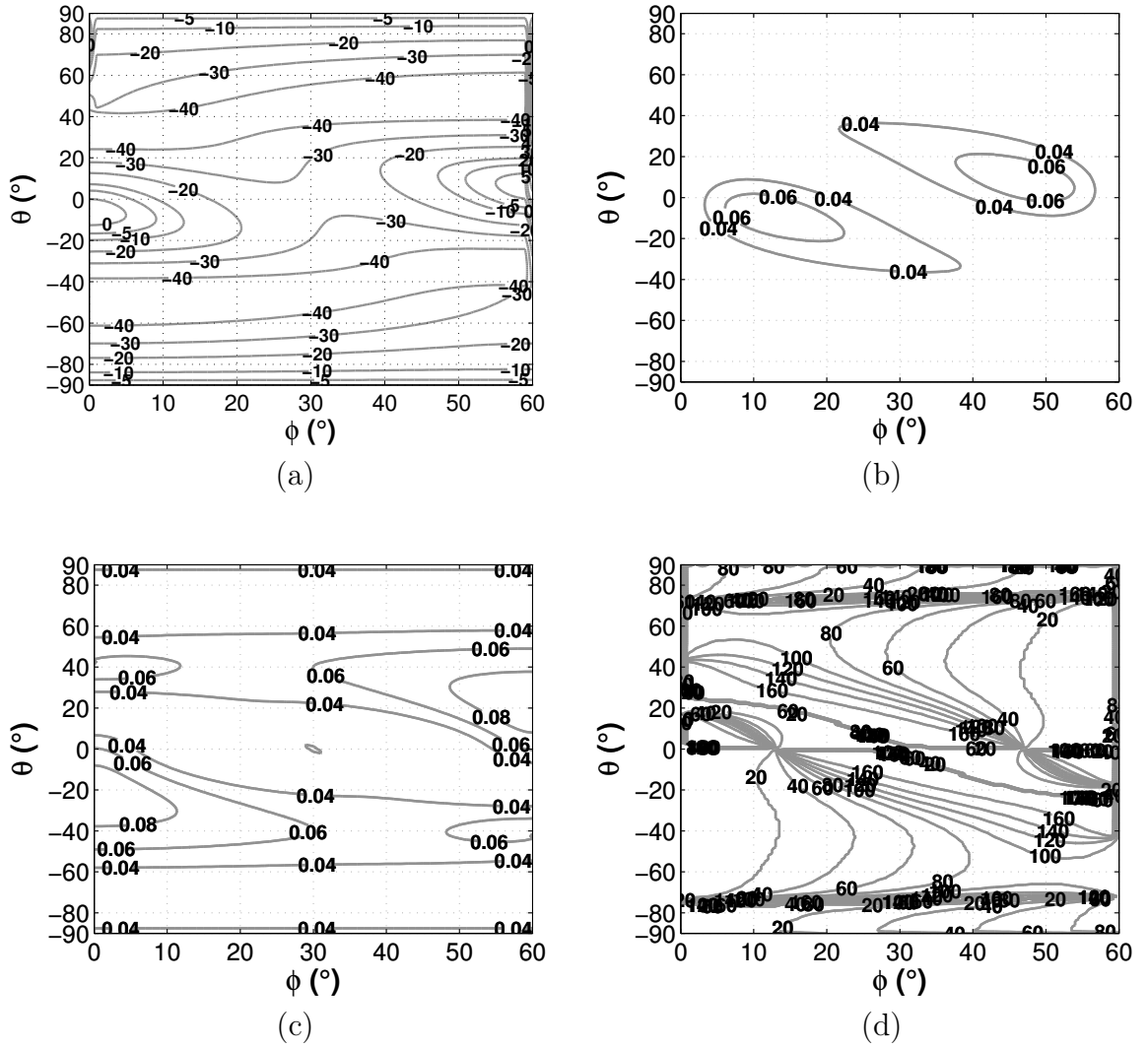
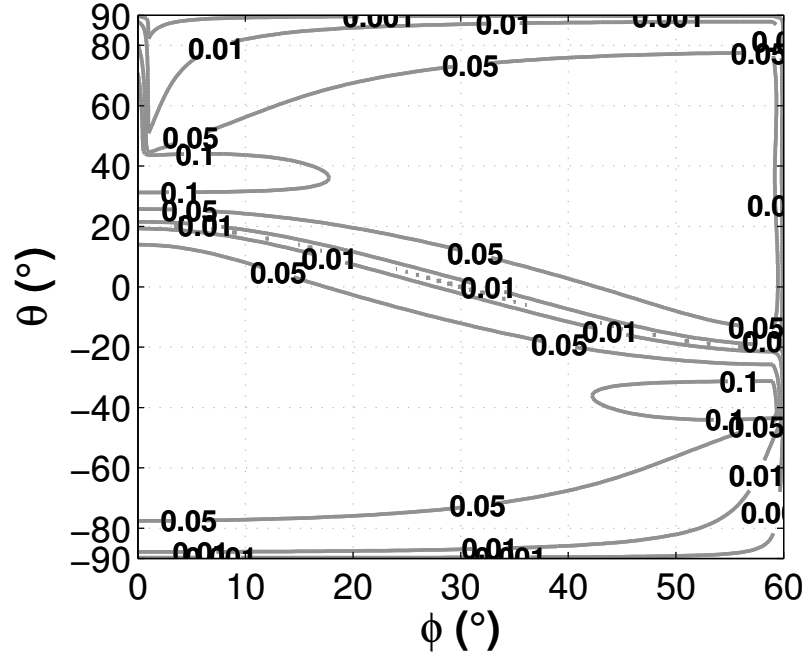


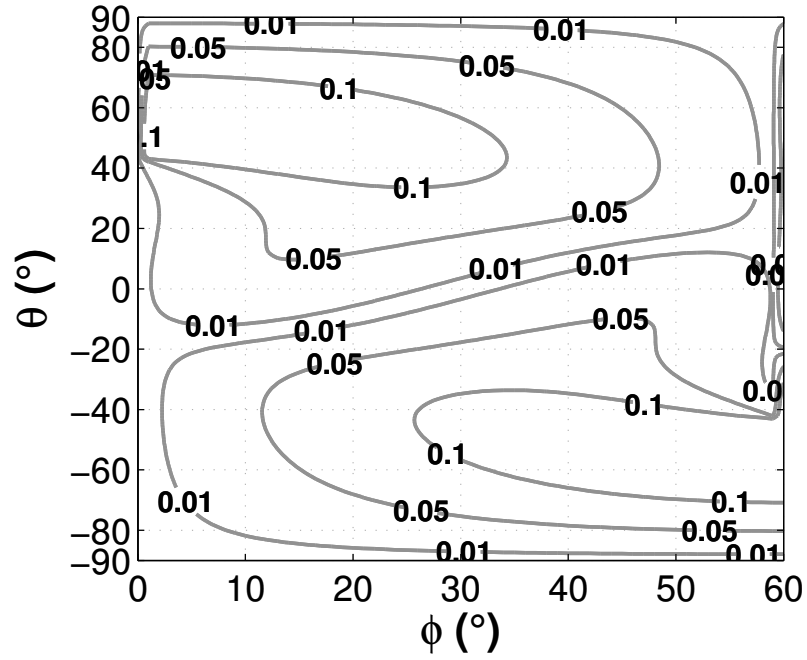
Figure 6.6. Predicted LGT BAW $Qs1$ -mode TCF and coupling at 150 °C. (a) TCF in $\text{ppm } ^\circ\text{C}^{-1}$, (b) thickness coupling k_{TE} , (c) lateral coupling k_{LE} , and (d) ψ_E for maximal k_{LE} .

Euler angle notation as $(0^\circ, \Theta, 90^\circ)$ and in BAW plate notation as $(YXwl)0^\circ, \theta$ or $(YXI)\theta$.

The pure shear modes were found by searching for shear modes for which the longitudinal component of the normalized eigenvector is less than 0.01 (i.e. less than 1 % of the shear component), shown in the Fig. 6.7. The eigenvector components are presented only at room temperature because they do not significantly change for the investigated LGT orientations over the temperature range of 25 °C to 900 °C.



(a)



(b)

Figure 6.7. LGT BAW longitudinal components of the eigenvector for *QS1* and *QS2* modes. (a) *QS1* mode at 25 °C, (b) *QS2* mode at 25 °C.

Along the plane $(0^\circ, \Theta, 90^\circ)$, the $S2$ mode is a pure TSM with displacement only in the rotated Y''' direction, where the predicted displacements in the thickness direction is numerically zero ($< 1 \times 10^{-15}$). The TSM $S2$ mode uncouples with the QL mode and the $QS1$ mode, as confirmed by the symmetry of the orientations, which is symmetry 4 using the notation of [422].

The $S2$ TSM thickness coupling and lateral coupling with $\Psi_E=90^\circ$ for the LGT orientations $(0^\circ, \Theta, 90^\circ)$ are shown in Fig. 6.8. The coupling of this mode is stronger than that of AT-cut quartz (0.063) for many of the orientations, including the region $(0^\circ, -58^\circ \rightarrow 10^\circ, 90^\circ)$ that contains turnover temperatures between 100°C and 550°C . The thickness coupling of the QL and $QS1$ modes is zero along this plane. The $S2$ TSM mode has maximum k_{LE} when $\Psi_E=90^\circ$, and for the same electric field direction $k_{LE}=0$ for QL and $QS1$ modes, which have maximal k_{LE} when $\Psi_E=0^\circ$. These results indicate that the $S2$ TSM can be selectively excited with either thickness or lateral electric field excitation.

Additionally, for the LGT BAW orientation $(30^\circ, 0^\circ, 90^\circ)$ the modes $S1$ and $S2$ are pure shear modes and $S2$ is temperature compensated at $\sim 550^\circ\text{C}$. Along this orientation, the $S1$ and $S2$ modes both have eigenvectors with longitudinal components $< 1 \times 10^{-16}$ so they decouple from the pure- L mode. Both shear modes are laterally excitable with $k_{LE} = 0.03$ and 0.18 for the $S1$ and $S2$ modes, respectively, with maximal excitation along $\Psi_E = 0^\circ$, and both have zero k_{TE} . The L mode is excited longitudinally but has $k_{LE} = 0$. Since the shear modes are both excitable with the same electric field angle, it might be desirable to design a sensor to utilize the different velocities and temperature dependencies of the $S2$ mode, which has a turnover temperature around 550°C , and the $S1$ mode, which has $\text{TCF}=-53\text{ppm}^\circ\text{C}^{-1}$ at 550°C .

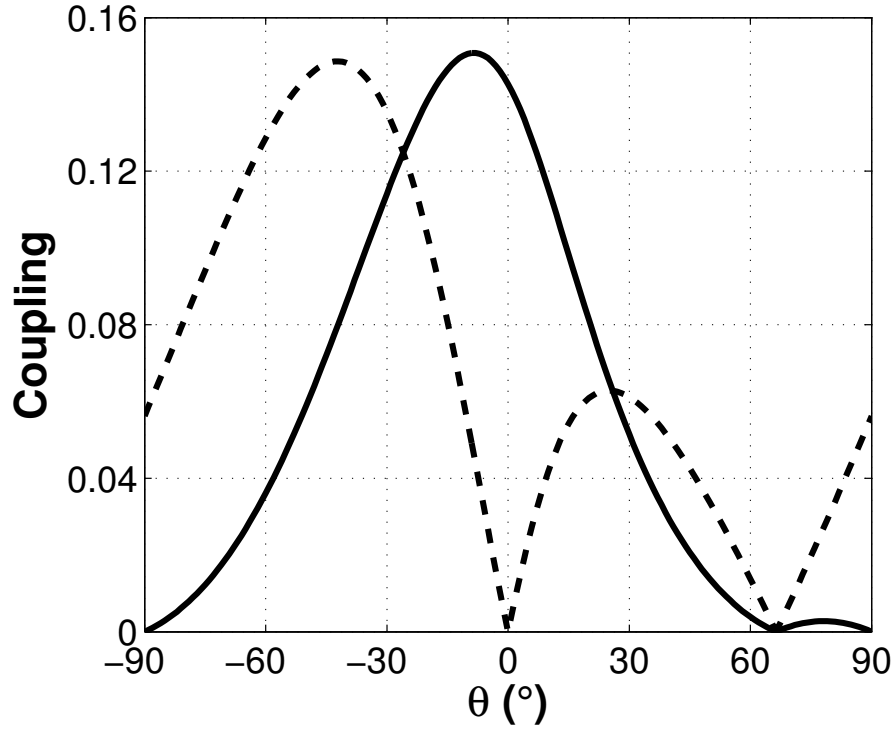


Figure 6.8. LGT BAW $S2$ TSM coupling for $(0^\circ, \Theta, 90^\circ)$ at 25°C . k_{TE} (solid line) and k_{LE} where $\Psi_E = 90^\circ$ (dashed line)

6.4 Conclusions

The extracted LGT AW constants, which were validated by SAW measurements up to 900°C , were used to predict the BAW temperature behavior at high temperatures.

New temperature-compensated LGT BAW orientations have been identified for operation at high temperatures. Orientations with turnover temperatures between 100°C and 550°C for the $QS2$ mode and up to 150°C for the $QS1$ mode can be selected for different applications. Additionally, orientations were identified with pure transverse-shear modes that are selectively excitable and have temperature compensation up to 550°C . The identified orientations are expected to enable new high-temperature applications in sensing and frequency control.

Chapter 7

CONCLUSIONS AND SUGGESTED FUTURE WORK

In this chapter, the research comprising this work is summarized, including the conclusions drawn from the work. Next the contributions to the field are presented. And finally, future work is suggested that can utilize and expand upon the results of this work.

7.1 Summary of Work and Conclusions

Chapter 2 reported on the extraction of langatate real and imaginary permittivity and conductivity up to 900 °C. The dielectric properties were determined from admittance measurements of parallel-plate capacitors fabricated on LGT X, Y, and Z axes. The electric field fringing was corrected for by measuring the capacitors with circular electrodes of successively increasing diameters and fitting the results to a surface plane with the dependent variables of temperature and the ratio of the wafer thickness to the electrode radius. The dielectric permittivity, polarization losses, and electrical conductivity were simultaneously extracted.

The extracted LGT ϵ'_{R11} was found to increase by up to 38 % and ϵ'_{R33} to decreased by 49 % at 900 °C, indicating the importance of measuring the permittivity constants at high temperatures. The LGT conductivity and dielectric polarization losses are minimal at room temperature, with the loss tangent $\tan \delta < 1 \times 10^{-7}$ at 25 °C and 1 MHz, but the losses increase with temperature and $\tan \delta$ is on the order of 1 at 900 °C and 1 MHz.

Chapter 3 presented the resonant ultrasound spectroscopy (RUS) measurement technique for high-temperature material characterization, which was used to extract the LGT elastic and piezoelectric constants up to 900 °C. For the first time, the complete set of the elastic, piezoelectric, and dielectric constants of LGT were

presented up to the referred high temperature. The RUS equations used to calculate the resonant spectrum of a crystal sample using Lagrangian minimization were detailed, along with the numerical process used to extract the crystal constants. Langatate parallelepiped samples were fabricated and had their spectra measured in a custom high-temperature furnace. The RUS extraction technique utilized mode group identification and the tracking of modes from lower temperatures to improve the mode matching at high temperatures.

In a first phase of this work, the LGT stiffened-elastic constants were extracted up to 1100 °C ignoring the piezoelectric effect. In a second phase of this work, a full set of the LGT elastic and piezoelectric constants was then determined up to 900 °C utilizing the dielectric constants from Chapter 2. The extracted LGT piezoelectricity constants at 900 °C were found to vary by as much as 77 % of the room temperature values, indicating the importance of their characterization at high temperature.

In Chapter 4 the accuracy of the extracted set of high-temperature (up to 900 °C) LGT acoustic wave elastic, piezoelectric, and dielectric constants was verified by comparing predicted SAW propagation properties using the constants to measured SAW propagation properties at high temperature. For the 6 tested orientations along the LGT plane (90° , 23° , Ψ) the measured and predicted SAW v_p agreed with an average RMS error of 0.2 % of the measured v_p for the temperature range of 25 °C to 900 °C and were within 0.9 % in the worst case. The calculated TCD had an average RMS error of 10.8 ppm °C⁻¹ from the measured value for the tested orientations over the entire temperature range of investigation. The agreement between the measured and predicted SAW propagation properties confirmed the accuracy of the extracted high-temperature LGT elastic, piezoelectric, and dielectric constants, which for the first time enables identifying orientations and designing high-temperature LGT AW devices up to 900 °C.

Additionally, the new set of LGT constants that includes the temperature dependence of the piezoelectric and dielectric constants, was found to have improved accuracy over the first set of constants that ignored the temperature dependence, resulting in the reduction of the average RMSE discrepancies between predicted and measured SAW v_p by 72 %, TCD by 14 %, and the turn-over temperature by 63 %. These improvements reveal the importance of including the dielectric and piezoelectric temperature behavior for accurate acoustic wave property predictions and device design at high temperatures.

For the first time, LGT SAW devices were fabricated and operated up to 900 °C, confirming the applicability of LGT as a high-temperature piezoelectric substrate for AW devices and sensors.

Chapter 5 investigated the high-temperature SAW phase velocity, frequency change, and TCD properties behavior of LGT up to 900 °C for three regions in space, namely, $(0^\circ, \Theta, \Psi)$, $(90^\circ, \Theta, \Psi)$, and $(\Phi, 90^\circ, \Psi)$. For the first time, LGT SAW orientations have been identified with zero TCD as high as 500 °C, with select orientations in the SAW plane $(90^\circ, 23^\circ, \Psi)$ having experimentally confirmed turn-over temperatures up to 413 °C. The uncovered LGT orientations with low TCD up to 900 °C have potential applications for frequency control, sensing, and signal processing. Temperature-sensitive orientations identified in those regions are relevant for harsh-environment temperature sensing.

Cut planes that can hold multiple LGT SAW orientations were identified in this work with coupling above 0.1 % and different temperature derivatives for the purpose of fabricating contrasting response SAW sensors on the same wafer. This feature allows the SAW devices to experience the same temperature and environmental conditions, such as pressure, and be used to separate the common frequency response due to temperature or pressure from other measurands. For verification of this technique, LGT SAW delay lines on the same wafer were measured up to 900 °C and used

as a differential temperature sensor to separate the temperature measurement from frequency drifts that are common to both devices.

High-temperature LGT BAW orientations were investigated in Chapter 6 and for the first time LGT BAW orientations were identified with turnover temperatures as high as 550 °C. LGT BAW orientations were found in which the slow-shear turnover temperatures ranges from 100 °C to 550 °C with piezoelectric coupling $0.04 < k_{TE} < 0.14$ for thickness coupling and k_{LE} up to 0.1 for lateral coupling. For the fast-shear, LGT orientations were identified with turnover temperatures up 150 °C. The identified orientations are expected to open new high-temperature applications in sensing and frequency control.

7.2 Statement of Contribution

Major contributions of this work relate to the field of high-temperature AW constants extraction, LGT material constants, and LGT SAW and BAW propagation properties calculation and experimental verification at high temperatures, as detailed next.

- The complex permittivity and conductivity of LGT were extracted in this work for the first time up to 900 °C [331, 334, 359].
- The method of simultaneous extraction of the dielectric permittivity, polarization losses, and conductivity was applied to piezoelectric crystals at high temperatures up to 900 °C [331, 334, 359].
- The set of LGT elastic, piezoelectric, and dielectric constants and temperature coefficients extracted up to 900 °C were presented for the first time, [328, 330, 331, 334]. The full set of measured LGT AW constants had only been previously published up to 150 °C.

- The temperature dependence of the LGT piezoelectric and dielectric constants at high temperature were determined and found to be relevant to the extraction of the elastic constants and the calculation of SAW propagation properties at high temperatures [331, 334].
- The RUS mode matching process at high temperatures was improved by using predicted temperature behavior from extracted constants and temperature coefficients at lower temperatures [328, 330, 331, 334].
- Langatate delay line SAW devices were fabricated and measured up to 900 °C, both validating the extracted high-temperature LGT AW constants and providing the first experimental demonstration of LGT SAW device operation up to 900 °C [329, 330].
- Langatate SAW orientations were identified with turnover temperatures up to 500 °C and with both high and low sensitivity to temperature in the range between 400 °C to 800 °C [332, 333].
- Langatate SAW cut planes were presented that contain multiple orientations for the creation of a suite of sensors on a single chip that have different temperature dependencies [332, 333].
- Langatate BAW orientations were identified with turnover temperatures between 100 °C and 550 °C with both thickness-field and lateral-field coupling, including orientations with transverse-shear modes [423].

7.3 Suggested Future Work

Future work based upon this work is suggested to further improve and validate the extracted constants, utilize the high-temperature extraction techniques on other

crystals, and to fabricate high-temperature LGT sensors and frequency control devices using the proposed SAW and BAW orientations.

- **Fabricate and perform RUS measurements on additional LGT samples**

The accuracy of the extracted high-temperature LGT elastic and piezoelectric constants could be further improved by the fabrication and RUS characterization of additional LGT parallelepiped samples. The RUS extraction process is sensitive to fabrication defects such as misalignment, non-parallel sides, damage on the sample edges, and surface quality. New samples could be cut and polished using other crystal orientations in order to provide different sample dependencies regarding the acoustic constants. The additional measurement of new LGT samples should help to average out systematic bias that may have been caused by undetected sample fabrication problems and to reduce the overall measurement uncertainty.

- **Acquire and characterize LGT from multiple boules and sources**

In this work, the LGT samples were obtained from two boules purchased from a single supplier, and the consistency of the crystal quality and material constants across the boules or between suppliers was not investigated. The room-temperature LGT uniformity within wafers [43, 152] and crystal quality consistency between suppliers have been studied [260, 261], but the effect at high temperature has not been studied. The quality and consistency of LGT could be investigated by extracting the acoustic constants and temperature coefficients of samples from different locations within each boule, multiple crystal boules, and different suppliers. However, it may be difficult to obtain multiple LGT suppliers in the near future because the growth of LGT is limited to a few companies and research groups.

- **Perform wide-band high-temperature dielectric spectroscopy of LGT**

The dielectric constants extracted in this work were measured at and below 1 MHz, as is the standard practice for piezoelectric crystals. The permittivity of any crystal is frequency dependent as frequency is increased so the permittivity of LGT might vary between the dielectric measurement frequencies and the acoustic device operation frequencies, which can be as high as a few GHz, as discussed in Chapter 2. Dielectric spectroscopy is the characterization of the permittivity over a wide range of frequencies and would reveal the actual LGT dielectric behavior at high frequencies. The measurements over the full frequency range from 1 MHz to 5 GHz would require a number of different measurement techniques, even if performed only at room temperature, and the high-temperature characterization is expected to present additional challenges. Examples of high-frequency dielectric constants extraction techniques include the measurement of the perturbation caused by a crystal sample inserted at a discontinuity of a transmission line and the characterization of dielectric resonators with a range of resonance frequencies.

- **Measure LGT acoustic losses at high-temperature and identify loss mechanisms**

The acoustic losses of LGT were observed in this work to generally increase with temperature and to have additional losses in the region around 500 °C to 800 °C. Further understanding of the LGT crystal structure changes is required to describe the physics of the observed loss mechanisms. The identification of loss mechanisms would provide a more complete physical knowledge of LGT and possibly provide crystal growers with a path to reduce the losses. The LGT acoustic losses and viscosity constants could be measured to quantify the losses and allow the prediction of acoustic device losses for new acoustic orientations.

- **Fabricate additional LGT SAW device orientations and test at high temperature**

In this work 6 LGT SAW orientations from a single cut plane were tested with fabricated devices. Additional LGT wafers could be cut and polished for high-temperature SAW devices to demonstrate other orientations identified in this work. The other orientations would have different dependencies on the acoustic constants and should provide additional verification of the extracted constants, as well as new performance data of high temperature LGT SAW sensors and/or frequency control devices.

- **Fabricate LGT BAW devices and test at high temperature**

The LGT BAW orientations with high-temperature turnover temperatures identified in this work should be fabricated into BAW devices and characterized at high temperature. Bulk acoustic wave measurements could be used to further validate the extracted constants used in the BAW predictions. The BAW devices could be excited using high-temperature electrodes deposited on the crystal surface, which mass loads the device, or by external electrodes, which provides weaker responses when compared to direct metallization. Additionally, the BAW device packaging and mounting can significantly alter the device response and turnover temperatures, so they should be carefully considered, in particular at high-temperature conditions.

- **Characterize other piezoelectric crystals at high temperature**

The RUS and dielectric measurement techniques used to characterize LGT should be applied to extract the acoustic constants of other crystals. In particular, the RUS technique could be used to extract the acoustic constants of LGS, LGN, $\text{Ca}_3\text{NbGa}_3\text{Si}_2\text{O}_{14}$, $\text{Ca}_3\text{TaGa}_3\text{Si}_2\text{O}_{14}$, $\text{Sr}_3\text{NbGa}_3\text{Si}_2\text{O}_{14}$, $\text{Sr}_3\text{TaGa}_3\text{Si}_2\text{O}_{14}$ and the oxyborate $\text{ReCa}_4\text{O}(\text{BO}_3)_3$ crystals (Re=rare earth element, such as

Gd, Y, or La) high-temperature piezoelectric crystals, which were discussed in Chapter 1. The extracted AW constants of many different high-temperature piezoelectric crystals would be useful for identifying the best material and device orientations for a given harsh-environment application. These high-temperature crystals are the focus of on-going research to improve the boule size and growth of high-quality crystals free of twinning, stress, or major defects and to extract the acoustic constants.

- **Utilize LGT devices in high-temperature sensor applications**

The LGT SAW and BAW orientations identified in this work should be used to fabricate high-temperature sensor and frequency control devices. The reported BAW and SAW orientations have relevant properties at high temperature, such as turnover temperatures up to 550 °C and both high and low temperature sensitivity up to 900 °C. The SAW planes identified with multiple high-temperature orientations with the above properties can be utilized to fabricate a suite of sensors on a single wafer to be wirelessly interrogated simultaneously for measurement of multiple measurands, such as temperature, pressure, strain, and corrosion. Additionally, high-temperature LGT BAW devices fabricated along the reported orientations should find use as oscillators, deposition rate monitors, mass sensors, corrosion sensors, and in the characterization of high-temperature liquids.

REFERENCES

- [1] R. Turner, P. Fuierer, R. Newnham, and T. Shrout, "Materials for high temperature acoustic and vibration sensors: a review," *Applied Acoustics*, vol. 41, no. 4, pp. 299–324, 1994.
- [2] P. Krempl, G. Schleinzner, and W. Wallnofer, "Gallium phosphate, GaPO_4 : A new piezoelectric crystal material for high-temperature sensorics," *Sensors and Actuators, A: Physical*, vol. 61, no. 1-3, pp. 361 – 363, 1997.
- [3] W. W. Manges, S. F. Smith, and G. O. Allgood, "It's time for sensors to go wireless; part 1: Technological underpinnings," *Sensors Magazine*, April 1 1999. [Online]. Available: <http://www.sensormag.com/networking-communications/its-time-sensors-go-wireless-part-1-technological-underpinni-775>
- [4] —, "It's time for sensors to go wireless; part 2: Take a good technology and make it an economic success," *Sensors Magazine*, May 1 1999. [Online]. Available: <http://www.sensormag.com/networking-communications/its-time-sensors-go-wireless-part-2-take-a-good-technology-a-776>
- [5] Industrial Wireless Workshop, "Industrial wireless technology for the 21st century," Office of Energy Efficiency and Renewable Energy, Department of Energy, 2002.
- [6] R. Fachberger, G. Bruckner, G. Knoll, R. Hauser, J. Biniash, and L. Reindl, "Applicability of LiNbO_3 , langasite and GaPO_4 in high temperature SAW sensors operating at radio frequencies," *IEEE Transactions on Ultrasonics, Ferroelectrics, and Frequency Control*, vol. 51, no. 11, pp. 1427–1431, Nov. 2004.
- [7] J. A. Thiele, "High temperature LGX acoustic wave devices and applications for gas sensors," Master's thesis, University of Maine, 2005.
- [8] C. Krause, "Myth: Wireless technologies are inherently unreliable," *Oak Ridge National Laboratory Review*, vol. 41, no. 3, pp. 22–23, 2008. [Online]. Available: http://www.ornl.gov/info/ornlreview/v41_3_08/article15.shtml
- [9] W. Cullinane and R. Strange, "Gas turbine engine validation instrumentation: measurements, sensors, and needs," in *Proceedings of the SPIE - The International Society for Optical Engineering*, vol. 3852, 1999, pp. 2 – 13.
- [10] B. Chorpening, D. Tucker, and S. Maley, "Sensors applications in 21st century fossil-fuel based power generation," in *Proc. of IEEE Sensors*, vol. 3, 2004, pp. 1153 – 1156.
- [11] M. N. Hamidon, V. Skarda, N. M. White, F. Krispel, P. Krempl, M. Binhack, and W. Buff, "High-temperature 434 MHz surface acoustic wave devices based on GaPO_4 ," *IEEE Transactions on Ultrasonics, Ferroelectrics, and Frequency Control*, vol. 53, no. 12, pp. 2465–2470, 2006.

- [12] J. Thiele and M. Pereira da Cunha, "High temperature LGS SAW gas sensor," *Sensors and Actuators, B: Chemical*, vol. 113, no. 2, pp. 816 – 822, 2006.
- [13] —, "Platinum and palladium high-temperature transducers on langasite," *IEEE Transactions on Ultrasonics, Ferroelectrics and Frequency Control*, vol. 52, no. 4, pp. 545 –549, 2005.
- [14] P. L. Dreike, D. M. Fleetwood, D. B. King, D. C. Sprauer, and T. E. Zipperian, "An overview of high-temperature electronic device technologies and potential applications," *IEEE Transactions on Components, Packaging, and Manufacturing Technology, Part A*, vol. 17, no. 4, pp. 594–609, Dec. 1994.
- [15] A. McNad, K. J. Kirk, and A. Cochran, "Ultrasonic transducers for high temperature applications," *IEE Proc.- Sci. Meas. Tech.*, vol. 145, no. 5, pp. 229–236, 1998.
- [16] P. Neudeck, R. Okojie, and L.-Y. Chen, "High-temperature electronics - a role for wide bandgap semiconductors?" *Proceedings of the IEEE*, vol. 90, no. 6, pp. 1065 – 1076, Jun 2002.
- [17] G. Hunter, P. Neudeck, R. Okojie, G. Beheim, J. Powell, and L. Chen, "An overview of high-temperature electronics and sensor development at NASA Glenn Research Center," *Transactions of the ASME. The Journal of Turbomachinery*, vol. 125, no. 4, pp. 658 – 664, 2003.
- [18] G. Hunter, G. Beheim, G. Ponchak, M. Scardelleti, R. Meredith, F. Dynys, P. Neudeck, J. Jordan, and L.-Y. Chen, "Development of high temperature wireless sensor technology based on silicon carbide electronics," *ECS Transactions*, vol. 33, no. 8, pp. 269–281, 2010.
- [19] G. W. Hunter, J. D. Lekki, and D. L. Simon, "Development and testing of propulsion health management," in *Workshop on Integrated Vehicle Health Mangement and Aviation Safety*, 2012.
- [20] H. Ostaffe, "RF energy harvesting enables wireless sensor networks," *Sensors Magazine*, October 13 2009. [Online]. Available: <http://www.sensorsmag.com/sensors-mag/rf-energy-harvesting-enables-wireless-sensor-networks-6175>
- [21] V. Magori, "Ultrasonic sensors in air," in *Proc. of the IEEE International Ultrasonics Symposium*, 1994, pp. 471–481.
- [22] K. Mizutani, E. Ishikawa, and K. Nagai, "Space thermometry using a double acoustic delay line oscillator," *Japanese Journal of Applied Physics*, vol. 39, no. 5B, pp. 3103–3106, 2000.
- [23] C. Kerr and P. Ivey, "Optical pyrometry for gas turbine aeroengines," *Sensor Review*, vol. 24, no. 4, pp. 378 – 86, 2004.

- [24] J. F. Rosenbaum, *Bulk Acoustic Wave Theory and Devices*. Boston: Artech House, 1988.
- [25] D. P. Morgan, *Surface-Wave Devices for Signal Processing*. New York: Elsevier, 1991.
- [26] E. Benes, M. Groschl, F. Seifert, and A. Pohl, "Comparison between BAW and SAW sensor principles," *IEEE Transactions on Ultrasonics, Ferroelectrics and Frequency Control*, vol. 45, no. 5, pp. 1314–1330, Sept. 1998.
- [27] L. Reindl, G. Scholl, T. Ostertag, H. Scherr, U. Wolff, and F. Schmidt, "Theory and application of passive SAW radio transponders as sensors," *IEEE Transactions on Ultrasonics, Ferroelectrics and Frequency Control*, vol. 45, no. 5, pp. 1281–1292, 1998.
- [28] L. Reindl, "Wireless passive SAW identification marks and sensors," in *2nd Int. Symp. Acoustic. Wave Devices for Future Mobile Communications, Chiba Univ.*, March 2004, paper ID 1B3.
- [29] K. Lakin, "Thin film resonator technology," *IEEE Transactions on Ultrasonics, Ferroelectrics and Frequency Control*, vol. 52, no. 5, pp. 707–716, 2005.
- [30] J.-H. Lin and Y.-H. Kao, "Wireless temperature sensing using a passive RFID tag with film bulk acoustic resonator," in *Proc. of the IEEE International Ultrasonics Symposium*, Nov. 2008, pp. 2209–2212.
- [31] J. A. Kosinski, "New piezoelectric substrates for SAW devices," *International Journal of High Speed Electronics and Systems*, vol. 10, no. 4, pp. 1017–1068, 2000.
- [32] J. A. Thiele and M. Pereira da Cunha, "High temperature surface acoustic wave devices: fabrication and characterisation," *Electronics Letters*, vol. 39, no. 10, pp. 818–819, 2003.
- [33] E. Belokoneva, M. Simonov, A. Butashin, B. Mill, and N. Belov, "Crystal structure of calcium gallogermanate $\text{Ca}_3\text{Ga}_2\text{Ge}_4\text{O}_{14}=\text{Ca}_3\text{Ge}(\text{Ga}_2\text{Ge})\text{Ge}_2\text{O}_{14}$ and its analog $\text{Ba}_3\text{Fe}_2\text{Ge}_4\text{O}_{14}=\text{Ba}_3\text{Fe}(\text{FeGe}_2)\text{Ge}_2\text{O}_{14}$," *Soviet Physics - Doklady*, vol. 25, no. 12, pp. 954–957, 1980.
- [34] M. Pereira da Cunha and S. de Azevedo Fagundes, "Investigation on recent quartz-like materials for SAW applications," *IEEE Transactions on Ultrasonics, Ferroelectrics, and Frequency Control*, vol. 46, no. 6, pp. 1583–1590, 1999.
- [35] D. C. Malocha, M. Pereira da Cunha, E. Adler, R. C. Smythe, S. Frederick, M. Chou, R. Helmbold, and Y. S. Zhou, "Recent measurements of material constants versus temperature for langatate, langanite and langasite," in *Proc. IEEE International Frequency Control Symposium*, 2000, pp. 200–205.

- [36] B. V. Mill and Y. V. Pisarevsky, “Langasite-type materials: from discovery to present state,” in *Proc. of the IEEE International Frequency Control Symposium*, 2000, pp. 133–144.
- [37] I. A. Andreev, “Two decades following the discovery of thermally stable elastic properties of $\text{La}_3\text{Ga}_5\text{SiO}_{14}$ crystal and coining of the term ‘langasite’ (a review).” *Technical Physics*, vol. 49, no. 9, pp. 1101 – 1103, 2004.
- [38] I. Andreev, “Single crystals of the langasite family: an intriguing combination of properties promising for acoustoelectronics,” *Technical Physics*, vol. 51, no. 6, pp. 758 – 64, 2006.
- [39] B. Chai, J. L. Lefaucheur, Y. Y. Ji, and H. Qiu, “Growth and evaluation of large size LGS ($\text{La}_3\text{Ga}_5\text{SiO}_{14}$) LGN ($\text{La}_3\text{Ga}_{5.5}\text{Nb}_{0.5}\text{O}_{14}$) and LGT ($\text{La}_3\text{Ga}_{5.5}\text{Ta}_{0.5}\text{O}_{14}$) single crystals,” in *Proc. of the IEEE International Frequency Control Symposium*, 1998, pp. 748–760.
- [40] B. Chai, H. Qiu, Y. Y. Ji, and J. L. Lefaucheur, “Growth of high quality single domain crystals of langasite family compounds,” in *Proc. of the IEEE International Frequency Control Symposium*, 1999, pp. 821–828.
- [41] J. Bohm, E. Chilla, C. Flannery, H.-J. Frohlich, T. Hauke, R. Heimann, M. Hengst, and U. Straube, “Czochralski growth and characterization of piezoelectric single crystals with langasite structure: $\text{La}_3\text{Ga}_5\text{SiO}_{14}$ (LGS), $\text{La}_3\text{Ga}_{5.5}\text{Nb}_{0.5}\text{O}_{14}$ (LGN) and $\text{La}_3\text{Ga}_{5.5}\text{Ta}_{0.5}\text{O}_{14}$ (LGT). II. Piezoelectric and elastic properties,” *Journal of Crystal Growth*, vol. 216, no. 1-4, pp. 293 – 298, 2000.
- [42] J. Bohm, R. Heimann, M. Hengst, R. Roewer, and J. Schindler, “Czochralski growth and characterization of piezoelectric single crystals with langasite structure: $\text{La}_3\text{Ga}_5\text{SiO}_{14}$ (LGS), $\text{La}_3\text{Ga}_{5.5}\text{Nb}_{0.5}\text{O}_{14}$ (LGN) and $\text{La}_3\text{Ga}_{5.5}\text{Ta}_{0.5}\text{O}_{14}$ (LGT). Part I.” *Journal of Crystal Growth*, vol. 204, no. 1-2, pp. 128 – 136, 1999.
- [43] R. Fachberger, T. Holzheu, E. Riha, E. Born, P. Pongratz, and H. Cerva, “Langasite and langatate nonuniform material properties correlated to the performance of SAW devices,” in *Proc. of the IEEE International Frequency Control Symposium*, 2001, pp. 235–239.
- [44] C. Besson, “Scientific challenges in oil and gas exploration and production,” in *OECD Global Science Forum*, 2006.
- [45] A. Talevski, S. Carlsen, and S. Petersen, “Research challenges in applying intelligent wireless sensors in the oil, gas and resources industries,” in *Proc. of IEEE International Conf. on Industrial Informatic*, 2009, pp. 464 – 469.
- [46] S. Carlsen, A. Skavhaug, S. Petersen, and P. Doyle, “Using wireless sensor networks to enable increased oil recovery,” in *Proc. of IEEE International Conf. on Emerging Technologies and Factory Automation*, Sept. 2008, pp. 1039 – 1048.

- [47] President's Committee of Advisors on Science and Technology, Panel of Energy Research and Development, *Report to the President on Federal Energy Research and Development for the Challenges of the 21st Century*, J. P. Holdren, Ed. Washington, D.C.: Report for Office of Science and Technology Policy, Executive Office of the President of the United States, 1997.
- [48] EG&G Technical Services Inc., *Fuel Cell Handbook*, 7th ed. for the National Energy Technology Lab, U.S. Department of Energy, 2004. [Online]. Available: <http://www.netl.doe.gov/technologies/coalpower/fuelcells/seca/refshelf.html>
- [49] R. Romanosky, "Development of harsh environment sensor platform for fossil energy applications," in *12th International Meeting on Chemical Sensors*, 2008, keynote Speaker.
- [50] Y. Yi, V. McDonell, J. Brouwer, M. Fujiwara, and M. Adachi, "Emissions sensors for high temperature fuel cell applications," in *Proc. of IEEE Sensors*, 2005, pp. 979–982.
- [51] R. G. DeAnna, "Wireless telemetry for gas-turbine applications," NASA Glenn Research Center, Tech. Rep., 2000. [Online]. Available: <http://gltrs.grc.nasa.gov/reports/2000/TM-2000-209815.pdf>
- [52] S. Maley, R. Romanosky, and Z.-Y. Chen, "Sensors and controls workshop summary report," National Energy Technology Lab., US Dept. of Energy, Tech. Rep., 2001, report number: DOE/NETL-2002/1162.
- [53] I. Stambler, "Diagnostic health monitoring will reduce new technology O&M risk," *Gas Turbine World*, vol. 36, no. 1, pp. 28–31, 2006.
- [54] N. Docquier and S. Candel, "Combustion control and sensors: a review," *Progress in Energy and Combustion Science*, vol. 28, no. 2, pp. 107 – 150, 2002.
- [55] R. A. Dennis, Ed., *The Gas Turbine Handbook*. National Energy Technology Laboratory, US Department of Energy, 2006.
- [56] J. C. Fulton, "Sensors and controls for the steel industry; a Department of Energy view," in *American Control Conference*, 1984, pp. 1862 –1863.
- [57] National Materials Advisory Board, *Materials for High-Temperature Semiconductor Devices*. Washington, D.C.: National Academic Press, 1995.
- [58] W. Fleming, "New automotive sensors: A review," *Sensors Journal, IEEE*, vol. 8, no. 11, pp. 1900 –1921, Nov. 2008.
- [59] P. J. Heaney, *Silica: Physical Behavior, Geochemistry and Material Applications*. Mineralogical Society of America, 1994, ch. 1: Structure and Chemistry of the Low-Pressure Silica Polymorphs, pp. 1–40.

- [60] J. Hornsteiner, E. Born, G. Fischerauer, and E. Riha, "Surface acoustic wave sensors for high-temperature applications," in *Proc. of the IEEE International Frequency Control Symposium*, 1998, pp. 615–620.
- [61] H. Seh, H. Fritze, and H. Tuller, "Defect chemistry of langasite. part III. predictions of electrical and gravimetric properties and application to operation of high temperature crystal microbalance," *Journal of Electroceramics*, vol. 18, no. 1-2, pp. 139 – 47, 2007.
- [62] H. Thanner, P. Krempl, W. Wallnofer, and P. Worsch, "GaPO₄ high temperature crystal microbalance with zero temperature coefficient," *Vacuum*, vol. 67, no. 3-4, pp. 687 – 91, 2002.
- [63] I. Josan, C. Boianceanu, G. Brezeanu, V. Obreja, M. Avram, D. Puscasu, and A. Ioncea, "Extreme environment temperature sensor based on silicon carbide schottky diode," in *Proc. International Semiconductor Conference*, vol. 2, 2009, pp. 525–528.
- [64] R. R. Grzybowski, "Advances in electronic packaging technologies to temperatures as high as 500 °C," in *Proc. High-Temperature Electronic Materials, Devices and Sensors Conference*, 1998, pp. 207–215.
- [65] —, "Long term behavior of passive components for high temperature applications - an update," in *Proc. High-Temperature Electronic Materials, Devices and Sensors Conference*, 1998, pp. 172–179.
- [66] R. Guidotti, "High-temperature batteries for geothermal and oil/gas borehole applications," in *Energy Conversion Engineering Conference and Exhibit*, vol. 2, 2000, pp. 1276 –1286.
- [67] L. B. Zhao, Y. L. Zhao, and Z. D. Jiang, "Design and fabrication of a piezoresistive pressure sensor for ultra high temperature environment," *Journal of Physics: Conference Series*, vol. 48, pp. 178–183, 2006.
- [68] S. Akbar, P. Dutta, and C. Lee, "High-temperature ceramic gas sensors: a review," *International Journal of Applied Ceramic Technology*, vol. 3, no. 4, pp. 302–311, 2006.
- [69] E. Birdsell and M. G. Allen, "Wireless chemical sensors for high temperature environments," in *Solid-State Sensors, Actuators, and Microsystems Workshop*, 2006, pp. 212–215.
- [70] J.-F. Lei and H. A. Will, "Thin-film thermocouples and strain-gauge technologies for engine applications," *Sensors and Actuators, A: Physical*, vol. 65, no. 2-3, pp. 187 – 193, 1998.
- [71] L. Michalski, K. Eckersdorf, J. Kucharski, and J. McGhee, *Temperature Measurement*, 2nd ed. New York: John Wiley & Sons, 2001.

- [72] C. S. Nelson, D. Chen, J. Ralph, and E. D’Herde, “The development of a RTD temperature sensor for exhaust applications,” in *SAE World Congress*, 2004, paper 2004-01-1421.
- [73] J. Gutleber, J. Brogan, R. Gambino, C. Gouldstone, R. Greenlaw, S. Sampath, J. Longtin, and D. Zhu, “Embedded temperature and heat flux sensors for advanced health monitoring of turbine engine components,” in *Aerospace Conference, 2006 IEEE*, 2006, p. 9 pp.
- [74] D. Mitchell, A. Kulkarni, E. Roesch, R. Subramanian, A. Burns, J. Brogan, R. Greenlaw, A. Lostetter, M. Schupbach, J. Fraley, and R. Waits, “Development and F-class industrial gas turbine engine testing of smart components with direct write embedded sensors and high temperature wireless telemetry,” in *Proceedings of the ASME Turbo Expo*, vol. 2, 2008, pp. 381–388.
- [75] G. Coviello, V. Finazzi, J. Villatoro, and V. Pruneri, “Thermally stabilized PCF-based sensor for temperature measurements up to 1000 °C,” *Optics Express*, vol. 17, no. 24, pp. 21 551–21 559, 2009.
- [76] D. Gahan, S. Fasham, and A. Harpin, “High temperature fiber optic pressure sensors for engine dynamics and health monitoring,” in *Proc. IEEE Avionics, Fiber-Optics and Phototonics and Photonics Technology Conf.*, 2009, pp. 23–24.
- [77] A. Wang, Y. Zhu, and G. Pickrell, “Optical fiber high-temperature sensors,” *Optics and Photonics News*, vol. 20, no. 3, pp. 26 – 31, 2009.
- [78] J. Wang, B. Dong, E. Lally, J. Gong, M. Han, and A. Wang, “Multiplexed high temperature sensing with sapphire fiber air gap-based extrinsic fabry-perot interferometers,” *Optics Letters*, vol. 35, no. 5, pp. 619–621, 2010.
- [79] M. Austin, “Sensor application opportunities for aerospace propulsion systems,” in *Proc. IEEE Avionics, Fiber-Optics and Phototonics and Photonics Technology Conf.*, 2009, pp. 21–22.
- [80] L. C. Lynnworth and V. Mágori, “Industrial process control sensors and systems,” in *Ultrasonic Instruments and Devices I - Reference for Modern Instrumentation, Techniques, and Technology*, ser. Physical Acoustics, A. D. P. R.N. Thurston and E. P. Papadakis, Eds. Waltham, Massachusetts: Academic Press, 1999, vol. 23, pp. 275 – 470.
- [81] T. Matsumoto, Y. Nagata, T. Nose, and K. Kawashima, “Laser ultrasonics for measurements of high-temperature elastic properties and internal temperature distribution,” *Review of Scientific Instruments*, vol. 72, no. 6, pp. 2777 – 2783, 2001.
- [82] P. Schmidt, D. Walker, D. Yuhas, and M. Mutton, “Thermal measurement of harsh environments using indirect acoustic pyrometry,” in *ASME Conference Proceedings*, no. 42959, 2007, pp. 55–61.

- [83] D. E. Yuhas, M. J. Mutton, J. R. Remiasz, and C. L. Vorres, "Ultrasonic measurements of bore temperature in large caliber guns," *AIP Conference Proceedings*, vol. 1096, no. 1, pp. 1759–1766, 2009.
- [84] L. C. Lynnworth, "Industrial applications of ultrasound, a review II: Measurements, tests, and process control using low-intensity ultrasound," *IEEE Transactions on Sonics and Ultrasonics*, vol. 22, no. 2, pp. 71–100, 1975.
- [85] W. K. Spratt and J. F. Vetelino, "Torsional acoustic waveguide sensor for temperature and liquid level," in *Proc. of the IEEE International Frequency Control Symposium*, 2009, pp. 850–854.
- [86] M. Kobayashi, C.-K. Jen, J. Bussiere, and K.-T. Wu, "High-temperature integrated and flexible ultrasonic transducers for nondestructive testing," *NDT & E International*, vol. 42, no. 2, pp. 157 – 161, 2009.
- [87] L. Kessler and D. Yuhas, "Acoustic microscopy–1979," *Proceedings of the IEEE*, vol. 67, no. 4, pp. 526 – 536, 1979.
- [88] C. Scruby and B. Moss, "Non-contact ultrasonic measurements on steel at elevated temperatures," *NDT&E International*, vol. 26, no. 4, pp. 177 – 188, 1993.
- [89] R. Dewhurst, C. Edwards, A. McKie, and S. Palmer, "A remote laser system for ultrasonic velocity measurement at high temperatures," *Journal of Applied Physics*, vol. 63, no. 4, pp. 1225 – 1227, 1988.
- [90] M. Dubois, A. Moreau, and J. Bussiere, "Ultrasonic velocity measurements during phase transformations in steels using laser ultrasonics," *Journal of Applied Physics*, vol. 89, no. 11, pp. 6487 – 6495, 2001.
- [91] M.-H. Nadal, C. Hubert, and R. Oltra, "High temperature shear modulus determination using a laser-ultrasonic surface acoustic-wave device," *Journal of Applied Physics*, vol. 106, p. 024906 (6 pages), 2009.
- [92] D. Queheillait and N. Wadley, "Temperature dependence of the elastic constants of solid and liquid $\text{Cd}_{0.96}\text{Zn}_{0.04}\text{Te}$ obtained by laser ultrasound," *Journal of Applied Physics*, vol. 83, no. 8, pp. 4124 – 4133, 1998.
- [93] A. Pohl, "A review of wireless SAW sensors," *IEEE Transactions on Ultrasonics, Ferroelectrics and Frequency Control*, vol. 47, no. 2, pp. 317 – 332, March 2000.
- [94] E. Mackensen and L. Reindl, *Smart Sensors and MEMS*. Springer Netherlands, 2005, ch. Wireless Passive SAW Identification Marks and Sensors, pp. 155–202.
- [95] G. Bruckner and R. Fachberger, "SAW ID tag for industrial application with large data capacity and anticollision capability," in *Proc. of the IEEE International Ultrasonics Symposium*, Nov. 2008, pp. 300 – 303.

- [96] A. Canabal, P. Davulis, E. Dudzik, and M. Pereira da Cunha, "CDMA and FSCW surface acoustic wave temperature sensors for wireless operation at high temperatures," in *Proc. IEEE International Ultrasonic Symposium*, 2009, pp. 807–810.
- [97] A. Canabal, P. Davulis, G. Harris, and M. Pereira da Cunha, "High-temperature battery-free wireless microwave acoustic resonator sensor system," *Electronics Letters*, vol. 46, no. 7, pp. 471–472, 2010.
- [98] V. Kalinin, B. Dixon, and J. Beckley, "Optimization of resonant frequency measurement algorithm for wireless passive SAW sensors," in *Proc. of the IEEE International Frequency Control Symposium*, April 2009, pp. 90–95.
- [99] V. Kalinin, "Passive wireless strain and temperature sensors based on SAW devices," in *IEEE Radio and Wireless Conference*, Sept. 2004, pp. 187–190.
- [100] S.-Q. Wang, J. Harada, and S. Uda, "A wireless surface acoustic wave temperature sensor using langasite as substrate material for high-temperature applications," *Japanese Journal of Applied Physics*, vol. 42, no. 9B, pp. 6124–6127, 2003.
- [101] R. Hauser, R. Fachberger, G. Bruckner, W. Smetana, R. Reicher, A. Stelzer, S. Scheiblhofer, and S. Schuster, "A wireless SAW-based temperature sensor for harsh environment," in *Proceedings of IEEE Sensors*, vol. 2, Oct. 2004, pp. 860–863.
- [102] R. Fachberger, G. Bruckner, R. Hauser, and L. Reindl, "Wireless SAW based high-temperature measurement systems," in *Proc. of the IEEE International Frequency Control Symposium*, 2006, pp. 358–367.
- [103] T. Aubert, O. Elmazria, and M. B. Assouar, "Wireless and batteryless surface acoustic wave sensors for high temperature environments," in *Proc. International Conference on Electronic Measurement. Instruments*, 2009, pp. 2–890–2–898.
- [104] J. J. Caron, J. C. Andle, and J. F. Vetelino, "Surface acoustic wave substrates for high temperature applications," in *Proc. IEEE International Frequency Control Symposium*, 1996, pp. 222–227.
- [105] G. Gautschi, *Piezoelectric Sensorics: Force, Strain, Pressure, Acceleration and Acoustic Emissions Sensors, Materials and Amplifiers*. New York: Springer, 2002.
- [106] D. L. White, "Beta-quartz as high-temperature piezoelectric material," *The Journal of the Acoustical Society of America*, vol. 31, no. 3, pp. 311–314, 1959.
- [107] T. Uno and S. Noge, "Piezoelectric and elastic properties of β phase quartz," *Ferroelectrics*, vol. 224, no. 1, pp. 63–70, 1999.

- [108] J. Haines, O. Cambon, D. A. Keen, M. G. Tucker, and M. T. Dove, "Structural disorder and loss of piezoelectric properties in alpha-quartz at high temperature," *Applied Physics Letters*, vol. 81, no. 16, pp. 2968–2970, 2002.
- [109] R. Bechmann, "Elastic and piezoelectric constants of alpha-quartz," *Phys. Rev.*, vol. 110, no. 5, pp. 1060–1061, Jun 1958.
- [110] D. S. Bailey, "A study of berlinite (alpha-AlPO₄) for microwave acoustic applications," Master's thesis, Electrical Engineering Dept., University of Maine, Orono, ME, 1983.
- [111] Y. Muraoka and K. Kihara, "The temperature dependence of the crystal structure of berlinite, a quartz-type form of AlPO₄," *Physics and Chemistry of Minerals*, vol. 24, pp. 243–253, 1997.
- [112] J. Haines, O. Cambon, E. Philippot, L. Chapon, and S. Hull, "A neutron diffraction study of the thermal stability of the α -quartz-type structure in germanium dioxide," *Journal of Solid State Chemistry*, vol. 166, no. 2, pp. 434 – 441, 2002.
- [113] O. Cambon, P. Yot, S. Rul, J. Haines, and E. Philippot, "Growth and dielectric characterization of large single crystals of GaAsO₄, a novel piezoelectric material," *Solid State Sciences*, vol. 5, no. 3, pp. 469 – 472, 2003.
- [114] O. Cambon, J. Haines, G. Fraysse, J. Detaint, B. Capelle, and A. Van der Lee, "Piezoelectric characterization and thermal stability of a high-performance - quartz-type material, gallium arsenate," *Journal of Applied Physics*, vol. 97, no. 7, pp. 74110 – 17, 2005.
- [115] Y. V. Pisarevsky, O. Y. Silvestrova, E. Philippot, D. V. Balitsky, D. Y. Pisharovsky, and V. S. Balitsky, "Piezoelectric, dielectric and elastic properties of germanium dioxide single crystals," in *Proc. IEEE International Frequency Control Symposium*, 2000, pp. 177–179.
- [116] O. Cambon and J. Haines, "Structure-piezoelectric property relationships in α -quartz isotopes: design and characterization of high performance piezoelectric materials," in *Proc. IEEE International Frequency Control Symposium*, 2003, pp. 650–653.
- [117] P. F. Bordui, R. G. Norwood, C. D. Bird, and J. T. Carella, "Stoichiometry issues in single-crystal lithium tantalate," *Journal of Applied Physics*, vol. 78, no. 7, pp. 4647–4650, 1995.
- [118] D. Damjanovic, "Materials for high temperature piezoelectric transducers," *Current Opinion in Solid State and Materials Science*, vol. 3, no. 5, pp. 469 – 73, 1998.
- [119] Z.-G. Gai, J.-F. Wang, W.-b. Sun, C.-M. Wang, M.-L. Zhao, S.-Q. Sun, B.-Q. Ming, P. Qi, L.-m. Zheng, J. Du, S. Zhang, and T. R. Shrout, "Ultrahigh

- temperature $\text{Bi}_3\text{Ti}_{0.96}\text{Sc}_{0.02}\text{Ta}_{0.02}\text{NbO}_9$ -based piezoelectric ceramics.” *Journal of Applied Physics*, vol. 104, no. 2, p. 024106 (4 pages), 2008.
- [120] M. Villegas, A. C. Caballero, T. Jardiel, C. Aragón, J. Maudes, and I. Caro, “Evaluation of piezoelectric properties of $\text{Bi}_4\text{Ti}_3\text{O}_{12}$ based ceramics at high temperature,” *Ferroelectrics*, vol. 393, no. 1, pp. 44 – 53, 2009.
 - [121] N. Schmarje, K. Kirk, and S. Cochran, “1-3 connectivity lithium niobate composites for high temperature operation,” *Ultrasonics*, vol. 47, no. 1-4, pp. 15 – 22, 2007.
 - [122] E. Born, J. Hornsteiner, T. Metzger, and E. Riha, “Diffusion of niobium in congruent lithium niobate,” *Physica Status Solidi A*, vol. 177, no. 2, pp. 393 – 400, 2000.
 - [123] R. Hauser, L. Reindl, and J. Biniash, “High-temperature stability of LiNbO_3 based SAW devices,” in *Proc. IEEE International Ultrasonics Symposium*, 2003, pp. 192–195.
 - [124] B. H. Fisher and D. C. Malocha, “Cryogenic liquid sensing using SAW devices,” in *Proc. IEEE International Frequency Control Symposium*, May 2007, pp. 505–510.
 - [125] S. Zhang, Y. Fei, E. Frantz, D. Snyder, B. Chai, and T. Shrout, “High-temperature piezoelectric single crystal $\text{ReCa}_4\text{O}(\text{BO}_3)_3$ for sensor applications,” *IEEE Transactions on Ultrasonics, Ferroelectrics, and Frequency Control*, vol. 55, pp. 2703–2708, 2008.
 - [126] S. Zhang, E. Frantz, R. Xia, W. Everson, J. Randi, D. W. Snyder, and T. R. Shrout, “Gadolinium calcium oxyborate piezoelectric single crystals for ultra-high temperature ($>1000^\circ\text{C}$) applications.” *Journal of Applied Physics*, vol. 104, no. 8, p. 084103 (7 pages), 2008.
 - [127] P. Schiopu, I. Cristea, N. Grosu, and A. Craciun, “Comparative study of GaPO_4 , langasite, and LiNbO_3 properties with application in surface acoustic waves microdevices,” in *Proc. International Spring Seminar on Electronics Technology*, 2009, pp. 1–7.
 - [128] W. Wallnofer, J. Stadler, and P. Krempel, “Temperature dependence of elastic constants of GaPO_4 and its influence of BAW and SAW devices,” in *7th European Frequency and Time Forum*, 1993, pp. 653–657.
 - [129] J. Detaint, J. Schwartzel, A. Zarka, B. Capelle, D. Cochet-Muchy, and E. Philippot, “Properties of the plane and plano-convex resonators using berlinite, gallium phosphate and langasite,” in *Proc. IEEE International Ultrasonics Symposium*, 1994, pp. 1051–1056.

- [130] P. W. Krempl, "Quartz homeotypic gallium-orthophosphate-a new high tech piezoelectric material," in *Proc. IEEE International Ultrasonics Symposium*, 1994, pp. 949–954.
- [131] P. Davulis, J. A. Kosinski, and M. Pereira da Cunha, "GaPO₄ stiffness and piezoelectric constants measurements using the combined thickness excitation and lateral field technique," in *Proc. of the IEEE International Frequency Control Symposium*, 2006, pp. 664–669.
- [132] Piezocryst Advanced Sensorics GmbH, "Piezoelectric materials," 2010. [Online]. Available: <http://www.piezocryst.com>
- [133] P. W. Krempl, C. Reiter, W. Wallnofer, and J. Neubig, "Temperature sensors based on GaPO₄," in *Proc. IEEE International Ultrasonics Symposium*, 2002, pp. 949–952.
- [134] P. M. Worsch, P. W. Krempl, and W. Wallnofer, "GaPO₄ crystals for sensor applications," in *Proc. of IEEE Sensors*, vol. 1, 2002, pp. 589 – 593.
- [135] W. Buff, M. Binhack, S. Klett, M. Hamsch, R. Hoffmann, F. Krispel, and W. Wallnofer, "SAW resonators at high temperatures," in *Proc. IEEE International Ultrasonic Symposium*, 2003, pp. 187–191.
- [136] M. Hamidon, V. Skarda, N. White, F. Krispel, P. Krempl, M. Binhack, and W. Buff, "Fabrication of high temperature surface acoustic wave devices for sensor applications," *Sensors and Actuators A (Physical)*, vol. 123-124, pp. 403 – 407, 2005.
- [137] J. Haines, O. Cambon, N. Prudhomme, G. Fraysse, D. A. Keen, L. C. Chapon, and M. G. Tucker, "High-temperature, structural disorder, phase transitions, and piezoelectric properties of GaPO₄," *Physical Review B (Condensed Matter and Materials Physics)*, vol. 73, no. 1, p. 014103, 2006.
- [138] E. Chilla, C. M. Flannery, H.-J. Frohlich, and U. Straube, "Elastic properties of langasite-type crystals determined by bulk and surface acoustic waves," *Journal of Applied Physics*, vol. 90, no. 12, pp. 6084–6091, 2001.
- [139] I. Andreev and M. Dubovik, "A new piezoelectric material, langasite (La₃Ga₅SiO₁₄), with a zero temperature coefficient of the elastic vibration frequency," *Soviet Technical Physics Letters*, vol. 10, no. 4, pp. 205 – 7, 1984.
- [140] N. F. Naumenko and L. P. Solie, "Optimal cut of langasite for high performance SAW devices," in *Proc. of the IEEE International Ultrasonics Symposium*, vol. 1, 1999, pp. 243–248 vol.1.
- [141] M. Pereira da Cunha, D. C. Malocha, E. L. Adler, and K. J. Casey, "Surface and pseudo surface acoustic waves in langatate: predictions and measurements," *IEEE Transactions on Ultrasonics, Ferroelectrics, and Frequency Control*, vol. 49, no. 9, pp. 1291–1299, 2002.

- [142] M. Dvoesherstov, S. Petrov, V. Cherednik, and A. Chirimanov, “New optimal orientations for surface acoustic waves in langasite, langanite, and langatate piezoelectric crystals,” *Technical Physics*, vol. 47, no. 8, pp. 1032 – 1037, 2002.
- [143] V. B. Gruzinenco, A. V. Medvedev, A. N. Matsak, and O. A. Buzanov, “Miniature BAW resonators and filters based on single crystals of strong piezoelectrics,” in *Proc. IEEE International Frequency Control Symposium*, 2003, pp. 654–656.
- [144] G. Douchet, F. Sthal, E. Bigler, and R. Bourquin, “Temperature compensated cuts in LGT crystal microresonators using length extensional mode,” *IEEE Transactions on Ultrasonics, Ferroelectrics, and Frequency Control*, vol. 56, no. 2, pp. 239–240, 2009.
- [145] —, “A comparison of vibrating beam resonators in quartz, GaPO_4 , LGS and LGT,” *Solid State Sciences*, vol. 12, no. 3, pp. 325–332, 2010.
- [146] O. Le Traon, S. Masson, C. Chartier, and D. Janiaud, “LGS and GaPO_4 piezoelectric crystals: New results,” *Solid State Sciences*, vol. 12, no. 3, pp. 318–324, 2010.
- [147] R. C. Smythe, R. C. Helmbold, I. Hague, G. E., and K. A. Snow, “Langasite, langanite, and langatate bulk-wave Y-cut resonators,” *IEEE Transactions on Ultrasonics, Ferroelectrics, and Frequency Control*, vol. 47, no. 2, pp. 355–360, 2000.
- [148] T. R. Beaucage, E. P. Beenfeldt, S. A. Speakman, W. D. Porter, E. A. Payzant, and M. Pereira da Cunha, “Comparison of high temperature crystal lattice and bulk thermal expansion measurements of LGT single crystal,” in *Proc. IEEE International Frequency Control Symposium*, 2006, pp. 658–663.
- [149] M. Pereira da Cunha, R. J. Lad, T. Moonlight, G. Bernhardt, and D. J. Frankel, “High temperature stability of langasite surface acoustic wave devices,” in *Proc. IEEE International Ultrasonics Symposium*, 2008, pp. 205–208.
- [150] J. Bardong, G. Bruckner, M. Kraft, and R. Fachberger, “Influence of packaging atmospheres on the durability of high-temperature SAW sensors,” in *Proc. of the IEEE Int’l Ultrason. Symp.*, 2009, pp. 1680–1683.
- [151] S. C. Moulzolf, D. J. Frankel, G. P. Bernhardt, B. Nugent, and R. J. Lad, “Thin film electrodes and passivation coatings for harsh environment microwave acoustic sensors,” *Proceedings of the SPIE, (Smart Sensors, Actuators, and MEMS V)*, vol. 8066, p. 806606 (9pp.), 2011.
- [152] R. Fachberger, E. Riha, E. Born, and P. Pongratz, “Homogeneity of langasite and langatate wafers for acoustic wave applications,” in *Proc. of the IEEE International Ultrasonics Symposium*, 2003, pp. 100–109.

- [153] B. H. T. Chai, A. N. P. Bustamante, and M. C. Chou, "A new class of ordered langasite structure compounds," in *Proc. of the IEEE International Frequency Control Symposium*, 2000, pp. 163–168.
- [154] H. Takeda, J. Sato, T. Kato, K. Kawasaki, H. Morikoshi, K. Shimamura, and T. Fukuda, "Synthesis and characterization of $\text{Sr}_3\text{TaGa}_3\text{Si}_2\text{O}_{14}$ single crystals," *Materials Research Bulletin*, vol. 35, no. 2, pp. 245 – 252, 2000.
- [155] M. M. C. Chou, S. Jen, and B. H. T. Chai, "Investigation of crystal growth and material constants of ordered langasite structure compounds," in *Proc. IEEE International Frequency Control Symposium*, 2001, pp. 250–254.
- [156] —, "New ordered langasite structure compounds-crystal growth and preliminary investigation of the material properties," in *Proc. IEEE Ultrasonics Symposium*, 2001, pp. 225–230.
- [157] D. Puccio, D. C. Malocha, and M. M. C. Chou, "Investigations of STGS, SNGS, CTGS, & CNGS materials for use in SAW applications," in *Proc. IEEE International Frequency Control Symposium*, 2003, pp. 627–630.
- [158] Y. Pisarevsky, B. Mill, N. Moiseeva, and A. Yakimov, "Ordered $\text{Ca}_3\text{TaGa}_3\text{Si}_2\text{O}_{14}$ crystals: growth, electromechanical and optical properties," in *18th European Frequency and Time Forum (EFTF 2004)*, 2004, pp. 216 – 219.
- [159] J. Chen, Y. Zheng, H. Kong, and E. Shi, "Piezoelectricity of $\text{A}_3\text{BC}_3\text{D}_2\text{O}_{14}$ structure crystals," *Applied Physics Letters*, vol. 89, no. 1, p. 12901 (3 pages), 2006.
- [160] S. Zhang, Y. Zheng, H. Kong, J. Xin, E. Frantz, and T. R. Shrout, "Characterization of high temperature piezoelectric crystals with an ordered langasite structure," *Journal of Applied Physics*, vol. 105, no. 11, p. 114107 (6 pages), 2009.
- [161] W. L. Johnson, S. A. Kim, and S. Uda, "Acoustic loss in langasite and langanite," in *Proc. IEEE International Frequency Control Symposium*, 2003, pp. 646–649.
- [162] W. L. Johnson, S. A. Kim, S. Uda, and C. F. Rivenbark, "Contributions to anelasticity in langasite and langatate," *Journal of Applied Physics*, vol. 110, no. 12, p. 123528, 2011.
- [163] R. C. Smythe, R. C. Helmbold, G. E. Hague, and K. A. Snow, "Langasite, langanite, and langatate resonators: recent results," in *Proc. IEEE International Frequency Control Symposium*, 1999, pp. 816–820.
- [164] Y. Kim and A. Ballato, "Force-frequency effect of Y-cut langanite and Y-cut langatate," *IEEE Transactions on Ultrasonics, Ferroelectrics, and Frequency Control*, vol. 50, no. 12, pp. 1678–1682, 2003.

- [165] J. Hornsteiner, E. Born, and E. Riha, “Langasite for high temperature surface acoustic wave applications,” *Physica Status Solidi A*, vol. 163, no. 1, pp. 3 – 4, 1997.
- [166] J. Mrosk, C. Ettl, L. Berger, P. Dabala, H. Fecht, G. Fischerauer, J. Hornsteiner, K. Riek, E. Riha, E. Born, M. Werner, A. Dommann, J. Auersperg, E. Kieselstein, B. Michel, and A. Mucha, “SAW sensors for high temperature applications,” in *Proc. IEEE Industrial Electronics Society Conf.*, vol. 4, 1998, pp. 2386–2390.
- [167] M. Honal, R. Fachberger, T. Holzheu, E. Riha, E. Born, P. Pongratz, and A. Bausewein, “Langasite surface acoustic wave sensors for high temperatures,” in *Proc. IEEE International Frequency Control Symposium*, 2000, pp. 113–118.
- [168] J. Mrosk, L. Berger, C. Ettl, H.-J. Fecht, G. Fischerauer, and A. Dommann, “Materials issues of SAW sensors for high-temperature applications,” *IEEE Transactions on Industrial Electronics*, vol. 48, no. 2, pp. 258 –264, Apr 2001.
- [169] J. A. Thiele and M. Pereira da Cunha, “High temperature LGS SAW devices with Pt/WO₃ and Pd sensing films,” in *Proc. of the IEEE International Ultrasonics Symposium*, 2003, pp. 1750–1753.
- [170] —, “Dual configuration high temperature hydrogen sensor on LGS SAW devices,” in *Proc. of the IEEE International Ultrasonics Symposium*, 2004, pp. 809–812.
- [171] M. Pereira da Cunha, T. Moonlight, R. Lad, G. Bernhardt, and D. J. Frankel, “Enabling very high temperature acoustic wave devices for sensor & frequency control applications,” in *Proc. IEEE International Ultrasonics Symposium*, 2007, pp. 2107–2110.
- [172] M. Pereira da Cunha, “Surface acoustic wave devices for high temperature applications,” U.S. Patent 7 285 894, 2007.
- [173] M. Pereira da Cunha, T. Moonlight, R. Lad, D. Frankel, and G. Bernhard, “High temperature sensing technology for applications up to 1000 °C,” in *Proc. IEEE Sensors*, 2008, pp. 752–755.
- [174] D. Frankel, G. Bernhardt, B. Sturtevant, T. Moonlight, M. Pereira da Cunha, and R. Lad, “Stable electrodes and ultrathin passivation coatings for high temperature sensors in harsh environments,” in *Proc. IEEE Sensors*, Oct. 2008, pp. 82 –85.
- [175] D. Gallimore, T. Moonlight, and M. Pereira da Cunha, “Extraction of Pt/Rh/ZrO₂ high temperature elastic constants,” in *Proc. of the IEEE International Ultrasonic Symposium*, 2009, pp. 2797–2800.

- [176] B. J. Meulendyk and M. Pereira da Cunha, "Suppression of transverse waveguide modes for SAW resonators with Pt and Pt/Rh/ZrO₂ electrodes," in *Proc. of the IEEE Int'l Ultrasonic Symp.*, 2009, pp. 2810–2813.
- [177] D. Richter, J. Sauerwald, H. Fritze, E. Ansorge, and B. Schmidt, "Miniaturized resonant gas sensors for high-temperature applications," in *Proc. IEEE Sensors*, 2008, pp. 1536 – 1539.
- [178] J. Bardong, M. Schulz, M. Schmitt, I. Shrena, D. Eisele, E. Mayer, L. Reindl, and H. Fritze, "Precise measurements of BAW and SAW properties of langasite in the temperature range from 25 °C to 1000 °C," in *Proc. of the IEEE International Frequency Control Symposium*, 2008, pp. 326 – 331.
- [179] M. Schulz, D. Richter, and H. Fritze, "Material and resonator design dependant loss in langasite bulk acoustic wave resonators at high temperatures," in *Proc. of the IEEE Int'l Ultrasonic Symp.*, 2009, pp. 1676–1679.
- [180] H. Fritze and H. Tuller, "Langasite for high-temperature bulk acoustic wave applications," *Applied Physics Letters*, vol. 78, no. 7, pp. 976 – 997, 2001.
- [181] H. Fritze, H. Seh, H. Tuller, and G. Borchardt, "Operation limits of langasite high temperature nanobalances," *Journal of the European Ceramic Society*, vol. 21, no. 10-11, pp. 1473 – 1477, 2001.
- [182] H. Fritze, M. Schulz, H. Seh, and H. Tuller, "High temperature operation and stability of langasite resonators," in *Semiconductor Materials for Sensing Symposium (in Mater. Res. Soc. Symp. Proc.)*, vol. 828, 2005, pp. 145–50.
- [183] D. Richter, H. Fritze, T. Schneider, P. Hauptmann, N. Bauersfeld, K.-D. Kramer, K. Wiesner, M. Fleischer, G. Karle, and A. Schubert, "Integrated high temperature gas sensor system based on bulk acoustic wave resonators," *Sensors and Actuators B: Chemical*, vol. 118, no. 1-2, pp. 466 – 471, 2006.
- [184] E. Ansorge, S. Hirsch, B. Schmidt, J. Sauerwald, and H. Fritze, "Design and fabrication of high-Q langasite resonator arrays for high temperature applications," in *Proc. IEEE International Frequency Control Symposium*, 2008, pp. 619–624.
- [185] E. Ansorge, S. Schimpf, S. Hirsch, J. Sauerwald, H. Fritze, and B. Schmidt, "Evaluation of langasite (La₃Ga₅SiO₁₄) as a material for high temperature microsystems," *Sensors and Actuators A: Physical*, vol. 130-131, pp. 393 – 396, 2006.
- [186] —, "Piezoelectric driven resonant beam array in langasite (La₃Ga₅SiO₁₄)," *Sensors and Actuators A: Physical*, vol. 132, no. 1, pp. 271 – 277, 2006.
- [187] J. Sauerwald, D. Richter, E. Ansorge, B. Schmidt, and H. Fritze, "Doped monolithic langasite structures for high temperature MEMS," *Solid State Ionics, Diffusion & Reactions*, vol. 179, no. 21-26, pp. 928 – 931, 2008.

- [188] J. Sauerwald, M. Schulz, D. Richter, and H. Fritze, “Micromachined piezoelectric structures for high-temperature sensors,” *Journal of Electroceramics*, vol. 22, no. 1, pp. 180 – 4, 2009.
- [189] R. Fachberger, G. Bruckner, R. Hauser, J. Biniasch, L. Reindl, and C. Ruppel, “Properties of radio frequency Rayleigh waves on langasite at elevated temperatures,” in *Proc. of the IEEE International Ultrasonics Symposium*, 2004, pp. 1223–1226.
- [190] I. Shrena, D. Eisele, E. Mayer, L. M. Reindl, J. Bardong, and M. Schmitt, “SAW-relevant material properties of langasite in the temperature range from 25 to 750 °C: New experimental results,” in *Proc. IEEE International Ultrasonics Symposium*, 2008, pp. 209–212.
- [191] E. Mayer, I. Shrena, D. Eisele, J. Bardong, M. Schmitt, and L. M. Reindl, “Characterization of langasite as a material for SAW based RFID and sensing systems at high temperatures,” in *Proc. IEEE MTT-S International Microwave Workshop on Wireless Sensing, Local Positioning, and RFID*, 2009, pp. 1–4.
- [192] J. Bardong, T. Aubert, N. Naumenko, G. Bruckner, S. Salzmann, and L. Reindl, “Experimental and theoretical investigations of some useful langasite cuts for high-temperature SAW applications,” *Ultrasonics, Ferroelectrics and Frequency Control, IEEE Transactions on*, vol. 60, no. 4, pp. 814–823, 2013.
- [193] P. Nicolay, O. Elmazria, F. Sarry, T. Aubert, L. Bouvot, and M. Hehn, “New measurement method to characterize piezoelectric SAW substrates at very high temperature,” in *Proc. IEEE International Ultrasonics Symposium*, 2008, pp. 1877–1880.
- [194] P. Zheng, D. W. Greve, I. J. Oppenheim, T.-L. Chin, and V. Malone, “Langasite surface acoustic wave sensors: Fabrication and testing,” *IEEE Transactions on Ultrasonics, Ferroelectrics, and Frequency Control*, vol. 59, no. 2, pp. 295–303, 2012.
- [195] M. Schulz and H. Fritze, “Electromechanical properties of langasite resonators at elevated temperatures,” *Renewable Energy*, vol. 33, no. 2, pp. 336 – 41, 2008.
- [196] M. Schulz, J. Sauerwald, D. Richter, and H. Fritze, “Electromechanical properties and defect chemistry of high-temperature piezoelectric materials,” *Ionics*, vol. 15, no. 2, pp. 157 – 161, 2009.
- [197] N. Nakamura, M. Sakamoto, H. Ogi, and M. Hirao, “Elastic constants of langasite and alpha quartz at high temperatures measured by antenna transmission acoustic resonance,” *Review of Scientific Instruments*, vol. 83, no. 7, p. 073901, 2012.
- [198] B. Mill, A. Butashin, G. Khodzhabyan, E. Belokoneva, and N. Belov, “Modified rare-earth gallates with a $\text{Ca}_3\text{Ga}_2\text{Ge}_4\text{O}_{14}$ structure,” *Soviet Physics -*

- Doklady*, vol. 27, no. 6, pp. 434 – 7, 1982, originally in Russian in *Doklady Akademii Nauk SSSR*, Vol. 264, N. 6, pp. 1385-1389.
- [199] A. Kaminskii, B. Mill, I. Silvestrova, and G. Khodzhabyan, “The nonlinear active material $(\text{La}_{1-x}\text{Nd}_x)_3\text{Ga}_3\text{SiO}_{14}$,” *Bulletin of the Academy of Sciences of the USSR, Physical Series*, vol. 47, no. 10, pp. 25 – 31, 1983.
 - [200] A. Kaminskii, B. Mill, G. Khodzhabyan, A. F. Konstantinova, A. I. Okorochkov, and I. Silvestrova, “Investigation of trigonal $(\text{La}_{1-x}\text{Nd}_x)_3\text{Ga}_3\text{SiO}_{14}$: Part 1. growth and optical properties,” *Physica Status Solidi (a)*, vol. 80, pp. 387–398, 1983.
 - [201] A. Kaminskii, I. Silvestrova, S. E. Sarkison, and G. A. Denisenko, “Investigation of trigonal $(\text{La}_{1-x}\text{Nd}_x)_3\text{Ga}_3\text{SiO}_{14}$: Part 2. spectral laser and electromechanical properties,” *Physica Status Solidi (a)*, vol. 80, pp. 607–620, 1983.
 - [202] V. B. Grouzinenko and V. V. Bezdelkin, “Piezoelectric resonators based on single crystals of strong piezoelectrics,” in *Proc. of the IEEE International Frequency Control Symposium*, 1991, pp. 212–216.
 - [203] S. A. Sakharov, I. M. Larinov, and V. A. Issaev, “Monolithic filters using strong piezoelectrics,” in *Proc. of the IEEE International Frequency Control Symposium*, 1991, pp. 181–183.
 - [204] A. A. Kaminskii, K. Kurbanov, A. A. Markosyan, B. V. Mill, S. E. Sarkisov, and G. G. Khodzhabyan, “Luminescence-absorption properties and low-threshold stimulated emission of Nd^{3+} ions in $\text{La}_3\text{Ga}_{5.5}\text{Ta}_{0.5}\text{O}_{14}$,” *Inorganic Materials*, vol. 21, pp. 1722–1726, 1985.
 - [205] H. Takeda, K. Sugiyama, K. Inaba, K. Shimamura, and T. Fukuda, “Crystal growth and structural characterization of new piezoelectric material $\text{La}_3\text{Ta}_{0.5}\text{Ga}_{5.5}\text{O}_{14}$,” *Japanese Journal of Applied Physics, Part 2*, vol. 36, no. 7B, pp. L919 – L921, 1997.
 - [206] Y. V. Pisarevsky, P. A. Senyushenkov, B. V. Mill, and N. A. Moiseeva, “Elastic, piezoelectric, dielectric properties of $\text{La}_3\text{Ga}_{5.5}\text{Ta}_{0.5}\text{O}_{14}$ single crystals,” in *Proc. IEEE International Frequency Control Symposium*, 1998, pp. 742–747.
 - [207] T. Fukuda, P. Takeda, K. Shimamura, H. Kawanaka, M. Kumatoriya, S. Murakami, J. Sato, and M. Sato, “Growth of new langasite single crystals for piezoelectric applications,” in *Proc. of the IEEE International Symposium on Applications of Ferroelectrics*, 1998, pp. 315 –319.
 - [208] R. C. Smythe, “Material and resonator properties of langasite and langatate: a progress report,” in *Proc. IEEE International Frequency Control Symposium*, 1998, pp. 761–765.

- [209] B. Mill, Y. Pisarevsky, and E. Belokoneva, "Synthesis, growth and some properties of single crystals with the $\text{Ca}_3\text{Ga}_2\text{Ge}_4\text{O}_{14}$ structure," in *Proceedings of the IEEE International Frequency Control Symposium*, 1999, pp. 829 – 834.
- [210] R. C. Smythe and G. E. Hague, "Determination of the piezoelectric constants of LGN, LGS, and LGT," in *Proc. IEEE International Frequency Control Symposium*, 2000, pp. 191–194.
- [211] I. H. Jung, W. J. Yang, A. Yoshikawa, T. Fukuda, and K. H. Auh, "Growth of $\text{La}_{3-x}\text{Ba}_x\text{Ta}_{0.5+x/2}\text{Ga}_{5.5-x/2}\text{O}_{14}$ compounds for the high-temperature piezoelectric applications," *Journal of Crystal Growth*, vol. 262, no. 1-4, pp. 40 – 47, 2004.
- [212] H. Takeda, S. Tanaka, S. Izukawa, H. Shimizu, T. Nishida, and T. Shiosaki, "Effective substitution of aluminum for gallium in langasite-type crystals for a pressure sensor use at high temperature," in *Proc. of the IEEE International Ultrasonics Symposium*, vol. 1, 2005, pp. 560–563.
- [213] S. Zhang, A. Yoshikawa, K. Kamada, E. Frantz, R. Xia, D. Snyder, T. Fukuda, and T. Shrout, "Growth and characterization of high temperature $\text{La}_3\text{Nb}_{0.5}\text{Ga}_{5.3}\text{Al}_{0.2}\text{O}_{14}$ (LNGA) and $\text{La}_3\text{Ta}_{0.5}\text{Ga}_{5.3}\text{Al}_{0.2}\text{O}_{14}$ (LTGA) piezoelectric single crystals," *Solid State Communications*, vol. 48, no. 5-6, pp. 213 – 216, 2008.
- [214] X. Zhang, D. Yuan, and S. Guo, "Sol-gel preparation of a new compound with $\text{Ca}_3\text{Ga}_2\text{Ge}_4\text{O}_{14}$ structure: $\text{La}_3\text{Al}_{5.5}\text{Ta}_{0.5}\text{O}_{14}$," *Journal of Crystal Growth*, vol. 308, no. 1, pp. 80 – 83, 2007.
- [215] M. M. C. Chou, "Investigation of piezoelectric crystals, $\text{La}_3\text{Ga}_{5.5}\text{Ta}_{0.5}\text{O}_{14}$ (LGT), $\text{La}_3\text{Ga}_{5.5}\text{Nb}_{0.5}\text{O}_{14}$ (LGN), $\text{La}_3\text{Ga}_5\text{SiO}_{14}$ (LGS)," Ph.D. dissertation, University of Central Florida, 2000.
- [216] C. Klemenz, M. Berkowski, B. Deveaud-Pledran, and D. C. Malocha, "Defect structure of langasite-type crystals: a challenge for applications," in *Proc. IEEE International Frequency Control Symposium*, 2002, pp. 301–306.
- [217] H. Takeda, T. Fukuda, H. Kawanaka, and N. Onozato, "Effect of starting melt composition on growth of $\text{La}_3\text{Ta}_{0.5}\text{Ga}_{5.5}\text{O}_{14}$ crystal," *Journal of Materials Science: Materials in Electronics*, vol. 12, no. 3, pp. 199 – 202, 2001.
- [218] H. Kimura, S. Uda, and X. Huang, "Relationship between incongruent-melting langatate ($\text{La}_3\text{Ta}_{0.5}\text{Ga}_{5.5}\text{O}_{14}$) and associated phases in the system $\text{La}_2\text{O}_3\text{--Ga}_2\text{O}_3\text{--Ta}_2\text{O}_5$," *Journal of Crystal Growth*, vol. 295, no. 1, pp. 36 – 43, 2006.
- [219] H. Kimura, S. Uda, O. Buzanov, X. Huang, and S. Koh, "The effect of growth atmosphere and Ir contamination on electric properties of $\text{La}_3\text{Ta}_{0.5}\text{Ga}_{5.5}\text{O}_{14}$ single crystal grown by the floating zone and Czochralski method," *Journal of Electroceramics*, vol. 20, no. 2, pp. 73 – 80, 2008.

- [220] T. Taishi, N. Bamba, K. Hoshikawa, and I. Yonenaga, "Single crystal growth of langataite ($\text{La}_3\text{Ta}_{0.5}\text{Ga}_{5.5}\text{O}_{14}$) by vertical bridgman (VB) method along $[2\bar{1}10]$ in air and in an Ar atmosphere," *Journal of Crystal Growth*, vol. 311, no. 1, pp. 205 – 209, 2008.
- [221] S. A. Sakharov, A. N. Zabelin, O. A. Buzanov, and M. Y. Roshchupkin, D.V. and. Barabanenkov, "Physical properties of lanthanum gallium tantalate crystals for high-temperature application," Fomos materials, Moscow, Russia, Tech. Rep., 2007. [Online]. Available: http://www.newpiezo.com/articles/index.htmlhttp://www.newpiezo.com/pdf/Properties_LGT.pdf
- [222] V. Chani, H. Takeda, and T. Fukuda, "Liquid phase epitaxy of films with langasite structure," *Materials Science & Engineering B (Solid-State Materials for Advanced Technology)*, vol. B60, no. 3, pp. 212 – 216, 1999.
- [223] C. Klemenzenz, "High-quality langasite films grown by liquid phase epitaxy," *Journal of Crystal Growth*, vol. 237-239, no. 1, pp. 714 – 19, 2002.
- [224] —, "High-quality $\text{La}_3\text{Ga}_{5.5}\text{Ta}_{0.5}\text{O}_{14}$ and $\text{La}_3\text{Ga}_{5.5}\text{Nb}_{0.5}\text{O}_{14}$ LPE films for oscillators and resonators," *Journal of Crystal Growth*, vol. 250, no. 1-2, pp. 34 – 40, 2003.
- [225] C. Klemenzenz and D. C. Malocha, "Epitaxial films of LGS, LGT, and LGN for SAW and BAW devices," in *Proc. IEEE International Frequency Control Symposium*, 2003, pp. 642–645.
- [226] C. Klemenzenz and A. Sayir, "In-situ Al:Ti-co-doped $\text{La}_3\text{Ga}_{5.5}\text{Ta}_{0.5}\text{O}_{14}$ films for high-Q resonators," in *Proceedings of the IEEE International Frequency Control Symposium*, 2006, pp. 676 – 680.
- [227] H. Kong, J. Wang, H. Zhang, X. Yin, X. Cheng, Y. Lin, X. Huand, X. Xu, and M. Jiang, "Growth and characterization of $\text{La}_3\text{Ga}_{5.5}\text{Ta}_{0.5}\text{O}_{14}$ crystal," *Crystal Research and Technology*, vol. 39, no. 8, pp. 686–691, 2004.
- [228] F.-P. Yu, D.-R. Yuan, X. Zhao, and S.-J. Zhang, "Investigation of langanite and langatate single crystals for high temperature sensing," in *Symposium on Piezoelectricity, Acoustic Waves and Device Applications (SPAWDA)*, 2010, pp. 564–569.
- [229] X.-n. Tu, Y.-q. Zheng, H.-k. Kong, Y.-f. Tu, K.-n. Xiong, and E.-w. Shi, "Growth habits and high temperature properties of langatate single crystal," in *Piezoelectricity, Acoustic Waves and Device Applications (SPAWDA), 2012 Symposium on*, 2012, pp. 289–292.
- [230] R. Fomos Materials Co., Moscow, "SAW wafer specification worksheet." [Online]. Available: http://www.newpiezo.com/doc/Fomos_SAW_wafer.doc
- [231] —. (2013) Fomos-materials - piezoelectric materials and devices. [Online]. Available: <http://newpiezo.com/>

- [232] J. Schreuer, "Elastic and piezoelectric properties of $\text{La}_3\text{Ga}_5\text{SiO}_{14}$ and $\text{La}_3\text{Ga}_{5.5}\text{Ta}_{0.5}\text{O}_{14}$: an application of resonant ultrasound spectroscopy," *IEEE Transactions on Ultrasonics, Ferroelectrics, and Frequency Control*, vol. 49, no. 11, pp. 1474–1479, 2002.
- [233] J. Stadel, L. Bohaty, M. Hengst, and R. Heimann, "Electro-optic, piezoelectric and dielectric properties of langasite ($\text{La}_3\text{Ga}_5\text{SiO}_{14}$), langanite ($\text{La}_3\text{Ga}_{5.5}\text{Nb}_{0.5}\text{O}_{14}$) and langatate ($\text{La}_3\text{Ga}_{5.5}\text{Ta}_{0.5}\text{O}_{14}$)," *Crystal Research and Technology*, vol. 37, no. 10, pp. 1113 – 20, 2002.
- [234] C. Hubert, M. Gauthier, F. Decremps, G. Syfosse, P. Munsch, A. Polian, B. E., and J. J. Boy, "Evaluation of non-linear elastic and piezoelectric properties of $\text{La}_3\text{Ta}_{0.5}\text{Ga}_{5.5}\text{O}_{14}$ single crystals under hydrostatic pressure," in *5th World Congress on Ultrasonics Proceedings*, Sept 2003, pp. 1253–1256.
- [235] U. Straube, H. Beige, J. Bohm, R. B. Heimann, T. Hauke, and M. Hengst, "Elastic, dielectric and piezoelectric coefficients of langasite-type crystals," in *Technol. Health Care*, ser. Abstracts of ESEM 2003, vol. 12, no. 2, 2004, pp. 164–167.
- [236] B. Sturtevant, P. Davulis, and M. Pereira da Cunha, "Pulse echo and combined resonance techniques: a full set of LGT acoustic wave constants and temperature coefficients," *IEEE Transactions on Ultrasonics, Ferroelectrics, and Frequency Control*, vol. 56, no. 4, pp. 788–797, 2009.
- [237] B. T. Sturtevant, "Ultrasonic characterization of single crystal langatate," Ph.D. dissertation, University of Maine, 2009.
- [238] N. Onozato, M. Adachi, and T. Karaki, "Surface acoustic wave properties of $\text{La}_3\text{Ta}_{0.5}\text{Ga}_{5.5}\text{O}_{14}$ single crystals," *Japanese Journal of Applied Physics*, vol. 39, no. 5B, pp. 3028 – 31, 2000.
- [239] R. Bourquin and B. Dulmet, "Thermal sensitivity of elastic coefficients of langasite and langatate," *IEEE Transactions on Ultrasonics, Ferroelectrics, and Frequency Control*, vol. 56, no. 10, pp. 2079–2085, 2009.
- [240] B. T. Sturtevant and M. Pereira da Cunha, "Assessment of langatate material constants and temperature coefficients using SAW delay line measurements," *IEEE Transactions on Ultrasonics, Ferroelectrics, and Frequency Control*, vol. 57, no. 3, pp. 533–539, March 2010.
- [241] A. Khan and A. Ballato, "Lateral field excitation predictions for plates of langasite and isomorphs driven in simple thickness modes," in *Proc. IEEE International Frequency Control Symposium*, 2000, pp. 180–185.
- [242] Y. Kim, A. Khan, and A. Ballato, "Resonance behavior of langanite and langatate plates driven by lateral field excitation," in *Proc. IEEE International Frequency Control Symposium*, 2001, pp. 272–277.

- [243] A. Khan and A. Ballato, "Piezoelectric coupling factor calculations for plates of langatate driven in simple thickness modes by lateral-field-excitation," *IEEE Transactions on Ultrasonics, Ferroelectrics, and Frequency Control*, vol. 49, no. 7, pp. 922–928, 2002.
- [244] Y. Kim, "Measurements of doubly-rotated-cuts of langasite isomorph," in *Proc. IEEE International Frequency Control Symposium*, 2006, pp. 563–566.
- [245] M. Pereira da Cunha, E. Adler, and D. Malocha, "Surface and pseudo surface acoustic waves in langatate," in *Proc. of the IEEE International Ultrasonics Symposium*, 1999, pp. 169–172.
- [246] N. F. Naumenko and L. P. Solie, "Optimal cut for SAW devices on langatate," U.S. Patent 6 097 131, 2000.
- [247] M. Pereira da Cunha and D. C. Malocha, "Experimental and predicted SAW temperature behavior of langatate," in *Proc. IEEE Ultrasonics Symposium*, vol. 1, 2000, pp. 245–248 vol.1.
- [248] ———, "Pure shear horizontal SAW on langatate," in *Proc. of the IEEE International Ultrasonics Symposium*, 2000, pp. 231–234.
- [249] D. Malocha, M. Pereira da Cunha, D. Puccio, and K. Casey, "Investigations of langanite and langatate materials for use in SAW device applications," in *Proceeding of the IEEE International Ultrasonics Symposium*, 2001, pp. 231 – 234.
- [250] N. Saldanha, D. Puccio, D. C. Malocha, and M. Pereira da Cunha, "Experimental and predicted TCF and SAW parameters on LGT $[0^\circ \ 13^\circ \ \psi]$ substrates," in *Proc. of the IEEE International Ultrasonics Symposium*, 2005, pp. 918–921.
- [251] M. Pereira da Cunha, "Surface acoustic wave sensor," U.S. Patent 7 053 522, 2006.
- [252] D. Puccio, D. C. Malocha, N. Saldanha, and M. Pereira da Cunha, "SAW parameters on Y-cut langasite structured materials," *IEEE Transactions on Ultrasonics, Ferroelectrics, and Frequency Control*, vol. 54, no. 9, pp. 1873–1881, 2007.
- [253] B. T. Sturtevant and M. Pereira da Cunha, "Assessment of langatate material constants and temperature coefficients using SAW delay line measurements," in *Proc. of the IEEE International Frequency Control Symposium*, 2009, pp. 160–165.
- [254] K. Inoue and K. Sato, "SAW device," U.S. Patent 6 323 577, 2001.
- [255] K. Inoue, K. Sato, H. Morikoshi, K. Kawasaki, and K. Uchida, "Surface acoustic wave device," U.S. Patent 6 429 570, 2002.

- [256] Z. Chen, L. Li, T. Han, W. Shi, X. Ji, and J. Wang, "Rotation-sensitive cuts for surface acoustic waves on LGT substrates," in *Proc. IEEE International Frequency Control Symposium*, 2005, pp. 188–192.
- [257] Y. Kim and A. Ballato, "Force-frequency effects of Y-cut langanite and Y-cut langatate," in *Proc. IEEE International Frequency Control Symposium*, 2002, pp. 328–332.
- [258] Y. Kim, "Amplitude-frequency effects of Y-cut langanite and langatate," in *Proc. IEEE International Frequency Control Symposium*, 2003, pp. 631–636.
- [259] —, "Amplitude-frequency effect of Y-cut langanite and langatate," *IEEE Transactions on Ultrasonics, Ferroelectrics, and Frequency Control*, vol. 50, no. 12, pp. 1683–1688, 2003.
- [260] J. Imbaud, J.-J. Boy, S. Galliou, R. Bourquin, and J. Romand, "Investigations on LGS and LGT crystals to realize BAW resonators," *IEEE Transactions on Ultrasonics, Ferroelectrics, and Frequency Control*, vol. 55, no. 11, pp. 2384–2391, 2008.
- [261] J.-J. Boy, "Crystal quality of lgt samples: Influence on baw resonators," in *Proc. Joint with the 22nd European Frequency and Time forum Frequency Control Symposium IEEE International*, 2009, pp. 166–170.
- [262] Y. Kim, "Thermal transient effect of Y-cut langanite and langatate," in *Proc. IEEE International Frequency Control Symposium*, 2004, pp. 613–616.
- [263] J. Imbaud, A. Assoud, R. Bourquin, J. J. Boy, S. Galliou, and J. P. Romand, "Investigations on 10 MHz LGS and LGT crystal resonators," in *Proc. of the IEEE International Frequency Control Symposium*, 2007, pp. 711–714.
- [264] J. Imbaud, S. Galliou, J. Romand, P. Abbe, and R. Bourquin, "Development of a 10 MHz oscillator working with an LGT crystal resonator: Preliminary results," *IEEE Transactions on Ultrasonics, Ferroelectrics, and Frequency Control*, vol. 55, no. 9, pp. 1913–1920, 2008.
- [265] J. Imbaud, S. Galliou, J. P. Romand, P. Abbe, and R. Bourquin, "Measurements of ultra-stable langatate crystal oscillators," in *Proc. of the IEEE International Frequency Control Symposium*, 2009, pp. 970–973.
- [266] F. Sthal, E. Bigler, and R. Bourquin, "Theoretical investigations of temperature-compensated cuts for vibrating beam LGT resonators," in *Proc. of the IEEE International Frequency Control Symposium*, 2007, pp. 681–684.
- [267] X. J. Ji, T. Han, W. K. Shi, and G. W. Zhang, "Investigation on SAW properties of LGS and optimal cuts for high-temperature applications," *IEEE Transactions on Ultrasonics, Ferroelectrics, and Frequency Control*, vol. 52, no. 11, pp. 2075–2080, 2005.

- [268] M. Pereira Da Cunha, D. Malocha, D. Puccio, J. Thiele, and T. Pollard, “High coupling, zero TCD SH wave on LGX,” in *Proceedings of the 2002 IEEE International Ultrasonics Symposium*, vol. 1, Oct. 2002, pp. 381 – 384.
- [269] M. Pereira da Cunha, D. Malocha, D. Puccio, J. Thiele, and T. Pollard, “LGX pure shear horizontal saw for liquid sensor applications,” *Sensors Journal, IEEE*, vol. 3, no. 5, pp. 554 – 561, Oct. 2003.
- [270] T. Beaucage, M. Pereira da Cunha, and L. Matthews, “Optical differential dilatometry for the determination of the coefficients of thermal expansion of single crystal solids,” in *Proc. of the IEEE International Ultrasonics Symposium*, 2006, pp. 788–791.
- [271] T. R. Beaucage, “High temperature LGT expansion measurements through multiple techniques,” Master’s thesis, Electrical and Computer Engineering Dept., University of Maine, Orono, ME, 2007.
- [272] D. C. Malocha, H. Francois-Saint-Cyr, K. Richardson, and R. Helmbold, “Measurements of LGS, LGN, and LGT thermal coefficients of expansion and density,” *IEEE Transactions on Ultrasonics, Ferroelectrics, and Frequency Control*, vol. 49, no. 3, pp. 350–355, 2002.
- [273] R. Schreuer, J. Rupp, and C. Thybaut, “Temperature dependence of elastic, piezoelectric and dielectric properties of $\text{La}_3\text{Ga}_5\text{SiO}_{14}$ and $\text{La}_3\text{Ga}_{5.5}\text{Ta}_{0.5}\text{O}_{14}$: An application of resonant ultrasound spectroscopy,” in *Proc. of the IEEE International Ultrasonics Symposium*, 2002, pp. 373–376.
- [274] A. Pavlovska, J. Schneider, S. Werner, B. Maximov, B. Mill, and C. Baetz, “Thermal expansion of lattice parameters of $\text{La}_3\text{Nb}_{0.5}\text{Ga}_{5.5}\text{O}_{14}$, $\text{La}_3\text{Ta}_{0.5}\text{Ga}_{5.5}\text{O}_{14}$ and $\text{La}_3\text{SbZn}_3\text{Ge}_2\text{O}_{14}$,” *Z. Kristallogr.*, vol. 218, pp. 187–192, 2003.
- [275] R. Heimann, M. Hengst, M. Rossberg, and J. Bohm, “Giant optical rotation in piezoelectric crystals with calcium gallium germanate structure,” *Physica Status Solidi A*, vol. 195, no. 2, pp. 468 – 474, 2003.
- [276] G. Kuz’micheva, E. Tyunina, E. Domoroshchina, V. Rybakov, and A. Dubovskii, “X-ray diffraction study of $\text{La}_3\text{Ga}_{5.5}\text{Ta}_{0.5}\text{O}_{14}$ and $\text{La}_3\text{Ga}_{5.5}\text{Nb}_{0.5}\text{O}_{14}$ langasite-type single crystals,” *Inorganic Materials*, vol. 41, no. 4, pp. 412 – 19, 2005.
- [277] G. Kuz’Micheva, O. Zaharko, E. Tyunina, V. Rybakov, I. Kaurova, E. Domoroshchina, and A. Dubovsky, “Point defects in langatate crystals,” *Crystallography Reports*, vol. 54, no. 2, pp. 279 – 282, 2009.
- [278] J. Schreuer and C. Thybaut, “Anelastic relaxation effects and elastic instabilities in CGG-type compounds,” in *Proc. of the IEEE International Ultrasonics Symposium*, 2005, pp. 695–698.

- [279] A. Sehirlioglu, A. Sayir, and C. Klemenzenz, "High-temperature properties of piezoelectric langatate single crystals," Glenn Research Center, NASA, Tech. Rep. 20080047443, 2007, Proceedings of the 13th US-Japan Seminar on Dielectric and Piezoelectric Ceramics.
- [280] R. Yaokawa, H. Kimura, K. Aota, and S. Uda, "Precipitation phenomena in and electrical resistivity of high-temperature treated langatate ($\text{La}_3\text{Ta}_{0.5}\text{Ga}_{5.5}\text{O}_{14}$)," *IEEE Transactions on Ultrasonics, Ferroelectrics, and Frequency Control*, vol. 58, no. 6, pp. 1131–1139, 2011.
- [281] W. Johnson, S. Kim, and D. Lauria, "Anelastic loss in langatate," in *Proc. IEEE International Frequency Control Symposium*, 2000, pp. 186–190.
- [282] W. L. Johnson, S. A. Kim, D. S. Lauria, and R. C. Smythe, "Acoustic damping in langatate as a function of temperature, frequency, and mechanical contact," in *Proc. IEEE International Ultrasonics Symposium*, 2002, pp. 961–964.
- [283] J. Schreuer, C. Thybaut, M. Prestat, J. Stade, and E. Haussuhl, "Towards an understanding of the anomalous electromechanical behaviour of langasite and related compounds at high temperatures," in *Proc. of the IEEE International Ultrasonics Symposium*, 2003, pp. 196–199.
- [284] T. Aubert, O. Elmazria, B. Assouar, E. Blampain, A. Hamdan, D. Genève, , and S. Weber, "Investigations on AlN/Sapphire piezoelectric bilayer structure for high-temperature SAW applications," *Ultrasonics, Ferroelectrics and Frequency Control, IEEE Transactions on*, vol. 59, no. 3, pp. 999–1005, 2012.
- [285] O. Ambacher, "Growth and applications of group III-nitrides," *Journal of Physics D: Applied Physics*, vol. 31, no. 20, p. 2653, 1998.
- [286] T. Aubert, O. Elmazria, B. Assouar, L. Bouvot, and M. Oudich, "Surface acoustic wave devices based on AlN/sapphire structure for high temperature applications," *Applied Physics Letters*, vol. 96, no. 20, p. 203503, 2010.
- [287] X. Y. Du, Y. Q. Fu, S. C. Tan, J. K. Luo, A. J. Flewitt, S. Maeng, S. H. Kim, Y. J. Choi, D. S. Lee, N. M. Park, J. Park, and W. I. Milne, "ZnO film for application in surface acoustic wave device," *Journal of Physics: Conference Series*, vol. 76, p. 012035 (6pp), 2007.
- [288] N. W. Emanetoglu, S. Liang, C. Gorla, Y. Lu, S. Jen, and R. Subramanian, "Epitaxial growth and characterization of high quality ZnO films for surface acoustic wave applications," in *Proc. IEEE International Ultrasonics Symposium*, 1997, pp. 195–200.
- [289] N. W. Emanetoglu, C. Gorla, Y. Liu, S. Liang, and Y. Lu, "Epitaxial ZnO piezoelectric thin films for SAW filters," *Materials Science in Semiconductor Processing*, vol. 2, no. 3, pp. 247 – 252, 1999.

- [290] S. Pearton, D. Norton, K. Ip, Y. Heo, and T. Steiner, “Recent advances in processing of ZnO,” *Journal of Vacuum Science & Technology B*, vol. 22, no. 3, pp. 932 – 948, 2004.
- [291] H. Morkoç and U. Özgür, *Zinc Oxide: Fundamentals, Materials and Device Technology*. Weinheim: Wiley-VHC, 2009.
- [292] T. Xu, G. Wu, G. Zhang, and Y. Hao, “The compatibility of ZnO piezoelectric film with micromachining process,” *Sensors and Actuators A: Physical*, vol. 104, no. 1, pp. 61 – 67, 2003.
- [293] C. Krier and R. Jaffee, “Oxidation of the platinum-group metals,” *Journal of the Less Common Metals*, vol. 5, no. 5, pp. 411 – 431, 1963.
- [294] T. Aubert, O. Elmazria, B. Assouar, L. Bouvot, Z. Bournebe, M. Hehn, S. Weber, M. Oudich, and P. Alnot, “Study of tantalum and iridium as adhesion layers for Pt/LGS high temperature SAW devices,” in *Proc. IEEE International Ultrasonics Symposium*, 2009, pp. 1672–1675.
- [295] G. Bernhardt, C. Silvestre, N. LeCursi, S. Moulzolf, D. Frankel, and R. Lad, “Performance of Zr and Ti adhesion layers for bonding of platinum metallization to sapphire substrates,” *Sensors and Actuators B (Chemical)*, vol. B77, no. 1-2, pp. 368 – 374, 2001.
- [296] J. Sauerwald, M. Schulz, D. Richter, and H. Fritze, “Diffusion in high-temperature piezoelectric single crystals,” *ECS Transactions*, vol. 25, no. 25, pp. 135–146, 2010.
- [297] *IEEE standard on piezoelectricity*, ANSI/IEEE Standard 176-1987 Std., 1988.
- [298] J. A. Kosinski, A. Ballato, and Y. Lu, “A finite plate technique for the determination of piezoelectric material constants,” *IEEE Transactions on Ultrasonics, Ferroelectrics, and Frequency Control*, vol. 43, no. 2, pp. 280–284, 1996.
- [299] B. T. Sturtevant, P. M. Davulis, and M. Pereira da Cunha, “A new set of LGT constants and temperature coefficients extracted through resonant and pulse echo techniques,” in *Proc. of the IEEE International Frequency Control Symposium*, 2007, pp. 754–758.
- [300] L. H. Dawson, “Piezoelectricity of crystal quartz,” *Phys. Rev.*, vol. 29, no. 4, pp. 532–541, Apr 1927.
- [301] R. D. Schulwas-Sorokina, “Is it possible to determine the piezoelectric constant at high temperature by the statical method?” *Phys. Rev.*, vol. 34, no. 11, pp. 1448–1450, Dec 1929.
- [302] E. P. Papadakis and T. P. Lerch, *Handbook of Elastic Properties of Solids, Liquids, and Gases, vol I: Dynamic Methods for Measuring the Elastic Properties of Solids*. San Diego, CA : Academic Press, 2001, ch. Pulse superposition, pulse-echo overlap, and related techniques, pp. 39–66.

- [303] B. Meulendyk and M. Pereira da Cunha, "Significance of power flow angle interference due to finite sample dimension in reflection measurements," in *Proc. of the IEEE International Frequency Control Symposium*, Aug. 2005, pp. 164–170.
- [304] B. J. Meulendyk, M. C. Wheeler, and M. Pereira da Cunha, "Analyses and mitigation of spurious scattered signals in acoustic wave reflection measurements," *Nondestructive Testing and Evaluation*, vol. 21, no. 3, pp. 155–169, 2006.
- [305] B. T. Sturtevant and M. Pereira da Cunha, "BAW phase velocity measurements by conventional pulse echo techniques with correction for couplant effect," in *Proc. of the IEEE International Ultrasonics Symposium*, 2006, pp. 2261–2264.
- [306] G. A. Alers and H. Ogi, *Handbook of Elastic Properties of Solids, Liquids, and Gases, vol I: Dynamic Methods for Measuring the Elastic Properties of Solids*. San Diego, CA : Academic Press, 2001, ch. EMAT Techniques, pp. 263–281.
- [307] M. Pereira da Cunha and J. Jordan, "Improved longitudinal EMAT transducer for elastic constant extraction," in *Proc. of the IEEE International Frequency Control Symposium*, 2005, pp. 426 –432.
- [308] H. Fritze, O. Schneider, H. Seh, H. L. Tuller, and G. Borchardt, "High temperature bulk acoustic wave properties of langasite," *Phys. Chem. Chem. Phys.*, vol. 5, pp. 5207–5214, 2003.
- [309] G. Kovacs, G. Trattnig, and E. Langer, "Accurate determination of material constants of piezoelectric crystal from SAW velocity measurements," in *Proc. of the IEEE International Ultrasonics Symposium*, 1988, pp. 269 –272.
- [310] G. Kovacs, M. Anhorn, H. E. Engan, G. Visintini, and C. C. W. Ruppel, "Improved material constants for LiNbO_3 and LiTaO_3 ," in *Proc. of the IEEE International Ultrasonics Symposium*, 1990, pp. 435 –438.
- [311] Y. Shimizu, A. Terazaki, and T. Sakaue, "Temperature dependence of SAW velocity for metal film on α -quartz," in *Proc. of the IEEE International Ultrasonics Symposium*, 1976, pp. 519 – 522.
- [312] J. Minowa, K. Nakagawa, K. Okuno, Y. Kobayashi, and M. Morimoto, "400 MHz SAW timing filter for optical fiber transmission systems," in *Proc. of the IEEE International Ultrasonics Symposium*, 1978, pp. 490 – 493.
- [313] M. Lewis, "Temperature compensation techniques for SAW devices," in *Proc. of the IEEE International Ultrasonics Symposium*, 1979, pp. 612 – 622.
- [314] D. Murray and E. Ash, "Precision measurement of SAW velocities," in *Proc. of the IEEE International Ultrasonics Symposium*, 1977, pp. 823 – 826.

- [315] M. Anhorn, H. Engan, and A. Ronnekleiv, “New SAW velocity measurements on Y-cut LiNbO₃,” in *Proc. of the IEEE International Ultrasonics Symposium*, 1987, pp. 279 – 284.
- [316] A. Migliori and J. L. Sarrao, *Resonant Ultrasound Spectroscopy: Applications to Physics, Material Measurements, and Nondestructive Evaluation*. New York: Wiley-Interscience, 1997.
- [317] M. Renken, S. Kim, K. Hollman, and C. Fortunko, “Accuracy of resonant ultrasound spectroscopy: an experimental study,” in *Proc. of the IEEE International Ultrasonics Symposium*, 1997, pp. 483 – 488.
- [318] I. Ohno, “Rectangular parallelepiped resonance method for piezoelectric crystals and elastic constants of alpha-quartz,” *Physics and Chemistry of Minerals*, vol. 17, no. 5, pp. 371–378, 1990.
- [319] I. Ohno, S. Yamamoto, O. Anderson, and J. Noda, “Determination of elastic constants of trigonal crystals by the rectangular parallelepiped resonance method,” *Journal of the Physics and Chemistry of Solids*, vol. 47, no. 12, pp. 1103 – 1108, 1986.
- [320] P. Heyliger, H. Ledbetter, and S. Kim, “Elastic constants of natural quartz,” *Journal of the Acoustical Society of America*, vol. 114, no. 2, pp. 644 – 650, 2003.
- [321] P. Heyliger and W. Johnson, “Traction-free vibrations of finite trigonal elastic cylinders,” *Journal of the Acoustical Society of America*, vol. 113, no. 4, pp. 1812 – 1825, 2003.
- [322] W. L. Johnson and P. R. Heyliger, “Symmetrization of Ritz approximation functions for vibrational analysis of trigonal cylinders,” *Journal of the Acoustical Society of America*, vol. 113, no. 4 I, pp. 1826 – 1832, 2003.
- [323] H. Ogi, T. Ohmori, N. Nakamura, and M. Hirao, “Elastic, anelastic, and piezoelectric coefficients of α -quartz determined by resonance ultrasound spectroscopy,” *Journal of Applied Physics*, vol. 100, no. 5, p. 53511 (7 pages), 2006.
- [324] I. Ohno, K. Harada, and C. Yoshitomi, “Temperature variation of elastic constants of quartz across the α - β transition,” *Physics and Chemistry of Minerals*, vol. 33, no. 1, pp. 1–9, 2006.
- [325] W. L. Johnson, C. F. Martino, S. A. Kim, and P. R. Heyliger, “Mode-selective acoustic spectroscopy of trigonal piezoelectric crystals,” *IEEE Transactions on Ultrasonics, Ferroelectrics, and Frequency Control*, vol. 55, no. 5, pp. 1133–1142, 2008.
- [326] H. Ogi, N. Nakamura, K. Sato, M. Hirao, and S. Uda, “Elastic, anelastic, and piezoelectric coefficients of langasite: resonance ultrasound spectroscopy with

- laser-Doppler interferometry,” *IEEE Transactions on Ultrasonics, Ferroelectrics and Frequency Control*, vol. 50, no. 5, pp. 553 – 560, 2003.
- [327] H. Ogi, N. Nakamura, M. Hirao, and H. Ledbetter, “Determination of elastic, anelastic, and piezoelectric coefficients of piezoelectric materials from a single specimen by acoustic resonance spectroscopy,” *Ultrasonics*, vol. 42, no. 1-9, pp. 183 – 187, 2004.
 - [328] P. Davulis, A. Shyam, E. Lara-Curzio, and M. Pereira da Cunha, “High temperature elastic constants of langatate from RUS measurements up to 1100 °C,” in *Proc. IEEE International Ultrasonics Symposium*, 2008, pp. 2150–2153.
 - [329] P. Davulis and M. Pereira da Cunha, “Measured versus predicted high temperature langatate behavior up to 900 °C,” in *Proc. IEEE International Frequency Control Symposium*, 2009, pp. 155–159.
 - [330] —, “High-temperature langatate elastic constants and experimental validation up to 900 °C,” *IEEE Transactions on Ultrasonics, Ferroelectrics, and Frequency Control*, vol. 57, no. 1, pp. 59–65, Jan 2010.
 - [331] —, “Impact of high-temperature dielectric and piezoelectric behavior on LGT acoustic wave properties up to 900 °C,” in *International Ultrasonics Symposium*, 2011.
 - [332] —, “Determination and experimental verification of high-temperature SAW orientations on langatate,” in *Proc. IEEE International Frequency Control Symposium*, 2011, pp. 1–6.
 - [333] —, “Determination and experimental verification of high-temperature SAW orientations on langatate,” *IEEE Transactions on Ultrasonics, Ferroelectrics, and Frequency Control*, vol. 59, no. 2, pp. 287–294, 2012.
 - [334] —, “A full set of langatate high-temperature acoustic wave constants: Elastic, piezoelectric, dielectric constants up to 900 °C,” *IEEE Transactions on Ultrasonics, Ferroelectrics, and Frequency Control*, vol. 60, no. 4, pp. 824–833, 2013.
 - [335] Y. Sumino, T. Goto, I. Ohno, O. Nishizawa, and M. Ozima, “Temperature variation of elastic constants of single-crystal forsterite between –190 and 400 °C,” *Journal of Physics of the Earth*, vol. 25, no. 4, pp. 377–392, 1977.
 - [336] I. Suzuki, O. Anderson, and Y. Sumino, “Elastic properties of a single-crystal forsterite Mg_2SiO_4 , up to 1200 K,” *Physics and Chemistry of Minerals*, vol. 10, no. 1, pp. 38–46, 1983.
 - [337] T. Goto and O. Anderson, “Apparatus for measuring elastic constants of single crystals by a resonance technique up to 1825 K,” *Review of Scientific Instruments*, vol. 59, no. 8, pp. 1405 – 1408, 1988.

- [338] T. Goto, O. Anderson, I. Ohno, and S. Yamamoto, “Elastic constants of corundum up to 1825 K,” *Journal of Geophysical Research*, vol. 94, no. B6, pp. 7588 – 7602, 1989.
- [339] K. Omura, K. Kurita, and M. Kumazawa, “Experimental study of pressure dependence of electrical conductivity of olivine at high temperatures,” *Physics of the Earth and Planetary Interiors*, vol. 57, no. 3-4, pp. 291–303, 1989.
- [340] O. L. Anderson, “Rectangular parallelepiped resonance—a technique of resonance ultrasound and its applications to the determination of elasticity at high temperatures,” *The Journal of the Acoustical Society of America*, vol. 91, no. 4, pp. 2245–2253, 1992.
- [341] O. Anderson, D. Isaak, and H. Oda, “High-temperature elastic constant data on minerals relevant to geophysics,” *Reviews of Geophysics*, vol. 30, no. 1, pp. 57 – 90, 1992.
- [342] J. Schreuer, B. Hildmann, and H. Schneider, “Elastic properties of mullite single crystals up to 1400 °C,” *Journal of the American Ceramic Society*, vol. 89, no. 5, pp. 1624 – 1631, 2006.
- [343] W. B. Westphal and J. Iglesias, “Dielectric spectroscopy of high-temperature materials,” Laboratory for Insulation Research, Mass. Inst. of Tech., Cambridge, Mass., Tech. Rep., 1971. [Online]. Available: <http://handle.dtic.mil/100.2/AD884597>
- [344] L. F. Chen, C. K. Ong, C. P. Neo, V. V. Varadan, and V. K. Varadan, *Microwave Electronics: Measurement and Materials Characterisation*. Hoboken: John Wiley & Sons, 2004.
- [345] W. B. Westphal, “Dielectric constant measurement and loss measurements on high-temperature materials,” Laboratory for Insulation Research, Mass. Inst. of Tech., Cambridge, Mass., Tech. Rep., 1963. [Online]. Available: <http://handle.dtic.mil/100.2/AD423686>
- [346] S. Bringham and M. Iskander, “Open-ended metallized ceramic coaxial probe for high-temperature dielectric properties measurements,” *IEEE Transactions on Microwave Theory and Techniques*, vol. 44, no. 6, pp. 926–935, 1996.
- [347] S. Bringham, M. Iskander, and M. White, “Thin-sample measurements and error analysis of high-temperature coaxial dielectric probes,” *IEEE Transactions on Microwave Theory and Techniques*, vol. 45, no. 12, pp. 2073–2083, 1997.
- [348] A. Orliukas, A. Kežionis, and E. Kazakevičius, “Impedance spectroscopy of solid electrolytes in the radio frequency range,” *Solid State Ionics*, vol. 176, no. 25-28, pp. 2037 – 2043, 2005.

- [349] A. Kežionis, E. Kazakevičius, T. Šalkus, and A. Orliukas, “Broadband high frequency impedance spectrometer with working temperatures up to 1200K,” *Solid State Ionics*, vol. 188, no. 1, pp. 110 – 113, 2011, 9th International Symposium on Systems with Fast Ionic Transport.
- [350] J. Baker-Jarvis, M. Janezic, R. Riddle, R. Johnk, P. Kabos, C. Holloway, R. Geyer, and C. Grosvenor, “Measuring the permittivity and permeability of lossy materials: Solids, liquids, metals, building materials, and negative-index materials,” NIST Technical Note 1536, Washington, DC., Tech. Rep., February 2005.
- [351] M. A. Omar, *Elementary Solid State Physics*, revised ed. New York: Addison-Wesley Publishing Company, 1993.
- [352] K. C. Kao, *Dielectric Phenomena in Solids*. New York: Elsevier Academic Press, 2004.
- [353] A. Jonscher, *Dielectric relaxation in solids*. London: Chelsea Dielectrics Press, 1983.
- [354] I. Bunget and M. Popescu, *Physics of solid dielectrics*, ser. Materials science monographs. New York: Elsevier, 1984.
- [355] V. Giordano, Y. Kersalé, and J.-J. Boy, “Dielectric properties of $\text{La}_3\text{Ga}_5\text{SiO}_{14}$ at microwave frequencies between 10 and 400 k,” *Applied Physics Letters*, vol. 78, no. 17, pp. 2545–2547, 2001.
- [356] J. A. Kosinski, J. Pastore, R. A., E. Bigler, M. Pereira da Cunha, D. C. Malocha, and J. Detaint, “A review of langasite material constants from BAW and SAW data: toward an improved data set,” in *Proc. IEEE International Frequency Control Symposium and PDA Exhibition*, 2001, pp. 278–286.
- [357] V. E. Bottom, “Dielectric constants of quartz,” *Journal of Applied Physics*, vol. 43, no. 4, pp. 1493–1495, 1972.
- [358] P. Davulis, B. T. Sturtevant, S. L. Duy, and M. Pereira da Cunha, “Revisiting LGT dielectric constants and temperature coefficients up to 120 °C,” in *Proc. IEEE Ultrasonics Symposium*, 2007, pp. 1397–1400.
- [359] P. Davulis and M. Pereira da Cunha, “Conductivity and complex permittivity of langatate at high temperature up to 900 °C,” in *Proc. IEEE Int. Frequency Control Symp.*, 2010, pp. 252–257.
- [360] H. Fritze, “High temperature piezoelectric materials: defect chemistry and electro-mechanical properties,” *Journal of Electroceramics*, vol. 17, no. 2-4, pp. 625 – 30, 2006.
- [361] H. Seh and H. Tuller, “Defects and transport in langasite I: acceptor-doped ($\text{La}_3\text{Ga}_5\text{SiO}_{14}$),” *Journal of Electroceramics*, vol. 16, no. 2, pp. 115 – 25, 2006.

- [362] I. Kaurova, G. Kuz'micheva, and A. Dubovskii, "Physicochemical properties of $\text{La}_3\text{Ga}_{5.5}\text{Ta}_{0.5}\text{O}_{14}$," *Inorganic Materials*, vol. 46, pp. 1131–1136, 2010.
- [363] G. H. Golub and C. F. V. Loan, "An analysis of the total least squares problem," *SIAM Journal on Numerical Analysis*, vol. 17, no. 6, pp. 883–893, 1980.
- [364] S. Van Huffel and J. Vandewalle, *The Total Least Squares Problem: Computational Aspects and Analysis*. Philadelphia: Society for Industrial and Applied Mathematics, 1991.
- [365] I. Markovsky, J. C. Willems, S. V. Huffel, and B. D. Moor, *Exact and Approximate Modeling of Linear Systems*. Philadelphia, PA: Society for Industrial and Applied Mathematics, 2006.
- [366] *Agilent 4284A Precision LCR Meter Operation Manual*, 8th ed., Agilent Technologies, Hyogo, Japan, January 2001, part number 04284-90040.
- [367] J. R. Taylor, *An Introduction to Error Analysis: The Study of Uncertainties in Physical Measurements*, 2nd ed. University Science Books, 1997.
- [368] P. R. Bevington and D. K. Robinson, *Data Reduction and Error Analysis*, 3rd ed. New York: McGraw-Hill, 2003.
- [369] H. Schwetlick and V. Tiller, "Numerical methods for estimating parameters in nonlinear models with errors in the variables," *Technometrics*, vol. 27, no. 1, pp. 17–24, 1985.
- [370] P. T. Boggs, R. H. Byrd, and R. B. Schnabel, "A stable and efficient algorithm for nonlinear orthogonal distance regression," *SIAM Journal on Scientific and Statistical Computing*, vol. 8, no. 6, pp. 1052–1078, 1987.
- [371] S. Van Huffel and J. Vandewalle, "On the accuracy of total least squares and least squares techniques in the presence of errors on all data," *Automatica*, vol. 25, no. 5, pp. 765 – 769, 1989.
- [372] Y. Sato and T. Usami, "Basic study on the oscillation of a homogeneous elastic sphere," *Geophysical Magazine*, vol. 31, pp. 15–62, 1962.
- [373] D. B. Fraser and R. C. LeCraw, "Novel method of measuring elastic and anelastic properties of solids," *Review of Scientific Instruments*, vol. 35, no. 9, pp. 1113–1115, 1964.
- [374] N. Soga and O. L. Anderson, "Elastic properties of tektites measured by resonant sphere technique," *Journal of Geophysical Research*, vol. 72, no. 6, pp. 1733–1739, 1967.
- [375] R. Holland, "Resonant properties of piezoelectric ceramic rectangular parallelepipeds," *The Journal of the Acoustical Society of America*, vol. 43, no. 5, pp. 988–997, 1968.

- [376] R. Holland and E. P. Eer Nisse, "Variational evaluation of admittances of multi-electroded three-dimensional piezoelectric structures," *IEEE Transactions on Sonics and Ultrasonics*, vol. 15, no. 2, pp. 119–131, 1968.
- [377] J. Demarest, H.H., "Cube-resonance method to determine the elastic constants of solids," *Journal of the Acoustical Society of America*, vol. 49, no. 3, pp. 768 – 775, 1971.
- [378] I. Ohno, "Free vibration of a rectangular parallelepiped crystal and its application to determination of elastic constants of orthorhombic crystals," *Journal of Physics of the Earth*, vol. 24, no. 4, pp. 355 – 379, 1976.
- [379] E. Mochizuki, "Application of group theory to free oscillations of an anisotropic rectangular parallelepiped," *Journal of Physics of the Earth*, vol. 35, no. 2, pp. 159 – 170, 1987.
- [380] W. Visscher, A. Migliori, T. Bell, and R. Reinert, "On the normal modes of free vibration of inhomogeneous and anisotropic elastic objects," *Journal of the Acoustical Society of America*, vol. 90, no. 4, pp. 2154 – 2162, 1991.
- [381] P. Heyliger, A. Jilani, H. Ledbetter, R. Leisure, and C.-L. Wang, "Elastic constants of isotropic cylinders using resonant ultrasound," *Journal of the Acoustical Society of America*, vol. 94, no. 3, pp. 1482 – 1487, 1993.
- [382] H. Ledbetter, C. Fortunko, and P. Heyliger, "Orthotropic elastic constants of a boron-aluminum fiber-reinforced composite: an acoustic-resonance-spectroscopy study," *Journal of Applied Physics*, vol. 78, no. 3, pp. 1542 – 1542, 1995.
- [383] H. Ogi, P. Heyliger, H. Ledbetter, and S. Kim, "Mode-selective resonance ultrasound spectroscopy of a layered parallelepiped," *Journal of the Acoustical Society of America*, vol. 108, no. 6, pp. 2829 – 2834, 2000.
- [384] N. Nakamura, H. Ogi, and M. Hirao, "Resonance ultrasound spectroscopy with laser-Doppler interferometry for studying elastic properties of thin films," *Ultrasonics*, vol. 42, no. 1-9, pp. 491 – 494, 2004.
- [385] H. Ogi, K. Sato, T. Asada, and M. Hirao, "Complete mode identification for resonance ultrasound spectroscopy," *Journal of the Acoustical Society of America*, vol. 112, no. 6, pp. 2553 – 7, 2002.
- [386] H. Ogi, H. Ledbetter, S. Kim, and M. Hirao, "Contactless mode-selective resonance ultrasound spectroscopy: Electromagnetic acoustic resonance," *Journal of the Acoustical Society of America*, vol. 106, no. 2, pp. 660 – 665, 1999.
- [387] K. Tozaki, T. Okazaki, A. Kojima, and Y. Yoshimura, "Method of measuring resonant frequencies of solids with parts per million resolution over a wide temperature range," *Review of Scientific Instruments*, vol. 76, no. 6, p. 66104 (3 pages), 2005.

- [388] M. K. Fig, “Resonant ultrasound spectroscopy in complex sample geometry,” Master’s thesis, Montana State University, 2005.
- [389] J. Plešek, R. Kolman, and M. Landa, “Using finite element method for the determination of elastic moduli by resonant ultrasound spectroscopy,” *Journal of the Acoustical Society of America*, vol. 116, no. 1, pp. 282 – 287, 2004.
- [390] H. Tiersten, “Hamilton’s principle for linear piezoelectric media,” *Proceedings of the IEEE*, vol. 55, no. 8, pp. 1523 – 1524, 1967.
- [391] H. F. Tiersten, *Linear Piezoelectric Plate Vibrations*. New York: Plenum Press, 1969.
- [392] E. P. Eer Nisse, “Resonances of one-dimensional composite piezoelectric and elastic structures,” *IEEE Transactions on Sonics and Ultrasonics*, vol. 14, no. 2, pp. 59–66, 1967.
- [393] E. Eer Nisse, “On variational techniques for piezoelectric device analysis,” *Proceedings of the IEEE*, vol. 55, no. 8, pp. 1524 – 1525, 1967.
- [394] E. P. Eer Nisse, “Variational method for electroelastic vibration analysis,” *IEEE Transactions on Sonics and Ultrasonics*, vol. 14, no. 4, pp. 153–159, 1967.
- [395] A. Migliori, J. Sarrao, W. M. Visscher, T. Bell, M. Lei, Z. Fisk, and R. Leisure, “Resonant ultrasound spectroscopic techniques for measurement of the elastic moduli of solids,” *Physica B: Condensed Matter*, vol. 183, no. 1-2, pp. 1 – 24, 1993.
- [396] M. T. Heath, *Scientific Computing: An Introductory Survey*, 2nd ed. Boston: McGraw-Hill, 2002.
- [397] C. B. Moler, *Numerical Computing with Matlab*. Philadelphia, PA: Society for Industrial and Applied Mathematics, 2004. [Online]. Available: http://www.mathworks.com/moler/index_ncm.html
- [398] A. Migliori and J. Maynard, “Implementation of a modern resonant ultrasound spectroscopy system for the measurement of the elastic moduli of small solid specimens,” *Review of Scientific Instruments*, vol. 76, no. 12, p. 121301 (7 pages), 2005.
- [399] R. G. Leisure, K. Foster, J. E. Hightower, and D. S. Agosta, “Internal friction studies by resonant ultrasound spectroscopy,” *Materials Science and Engineering A*, vol. 370, no. 1-2, pp. 34 – 40, 2004, 13th International Conference on Internal Friction and Ultrasonic Attenuation in Solids.
- [400] “Standards on piezoelectric crystals, 1949,” *Proceedings of the IRE*, vol. 37, pp. 1378–1395, 1949.

- [401] W. Johnson, S. Kim, S. Uda, and C. Rivenbark, "Acoustic damping in resonators of langasite and langatate at elevated temperatures," in *Proc. of IEEE Sensors*, oct. 2011, pp. 1636–1639.
- [402] C. Hubert, M. Gauthier, F. Decremps, G. Syfosse, A. Polian, J. Itié, P. Munsch, E. Bigler, and J. Boy, "Structural and mechanical stability of $\text{La}_3\text{Ga}_{5.5}\text{Ta}_{0.5}\text{O}_{14}$ single crystal under hydrostatic pressure," *J. Phys. IV France*, vol. 126, pp. 43–46, Jun 2005.
- [403] E. Adler, "Matrix methods applied to acoustic waves in multilayers," *Ultrasonics, Ferroelectrics and Frequency Control, IEEE Transactions on*, vol. 37, no. 6, pp. 485–490, Nov. 1990.
- [404] M. Pereira da Cunha and S. de A Fagundes, "Metal strip reflectivity and NSPUDT orientations in langanite, langasite, and gallium phosphate," *IEEE Transactions on Ultrasonics, Ferroelectrics, and Frequency Control*, vol. 49, no. 6, pp. 815–819, Jun. 2002.
- [405] M. B. Schulz, B. J. Matsinger, and M. G. Holland, "Temperature dependence of surface acoustic wave velocity on alpha quartz," *Journal of Applied Physics*, vol. 41, no. 7, pp. 2755–2765, 1970.
- [406] A. J. Slobodnik, "The temperature coefficients of acoustic surface wave velocity and delay on lithium niobate, lithium tantalate, quartz, and tellurium dioxide," Air Force Cambridge Research Labs, Bedford, MA, Tech. Rep. AFCRL-72-008, 1972.
- [407] B. Taylor and C. Kuyatt, "Guidelines for evaluating and expressing the uncertainty of NIST measurement results," NIST Technical Note 1297, Tech. Rep., September 1994.
- [408] L. D. Doucette, M. P. da Cunha, and R. J. Lad, "Precise orientation of single crystals by a simple x-ray diffraction rocking curve method," *Review of Scientific Instruments*, vol. 76, no. 3, p. 036106, 2005.
- [409] B. T. Sturtevant, M. Pereira da Cunha, and R. J. Lad, "Determination of the absolute orientation of langatate crystals using X-ray diffraction," in *Proc. of the IEEE International Ultrasonics Symposium*, 2008, pp. 741–744.
- [410] I. Shrena, D. Eisele, J. Bardong, E. Mayer, and L. Reindl, "High-precision signal processing algorithm to evaluate saw properties as a function of temperature," *Ultrasonics, Ferroelectrics and Frequency Control, IEEE Transactions on*, vol. 60, no. 4, pp. 805–813, 2013.
- [411] T. Han, X. Ji, and W. Shi, "Optimal pressure-sensitive cuts for surface acoustic waves on langasite," *Science in China Series F: Information Sciences*, vol. 49, no. 2, pp. 254–261, 2006.

- [412] S. Sakharov, S. Kondratiev, A. Zabelin, N. Naumenko, A. Azarov, S. Zhgoon, and A. Shvetsov, "Theoretical and experimental investigation of langasite as material for wireless high temperature SAW sensors," in *Proc. IEEE International Ultrasonics Symposium*, oct. 2010, pp. 535–538.
- [413] A. Bungo, C. Jian, K. Yamaguchi, Y. Sawada, R. Kimura, and S. Uda, "Experimental and theoretical analysis of SAW properties of langasite substrates with euler angle $(0^\circ, 140^\circ, \psi)$," in *Proc. IEEE International Ultrasonics Symposium*, 1999, pp. 231–234.
- [414] F. Yu, X. Zhao, L. Pan, F. Li, D. Yuan, and S. Zhang, "Investigation of zero temperature compensated cuts in langasite-type piezocrystals for high temperature applications," *Journal of Physics D: Applied Physics*, vol. 43, no. 16, p. 165402, 2010.
- [415] W. Buff, S. Klett, M. Rusko, J. Ehrenpfordt, and M. Goroli, "Passive remote sensing for temperature and pressure using SAW resonator devices," *IEEE Transactions on Ultrasonics, Ferroelectrics, and Frequency Control*, vol. 45, no. 5, pp. 1388–1392, 1998.
- [416] V. Kalinin, G. Bown, and A. Leigh, "Contactless torque and temperature sensor based on SAW resonators," in *Ultrasonics Symposium, 2006. IEEE*, Oct. 2006, pp. 1490–1493.
- [417] M. Schulz, "Untersuchung der eigenschaften von langasit für hochtemperaturanwendungen (investigating the properties of langasite for high temperature applications)," Ph.D. dissertation, Technical University of Clausthal, 2007.
- [418] M. Pereira da Cunha, E. Adler, and D. Malocha, "BAW temperature sensitivity and coupling in langanite," *IEEE Transactions on Ultrasonics, Ferroelectrics and Frequency Control*, vol. 49, no. 5, pp. 656–663, may 2002.
- [419] C.-K. Jen, G. Farnell, E. Adler, and J. Oliverira, "Interactive computer-aided analysis for bulk acoustic waves in materials of arbitrary anisotropy and piezoelectricity," *Sonics and Ultrasonics, IEEE Transactions on*, vol. 32, no. 1, pp. 56–60, 1985.
- [420] A. Ballato, *Physical Acoustics*. New York: Academic, 1977, vol. 13, ch. Doubly rotated thickness mode plate vibrators, pp. 115–181.
- [421] D. McCann, J. McGann, J. Parks, D. Frankel, M. da Cunha, and J. Vetelino, "A lateral-field-excited litao3 high-frequency bulk acoustic wave sensor," *IEEE Transactions on Ultrasonics, Ferroelectrics, and Frequency Control*, vol. 56, no. 4, pp. 779–787, 2009.
- [422] G. Farnell and E. Adler, "Elastic wave propagation in thin layers," in *Physical Acoustics*, W. P. Mason and R. N. Thurston, Eds. New York: Academic Press, 1972, vol. 9, pp. 35–127.

- [423] P. Davulis and M. Pereira da Cunha, “Temperature-compensated BAW orientations over 500 °C on LGT for frequency control and sensor applications,” *Electronics Letters*, vol. 49, no. 3, pp. 170 – 171, 2013.
- [424] I. Markovsky and S. V. Huffel, “A MATLAB toolbox for weighted total least squares approximation,” Dept. EE, K.U. Leuven, Tech. Rep. 04–220, 2004.
- [425] P. Guillaume and R. Pintelon, “A gauss-newton-like optimization algorithm for weighted nonlinear least-squares problems,” *IEEE Transactions on Signal Processing*, vol. 44, no. 9, pp. 2222–2228, Sept. 1996.
- [426] W. P. Mason, *Piezoelectric Crystals and Their Application to Ultrasonics*. New York: Van Nostrand, 1950.
- [427] B. A. Auld, *Acoustic Fields and Waves in Solids*. New York: John Wiley & Sons, 1973, vol. 1.
- [428] R. K. Jain and S. R. K. Iyengar, *Advanced Engineering Mathematics*, 2nd ed. Pangbourne: Alpha Science International Ltd., 2004.

Appendix A

ACOUSTIC CONSTANTS OF CRYSTAL CLASS 32

The analysis and simulation of acoustic waves on piezoelectric crystals requires knowledge of the relevant acoustic properties of the substrate, namely the elastic stiffness, piezoelectric constants, permittivity, and density, which are used to calculate the acoustic phase velocity, mode displacement, coupling, and other relevant acoustic properties.

Langatate, langasite, gallium orthophosphate, and quartz have class 32 crystal symmetry and share the same matrix structure for the fundamental acoustic wave constants, given below [297].

Class 32 crystals have six independent elastic constants and the elastic stiffness matrix has the form

$$c = \begin{pmatrix} c_{11} & c_{12} & c_{13} & c_{14} & 0 & 0 \\ c_{12} & c_{11} & c_{13} & -c_{14} & 0 & 0 \\ c_{13} & c_{13} & c_{33} & 0 & 0 & 0 \\ c_{14} & -c_{14} & 0 & c_{44} & 0 & 0 \\ 0 & 0 & 0 & 0 & c_{44} & c_{14} \\ 0 & 0 & 0 & 0 & c_{14} & c_{66} \end{pmatrix} \quad (\text{A.1})$$

where $c_{12} = c_{11} - 2c_{66}$.

Class 32 crystals have two piezoelectric constants and the matrix has the form

$$e = \begin{pmatrix} e_{11} & -e_{11} & 0 & e_{14} & 0 & 0 \\ 0 & 0 & 0 & 0 & -e_{14} & -2e_{11} \\ 0 & 0 & 0 & 0 & 0 & 0 \end{pmatrix} \quad (\text{A.2})$$

There are two dielectric constants for class 32 crystals and the dielectric matrix is

$$\epsilon = \begin{pmatrix} \epsilon_{11} & 0 & 0 \\ 0 & \epsilon_{11} & 0 \\ 0 & 0 & \epsilon_{33} \end{pmatrix} \quad (\text{A.3})$$

Other crystal properties may have a significant role in acoustic performance, such as material losses. In particular, the viscosity, ν , has the same matrix form as the elastic constants; and the thermal expansion, polarization, ϵ'' , and conductivity, σ , have the same matrix form as the dielectric constants.

Appendix B

DIELECTRIC CONSTANTS FITTING AND EXTRACTION DETAILS

The dielectric fitting and extraction process discussed in Section 2.2 is further detailed and discussed here.

The dielectric constants ϵ'_R , ϵ''_R , and σ and corresponding temperature coefficients were extracted from the measurement data using best-fit surfaces. When extracting ϵ'_R the data surface for ϵ'_{R11} required two third-order polynomials, each with separate temperature regions, whereas ϵ'_{R33} only required one third-order polynomial, as described in Section 2.1.4. The surfaces for ϵ'_{R11} and ϵ'_{R33} were calculated from (2.13).

The fitting for ϵ'_{R33} will be presented first because it only requires a single polynomial so is simpler. For ϵ'_{R33} the temperature difference of the i^{th} measurement is

$$\Delta_i = T_i - T_0, \quad (\text{B.1})$$

where T_i is the temperature of the i^{th} measurement and T_0 is the reference temperature and for ϵ'_{R33} $T_0 = 25^\circ\text{C}$. Combining (2.13) and (B.1) yields

$$\epsilon'_{meas33}(T) = \epsilon'_{R33} \left[1 + \sum_{n=1}^3 TC_{\epsilon'}^{(n)} \Delta_i^n \right] + \frac{2\alpha'}{\epsilon_0} \left(\frac{h_i}{r_i} \right), \quad (\text{B.2})$$

where the wafer thickness and electrode radius at the temperature of the i^{th} measurement are

$$\begin{aligned} h_i &= h(T_i) = h \left[1 + \sum_{n=1}^3 TC_h^{(n)} \Delta_i^n \right] \\ r_i &= r(T_i) = r \left[1 + \sum_{n=1}^3 TC_r^{(n)} \Delta_i^n \right]. \end{aligned} \quad (\text{B.3})$$

The fitting equation (B.2) for ϵ'_{R33} is rewritten in matrix form, with i the measurement index,

$$\begin{bmatrix} 1 & \Delta_1 & \Delta_1^2 & \Delta_1^3 & h_1/r_1 \\ \vdots & \vdots & \vdots & \vdots & \vdots \\ 1 & \Delta_i & \Delta_i^2 & \Delta_i^3 & h_i/r_i \end{bmatrix} \begin{bmatrix} \epsilon'_{R33} \\ TC_{\epsilon'_{33}}^{(1)} \\ TC_{\epsilon'_{33}}^{(2)} \\ TC_{\epsilon'_{33}}^{(3)} \\ \frac{2\alpha'_{33}}{\epsilon_0} \end{bmatrix} = \begin{bmatrix} \epsilon'_{meas33}(T_1) \\ \vdots \\ \epsilon'_{meas33}(T_i) \end{bmatrix}. \quad (\text{B.4})$$

The first matrix contains the temperature and capacitor size data for each measurement, the second matrix on the left hand side is a vector of the unknown fitting parameters, and the matrix on the right hand side contains the measured capacitances.

For ϵ'_{R11} the temperature data is broken into two regions: region a where $25^\circ\text{C} \leq T_i < 500^\circ\text{C}$ and region b where $500^\circ\text{C} \leq T_i \leq 925^\circ\text{C}$, with $T_{0a} = 25^\circ\text{C}$ and $T_{0b} = 500^\circ\text{C}$. The temperature differences of the i^{th} measurement, Δ_a and Δ_b , were defined so that both independent temperature-coefficient polynomials can be extracted simultaneously using the same α' and enforce ϵ'_{11} to be continuous with temperature. Over the first temperature range, $\Delta_a = T_i - T_{0a}$ and $\Delta_b = 0$ and in the second temperature region $\Delta_a = T_{0b} - T_{0a} = 475^\circ\text{C}$ and $\Delta_b = T_i - T_{0b}$. These parameters are calculated by

$$\begin{aligned} \Delta_{ai} &= \min(T_i, T_{0b}) - T_{0a} \\ \Delta_{bi} &= \max(T_i, T_{0b}) - T_{0b}. \end{aligned} \quad (\text{B.5})$$

Combining (B.5) with the temperature coefficient equation (2.13) yields

$$\epsilon'_{meas11}(T) = \epsilon'_{R11} \left[1 + \sum_{n=1}^3 TC_{\epsilon'}^{(a,n)} \Delta_{ai}^n + \sum_{n=1}^3 TC_{\epsilon'}^{(b,n)} \Delta_{bi}^n \right] + \frac{2\alpha'}{\epsilon_0} \left(\frac{h_i}{r_i} \right), \quad (\text{B.6})$$

The fitting equation for ϵ'_{R11} can be rewritten in matrix form, with i the measurement index,

$$\begin{bmatrix} 1 & \Delta_{a1} & \Delta_{a1}^2 & \Delta_{a1}^3 & \Delta_{b1} & \Delta_{b1}^2 & \Delta_{b1}^3 & h_1/r_1 \\ \vdots & \vdots & \vdots & \vdots & \vdots & \vdots & \vdots & \vdots \\ 1 & \Delta_{ai} & \Delta_{ai}^2 & \Delta_{ai}^3 & \Delta_{bi} & \Delta_{bi}^2 & \Delta_{bi}^3 & h_i/r_i \end{bmatrix} \begin{bmatrix} \epsilon'_{R11} \\ TC_{\epsilon'_{11}}^{(a,1)} \\ TC_{\epsilon'_{11}}^{(a,2)} \\ TC_{\epsilon'_{11}}^{(a,3)} \\ TC_{\epsilon'_{11}}^{(b,1)} \\ TC_{\epsilon'_{11}}^{(b,2)} \\ TC_{\epsilon'_{11}}^{(b,3)} \\ \frac{2\alpha'_{11}}{\epsilon_0} \end{bmatrix} = \begin{bmatrix} \epsilon'_{meas11}(T_1) \\ \vdots \\ \epsilon'_{meas11}(T_i) \end{bmatrix}. \quad (\text{B.7})$$

The data variables h/r , ϵ'_{meas} , Δ , Δ_a , and Δ_b are normalized by their mean and scaled by their standard deviation prior to the fitting so that the matrix elements are closer in magnitude and the matrices being solved have lower condition numbers for numerical stability [397].

The matrix representations of the surface fitting, (B.4) and (B.7), have the familiar linear system form of $Ax = B$, where A is the data matrix of the independent variables (temperature and h/r), B is the data matrix of the dependent variable (measured permittivity), and x is the vectors of unknown coefficients of the surface fit. The surface fit is calculated by total least squares (TLS) minimization, which accounts for the uncertainty in both the dependent and independent variables [363–365]. The ordinary least squares (OLS) solution $x = B \backslash A$ assumes that there is uncertainty only in the measurement of the dependent variables, which is not the case in this work. In the fitting the temperature and h/r ratio are the independent variables and are measured with a non-negligible uncertainty, necessitating TLS for accurate fitting.

Weighted TLS (WTLS) extends TLS to include the uncertainty of the known variables in the data fitting [365, 424] and was used to in the data extraction to include the estimated uncertainties in all the measured variables. The calculation

utilizes a covariance matrices for each measurement data point, with the diagonal elements the uncertainties and and the cross terms the correlation between measured quantities.

The TLS formulation starts from the familiar form for a system of linear equations

$$AX \approx B \quad (\text{B.8})$$

where A is a n by m matrix of the independent variables, X is a m by p matrix of the unknown fitting parameters, and B is a n by p matrix of the dependent variables; n is the number of measurements, m is the number of dependent variables and fitting parameters, and p is the number of independent variables. The A and B are determined via measurements with error and the TLS solution to (B.8) is where the error in both A and B are minimized, specifically [365, 424]

$$\min_{\Delta A, \Delta B, \hat{X}} \|[\Delta A \Delta B]\|_F^2 \quad \text{subject to} \quad (A - \Delta A) \hat{X} = B - \Delta B, \quad (\text{B.9})$$

where F indicates the Frobenius matrix norm, \hat{X} is the TLS solution, and $[\Delta A \Delta B]$ are the TLS correction matrices.

Weighted TLS modifies the problem by weighting each measurement by the estimated uncertainty [365]. The WTLS problem is a optimization problem to find the solution, \hat{X}_{wtls} , that minimizes the weighted TLS misfit, M_{wtls} , and is defined by [365]

$$\hat{X}_{wtls} = \arg \min_X M_{wtls}(X). \quad (\text{B.10})$$

The WTLS misfit is calculated by [365]

$$M_{wtls}(X) = \sqrt{\sum_{i=1}^n d_i^\top R^\top (R W_i^{-1} R^\top)^{-1} R d_i} \quad (\text{B.11})$$

where

$$D = [A^\top; B^\top] = [d_1 \cdots d_i \cdots d_n],$$

$$R = [X^\top, -I],$$

$$W_i = V_i^{-1},$$

and V_i is the covariance matrix of the problem variables for the i^{TH} measurement with the diagonal terms the estimated measurement uncertainty of each variable.

The weighted TLS solution for the unknown model parameter vector is the calculated using the normalized data set of h/r , ϵ'_{meas} , and Δ . The results from the fitting of the normalized data set are used to calculate the constants and temperature coefficients for the non-normalized variables. The uncertainty of the model parameters is calculated from the covariance matrix of the solution [425] and are propagated through the denormalization utilizing standard error propagation analysis [367]. The uncertainty bounds of the best-fit function is smaller for the parameters using the normalized data than for the temperature coefficient parameters for the unmodified data because they are referenced to room temperature, which is at the edge of the normalized data set so has higher uncertainty. The uncertainty determined for each fitting parameter reflects the estimated accuracy of that value but lead to an over estimate of the total uncertainty of the best-fit curve. Therefore the uncertainty of the fit curve using the normalized data will be reported to better reflect the actual uncertainty in predicting the measured variable at a specific temperature.

Appendix C

ADDITIONAL RUS CALCULATION, FABRICATION, AND MEASUREMENT DETAILS

C.1 Derivation of the Lagrangian for Piezoelectric Material

The Lagrangian integral for a piezoelectric crystal, given in (3.2), is used in Chapter 3 to determine the natural vibration modes of a piezoelectric crystal sample. It is derived here from the fundamental piezoelectric constitutive equations, following the derivations by Tiersten [390, 391] and by Holland and Eer Nisse [375, 376, 392–394]. Samples under RUS inspection are bare, without electrodes, are supported and excited by negligible forces, and experience low amplitude vibrations, therefore the RUS spectra can be calculated as the natural modes of vibration.

The Lagrangian minimization technique, utilized in 3 to determine the resonant vibration modes of a piezoelectric crystal sample, originates from Hamilton’s variational principle [390, 391]. Hamilton’s principle is a fundamental formulation in physics that is used to describe a system with the variation of a single function containing the kinetic and potential energies. The energy relations, boundary conditions, and constitutive equations can be used to determine the equations of motion of a system [390, 391].

According to Hamilton’s principle a system that is conservative and holonomic (the variables depend on position and time) can be described using the Lagrangian function, L , and the system dynamics can be described by the equation [390, 391]

$$\delta \int_{t_0}^t L \, dt = 0 \tag{C.1}$$

where the differential, δ , indicates the variation in the Lagrangian due to small variations in the generalized coordinates and velocities, which for a piezoelectric medium are given by the displacements and electric potential [390, 391].

The Lagrangian function of a piezoelectric medium is defined as as [390, 391]

$$L = \iiint_V [K - H] \, dV \quad (\text{C.2})$$

where K is the kinetic energy and H is the electric enthalpy, which is the system potential energy of the system minus the electric potential energy of the space displaced by the piezoelectric medium.

The kinetic energy is [390, 391]

$$K = \frac{1}{2} \rho v_j^2, \quad (\text{C.3})$$

where v_j is the particle velocity along the x_j direction.

The electric enthalpy is [297, 390, 391, 426]

$$H = U - E_i D_i, \quad (\text{C.4})$$

where U is the stored potential energy of the piezoelectric media, E_i is the electric field, and D_i is the electric displacement field.

The energy is described by the first law of thermodynamics [297, 391]

$$\dot{U} = \mathcal{T}_{ij} \dot{S}_{ij} + E_i \dot{D}_i, \quad (\text{C.5})$$

where \mathcal{T}_{ij} is the strain tensor.

The time differential of the electric enthalpy (C.4) is

$$\dot{H} = \dot{U} - D_i \dot{E}_i - E_i \dot{D}_i, \quad (\text{C.6})$$

and combining (C.5) yields

$$\dot{H} = \mathcal{T}_{ij} \dot{S}_{ij} - D_i \dot{E}_i. \quad (\text{C.7})$$

The time-differentials in (C.7) imply that H is a function of S_{ij} and E_i , so (C.7) becomes [391]

$$\dot{H} = \frac{\partial H}{\partial S_{ij}} \dot{S}_{ij} + \frac{\partial H}{\partial E_i} \dot{E}_i. \quad (\text{C.8})$$

According to [297, 390, 391] the electric enthalpy is given by

$$H = \frac{1}{2}c_{ijkl}^E S_{ij}S_{kl} - e_{kij}E_k S_{ij} - \frac{1}{2}\epsilon_{ij}^S E_i E_j, \quad (\text{C.9})$$

which will be shown to be consistent with the piezoelectric constitutive equations.

Comparing (C.7) and (C.8) yields

$$\mathcal{T}_{ij} = \frac{\partial H}{\partial S_{ij}} \quad (\text{C.10})$$

and

$$D_i = -\frac{\partial H}{\partial E_i}. \quad (\text{C.11})$$

Taking the derivative (C.9) with respect to S_{ij} and yields

$$\frac{\partial H}{\partial S_{ij}} = c_{ijkl}^E S_{kl} - e_{kij}E_k, \quad (\text{C.12})$$

noting that

$$\frac{\partial S_{ij}}{\partial S_{ij}} = 0 \text{ for } i \neq j.$$

The derivative (C.9) with respect to E_i is

$$\frac{\partial H}{\partial E_i} = -e_{ijk}S_{kl} - \epsilon_{ij}^S E_j. \quad (\text{C.13})$$

Combining (C.10) through (C.13) yields the piezoelectric constitutive equations [297, 390, 391]

$$\begin{aligned} \mathcal{T}_{ij} &= c_{ijkl}^E S_{kl} - e_{kij}E_k \\ D_i &= e_{ikl}S_{kl} + \epsilon_{ij}^S E_j. \end{aligned} \quad (\text{C.14})$$

Now the Lagrangian equation (C.2) for a free piezoelectric media can be found using the electric enthalpy (C.9) and is

$$L = \iiint_V \left[\frac{1}{2}\rho v_j^2 - \frac{1}{2}c_{ijkl}^E S_{ij}S_{kl} + e_{ijk}E_i S_{jk} + \frac{1}{2}\epsilon_{ij}^S E_i E_j \right] dV. \quad (\text{C.15})$$

C.2 Expanded Interaction Matrices for Legendre Basis Functions

In this section the elastic, piezoelectric, and dielectric interaction matrices are expanded for calculation with Legendre polynomial basis functions for rectangular parallelepiped samples with crystal class 32 symmetry.

The elastic, piezoelectric, and dielectric interaction matrices, defined in (3.15), (3.16), and (3.17), respectively, can be simplified by for a homogeneous elastic medium since $S_{ij} = S_{ji}$ and the acoustic constants do not change with position [427]. The interaction matrices with explicit derivatives and summations become

$$\Gamma_{pp'} = \sum_{j=1}^3 \sum_{j'=1}^3 c_{ijj'j'} \iiint_V \frac{d\Psi^{(p)}}{dx_j} \frac{d\Psi^{(p')}}{dx_{j'}} dV \quad (\text{C.16})$$

$$\Omega_{pr} = \sum_{j=1}^3 \sum_{j'=1}^3 e_{jj'ij} \iiint_V \frac{d\Psi^{(r)}}{dx'_j} \frac{d\Psi^{(p)}}{dx_j} dV \quad (\text{C.17})$$

$$\Lambda_{rr'} = \sum_{j=1}^3 \sum_{j'=1}^3 \epsilon_{ij} \iiint_V \frac{d\Psi^{(r)}}{dx_j} \frac{d\Psi^{(r')}}{dx'_j} dV \quad (\text{C.18})$$

where, as defined in Section 3.2.1, the matrix index p represent a set of the direction index i and basis indices (α, β, γ) and the matrix index r represents a set of (α, β, γ) , and the integration is over the volume of the sample.

The integration of the basis functions is common to each interaction matrix and can be defined as

$$G_{j,j'}^{(k,k')} = \iiint_V \frac{d\Psi^{(k)}}{dx_j} \frac{d\Psi^{(k')}}{dx_{j'}} dV. \quad (\text{C.19})$$

There are nine G matrices for different combinations of (j, j') and the indices (k, k') can be either p, p', r , or r' .

The interaction matrices can be easily calculated from the acoustic constants and the integrated basis G matrices, which depend only on the sample geometry and the

basis functions.

$$\Gamma_{pp'} = \sum_{j=1}^3 \sum_{j'=1}^3 c_{ijj'} G_{j,j'}^{(p,p')} \quad (\text{C.20})$$

$$\Omega_{pr} = \sum_{j=1}^3 \sum_{j'=1}^3 e_{j'ij} G_{j,j'}^{(p,r)} \quad (\text{C.21})$$

$$\Lambda_{rr'} = \sum_{j=1}^3 \sum_{j'=1}^3 \epsilon_{ij} G_{j,j'}^{(r,r')} \quad (\text{C.22})$$

For Legendre polynomial basis functions, defined in (3.11), and a parallelepiped samples with edge lengths $2l_1$, $2l_2$, and $2l_3$, the integrated basis matrices become

$$G_{j,j'}^{(k,k')} = (l_1 l_2 l_3)^{-1} \iiint_V \left[\frac{d}{dx_j} \left(\bar{P}_\alpha(x_1/l_1) \bar{P}_\beta(x_2/l_2) \bar{P}_\gamma(x_3/l_3) \right) \cdots \right. \\ \left. \frac{d}{dx_{j'}} \left(\bar{P}_{\alpha'}(x_1/l_1) \bar{P}_{\beta'}(x_2/l_2) \bar{P}_{\gamma'}(x_3/l_3) \right) \right] dV. \quad (\text{C.23})$$

The volume integration can be split into separate integrations over each direction since each Legendre polynomial depends on only one direction. The derivatives alter the x_j and $x_{j'}$ integrations, so depending on (j, j') an integration could include the derivative of none, one, or both of the Legendre polynomials.

Legendre polynomials are orthogonal, given by (3.12), so when there are no derivatives in the integration of x_j it becomes

$$\frac{1}{l_j} \int_{-l_j}^{l_j} \bar{P}_\eta(x_j/l_j) \bar{P}_{\eta'}(x_j/l_j) dx_j = \int_{-1}^1 \bar{P}_\eta(u) \bar{P}_{\eta'}(u) du = \delta_{\eta,\eta'} \quad (\text{C.24})$$

where j is the particular direction being integrated and η is replaced by the relevant index α , β , or γ .

The derivative of a Legendre polynomial of degree n can be replaced with lower order polynomials by the following relation [428]

$$\begin{aligned} \frac{d}{dx} \left(P_n(x) \right) &= (2(n-1)+1)P_{n-1} + (2(n-3)+1)P_{n-3} + \cdots \\ &= \sum_i (2(n-2i-1)+1)P_{n-2i-1} \end{aligned} \quad (\text{C.25})$$

where

$$i = \begin{cases} 0, 1, 2, \dots, n/2 - 1 & \text{when } n \text{ is even} \\ 0, 1, 2, \dots, n/2 - 1/2 & \text{when } n \text{ is odd.} \end{cases}$$

The stopping condition for i is such that the order of the Legendre polynomial doesn't become negative. The differentiation recursion relation is rewritten for normalized Legendre polynomials, $\bar{P}_\alpha(x) = \sqrt{(2\alpha+1)/(2)}P_\alpha$, to be

$$\begin{aligned} \frac{d}{dx}(\bar{P}_n(x)) &= \sqrt{2n+1} \left(\sqrt{2(n-1)+1} \bar{P}_{n-1} + \sqrt{2(n-3)+1} \bar{P}_{n-3} + \dots \right) \\ &= \sqrt{2n+1} \sum_i \sqrt{2(n-2i-1)+1} \bar{P}_{n-2i-1}. \end{aligned} \quad (\text{C.26})$$

The integration term that contains a single derivative is

$$\frac{1}{l_j} \int_{-l_j}^{l_j} \bar{P}_\eta(x_j/l_j) \frac{d}{dx_j}(\bar{P}_{\eta'}(x_j/l_j)) dx_j = \frac{1}{l_j} \int_{-1}^1 \bar{P}_\eta(u) \frac{d}{du}(\bar{P}_{\eta'}(u)) du \quad (\text{C.27})$$

where the derivative is taken with respect to η' here without loss of generality.

The derivative is replaced by Legendre polynomials of lower order and opposite parity with (C.26). The integral is non-zero only when the term $(\eta' - 2i - 1) = \eta$ holds true for some non-negative number i due to the orthogonal Legendre polynomials. Therefore, the integral (C.27) becomes

$$\frac{1}{l_j} \int_{-l_j}^{l_j} \bar{P}_\eta(x_j/l_j) \frac{d}{dx_j}(\bar{P}_{\eta'}(x_j/l_j)) dx_j = \frac{1}{l_j} E_{\eta\eta'} \quad (\text{C.28})$$

where $E_{\eta\eta'}$ is defined by

$$E_{\eta\eta'} = \begin{cases} \sqrt{2\eta+1} \sqrt{2\eta'+1} & \text{for } \eta < \eta' \text{ \& } \eta + \eta' = \text{odd} \\ 0 & \text{otherwise.} \end{cases} \quad (\text{C.29})$$

If the integration along x_j has derivatives on both polynomials, it is

$$\begin{aligned} \frac{1}{l_j^2} D_{\eta\eta'} &= \frac{1}{l_j} \int_{-l_j}^{l_j} \frac{d}{dx_j} \bar{P}_\eta(x_j/l_j) \frac{d}{dx_j}(\bar{P}_{\eta'}(x_j/l_j)) dx_j \\ &= \frac{1}{l_j^2} \int_{-1}^1 \frac{d}{du} \bar{P}_\eta(u) \frac{d}{du}(\bar{P}_{\eta'}(u)) du \end{aligned} \quad (\text{C.30})$$

where $D_{\eta\eta'}$ is the matrix of the solved integrations that will be given next.

The derivatives are each replaced by (C.26) a collection of Legendre polynomials of opposite parity and lower order which are multiplied together. If the two differentiated polynomials have different parity then none of orders of the two sets will be the same so the integral will be zero. If the differentiated polynomials have the same parity then the replaced sets do as well and there will be multiple non-zero terms and the integral (C.30) becomes

$$D_{\eta\eta'} = \int_{-1}^1 \left[\sqrt{2\eta+1} \left(\sum_i \sqrt{2(\eta-2i-1)+1} \bar{P}_{(\eta-2i-1)} \right) \cdots \right. \\ \left. \sqrt{2\eta'+1} \left(\sum_{i'} \sqrt{2(\eta'-2i'-1)+1} \bar{P}_{(\eta'-2i'-1)} \right) \right] du. \quad (\text{C.31})$$

The indices η and η' are interchangeable in (C.31), i.e. $D_{\eta\eta'} = D_{\eta'\eta}$ so we can choose them such that $\eta \geq \eta'$. The polynomial terms in the η summation that are higher order than η' can be removed because they are orthogonal to the other terms. Then the multiplied summations are each the same and the cross-terms where the orders are not equal will be removed, resulting in

$$D_{\eta\eta'} = \sqrt{2\eta+1} \sqrt{2\eta'+1} \sum_{i'} (2(\eta'-2i'-1)+1) \int_{-1}^1 \bar{P}_{(\eta-2i-1)} \bar{P}_{(\eta'-2i'-1)} du \\ = \sqrt{2\eta+1} \sqrt{2\eta'+1} \sum_{i'} (2(\eta'-2i'-1)+1). \quad (\text{C.32})$$

for $\eta \geq \eta'$ and $\eta + \eta' = \text{even}$. The summation in (C.32) can be further simplified because it is finite with either $\eta'/2$ terms if η' is even or $(\eta'+1)/2$ terms if η' is odd and both cases result in

$$D_{\eta\eta'} = \left\{ \begin{array}{ll} \frac{1}{2} \eta' (\eta' + 1) \sqrt{2\eta+1} \sqrt{2\eta'+1} & \eta + \eta' = \text{even} \\ 0 & \eta + \eta' = \text{odd} \end{array} \right\} \text{ with } \eta \geq \eta'. \quad (\text{C.33})$$

The matrices $G_{jj'}$ in (C.23) can now be simplified using the possible cases for the combinations of derivatives given by (C.24), (C.29), and (C.33).

$$\begin{aligned}
G_{11} &= D_{\alpha\alpha'} \delta_{\beta\beta'} \delta_{\gamma\gamma'} / l_1^2 \\
G_{22} &= \delta_{\alpha\alpha'} D_{\beta\beta'} \delta_{\gamma\gamma'} / l_2^2 \\
G_{33} &= \delta_{\alpha\alpha'} \delta_{\beta\beta'} D_{\gamma\gamma'} / l_3^2 \\
G_{32} &= \delta_{\alpha\alpha'} E_{\beta\beta'} E_{\gamma\gamma'} / (l_2 l_3) \\
G_{23} &= \delta_{\alpha\alpha'} E_{\beta'\beta} E_{\gamma\gamma'} / (l_2 l_3) \\
G_{13} &= E_{\alpha'\alpha} \delta_{\beta\beta} E_{\gamma\gamma'} / (l_1 l_3) \\
G_{31} &= E_{\alpha\alpha'} \delta_{\beta\beta} E_{\gamma'\gamma} / (l_1 l_3) \\
G_{21} &= E_{\alpha\alpha'} E_{\beta'\beta} \delta_{\gamma\gamma'} / (l_1 l_2) \\
G_{12} &= E_{\alpha'\alpha} E_{\beta\beta'} \delta_{\gamma\gamma'} / (l_1 l_2)
\end{aligned} \tag{C.34}$$

The matrices $G_{jj'}$ correspond to $G_1 \cdots G_9$ used in [319].

The acoustic constants can be converted from tensor form to matrices using the Voigt or matrix notation to define $c_{ijkl} = c_{pq}$ and $e_{ikl} = e_{ip}$, with p and q given in Table C.1.

ij or kl	p or q
11	1
22	2
33	3
32 or 23	4
13 or 31	5
12 or 21	6

Table C.1. Voigt index notation

From (C.20), (C.21), and (C.22), the interaction matrices are

$$\begin{array}{ll}
(i,i') = & \Gamma_{pp'} = \\
(1,1) & c_{11}G_{11} + c_{66}G_{22} + c_{55}G_{33} + c_{56}G_{32} + c_{56}G_{23} + \\
& c_{15}G_{13} + c_{15}G_{31} + c_{16}G_{21} + c_{16}G_{12} \\
(1,2) & c_{16}G_{11} + c_{26}G_{22} + c_{45}G_{33} + c_{25}G_{32} + c_{46}G_{23} + \\
& c_{14}G_{13} + c_{56}G_{31} + c_{66}G_{21} + c_{12}G_{12} \\
(1,3) & c_{15}G_{11} + c_{46}G_{22} + c_{35}G_{33} + c_{45}G_{32} + c_{36}G_{23} + \\
& c_{13}G_{13} + c_{55}G_{31} + c_{56}G_{21} + c_{14}G_{12} \\
(2,1) & c_{16}G_{11} + c_{26}G_{22} + c_{45}G_{33} + c_{46}G_{32} + c_{25}G_{23} + \\
& c_{56}G_{13} + c_{14}G_{31} + c_{12}G_{21} + c_{66}G_{12} \\
(2,2) & c_{66}G_{11} + c_{22}G_{22} + c_{44}G_{33} + c_{24}G_{32} + c_{24}G_{23} + \\
& c_{46}G_{13} + c_{46}G_{31} + c_{26}G_{21} + c_{26}G_{12} \\
(2,3) & c_{56}G_{11} + c_{24}G_{34} + c_{34}G_{33} + c_{44}G_{32} + c_{23}G_{23} + \\
& c_{36}G_{13} + c_{45}G_{31} + c_{25}G_{21} + c_{46}G_{12} \\
(3,1) & c_{15}G_{11} + c_{46}G_{22} + c_{35}G_{33} + c_{36}G_{32} + c_{45}G_{23} + \\
& c_{55}G_{13} + c_{13}G_{31} + c_{14}G_{21} + c_{56}G_{12} \\
(3,2) & c_{56}G_{11} + c_{24}G_{34} + c_{34}G_{33} + c_{23}G_{32} + c_{44}G_{23} + \\
& c_{45}G_{13} + c_{36}G_{31} + c_{46}G_{21} + c_{25}G_{12} \\
(3,3) & c_{55}G_{11} + c_{44}G_{34} + c_{33}G_{33} + c_{34}G_{32} + c_{34}G_{23} + \\
& c_{35}G_{13} + c_{35}G_{31} + c_{45}G_{21} + c_{45}G_{12}
\end{array} \tag{C.35}$$

$$(i) = \Omega_{pp'} =$$

$$\begin{aligned}
(1) \quad & e_{11}G_{11} + e_{26}G_{22} + e_{35}G_{33} + e_{25}G_{32} + e_{36}G_{23} + \\
& e_{31}G_{13} + e_{15}G_{31} + e_{16}G_{21} + e_{21}G_{12} \\
(2) \quad & e_{16}G_{11} + e_{22}G_{22} + e_{34}G_{33} + e_{24}G_{32} + e_{32}G_{23} + \\
& e_{36}G_{13} + e_{14}G_{31} + e_{12}G_{21} + e_{26}G_{12} \\
(3) \quad & e_{15}G_{11} + e_{24}G_{22} + e_{33}G_{33} + e_{23}G_{32} + e_{34}G_{23} + \\
& e_{35}G_{13} + e_{13}G_{31} + e_{14}G_{21} + e_{25}G_{12}
\end{aligned} \tag{C.36}$$

$$\begin{aligned}
\Lambda_{pp'} = & \epsilon_{11}G_{11} + \epsilon_{22}G_{22} + \epsilon_{33}G_{33} + \epsilon_{23}G_{32} + \epsilon_{23}G_{23} \cdots \\
& \epsilon_{13}G_{13} + \epsilon_{13}G_{31} + \epsilon_{12}G_{21} + \epsilon_{12}G_{12}
\end{aligned} \tag{C.37}$$

For class 32 crystals (e.g. LGT, LGS, and quartz) the elastic, piezoelectric and dielectric constants matrices are given by (A.1), (A.2), and (A.3) and the RUS interaction matrices reduce to

$$(i,i') = \Gamma_{pp'} =$$

$$\begin{aligned}
(1,1) \quad & c_{11}G_{11} + c_{66}G_{22} + c_{44}G_{33} + 2c_{14}G_{32} + 2c_{14}G_{23} \\
(1,2) \quad & 2c_{14}G_{33} + c_{14}G_{13} + 2c_{14}G_{31} + c_{66}G_{21} + (c_{11} + 2c_{66})G_{12} \\
(1,3) \quad & c_{13}G_{13} + c_{44}G_{31} + 2c_{14}G_{21} + c_{14}G_{12} \\
(2,1) \quad & 2c_{14}G_{13} + c_{14}G_{31} + (c_{11} + 2c_{66})G_{21} + c_{66}G_{12} \\
(2,2) \quad & c_{66}G_{11} + c_{11}G_{22} + c_{44}G_{33} - c_{14}G_{32} - c_{14}G_{23} \\
(2,3) \quad & 2c_{14}G_{11} - c_{14}G_{34} + c_{44}G_{32} + c_{13}G_{23} \\
(3,1) \quad & c_{44}G_{13} + c_{13}G_{31} + c_{14}G_{21} + 2c_{14}G_{12} \\
(3,2) \quad & 2c_{14}G_{11} - c_{14}G_{34} + c_{13}G_{32} + c_{44}G_{23} \\
(3,3) \quad & c_{44}G_{11} + c_{44}G_{34} + c_{33}G_{33}
\end{aligned} \tag{C.38}$$

$$\begin{array}{ll}
\text{(i)} = & \Omega_{pp'} = \\
\hline
(1) & e_{11}G_{11} - 2e_{11}G_{22} - e_{14}G_{32} \\
(2) & e_{14}G_{31} - e_{11}G_{21} - 2e_{11}G_{12} \\
(3) & e_{14}G_{21} - e_{14}G_{12}
\end{array} \tag{C.39}$$

$$\Lambda_{pp'} = \epsilon_{11}G_{11} + \epsilon_{22}G_{22} + \epsilon_{33}G_{33} \tag{C.40}$$

C.3 Group Theory for Resonant Modes

Group theory has been applied to RUS to separate the eigenvalue problem into separate orthogonal problems by using the symmetry of the crystal sample [316, 318, 319, 377–380, 395]. When the RUS sample shape and crystal lattice have common symmetries the basis functions can be grouped into smaller orthogonal sets. This splits the eigenvalue problem into separate smaller matrices and reduces calculation time because the computational cost scales with the cube of the matrix rank [316, 318, 319, 377–380, 395]. The separate matrices are solved independently to determine the resonant modes that belong to the particular mode group and are combined to determine the resonant modes of the RUS sample.

For a rectangular parallelepiped fabricated from a class 32 crystal, such as LGT, the basis functions and resultant vibration modes can be divided into four groups when the sample faces are aligned along the crystalline axes [318, 319, 379], as was the case in this work discussed in Section 3.2. The mode groups are denoted A_g , B_g , A_u , and B_u by [379] and are separated by the symmetry operations of the displacements and electric potential. In this work, the groups are simply labeled by number, 1 through 4, for the groups A_g , B_g , A_u , and B_u . When using Legendre polynomial basis functions, defined in (3.11), the groups are found using the symmetry or antisymmetry about the origin of the function, which are given by the parity of the Legendre polynomial degree in Table C.2, after [318, Table 1].

Mode Group		Displacement						Electric potential	
		u_1		u_2		u_3		ϕ	
		α	$\beta + \gamma$	α	$\beta + \gamma$	α	$\beta + \gamma$	α	$\beta + \gamma$
1	A_g	O	E	E	O	E	O	O	E
2	B_g	E	O	O	E	O	E	E	O
3	A_u	E	E	O	O	O	O	E	E
4	B_u	O	O	E	E	E	E	O	O

Table C.2. Mode grouping of the Legendre polynomial basis functions. Given by the polynomial degrees (α , β , and γ) parity with E=even, O=odd. After [318, Table 1]

The basis functions are sorted by into four groups according to Table C.2 and used separately to define independent elastic, piezoelectric, and dielectric interaction matrices ((3.15), (3.16), and (3.17)), which are used to define independent eigenvalues problems. The problems are solved separately and the resultant resonant frequencies are combined to form the spectra.

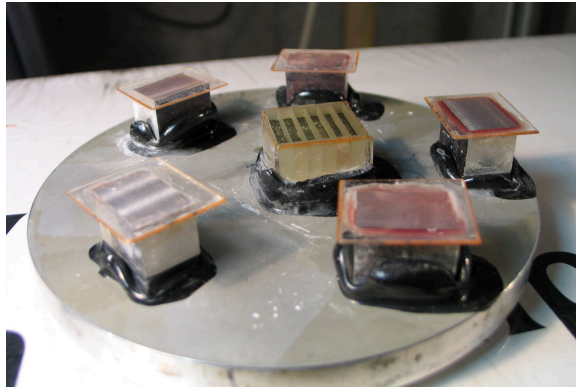
C.4 RUS Sample Fabrication Process

The RUS sample fabrication overviewed in Section 3.3.1 is discussed with further detail in this section. The UMaine LGT samples were aligned with a PANalytical X'Pert Pro MRD X-ray diffractometer (PANalytical Inc., Natick, Corp., Waltham, MA) and cut with an inner diameter saw (Meyer-Berger, Steffisberg, Switzerland) to nominal dimensions of (2.9 mm, 12.6 mm, 18.6 mm). The process starts by epoxying the crystal boule to the chuck on the saw and manually aligning the cut to the faces of the boules, which correspond to the crystal axes. A thin crystal wafer is cut and the orientation is determined by XRD. The misalignment from the desired orientation is precisely determined and corrected on the inner diameter saw, which has two degrees of freedom to correct rotation without removing the samples from the chuck [237, 408, 409]. Once the orientation is corrected, new cuts are made to define one side of the parallelepiped and the process is repeated until all sides of the

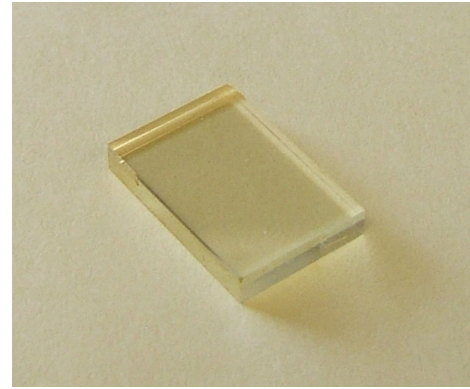
samples have been cut. The sample preparation process process (alignment, cutting, grinding, and polishing) at UMaine was shown to have achieved wafer orientations within 6 arcminutes [240].

The cut samples were then attached to an aluminum plate with melted polishing pitch (#16 black blocking pitch, Universal Photonics, Hicksville, NY) and then placed sample face down on an optically flat glass plate so that the samples are aligned together and planar. The setup was left overnight for the pitch to cool and harden. Then the wafers were ground to a uniform roughness before being polished to an optical quality using abrasive alumina slurries on automatic rotating polishing machines (R. Howard Strasbaugh 6U, Lynwood, CA). Alumina abrasives are used successively with progressively smaller diameters, from 30 μm to 1 μm (Micro Abrasives Corporation, Westfield, MA). The parallelepiped samples are then rotated and the process is repeated until all the faces are polished. When polishing the largest faces, the samples were laid flat on the plate and evenly spaced on the aluminum plate. However, to polish the narrow edges, the samples were first waxed together in a stack and attached in the center of the aluminum plate because it would be difficult to align the size samples separately when they are resting on the small side (2.9 mm). The combined samples only would not be stable, which would lead to uneven polishing across the sample faces. The polishing plate stability was ensured by placing five metal spacers with glass wafers on the bottom around the plate to form support pillars, as shown in Fig. C.1a. The glass wafer are polished at the same time as the LGT and ensure that the plate is level so that the sample faces are evenly polished. Extra care was taken in the sample handling and fabrication to preserve the sharp corners and parallelism, which would alter the resonant spectra [316]. One of the finished LGT samples is shown in Fig. C.1b.

The dimensions of the completed samples were measured with a Heidenhain-Metro precision length gage (Heidenhain Corp., Schaumburg, IL), the results are reported



(a)



(b)

Figure C.1. LGT samples polished for RUS. (a) samples in the center of aluminum plate surrounded by spacers to polish the smaller sample edges, (b) completed LGT parallelepiped sample

in Section 3.3.1. Multiple measurements on each side of the sample were made so that the random error could be reduced.

C.5 RUS Spectra Measurement Process

The RUS measurement process, frequency determination, and mode identification are given in more detail in this appendix. The first step in the RUS extraction process is to measure the RUS spectra, then the frequencies of the resonant peaks are determined, and the modes are identified over the measured temperature range.

The UMaine RUS measurement fixture and furnace are shown in Fig. 3.3 on page 99.

The RUS spectra measurement procedure for the UMaine high-temperature RUS fixture is as follows:

1. Remove metal panels from the RUS enclosure, labeled (i) in Fig. 3.3, and furnace heater section, (ii) in Fig. 3.3, from the transducer stand (iii) in Fig. 3.3.

2. Reposition the transducer stands, (v) in Fig. 3.3, so that buffer rods form a level tripod, (iv) in Fig. 3.3, and are spaced correctly for the sample to be able to rest on them. If the tripod is not level the sample may fall and be damaged.
3. Set up the RU Spec measurement system. For the LGT samples used in this work, the start frequency was set to 1 kHz, the frequency span to 499 kHz, and the frequency resolution to 16.97 Hz. For other samples the frequency range should be set below the first resonant mode of the sample and high enough to capture the modes required for the fitting process.
4. Record the background spectrum of the buffer rods only.
5. Place the sample on the buffer rods and measure a spectrum. Reposition the sample to attempt to get a stronger response and an increased number of high magnitude modes do to the transducer placement on the crystal.
6. Replace the heater and enclosure panels carefully so the sample is not disturbed.
7. Allow the measured temperature reading to return to a stable value. Measure the room-temperature resonance spectrum and the thermocouple reading.
8. Change the furnace set point to next measurement temperature and wait for the temperature to stabilize. Record the spectrum and thermocouple readings.
9. Repeat the previous steps until all desired temperatures are measured. Then turn off the furnace and let it cool to room temperature before opening the furnace enclosure.

The resonant frequencies were determined from the peaks in the spectrum measurements. Most of the resonant modes have strong, obvious peaks and there is no ambiguity in the location of the resonant frequency. However, some modes have weak amplitudes near the noise level and others were affected by modes with

larger amplitude. Therefore the spectra without the sample in place was captured to record the background noise and transducer modes so that the any false peaks will not be selected. The background signal cannot simply be subtracted from the spectrum measurements because the background modes shift with temperature due the heating of the transducers when the furnace is active. Instead the background helped the user to not select background modes as resonant peaks.

The resonant modes of the sample under test were extracted from the resonant spectra measurements using a script custom-written in MATLAB (Mathworks, Natick, MA) to identify candidate resonant peaks by finding local maxima. User input was required to remove background noise peaks and to identify peaks that were weak or close to other peaks. At room temperature the crystal resonant peaks were strong and match well with predicted modes from established room-temperature constants, allowing mode identification with minimal user input. However, as the measurement temperature increased, the peaks got weaker due to the intrinsic acoustic losses and the modes were less distinguishable from the noise. The user attempted to track each individual mode as it shifts with temperature so that it is correctly matched with the corresponding calculated mode. Modes that overlap, cross, or were ambiguous were noted by the user, not used in the initial fitting process, and only considered in the analysis if the mode identity and traceability could be established.

The mode matching process consisted of using a preliminary set of material constants to calculate the resonant modes and aligning the predicted and measurement modes. If the starting set of constants was accurate, the measurement and predicted modes would be very close and it was simple to identify the measured modes. However, even with good constants some of the measured modes were be close to each other and difficult to identify. Additionally, the agreement between the measured and predicted modes was typically worse at higher frequencies. Therefore, the modes that were obviously aligned with the predicted modes were included in

the extraction process and the others were ignored for the time being. The reduced set of modes was then used to extract a new set of constants. Next, the revised constants were used to calculate the resonant modes and the mode matching process was repeated with more modes included because the new constants were more accurate than the starting set of constants. The final extracted set of constants was still accepted even if up to 5 % of the modes were not included in the fitting because it is preferable to ignore modes instead of using the wrong modes in the minimization [316].

The mode matching at elevated temperatures was further complicated by modes that cross each other due to different temperature coefficients and modes that decay with temperature. It was found that a preliminary set of constants and temperature coefficients could be used to predict mode behavior with temperature as further means of mode identification and separation. The LGT constants extracted up to 400 °C were used to determine preliminary temperature coefficient polynomials and extrapolated to high temperatures in order to aid mode identification above 400 °C.

In this work, the resonant modes are described by both the mode group, described in Section C.3, and the mode order within the group. When the modes were identified only by the order, ignoring the groups, they were often found to switch order in the fitting process as new trial sets of constants were used by the optimization function. This created a mode mismatch that could not be corrected because it occurs dynamically in the minimization. By including the mode groups, the mode switching was much less common because the modes in different groups cannot be confused, reducing the sensitivity of the fit constants to the start values. The inclusion of group identification was very important to the extraction of constants at elevated temperature where the actual constants may be quite different from the previous temperature constants used to start the minimization.

The spectrum from successive temperatures were plotted with the vertical scale shifted so that the spectra from multiple temperatures could be observed at the same

time. This allowed the user to see the mode trend with temperature and the shape of a mode to differentiate it from background signals. As an example, the temperature variation of selected resonance modes of an LGT sample is shown in Fig. C.2 with measurements at each 50 °C from room temperature to 1100 °C.

C.6 Jacobian Matrix for Minimization Process

The minimization procedure utilizes the the derivatives of each resonant frequency with respect to each of the acoustic parameters, contained in the Jacobian matrix, to estimate how a change in the parameters would improve frequency fitting. The (m, n) element of the Jacobian matrix is $\partial f_m / \partial x_n$, where f_m is the m^{th} calculated resonant frequency and x_n is the n^{th} acoustic parameters being fit, where for class 32 crystals $x = \{c_{11}, c_{13}, c_{14}, c_{33}, c_{44}, c_{66}, e_{11}, e_{14}\}$.

The fit acoustic parameters and the resonance frequencies are related by the eigenvalue problem (3.25), taking the partial derivative with respect to one of the acoustic parameters x_n yields

$$\begin{aligned} \frac{\partial}{\partial x_n} (\rho \omega^2 I \mathbf{a}) &= \frac{\partial}{\partial x_n} \left((\Gamma + \Omega \Lambda^{-1} \Omega^t) \mathbf{a} \right) \\ \frac{\partial(\rho \omega^2)}{\partial x_n} I \mathbf{a} + \rho \omega^2 I \frac{\partial \mathbf{a}}{\partial x_n} &= \frac{\partial (\Gamma + \Omega \Lambda^{-1} \Omega^t)}{\partial x_n} \mathbf{a} + (\Gamma + \Omega \Lambda^{-1} \Omega^t) \frac{\partial \mathbf{a}}{\partial x_n}. \end{aligned} \quad (\text{C.41})$$

Rearrange to gather the eigenvectors.

$$(\rho \omega^2 I - (\Gamma + \Omega \Lambda^{-1} \Omega^t)) \frac{\partial \mathbf{a}}{\partial x_n} = \left(-\rho \frac{\partial \omega^2}{\partial x_n} I + \frac{\partial (\Gamma + \Omega \Lambda^{-1} \Omega^t)}{\partial x_n} \right) \mathbf{a} \quad (\text{C.42})$$

Multiply on the left by the left eigenvectors, which are \mathbf{a}^t since the matrix $(\Gamma + \Omega \Lambda^{-1} \Omega^t)$ is symmetric.

$$\mathbf{a}^t (\rho \omega^2 I - (\Gamma + \Omega \Lambda^{-1} \Omega^t)) \frac{\partial \mathbf{a}}{\partial x_n} = \mathbf{a}^t \left(-\rho \frac{\partial \omega^2}{\partial x_n} I + \frac{\partial (\Gamma + \Omega \Lambda^{-1} \Omega^t)}{\partial x_n} \right) \mathbf{a} \quad (\text{C.43})$$

Note that $\mathbf{a}^t I \mathbf{a} = 1$, therefore

$$\mathbf{a}^t \left(-\rho \frac{\partial \omega^2}{\partial x_n} I \right) \mathbf{a} = -\rho \frac{\partial \omega^2}{\partial x_n} \mathbf{a}^t I \mathbf{a} = -\rho \frac{\partial \omega^2}{\partial x_n} \quad (\text{C.44})$$

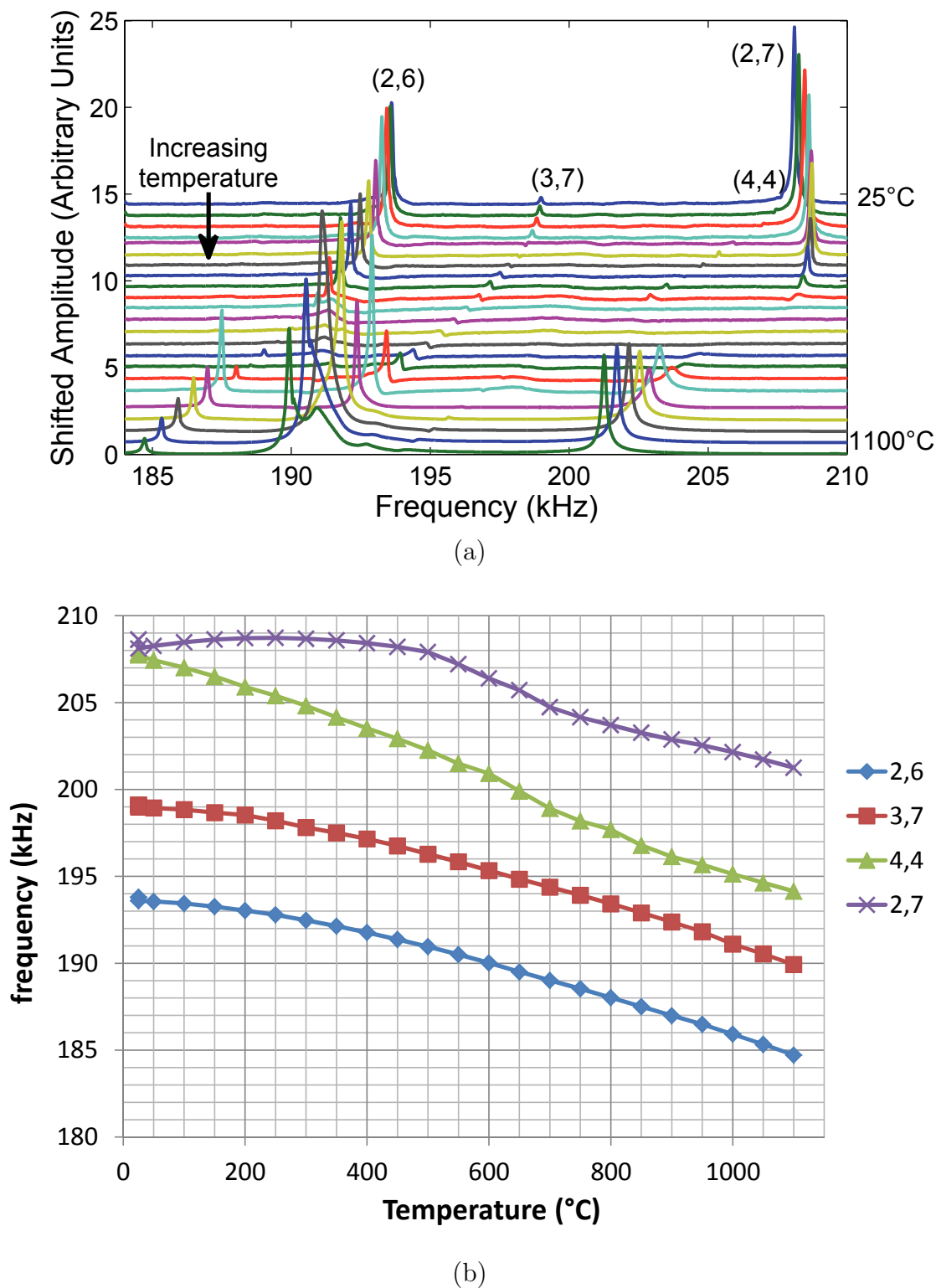


Figure C.2. Example LGT RUS spectra from 25 to 1100°C for selected modes of sample LGT10. (a) Spectra shown at every 50°C with amplitudes shifted downward with increasing temperature to show temperature behavior, (b) extracted frequencies for modes (2,6), diamond; (3,7), square; (4,4), triangle; and (2,7), x.

The term $\mathbf{a}^t (\rho\omega^2 I - (\Gamma + \Omega\Lambda^{-1}\Omega^t))$ is the left-eigenvector equation so is equal to zero and the terms on the right-hand side of (C.43) can be equated.

$$\begin{aligned}\rho \frac{\partial \omega^2}{\partial x_n} &= \frac{\partial (\Gamma + \Omega\Lambda^{-1}\Omega^t)}{\partial x_n} \mathbf{a} \\ 8\pi^2 \rho f \frac{\partial f}{\partial x_n} &= \frac{\partial (\Gamma + \Omega\Lambda^{-1}\Omega^t)}{\partial x_n} \mathbf{a}\end{aligned}\tag{C.45}$$

Thus the derivative of the m^{th} resonant frequency is

$$\frac{\partial f_m}{\partial x_n} = \frac{1}{8\pi^2 \rho f} \mathbf{a}_m^t \left(\frac{\partial \Gamma}{\partial x_n} + \frac{\partial \Omega}{\partial x_n} \Lambda^{-1} \Omega^t + \Omega \frac{\partial \Lambda^{-1}}{\partial x_n} \Omega^t + \Omega \Lambda^{-1} \frac{\partial \Omega^t}{\partial x_n} \right) \mathbf{a}_m. \tag{C.46}$$

The derivative of Λ^{-1} is found using

$$\begin{aligned}\Lambda^{-1} \Lambda &= I \\ \frac{\partial \Lambda^{-1}}{\partial x_n} \Lambda + \Lambda^{-1} \frac{\partial \Lambda}{\partial x_n} &= \frac{\partial I}{\partial x_n} = 0 \\ \frac{\partial \Lambda^{-1}}{\partial x_n} &= -\Lambda^{-1} \frac{\partial \Lambda}{\partial x_n} \Lambda^{-1}.\end{aligned}\tag{C.47}$$

Recall that ϵ^S is in general a function of ϵ^T , c , and e , as shown in (2.6).

Combining the above, interaction matrices and their derivatives given in (C.38), (C.39), and (C.40) for class 32 crystals can be easily used to calculate the derivative of each frequency with respect to each acoustic parameter by

$$\frac{\partial f_m}{\partial x_n} = \frac{1}{8\pi^2 \rho f} \mathbf{a}_m^t \left(\frac{\partial \Gamma}{\partial x_n} + \frac{\partial \Omega}{\partial x_n} \Lambda^{-1} \Omega^t - \Omega \Lambda^{-1} \frac{\partial \Lambda}{\partial x_n} \Lambda^{-1} \Omega^t + \Omega \Lambda^{-1} \frac{\partial \Omega^t}{\partial x_n} \right) \mathbf{a}_m. \tag{C.48}$$

BIOGRAPHY OF THE AUTHOR

Peter Davulis was born in May 1983 to John and Theresa Davulis. He grew up in Hallowell, Maine graduated from Hale-Dale High School in 2002. He received his B.S. in Electrical Engineering with a minor in Mathematics in 2006 and M.S. in Electrical Engineering in 2010 from the University of Maine in Orono, Maine.

Peter was first exposed to academic research and started working with Dr. Mauricio Pereira da Cunha in 2005 as a Fellow in the NSF Research Experience for Undergraduates program run by Dr. John Vetelino. In 2006, Peter enrolled in the Electrical Engineering Ph.D. program at the University of Maine and received his M.S.E.E. in 2010. In addition to his dissertation work, since 2008 he has been working under Dr. Mauricio Pereira da Cunha to develop high-temperature SAW sensors, assisting with device characterization, high-temperature measurement automation, wireless communication, and antenna design. Peter has co-authored 2 patent application, 6 peer-reviewed journal publications, and 14 international conference presentations, with more in the submission process. In 2006 he received a Provost Fellowship and in 2010 was a co-winner of the College of Engineering Graduate Assistant Research Award. He received the IEEE Ultrasonics, Ferroelectrics, and Frequency Control Society Student Paper Competition Award for his paper presented at at the 2011 IEEE International Ultrasonics Symposium.

Peter Mark Davulis is a candidate for the Doctor of Philosophy degree in Electrical and Computer Engineering from The University of Maine in December 2013.